Investigations of Multi-component mixtures and complex systems with longer-ranged interactions

Thesis Submitted for the Degree of

Doctor of Philosophy (Science)

of

Jadavpur University

By

Juriti Rajbangshi

Department of Chemical, Biological and Macromolecular Sciences,
S. N. Bose National Centre for Basic Sciences,
Block-JD, Sector-III, Salt Lake
Kolkata-700106, India

February 2021

सत्येन्द्र नाथ बसु राष्ट्रीय मौलिक विज्ञान केन्द्र
SATYENDRA NATH BOSE NATIONAL
CENTRE FOR BASIC SCIENCES
सत्येन्द्र नाथ वसु जातीय मौल विज्ञान केन्द्र

CERTIFICATE FROM THE SUPERVISOR

This is to certify that the thesis entitled "**Investigations of Multi-component mixtures and complex systems with longer-ranged interactions**" submitted by **Smt. Juriti Rajbangshi** (Index No. **252|15|Chem.|24**), who got her name registered on 05/11/2015 for the award of Ph.D. (Science) degree of Jadavpur University, is absolutely based upon her own work under the supervision of **Prof. Ranjit Biswas** and that neither this thesis nor any part of it has been submitted for either any degree/diploma or any other academic award anywhere before.

Ranjit Biswas 22 Feb 2021

Dr. Ranjit Biswas

Senior Professor,

Department of Chemical, Biological and Macromolecular Sciences

S. N. Bose National Centre for Basic Sciences

Block-JD, Sector-III, Salt Lake,

Kolkata-700106, West Bengal, India

DR. RANJIT BISWAS
Senior Professor
Dept. of Chemical, Biological & Macromolecular Sciences
S. N. Bose National Centre for Basic Sciences
Block - JD, Sector-III, Salt Lake, Kolkata - 700 106, India

Dedicated to

My Parents Basundhar Rajbangshi (Deuta),

Saibya Deka (Maa)

And

In the memory of my grandmother

Late Thageswari Deka (Aita)

Acknowledgement

On arriving at the completion of this thesis work, I must express my gratitude to the people, who enriched the journey in many ways. This thesis would not have been possible without their constant support and blessings.

First of all, I would like to express my sincere thanks and deepest gratitude to my supervisor, Prof. Ranjit Biswas. His untiring help, excellent guidance and constant encouragement motivated me always to perform my best. I would also like to thank him for guiding me not only in research but also in life. His patience and immense support helped me to overcome many crisis situations during my PhD journey and to complete my thesis. I am extremely fortunate enough to have worked under the guidance of such a good and ethical person like him and all of his suggestions during these PhD days are priceless. Lastly, I am highly indebted to him for his kind and affectionate attitude, who always stood by me from the very first day of PhD journey.

I express my sincere gratitude to Prof. Pradip Kumar Ghorai, Department of Chemical Sciences, IISER Kolkata for all his help during my simulation work. I would also like to thank Dr. Hemant Kashyap, associate professor, Department of Chemistry, IIT Delhi and his student Aditya Gupta for their great help in learning some simulation software.

My sincere thanks to all the members of my Thesis committee Prof. Samir Kumar Pal (SNBNCBS) and Prof. Goutam Gangopadhyay (SNBNCBS) for devoting their valuable time for me.

I acknowledge all the associates of the Computer Services Cell for their prompt technical assistance regarding any computer and computational clusters related issues. I would like to thank all the faculty members of SNBNCBS, research scholars and non-teaching staffs for their kind help and co-operation. I would also like to thank Ms. Nibedita Konar for all of her help and support during the PhD days. I thank all the canteen boys and cooking team of SNB mess during my stay at SNBNCBS.

I am grateful to S. N. Bose National Centre for Basic Sciences for providing the research fellowship and all academic help.

I heartily thank my present lab mates: Atanu, Kajal, Dhrubajyoti, Jayanta, Narayan, and Amrita for providing me a co-operative environment inside the lab. I am also grateful to them for their all help during the PhD days. I thank the past members of our research group: Dr. Tuhin Pradhan, Dr. Hemant Kashyap, Dr. Harun Al. Rasid Gazi, Dr. Biswajit Guchhait, Dr. Snehasis Daschakraborty, Dr. Tamisra Pal, Dr. Sandipa Indra, Dr. Suman Das, Dr. Kallol Mukherjee, Dr. Anuradha Das, Dr. Ejaj Tarif, and Dr. Shirshendu Dinda for their support and motivation in various academic and non-academic purposes. Especially, I would like to express my sincere thanks to Atanu Baksi for all of his help regarding the programming language and Dr. Tamisra Pal for helping me in learning simulation technique in early PhD days.

I convey my deepest gratitude to Dr. Parijat Das (Biswas) for her caring attitude and especially I am thankful to her for helping me in any medical related issues. I will cherish all the sweat moments I have spent with little Rwitoban (Rwik) and Arshaman (Sham). Every meeting with Rwik and Sham in SNBNCBS were very special to me.

I am very much lucky to have such a group of good friends: Samrat, Dhrimadri, Anuvab, Atanu, Bihalan, Pallabi, Prantik, Sayoni, Debabrata, Mithun. I am very much thankful to them for giving me positive energy in all ups and downs throughout my PhD life.

I am highly indebted to my M.Sc. teacher Professor Prodeep Phukan (Gauhati University) for his constant motivation and encouragement towards research. I want to offer my great respect to that person, who introduced me to the field of science, who supports me constantly and one who have extreme faith on me, he is my B.Sc. teacher Dr. Atul Prasad Sikdar (Mangaldai College, Gauhati University). I am fortunate enough to have a “sikhyaguru” like him in my life. I would like to thank each and every teacher of my academic life. Especially I am greatly thankful to my high school teachers Harnath Deka and Bipin Chandra Baruah for their dedication and continuous support.

I am very much thankful to all of my good friends, particularly three of my high school friends Jiaul, Manas (Papu) and Munmi for giving me positive energy and motivation since the high school days.

I express sincere thanks to the three special persons who helped me a lot during the journey to PhD life in many ways, Dr. Jnanjyoti Sarmah, Dr. Paramananda Rajbongshi and Pramod Rajbongshi.

Finally, this journey has been possible due to the constant support of my family. Here, I want to thank and express my deepest feelings to my father Mr. Basundhar Rajbangshi and my mother Saibya Deka for their huge dedication, sacrifices and immense encouragement. I thank my two brothers Apurba and Juwel, who has been the source of love, support and motivation all the times. I have no words to express my deepest gratitude to my beloved grandmother Late Thageswari Deka, who always stood by me like a pillar.

I am thankful to all of my family members: Bordeuta-Borma, dada-bou, mama-mami, mahi and all of my cousins. Especially, I thank my cousin brother Bhaskar Deka and Kallol (Pal), my cousin sisters Rajashri (Maina), Himadri (Pulu), Satabdi (Poli), Chayanika and Karsihma, sister-in-law Karabi Deka Choudhury. I convey my affection to little Kuku (my niece), Remi (my nephew) and Bharbi (my nephew).

At last, I would like to thank all those people, who have directly or indirectly helped me at various stages of PhD life.

Abstract

In this Thesis, the molecular arrangements and motions in complex liquids and multi-component mixtures have been investigated, where longer-ranged interactions and the liquid-phase separation line critically affect the liquid phase structure and dynamics. These systems remain in liquid phase at room temperature via depression of freezing points either due to non-localization of charges or because of extensive H-bond interactions between components. Ionic Liquids (ILs) and deep eutectic solvents (DESs) are the examples for these two types of systems which are also very useful reaction media for chemical reactions. Both ILs and DESs possess tremendous application potential and technological relevance as they are moisture-stable, heat-resistant (up to certain limit), and can solubilise a wide variety of environment. In addition, some DESs are biodegradable, cheaper than ILs and can be handled with relative ease. Addition of molecular solvents to ILs can alter viscosity and polarity dramatically. Polarity of DESs can also be altered through the choice of components. As a result, solvent engineering for tailoring a reaction toward a designed product becomes easier with these media.

In first part of my thesis, the structure and dynamics of [BMIM][PF_6] + acetonitrile/1,4-dioxane/hexane binary mixtures been studied in molecular details through atomistic simulations. These simulation studies investigate the cosolvent polarity and concentration dependencies of solution structure of these binary mixtures through the examination of radial and spatial distribution functions, coordination numbers and the Voronoi polyhedra analyses. The cosolvent polarity dominates the solution structure at high IL concentrations, and the IL segregates into polar and non-polar domains in the dilute IL solutions, their extent being strongly dependent upon cosolvent polarity. Also, Voronoi polyhedra analyses indicate broader void and neck distributions upon dilution of the IL by cosolvents, suggesting increased heterogeneity in the solution structure of the binary mixtures. Moreover, the effects of addition of cosolvents on dynamics of IL have been examined via the calculations of mean square displacements (MSDs), non-Gaussian and new non-Gaussian parameters, four-point correlation functions and other dynamical heterogeneity parameters. Diffusivity of the IL ions and the DH time scales become faster on adding the co-solvent in the IL mixtures and subsequently they show the cosolvent polarity dependence.

Next, molecular dynamics simulations of (choline chloride + urea) deep eutectics solvents (DESs) at various temperatures have been performed to investigate the heterogeneous reorientation and H-bond fluctuation dynamics in these systems. Simulated rank-dependent collective single particle reorientational and structural H-bond relaxations in these DESs explain the microscopic origin of the time scales obtained from available temperature dependent Dielectric relaxation (DR) measurements. Experimental evidence of pronounced heterogeneous reorientation dynamics indicated by strong fractional viscosity dependence of average DR times is further supported by strong translation-rotation decoupling and significant deviation of average simulated reorientational correlation time from Debye's law of stochastic angular displacements. The stretched exponential relaxations of simulated self-dynamic structure factors and non-Gaussian single particle displacement distributions also support the strong dynamical heterogeneity in these DESs.

In the other section of the Thesis, extensive and thorough simulation study of a recently reported naturally abundant deep eutectic solvent (DES), (Betaine + Urea + Water) in the weight ratio (11.7:12:1) have been discussed. Here, the simulation results provide a detailed investigation of structure and dynamics of this DES. Presence of strong dynamic heterogeneity in this system has already been indicated by the break-down of hydrodynamics via the fractional viscosity dependence of solute solvation and rotation times. Our simulated dynamic heterogeneity features such as non-Gaussian distributions and self-dynamic structure factors confirm the dynamically heterogeneous nature of the DES system. In addition, signature of water clustering is reflected from the comparison of simulated radial distribution functions (RDFs) in the present DES and that in neat water system. Moreover, we have studied the detailed hydrogen bond structure and dynamics of inter-species water molecules in this DES, where water is present as a minor yet integral component, which show a drastically deviated H-bond structure in this DES compared to that in neat water system. Also, the effects of ionic environment on H-bond structure and dynamics have been studied by comparing the results between this ionic betaine-based DES and neutral (Glucose + Urea + Water) DES. Water hydrogen bond length as well as the water-water H-bond relaxation dynamics respond to the effect of ionic environment.

List of Publications

1. *"Cosolvent polarity dependence of solution structure in [BMIM] [PF_6] + acetonitrile/1,4-dioxane/hexane binary mixtures: Insights from composition dependent Voronoi polyhedra analyses, iso-surfaces and radial distribution functions"* by **Juriti Rajbangshi**, Swarup Banerjee, Pradip Kr. Ghorai, and Ranjit Biswas, J. Mol. Liq**. 317**, 113746 (2020).

2. *"Heterogeneous Dynamics, Correlated Time and Length Scales in Ionic Deep Eutectics: Anion and Temperature Dependence"* by Swarup Banerjee, Pradip Kr. Ghorai, Suman Das, **Juriti Rajbangshi,** and Ranjit Biswas, J. Chem. Phys. **153**, 234502 (2020).

3. *"Heterogeneous Dynamics in [BMIM][PF_6] + Cosolvent Binary Mixtures: Does It Depend Upon Cosolvent Polarity?"* by **Juriti Rajbangshi,** and Ranjit Biswas, J. Mol. Liq**.** (2021) (submitted).

4. *"Heterogeneous Orientational Relaxations and Translation-Rotation Decoupling in (Choline Chloride + Urea) Deep Eutectic Solvents: Investigation Through Molecular Dynamics Simulations and Dielectric Relaxation Measurements"* by **Juriti Rajbangshi**, Kallol Mukherjee, and Ranjit Biswas, J. Phys. Chem. B, (2021) (submitted).

5. "*Dynamic Heterogeneity in a Naturally Abundant Deep Eutectic Solvent [Betaine + Urea + Water]: A Molecular Dynamics Simulation Study*" by **Juriti Rajbangshi,** Atanu Baksi, and Ranjit Biswas, J. Phys. Chem. B, (2021) (submitted).

6. "*Structure and Dynamics of Water in a Naturally Abundant Deep Eutectic Solvents (NADES) [Betaine + Urea + Water]: Comparison between Charged and Neutral NADESs"* by **Juriti Rajbangshi,** Atanu Baksi, and Ranjit Biswas, J. Phys. Chem. B, (2021) (submitted).

7. **"*Water in Biodegradable Glucose-Water-Urea Deep Eutectic Solvent: Modifications of Structure and Dynamics in a Crowded Environment*" by Atanu Baksi, **Juriti Rajbangshi**, and Ranjit Biswas, Phys. Chem. Phys. Chem. (2021) (submitted).

8. **"*Solution Structure and Heterogeneous Dynamics in a Naturally Abundant Deep Eutectic Solvents (NADES) [Glucose + Urea + Water]: Investigation via Molecular Dynamics Simulation Study"* by Atanu Baksi, **Juriti Rajbangshi**, and Ranjit Biswas (Manuscript in preparation)

9. **"*Water Structure and Dynamics in "Crowded" Environments provided by Deep Eutectic Solvents to Room temperature Ionic Liquids: How Different are They?"* By Atanu Baksi, **Juriti Rajbangshi**, and Ranjit Biswas (Manuscript in preparation)

**not included in this thesis.

Contents

Chapter 1

Introduction

Role of solvent as reaction media and their dynamics on chemical reactions have been an important subject in physical chemistry. As dynamic solvent response dramatically changes in presence of long-range interactions [1–11] in a given reaction medium, presence of such interactions can profoundly impact the outcome of a diffusion-limited chemical reaction. For such diffusion-controlled reactions, medium heterogeneity can play a decisive role in controlling the reaction rates. Spatial and temporal heterogeneities in a medium can be introduced by inducing metastability. This metastability may arise by lowering the solution temperature or by other means. For chemical reactions, heterogeneity effects should arise from alternative sources because a majority of the chemical reactions occur at temperatures much above the glass transition temperatures. Ionic liquids [12,13] are ready examples for such room temperature metastable liquids because shape and size asymmetries coupled with side-chain motions (entropy gain) generates structural frustration which, in turn, resist oppositely charged ions to sit firmly in their designated lattice points. Extended charge distributions and side chain motions of the large multiple groups attached to the molecular ions constituting ionic liquids are responsible for producing the molten state at or near the room temperature. Deep eutectic solvents (DESs) [14–22] constitute another example of such metastable liquids which supports spatial and temporal heterogeneity of varying degrees. As in ionic liquids, ionic DESs also possess ion-ion $\left(u_{ij}(r_{ij}) \propto r_{ij}^{-1}\right)$, ion-dipole $\left(\propto r_{ij}^{-2}\right)$ and dipole-dipole $\left(\propto r_{ij}^{-3}\right)$ interactions. These two media possess tremendous potential for industrial applications [12,23], as they can successfully replace a large number of common but hazardous organic solvents as reaction media. The role of these solvents as reaction media can be improved by adding cosolvents into them, as dilution with cosolvents alter the viscosity and polarity dramatically. DESs are the multi-component molten mixtures and obtained via mixing the pre-weighed constituents, melting and then allowing slowly to cool down to room temperature[19]. Depression of freezing points in these systems mainly arises from the extensive interspecies H-bonding and the gain in entropy for being in the liquid phase. Since, tailoring reactions towards the desired products becomes easier with these media, DESs have become popular. However, for smarter and more appropriate applications, one requires a thorough understanding of interaction and dynamics in these systems. Signatures of spatial and temporal heterogeneities is a common characteristic

of ionic liquids and DESs, and both experimental [24–43] and simulation studies [44–54] have repeatedly reflected that.

Medium heterogeneity suggests the presence of spatial and temporal local features at the microscopic length-scales in liquid systems, and it affects the transport properties of the same[55–58]. The heterogeneity impact on transport properties comes via departures from the hydrodynamic solvent friction dependence. Structural or spatial heterogeneity [59–70] indicates different local arrangement of molecules producing micro-domains (spatial correlations), whereas temporal heterogeneity[71–75] (or dynamical heterogeneity) refers to the temporally correlated domains distributions relaxation rates. These spatial and temporal correlations lead to the existence of mobile and immobile particles in a given metastable system. On the basis of classification of these mobile and immobile particles, transport properties of metastable liquids can be understood. As a consequence of spatial heterogeneity in a given system, temporal heterogeneity may occur. However, the presence of temporal heterogeneity does not necessarily guarantee the spatial heterogeneity. The signature of dynamic heterogeneities has been indicated via the experimental evidence of breakdown of hydrodynamic relations [24–26,30,76]. In heterogenous systems, particle displacements show deviation from the Gaussian distribution for homogeneous liquids [77]. It is known that a dramatic slowing down of dynamics[78] occurs for super-cooled liquids near glass transition, and this is obvious from the temperature-dependent viscosity (η), diffusion coefficient (D), structural relaxation time (τ) and other measures of liquid dynamics. A remarkable slowing down in momentum transfer occurs near glass transition, where viscosity becomes ~ 10^{13} P. In such liquids, dynamics of a particular region may be different from its adjacent regions. The calculated density correlation functions in these systems may show stretched exponential relaxation behaviour with the exponent value, β, much less than unity.

Various experimental studies including the time-dependent fluorescence Stokes shift (TDFSS), and dynamic fluorescence anisotropy measurements have provided evidences for the existence of dynamic heterogeneity in several neat ILs [35,79–85]. In addition, heterogeneous dynamics in binary mixtures of IL with small molecular solvents have been characterized by TDFSS and dielectric relaxation (DR) measurements [38,41,42,47,49,86]. Subsequently, simulation studies of neat ILs and their binary mixtures [54] have revealed the presence of DH via non-Gaussian features,

single particle displacement distributions and van Hove correlations. Although, the heterogeneous dynamics in several neat ILs have been investigated in various experimental [84,87–90] and simulation studies [75,83,91–93], the same in their binary mixtures with common small molecular solvents [54] are limited. As already mentioned above, addition of cosolvents into ILs reduces the viscosity co-efficient (η) due to screening of Coulomb interactions, and the dependence of η on solvent composition [76] suggests significant changes in the spatial and the temporal correlations. The impact of polarity of cosolvents on the interaction and dynamics of binary mixtures of ILs with cosolvents have remained unexplored. The focus of the present Thesis is, therefore, the investigation of spatio-temporal heterogeneity and its impacts on several solvent properties of ILs, binary mixtures of ILs with common solvents, and deep eutectic solvents. In addition, attempts have been made to uncover the impact of cosolvent polarity on the spatio-temporal heterogeneity inherent to a neat ionic liquid. As described before, DESs have become one of the preferred alternatives to common solvents as reaction media due to their low toxicity, easy transportation, easy synthesis protocol [14–21] and a wide window of choice for constituents forms ionic and non-ionic compounds [16]. For example, ionic DESs are chosen by taking electrolytes as one of the components and non-ionic DESs can be obtained by mixing and melting non-ionic compounds. DES made of amide and urea [31] is an example. In addition, mixture of quaternary ammonium salt such as choline chloride and amides, salts, sugars or alcohols [15,16] give a new set of ionic DESs. Time resolved fluorescence studies and computer simulations [25,30] provide evidences for presence of dynamic heterogeneity in several acetamide based ionic DESs. Signatures of heterogeneous dynamics in acetamide [24] and choline chloride based [29] ionic DESs have been revealed via the fractional viscosity dependence of measured solvation and rotation rates of dissolved solute probes.

We have carried out extensive simulation studies of (choline chloride + urea) ionic DES to explore the heterogeneous reorientation dynamics in these systems. Simulated rank dependent collective single particle reorientational and structural H-bond relaxations can explain the microscopic origin of the available DR time scales for this particular DES. The experimental evidence of pronounced dynamic heterogeneity, indicated by the strong fractional viscosity dependence of the experimental average DR times, is supported by a strong translation-rotation decoupling and significant deviation of the simulated average reorientational correlation times from the Debye law of stochastic angular displacements. The presence of strong dynamic heterogeneity in these DESs is further confirmed by the stretched exponential behavior of the

simulated self-dynamic structure factors and non-Gaussian single particle displacement distributions.

There exist another class of green and eco-sustainable DESs containing naturally abundant compounds such as amino acids, urea, sugars etc [20,94–98]. These DESs are called the naturally abundant DESs (NADESs) [99–106]. To understand the interaction and dynamics in one such NADES that contain betaine (trimethyl derivative of glycine amino acid), urea and water, steady state and time-resolved fluorescence measurements[107] have been performed recently. These measurements have revealed a strong fractional viscosity dependence of the average solute rotation and solvation rates. We have performed molecular dynamics simulation study of [{Bet+Ure+wat}, weight ratio (11.7:12:1)] DES to explore the microscopic origin of the experimentally observed fractional viscosity dependence. Simulated non-Gaussian displacement distributions confirm the experimental evidence of strong heterogeneous dynamics in this DES. Also, drastically different dynamics of water in this system is reflected by the enormous slow relaxation and long correlated timescales. In addition, the molecular level view of water structure and dynamics in this type of hydrogen-bonded system have been investigated. Note in this NADES that water is present as an integral yet minor component. Also, we have explored the effects of ionic environment on water structure and dynamics in this [Bet+Ure+Wat] ionic DES and compared with another reported glucose-based neutral DES [Glu+Ure+Wat] [108].

The work that constitutes this Thesis has been described in 7 different chapters where the first chapter is the Introduction. In chapter 2, composition dependence of solution structures of the binary mixtures of 1-butyl-3methyl-imidazolium hexafluorophosphate ([BMIM] [PF_6]), and three different cosolvents of comparable sizes but differing polarities have been explored via molecular dynamics simulation study, which provides detailed analysis of dependence of microscopic solution structure of these IL mixtures on the nature of interaction between IL and cosolvents. The cosolvents used here are acetonitrile (dipolar), 1,4-doxane (quadrupolar) and hexane (non-polar) and seven different IL mole fractions F_{IL}=1.0, 0.90, 0.75, 0.50, 0.25, 0.10, 0.0 have been considered. The interaction of these cosolvents with the IL provides microscopic reflection of differing solubilities via the calculations of radial distribution functions and it indicates the preferable interaction between IL with both acetonitrile and dioxane than that with

hexane. This makes acetonitrile and dioxane more miscible in [BMIM] [PF_6] than hexane. Examination of composition dependent radial distribution functions (RDFs) in these three binary mixtures reveal that IL solution structure is dominated by cosolvent clustering at high IL concentrations, and segregation of IL into polar and non-polar domain in dilute IL solutions. Also, the extent of aggregation behavior of [BMIM] [PF_6] IL at low IL mole fraction is maximum in non-polar solvent hexane, which can be explained by relatively shorter Debye screening length. This observation is further confirmed by the calculation of co-ordination number. Also, pronounced microscopic phase segregation in (IL + hexane) mixtures is clearly evident from spatial distribution functions. In addition, Voronoi polyhedra analysis suggests increased heterogeneity in the solution structure of the diluted IL mixtures through the broader void and neck distributions upon adding cosolvents into IL.

Composition dependence of modifications on motional features of both the IL ions and cosolvents in ([BMIM] [PF_6] IL + cosolvent) mixtures via molecular dynamics simulations are presented in chapter 3. Simulated mean square displacements (MSDs) for both of ions and cosolvents indicate cage softening upon successive addition of cosolvents into the IL, as the extent of sub-diffusive regime decreases in dilute IL solutions. Accordingly, the diffusion coefficient values increases and larger diffusion coefficient values are obtained in (IL+acetonitrile) mixtures because of favorable interaction between the IL and acetonitrile. To search the signatures of dynamic heterogeneity and their dependence of concentrations and cosolvent polarity, several heterogeneity parameters such as non-Gaussian (NG), new non-Gaussian (NNG) parameters, single particle displacement distributions have been calculated in these systems. The peak heights and time scales obtained from NG and NNG parameters respond significantly to both cosolvent polarity and mixture compositions, where they become faster in dilute IL solutions and among all the cosolvents they become fastest in presence of acetonitrile. Composition dependent single particle displacement distribution suggests that the deviation from Gaussian distribution becomes lower in dilute IL solutions. In addition, four-point correlation functions, overlap functions, self-intermediate functions have been calculated to examine the heterogeneous relaxations in these IL mixtures. The relaxation and correlated time scales also show the similar polarity dependence.

In chapter 4, we report a simulation study of [f choline chloride + (1-f) urea] deep eutectic solvent (DES) for f = 0.33 at temperature range $293 \leq T/K \leq 333$ to explore the heterogeneous reorientation dynamics in these systems. Simulated collective reorientational and structural hydrogen bond relaxations in these DESs explain the microscopic origin of the time scales obtained from dielectric relaxation (DR) measurements of the same DESs in the frequency window $0.2 \leq \nu(GHz) \leq 50$ at various temperatures. Experimental observations of pronounced fractional viscosity dependence of average DR time scales suggests the presence of dynamic heterogeneity in these DESs, which is further confirmed by the deviation of Debye's $l(l+1)$ law as the ratio of simulated reorientation correlation times $\langle\tau\rangle_{l=1}/\langle\tau\rangle_{l=2} < 3$ is obtained for these systems. In addition, calculated translation-rotation decoupling indicates the presence of dynamic heterogeneity in these DESs. Simulated mean square displacements (MSDs) and various non-Gaussian parameters have been calculated here to explore the extent of translational heterogeneity in these systems. Temperature dependence of MSDs suggests a prolonged sub-diffusive behavior, which is the first indication of heterogeneous translational dynamics in these DESs and at higher temperature partial homogenization occurs. Appearance of nanoseconds or even slower DH time scales in these DESs is a reflection of stronger heterogeneity in particle displacements. Such slower time scales correlate the time scales obtained from earlier dynamic stokes shift and fluorescence anisotropy measurements [29].

In chapter 5, we present simulation results on a recently experimentally studied NADES, [{Bet+Ure+Wat}, weight ratio (11.7:12:1)] and make an attempt to explain the microscopic origin of the fractional viscosity dependence of solute-centric non-reactive relaxation rates in this medium. Simulated radial distribution functions (RDFs) suggests signature of water clustering in this system. Evidence of rattling-in-cage motion of the particles is indicated from sub-diffusive mean square displacements (MSDs), which is an indication of presence of dynamic heterogeneity in this system. Enormous slowing down of relaxation rates and long correlated timescales for water in this DES (in comparison to those in neat water) have been found. All these indicate that motional anomaly at the molecular level of the DES components is responsible for the experimental observations.

In chapter 6, we report results of our detailed simulation study of H-bond structure and dynamics of water molecules in the NADES investigated in the previous chapter. We compare

these results with the simulation results of a neutral glucose based NADES ([Glu+Ure+Wat, weight ratio (6:4:1)])[108] and neat water system. Water H-bond lengths obtained in this DES is more constrained than in the glucose-based DES. Also, the effect of ionic environment on water-water H-bond fluctuation dynamics, both continuous and structural, have been explored. Simulated water-water H-bond dynamics in this ionic NADES have been found to be slower than those obtained for the glucose-based DES.

Chapter 7 ends the Thesis with a brief concluding remark. In addition, several relevant yet interesting problems have been briefly discussed which can be considered for future studies.

References

[1] B. Bagchi, Annu. Rev. Phys. Chem. **40**, 115 (1989).

[2] E.W. Castner Jr, C.J. Margulis, M. Maroncelli, and J.F. Wishart, Annu. Rev. Phys. Chem. **62**, 85 (2011).

[3] R.F. Grote and J.T. Hynes, J. Chem. Phys. **73**, 2715 (1980).

[4] J.T. Hynes, Annu. Rev. Phys. Chem. **36**, 573 (1985).

[5] J.T. Hynes, in *Ultrafast Dyn. Chem. Syst.* (Springer, 1994), pp. 345–381.

[6] M.T. Klein, L.A. Torry, B.C. Wu, S.H. Townsend, and S.C. Paspek, J. Supercrit. Fluids **3**, 222 (1990).

[7] X. Li, M. Liang, A. Chakraborty, M. Kondo, and M. Maroncelli, J. Phys. Chem. B **115**, 6592 (2011).

[8] M. Liang, A. Kaintz, G.A. Baker, and M. Maroncelli, J. Phys. Chem. B **116**, 1370 (2012).

[9] Y. Nagasawa and H. Miyasaka, Phys. Chem. Chem. Phys. **16**, 13008 (2014).

[10] G.A. Voth and R.M. Hochstrasser, J. Phys. Chem. **100**, 13034 (1996).

[11] A. Warshel, J. Phys. Chem. **86**, 2218 (1982).

[12] H. Zhang, L. Bu, M. Li, K. Hong, A. Visser, R. Rogers, and J. Mays, in (2001), pp. 114–124.

[13] P. Wasserscheid and T. Welton, Ionic Liquids in Synthesis (2003).

[14] P.G. Jessop, D.A. Jessop, D. Fu, and L. Phan, Green Chem. **14**, 1245 (2012).

[15] Q. Zhang, K.D.O. Vigier, S. Royer, and F. Jerome, Chem. Soc. Rev. **41**, 7108 (2012).

[16] M. Francisco, A. van den Bruinhorst, and M.C. Kroon, Angew. Chem. Int. Ed. **52**, 3074 (2013).

[17] J.-H. Liao, P.-C. Wu, and Y.-H. Bai, Inorg. Chem. Commun. **8**, 390 (2005).

[18] P. Nockemann, B. Thijs, K. Driesen, C.R. Janssen, K. Van Hecke, L. Van Meervelt, S. Kossmann, B. Kirchner, and K. Binnemans, J. Phys. Chem. B **111**, 5254 (2007).

[19] A.P. Abbott, G. Capper, D.L. Davies, R.K. Rasheed, and V. Tambyrajah, Chem. Commun. 70 (2003).

[20] A.P. Abbott, D. Boothby, G. Capper, D.L. Davies, and R.K. Rasheed, J. Am. Chem. Soc. **126**, 9142 (2004).

[21] D.V. Wagle, H. Zhao, and G.A. Baker, Acc. Chem. Res. **47**, 2299 (2014).

[22] P. Liu, J.-W. Hao, L.-P. Mo, and Z.-H. Zhang, RSC Adv. **5**, 48675 (2015).

[23] N.V. Plechkova and K.R. Seddon, Chem. Soc. Rev. **37**, 123 (2008).

[24] B. Guchhait, H. Al Rasid Gazi, H.K. Kashyap, and R. Biswas, J. Phys. Chem. B **114**, 5066 (2010).

[25] B. Guchhait, S. Das, S. Daschakraborty, and R. Biswas, J. Chem. Phys. **140**, 104514 (2014).

[26] B. Guchhait, S. Daschakraborty, and R. Biswas, J. Chem. Phys. **136**, 174503 (2012).

[27] S.N. Tripathy, Z. Wojnarowska, J. Knapik, H. Shirota, R. Biswas, and M. Paluch, J. Chem. Phys. **142**, 184504 (2015).

[28] R. Biswas, A. Das, and H. Shirota, J. Chem. Phys. **141**, 134506 (2014).

[29] A. Das and R. Biswas, J. Phys. Chem. B **119**, 10102 (2015).

[30] A. Das, S. Das, and R. Biswas, Chem. Phys. Lett. **581**, 47 (2013).

[31] A. Das, S. Das, and R. Biswas, J. Chem. Phys. **142**, 034505 (2015).

[32] H.A.R. Gazi, B. Guchhait, S. Daschakraborty, and R. Biswas, Chem. Phys. Lett. **501**, 358 (2011).

[33] A. Samanta, J. Phys. Chem. Lett. **1**, 1557 (2010).

[34] A. Samanta, J. Phys. Chem. B **110**, 13704 (2006).

[35] J.A. Ingram, R.S. Moog, N. Ito, R. Biswas, and M. Maroncelli, J. Phys. Chem. B **107**, 5926 (2003).

[36] S. Arzhantsev, H. Jin, G.A. Baker, and M. Maroncelli, J. Phys. Chem. B **111**, 4978 (2007).

[37] X.-X. Zhang, M. Liang, N.P. Ernsting, and M. Maroncelli, J. Phys. Chem. B **117**, 4291 (2013).

[38] X.-X. Zhang, M. Liang, J. Hunger, R. Buchner, and M. Maroncelli, J. Phys. Chem. B **117**, 15356 (2013).

[39] A. Stoppa, J. Hunger, R. Buchner, G. Hefter, A. Thoman, and H. Helm, J. Phys. Chem. B **112**, 4854 (2008).

[40] J. Hunger, A. Stoppa, S. Schrödle, G. Hefter, and R. Buchner, Chem. Phys. Chem. **10**, 723 (2009).

[41] M. Liang, X.-X. Zhang, A. Kaintz, N.P. Ernsting, and M. Maroncelli, J. Phys. Chem. B **118**, 1340 (2014).

[42] A. Stoppa, J. Hunger, G. Hefter, and R. Buchner, J. Phys. Chem. B **116**, 7509 (2012).

[43] D. Chakrabarty, A. Chakraborty, D. Seth, and N. Sarkar, J. Phys. Chem. A **109**, 1764 (2005).

[44] S. Daschakraborty and R. Biswas, Chem. Phys. Lett. **510**, 202 (2011).

[45] S. Daschakraborty and R. Biswas, Chem. Phys. Lett. **545**, 54 (2012).

[46] S. Daschakraborty and R. Biswas, J. Chem. Phys. **137**, 114501 (2012).

[47] S. Daschakraborty and R. Biswas, J. Phys. Chem. B **118**, 1327 (2014).

[48] S. Daschakraborty and R. Biswas, J. Chem. Phys. **140**, 014504 (2014).

[49] S. Daschakraborty and B. Ranjit, J. Phys. Chem. B **115**, 4011 (2011).

[50] H.K. Kashyap and R. Biswas, J. Phys. Chem. B **112**, 12431 (2008).

[51] H.K. Kashyap and R. Biswas, J. Phys. Chem. B **114**, 254 (2010).

[52] H.K. Kashyap and R. Biswas, J. Phys. Chem. B **114**, 16811 (2010).

[53] T. Pal and R. Biswas, J. Chem. Phys. **141**, 104501 (2014).

[54] T. Pal and R. Biswas, J. Phys. Chem. B **119**, 15683 (2015).

[55] P.G. Debenedetti and F.H. Stillinger, Nature **410**, 259 (2001).

[56] D. Chakrabarti and B. Bagchi, Phys. Rev. Lett. **96**, 187801 (2006).

[57] A. Heuer, J. Phys. Condens. Matter **20**, 373101 (2008).

[58] S. Sastry, P.G. Debenedetti, and F.H. Stillinger, Nature **393**, 554 (1998).

[59] M.D. Ediger, Annu. Rev. Phys. Chem. **51**, 99 (2000).

[60] S.C. Glotzer, J. Non-Cryst. Solids **274**, 342 (2000).

[61] S.C. Glotzer, V.N. Novikov, and T.B. Schrøder, J. Chem. Phys. **112**, 509 (2000).

[62] N. Lačević, F.W. Starr, T. Schrøder, V. Novikov, and S. Glotzer, Phys. Rev. E **66**, 030101 (2002).

[63] N. Lačević, F.W. Starr, T. Schrøder, and S. Glotzer, J. Chem. Phys. **119**, 7372 (2003).

[64] G. Szamel and E. Flenner, Phys. Rev. E **74**, 021507 (2006).

[65] E. Flenner and G. Szamel, Phys. Rev. E **70**, 052501 (2004).

[66] J.-P. Hansen, Phys. Stat. Mech. Its Appl. **201**, 138 (1993).

[67] C. Toninelli, M. Wyart, L. Berthier, G. Biroli, and J.-P. Bouchaud, Phys. Rev. E **71**, 041505 (2005).

[68] C. Bennemann, C. Donati, J. Baschnagel, and S.C. Glotzer, Nature **399**, 246 (1999).

[69] K. Kim and S. Saito, J. Chem. Phys. **138**, 12A506 (2013).

[70] C. Donati, S. Franz, S.C. Glotzer, and G. Parisi, J. Non-Cryst. Solids **307**, 215 (2002).

[71] S.S. Sarangi, W. Zhao, F. Müller-Plathe, and S. Balasubramanian, Chem. Phys. Chem. **11**, 2001 (2010).

[72] K. Kim and S. Saito, J. Chem. Phys. **133**, 044511 (2010).

[73] E. Flenner and G. Szamel, Phys. Rev. E **72**, 011205 (2005).

[74] T. Pal and R. Biswas, Chem. Phys. Lett. **517**, 180 (2011).

[75] T. Pal and R. Biswas, Theor. Chem. Acc. **132**, 1348 (2013).

[76] J.-P. Hansen and I.R. McDonald, *Theory of Simple Liquids* (Elsevier, 1990).

[77] G. Szamel and E. Flenner, Europhys. Lett. **67**, 779 (2004).

[78] S. Karmakar, C. Dasgupta, and S. Sastry, Annu. Rev. Condens. Matter Phys **5**, 255 (2014).

[79] J. Hunger, A. Stoppa, S. Schrödle, G. Hefter, and R. Buchner, Chem. Phys. Chem **10**, 723 (2009).

[80] A. Stoppa, J. Hunger, R. Buchner, G. Hefter, A. Thoman, and H. Helm, J. Phys. Chem. B **112**, 4854 (2008).

[81] O. Zech, J. Hunger, J.R. Sangoro, C. Iacob, F. Kremer, W. Kunz, and R. Buchner, Phys. Chem. Chem. Phys. **12**, 14341 (2010).

[82] X.-X. Zhang, M. Liang, N.P. Ernsting, and M. Maroncelli, J. Phys. Chem. B **117**, 4291 (2013).

[83] D. Roy, N. Patel, S. Conte, and M. Maroncelli, J. Phys. Chem. B **114**, 8410 (2010).

[84] H. Jin, X. Li, and M. Maroncelli, J. Phys. Chem. B **111**, 13473 (2007).

[85] S. Arzhantsev, H. Jin, G.A. Baker, and M. Maroncelli, J. Phys. Chem. B **111**, 4978 (2007).

[86] S. Daschakraborty and R. Biswas, J. Chem. Phys. **144**, 104505 (2016).

[87] D.K. Sasmal, A.K. Mandal, T. Mondal, and K. Bhattacharyya, J. Phys. Chem. B **115**, 7781 (2011).

[88] S. Patra and A. Samanta, J. Phys. Chem. B **116**, 12275 (2012).

[89] A. Adhikari, K. Sahu, S. Dey, S. Ghosh, U. Mandal, and K. Bhattacharyya, J. Phys. Chem. B **111**, 12809 (2007).

[90] D.C. Khara and A. Samanta, J. Phys. Chem. B **116**, 13430 (2012).

[91] Z. Hu and C.J. Margulis, Proc. Natl. Acad. Sci. **103**, 831 (2006).

[92] H.V. Annapureddy, H.K. Kashyap, P.M. De Biase, and C.J. Margulis, J. Phys. Chem. B **114**, 16838 (2010).

[93] J. Habasaki and K. Ngai, J. Chem. Phys. **129**, 194501 (2008).

[94] M. Espino, M. de los Ángeles Fernández, F.J. Gomez, and M.F. Silva, TrAC Trends Anal. Chem. **76**, 126 (2016).

[95] Y. Dai, E. Rozema, R. Verpoorte, and Y.H. Choi, J. Chromatogr. A **1434**, 50 (2016).

[96] S. Gore, S. Baskaran, and B. Koenig, Green Chem. **13**, 1009 (2011).

[97] W.-C. Huang, D. Zhao, N. Guo, C. Xue, and X. Mao, J. Agric. Food Chem. **66**, 11897 (2018).

[98] Y.H. Choi, J. van Spronsen, Y. Dai, M. Verberne, F. Hollmann, I.W. Arends, G.-J. Witkamp, and R. Verpoorte, Plant Physiol. **156**, 1701 (2011).

[99] A. Paiva, R. Craveiro, I. Aroso, M. Martins, R.L. Reis, and A.R.C. Duarte, ACS Sustain. Chem. Eng. **2**, 1063 (2014).

[100] Y. Dai, J. van Spronsen, G.-J. Witkamp, R. Verpoorte, and Y.H. Choi, Anal. Chim. Acta **766**, 61 (2013).

[101] M. Faggian, S. Sut, B. Perissutti, V. Baldan, I. Grabnar, and S. Dall'Acqua, Molecules **21**, 1531 (2016).

[102] A. Hayyan, M.A. Hashim, M. Hayyan, F.S. Mjalli, and I.M. AlNashef, J. Clean. Prod. **65**, 246 (2014).

[103] M.H. Zainal-Abidin, M. Hayyan, A. Hayyan, and N.S. Jayakumar, Anal. Chim. Acta **979**, 1 (2017).

[104] I.M. Aroso, R. Craveiro, Â. Rocha, M. Dionísio, S. Barreiros, R.L. Reis, A. Paiva, and A.R.C. Duarte, Int. J. Pharm. **492**, 73 (2015).

[105] M.B. Haider, D. Jha, B. Marriyappan Sivagnanam, and R. Kumar, J. Chem. Eng. Data **63**, 2671 (2018).

[106] L. Millia, V. Dall'Asta, C. Ferrara, V. Berbenni, E. Quartarone, F.M. Perna, V. Capriati, and P. Mustarelli, Solid State Ion. **323**, 44 (2018).

[107] E. Tarif, J. Mondal, and R. Biswas, J. Mol. Liq. **303**, 112451 (2020).

[108] A. Baksi, J. Rajbangshi, and R. Biswas, Phys. Chem. Chem. Phys. 2021 (Submitted)

Chapter 2

Cosolvent polarity dependence of solution structure in [BMIM][PF_6] + acetonitrile/1,4-dioxane/hexane binary mixtures: Insights from composition dependent Voronoi polyhedra analyses, iso-surfaces and radial distribution functions

2.1 Introduction

Room temperature ionic liquids (RTILs) are generally defined as molten electrolytes that constitute liquid phase below 373 K (<100° C) [1] and composed of ions that are large and asymmetric in which electronic charges are delocalized over extended regions. Usually, RTIL cations or anions possess organic moieties with large alkyl chains and in combinations with relatively smaller and more compact counter-ions produce a large variety of RTILs [2]. This extended charge delocalization and the entropy gain (mainly rotational) from the motions of the long alkyl chains drive the lattice frustration and provide stability to the liquid phase at temperatures much lower than those expected for systems governed by charge-charge interactions. This may be considered as a sort of metastability which can give rise to relaxation signatures reminiscent of those observed for deeply supercooled systems near glass transition. These signatures often include multi-exponential or stretched exponential relaxation kinetics, Vogel-Fulcher-Tammann [1] behavior of temperature dependent viscosity and evidences for microscopic phase segregation. The charge-charge electrostatic interactions in RTILs, although diffused in comparison to that in room temperature solid electrolytes composed of singly charged atomic ions, gives rise to several desirable solvent properties such as negligible vapor pressure, non-inflammability, high electrical conductivity [2-8] and wide liquid range [9] etc. These properties have made the RTILs candidates for large scale applications in the industry and technology sectors [10]. However, the high viscosity of RTILs poses a barrier for direct applications of pure ILs [11,12] and, as a result, conventional molecular co-solvents are often mixed with these ILs to enhance the fluidity and other physico-chemical properties for generating designer solvents from these RTIL+cosolvent binary mixtures for targeted applications. Interestingly, binary mixtures of RTILs with non-aqueous solvents have not been

studied extensively, although aqueous mixtures have been studied extensively by applying different experimental techniques [13-15], and computer simulations [16-20]. Therefore, a systematic study of binary mixtures of RTILs with small molecular non-aqueous solvents detailing the composition dependent microscopic solution structure and relaxation dynamics are required not only from basic scientific point of view but also for consideration of these mixtures as industrially important reaction media.

The microscopic segregation of neat ILs into polar and non-polar domains and the consequent impact on motional features of the constituent ions have added extra importance to these Coulomb fluids. Addition of water has been reported to facilitate this self-segregation and domain formation [13]. The nanoscale spatial heterogeneity and the heterogeneity in the dynamics of ILs based on the 1-alkyl-3-methylimidazoilum cation $[C_nmim]^+$ have been reported in many MD simulations [18,21-31]. An early indication of spatial heterogeneity in imidazolium-based ILs was found in Raman spectroscopic measurements [32], which suggested local structure formation in these ILs. Subsequent computer simulations [21] predicted a low wave vector peak (in addition to the nearest-neighbour peak) which was found to become more prominent with the increase in the alkyl chain length from C1 to C8, suggesting longer-ranged ordering [22] in these ILs. A multiscale coarse-gaining (MS-CG) MD simulation study of $[C_nmim]$ $[NO_3]$ IL indicated aggregation of alkyl chains for the ILs having C_4 to C_8, and no such aggregations for ILs with shorter chains. Nanoscale structural organization in neat 1-alkyl-3-methylimidazolium-based ionic liquids and the effects of changing the alkyl chain length were explored by other authors[22], which suggested the formation of two distinct yet microscopic domains, where the imidazoilum ring of the cation and the anion formed a polar tridimensional network and the non-polar domains by the alkyl tails of the cation.

Because of the presence of microscopic segregations in ILs, the solute-solvent interaction in these ILs becomes complex [33,34], hosting and solvation of solute molecules in such spatially heterogeneous media becomes different from that in otherwise homogeneous media. Single crystal X-ray crystallographic measurements and near-infrared Raman spectroscopic studies [35] explored the impact of water on the molecular structure of 1-butyronitrile-3-methylimidazolium halide IL. Local structure and intermolecular dynamics of an equimolar mixture of [dmim] $[NTf_2]$ + benzene, were examined via MD simulations and OKE

spectroscopic measurements [36]. Structural and transport properties of $[P_{14,6,6,6}]$ $[NTf_2]$ + hexane binary mixtures were investigated by using high-energy X-ray scattering and PG-SE NMR measurements [37], where the persistence of the characteristic structure of the IL was noticed even up to 80% dilution in hexane. The nanoscale structural organization and intermolecular dynamics in $[C_5mim]$ $[NTf_2]$ + CS_2 binary mixtures and their concentration dependence were studied via MD simulations and OKE spectral analysis [38]. Computer simulation studies of binary mixtures of imidazolium-based IL, $[C_6mim]$ [FSI] and dipolar acetonitrile, reported significant enhancements of self-diffusion and conductivities along with the modifications in structural arrangements of IL on adding acetonitrile [39]. In yet another simulation study, the solution structure along with solvation and frictional characteristics of $[Im_{41}]$ $[BF_4]$ + acetonitrile binary mixtures were investigated [40]. In addition, a few more experimental and theoretical studies explored the composition dependence of solvation response in binary mixtures of RTILs with non-aqueous small molecular solvents [41,42].

Although the above-mentioned experimental and simulation studies explored structure and dynamics of several RTIL+cosolvent binary mixtures, they are individual and disjointed endeavours in the sense that they do not represent a unified comprehensive attempt because in those studies the dependencies of polar-non-polar domain segregation in a given RTIL on the polarity and concentration of co-solvent were not investigated and the impact of the cosolvent-IL interactions operative at various lengthscales not explored. Such a thorough study is presented here for the first time where cosolvents of three different polarities have been chosen and the composition dependent solution structural properties, from neat to neat through several binary compositions at 298 K, monitored via the radial and spatial distribution functions, Voronoi polyhedra analyses, and coordination numbers. The three cosolvents are acetonitrile (dipolar), 1,4-dioxane (hereafter dioxane; quadrupolar) and hexane (nonpolar) whose sizes (van der Waal radii) are not too different from those of the constituent ions of the RTIL considered here, 1-butyl-3-methylimidazolium hexafluorophosphate ([BMIM] $[PF_6]$). Table 2.1 [41,43-47] summarizes representative physicochemical properties of these solvents to facilitate comparison and to stress the complexities of interactions in these binary mixtures.

Table 2.1: Physicochemical properties of the three co-solvents and [BMIM] [PF_6].

Solvent	MW (gm)	μ (D)	<Q> (D Å)	ε_0	Diameter (Å)
[BMIM][PF_6]	~284	[BMIM]+: ~ 4	N/A	16	$[BMIM]^+$: 6.8 $[PF_6]^-$: 5.4
Hexane	~78	0	0.6	1.88	7.5
Dioxane	~88	0	11.68	2.2	6.4
Acetonitrile	~41	3.92	2.49	35.9	5.5

Note the viscosities of these small molecular cosolvents are ~250-1000 times lower than that of [BMIM] [PF_6] which can modify the particle mobilities significantly in binary mixtures. The static dielectric constants (ε_0) for dioxane and hexane are drastically different from those for [BMIM] [PF_6] and acetonitrile, while ε_0 for acetonitrile is more than double of that estimated for the IL. Interestingly, the dipole moment values of both acetonitrile and the IL are large and similar, while those for dioxane and hexane are estimated to be zero. The single most important molecular property that separates dioxane from the other two cosolvents is the very large value of its quadrupole moment. Naturally, therefore, the charge-quadrupole interactions dictate the relative spatial distributions of the co-solvent around IL ions in [BMIM] [PF_6] + dioxane binary mixtures, whereas the charge-dipole and charge-dispersive interactions assume the center-stage for the same in [BMIM][PF_6] + acetonitrile and [BMIM][PF_6] + hexane binary mixtures respectively.

Note the over-all solution structure in these binary mixtures derives contributions from other additional interaction contributions as well. For example, intra-species ion-ion, ion-dipole, dipole-dipole and dispersion interactions are common to all the three different types of binary

mixtures at all finite IL concentrations because of the presence of the IL itself. Inter-species dipole-dipole (for acetonitrile mixture), quadrupole-ion and quadrupole-dipole (for dioxane mixture) and dispersive (for hexane mixture) interactions contribute to the composition dependent solution structures and liquid-liquid phase separations. In addition, interactions among the cosolvent molecules contribute. The distance dependence (that is, interaction lengthscales) of these interactions and their approximate energy scales are shown in Table 2.2 [48]. An examination of this Table can perhaps provide a clue to what piece or pieces of interactions should guide solution structures in these three different binary mixtures as the concentration of the IL is gradually altered. While stating these we would like to mention that in real IL + cosolvent binary mixtures other species such as ion-pairs (both solvent-separated and solvent-shared), triple ions etc. are likely to be present and these are not considered here because the present simulations assume the IL, [BMIM] [PF_6], to be completely dissociated into its constituent ions, $[BMIM]^+$ and $[PF_6]^-$.

Table 2.2: Distance dependence of various molecular interactions and their approximate energy scales**.**

Interaction Type	Distance Dependence	Energy Scale (kJ/mol)
Ion-Ion	r^{-1}	~250
Ion-Dipole	r^{-2}	~15
Dipole-Dipole	r^{-3}	~2
Quadrupole-Quadrupole	r^{-7}	-
Quadrupole-Dipole	r^{-5}	-
Quadrupole-Ion	r^{-3}	-
Dispersion (London)	r^{-6}	2
H-Bonding	-	~2.5

2.2 Details of calculations

2.2.1 Force field and simulation details

Computer simulation results presented in this paper were obtained via performing all-atom molecular dynamics simulations for the three different types of binary mixtures at different compositions using the simulation package GROMACS 4.5.6[49]. For all simulations, the temperature was kept fixed at 298 K. The chemical structures of $[BMIM]^+$ and $[PF_6]^-$ ions, the three co-solvent molecules of differing polarities and the scheme employed for the nomenclature of the different constituent atoms are provided in Figure 2.A.1 (Appendix 2.A). The following seven IL mole-fractions (F_{IL}), covering neat to neat, were investigated: F_{IL}=1.00, 0.90, 0.75, 0.50, 0.25, 0.10, 0.00. The numbers of ion-pairs and co-solvent molecules to obtain the required mole-fractions have been provided in Table 2.3.

Table 2.3: Number of IL ions and co-solvent molecules used in the simulations at different IL mole fractions (F_{IL}).

F_{IL}	$[BMIM]^+$	$[PF_6]^-$	Co-solvent molecules
1.00	128	128	0
0.90	230	230	26
0.75	192	192	64
0.50	128	128	128
0.25	64	64	192
0.10	26	26	230
0.00	0	0	256

The following generalized form described the potential energy function for [BMIM] [PF_6] and the non-polar hexane:

$$U(r) = \sum_{bonds} K_r\left(r - r_{eq}\right)^2 + \sum_{bonds} K_\theta\left(\theta - \theta_{eq}\right)^2 + \sum_{dihedrals}[\frac{V_1}{2}(1 + cos\varphi) + \frac{V_2}{2}(1 - cos2\varphi) + \frac{V_3}{2}(1 + cos3\varphi)] + \sum_{i<j}^{atoms}\left(\frac{A_{ij}}{R_{ij}{}^{12}} - \frac{B_{ij}}{R_{ij}{}^{6}}\right) + \sum_{i<j}^{atoms}\frac{q_i q_j}{4\pi\varepsilon_0 R_{ij}} \quad (2.1)$$

where K_r and r_{eq} denote respectively the bond force-constant and the equilibrium bond distance, K_θ the angle force constant and θ the equilibrium angle. V_1, V_2 and V_3 represent the coefficients of Fourier series and ϕ the dihedral angle. R_{ij} is the distance between the atoms i and j, ε_0 the permittivity of the vacuum and q_i, q_j are their respective partial charges. The parameters for the intramolecular interaction for the $[BMIM]^+$ cation are from a simulation study reported earlier, [50] and those for the $[PF_6]^-$ anion from another study [51]. The intermolecular interactions include both the Lennard-Jones (LJ) and the Coulomb interactions. The LJ interactions between the unlike atoms were calculated by employing the Lorentz-Berthelot combining rules [52]. As done earlier, [53] the total charge on the cation and anion were reduced to ±0.8 *e*. The partial atomic charges and some of the modified Lennard-Jones parameters were also taken from an earlier study [53]. Table 2.B.1 - 2.B.5 (Appendix 2.B) summarizes the force field parameters used in the present simulations for representing the IL ions.

For hexane, the OPLS-AA force field parameters available in the literature [54] were employed, and are summarized in Table 2.B.6 – 2.B.9 (Appendix 2.B).

The following potential energy function described dioxane [55],

$$U(r) = \sum_{bonds} K_r(r - r_o)^2 + \sum_{angles} K_\theta(\theta - \theta_o)^2 + \sum_{dihedrals}[\frac{V_1}{2}(1 + cos\varphi) + \frac{V_2}{2}(1 - cos2\varphi) + \frac{V_3}{2}(1 + cos3\varphi)] + [\sum_{i<j}^{atoms}\{4\epsilon_{ij}[\left({}^{\sigma_{ij}}/_{r_{ij}}\right)^{12} - \left({}^{\sigma_{ij}}/_{r_{ij}}\right)^{6}] + {}^{q_i q_j}/_{4\pi\varepsilon_o r_{ij}}\}] \quad (2.2)$$

where, σ_{ij} denotes the van der Waals radius, ε_{ij} the well depth and the rest have as already been discussed. The interaction parameters and the initial co-ordinates for dioxane were taken from existing literature [55] and all the bonds were kept constrained throughout the simulations. Table 2.B.10 – 2.B.14 (Appendix 2.B) summarizes the interaction parameters for dioxane.

The OPLS/AA force field parameters and the molecular geometries for acetonitrile molecule reported earlier [56] and displayed in Web page http://virtualchemistry.org/ were used in the simulations performed here for [BMIM] [PF_6] + acetonitrile binary mixtures. By following this work [56], the moment of inertia and the total mass were maintained by adding a virtual construction site to the topologies to keep the nitrile group perfectly linear [57].

All the simulations were carried out in a cubic box employing periodic boundary conditions. The optimized geometries of the $[BMIM]^+$ and $[PF_6]^-$ ions and hexane molecules were obtained from *ab initio* calculations using the HF/6-31 + G(d) basis set in Gaussian03 program [58], and the starting configurations of the systems were built by using the Packmol software [59]. We used the initial co-ordinates for dioxane and acetonitrile molecules from earlier studies [55,56]. The structures of the ions and all the three co-solvent molecules were relaxed through energy minimization (EM) process via steepest descent algorithm in GROMACS [49]. All the bonds were kept constrained using the LINCS algorithm [60] with lincs order of 8. The cut-off radius for short-range interaction was set to 15 Å and the long-range electrostatic interactions were treated with particle mesh Ewald (PME) summation technique [61]. Each system was initially equilibrated at 450 K under 1 atm pressure in NPT ensemble using velocity rescaling thermostat [62] and Berendsen barostat [63] with coupling constants 0.5 ps and 2.0 ps respectively. Then the system was cooled down to 298 K by a step-down process with a step size of 50 K and each step was run for a duration of 100 ps. The system was again equilibrated in the NPT ensemble at 298 K for 4 ns to get the required density, which was further followed by equilibration in the NVT ensemble for 2ns, using the velocity rescaling thermostat [62]. The densities of the systems obtained from the present simulation were in good agreement with the experimental values (see Table 2.4 below). The equation of motion was solved by the leap-frog algorithm [52] using a time step of 2 fs. The production run was for 100 ns for all the mole fractions and the trajectories were saved after every 0.1 ps for the analyses. For visualization of the molecules, the Visual Molecular Dynamics (VMD) [64] program was employed.

Table 2.4: Comparison of simulated densities from the present simulations with those from experiments, and from earlier simulations.

System	Present simulation (gm/cc)	Experiment (gm/cc)	Earlier simulation (gm/cc)
[BMIM][PF_6] IL	1.408	1.369	1.389
Acetonitrile	0.754	0.776	0.755
Dioxane	1.060	1.0286	1.030
Hexane	0.658	0.659	0.658

2.2.2 Voronoi Polyhedra Analysis

By following the work reported earlier, [65] the Voronoi polyhedron (VP) region Π_i of atom i inside a box V of finite size is defined by the following expression,

$$\Pi_i = \{x | d(x, x_i) < d(x, x_j), d(x, x_i) < d(x, x_k)\} \quad (2.3)$$

for all $j \neq i$ and for all k respectively and Π_i is the set of points which is nearer to x_i than any other x_j's and x_k's. Each VP region is the intersection perpendicular bisectors of the segments which join the x_i and each of the other x_j's and x_k's. The set of Π_i's and its periodic repetitions will constitute a tessellation of space, called Voronoi tessellation.

If the two Voronoi polyhedra Π_i and Π_j of atoms i and j share a common face then atoms i and j are called as contiguous pair. Therefore, two molecules would be called neighbors if their VP shares a common face and hence, the number of shared faces could give the number of neighboring particles around the central particle [66]. Upon joining these contiguous pairs of atoms, a tetrahedron network containing a set of four atoms is formed, which creates a new tessellation called "Delaunay tessellation". The Delaunay tetrahedron (DT) and the Voronoi polyhedra (VP) are dual to each other and the circumcenter of a DT is a vertex of the VP. That is why there exists an atom at the center of a VP, whereas the circumsphere of a DT is vacant. The graphical representations of construction of the Voronoi polyhedra are available in several

earlier works [65-68]. After the construction of the Voronoi polyhedra, one can study the distribution of void and neck radii. The vertices and edges of a VP are in equal distance from the nearest surrounding particles. If each particle will be a sphere of finite radius, then the radius of void (r_{void}) may be defined as the distance between a VP vertex and the surrounding particles (r) minus the radius of the corresponding particle (r_p); that is, $r_{void} = r - r_p$. Again, these voids are connected through channels, which are called necks and the radius of these necks r_{neck} is defined as a perpendicular distance between a VP edge and the surrounding particle (r_1) minus the particle radius [66,67] (r_p): $r_{neck} = r_1 - r_p$.

The Voronoi polyhedral (VP) method was extensively used in the literature to determine the structures of soft matter systems [69-71] and different solvents like methanol [72-74], ethanol [75,76] ammonia [77] and water [78,79]. This method can be utilized to determine the structure of the 'pore space' or 'void space' which helps to understand the local densities and environments of the cation-anion pairs in these IL + cosolvent binary mixtures, depending on topology at different concentrations of [BMIM][PF_6]. Considering the molecules as a spherical atom, we used centre of mass (c.o.m.) of the ions to perform the VP analysis. The VP of a molecule i, is referred to as the locations of all those points which are closer to i than to any other molecules in the system. To construct the VP of the i^{th} molecule, at first, we find all the nearest neighbour molecules that are within the radius denoted as r_0, which in turn can be calculated from the radial distribution function, g(r) of the ion pairs. In order to get a simple understanding about voids, we have to first determine the perpendicular bisector planes to lines joining i and all other nearest neighbour molecules, which intersect in a line. When three such lines intersect to a point, generates a VP vertex indicating largest empty spherical free space present between the molecules. Therefore, void radius can be defined as the distance between the VP vertex and the i^{th} atom, subtracting the atomic radius. On the other hand, neck radius can be defined as the perpendicular distance between the atom and the edge of the VP, subtracting the atomic radius. For this study, we carried out the VP analysis* employing the algorithm described earlier [65,68].

* Voronoi Polyhedra Analysis have been performed in collaboration with Prof. Pradip Kumar Ghorai (IISER Kolkata), India. It has been already published (Journal of Molecular Liquids 317 (2020) 113746)

2.3 Results and Discussion

2.3.1 Densities: fidelity check of the force field

Figure 2.1 shows the simulated densities of the neat systems considered here, namely, [BMIM], [PF_6], acetonitrile, dioxane, and hexane and compares with those from earlier simulations [53,55,56,80] and experiments [81-84]. Clearly, densities for the neat systems from the present simulations are in good agreement with those from earlier reports [55,56,80-82,84].

Figure 2.1 also displays the simulated densities of the three binary mixtures, ([BMIM][PF_6] + acetonitrile /dioxane/hexane), at five different IL mole fractions, F_{IL}=0.90, 0.75, 0.50, 0.25, 0.10, and compares with the available experimental data [85,86]. Clearly, the composition dependent densities obtained from the present simulations of [BMIM] [PF_6] + acetonitrile binary mixtures are in good agreement with the experimental data [85]. The composition dependent densities of the ([BMIM] [PF_6] + dioxane) binary mixtures were measured in-house by using an automated density-cum-sound analyzer (DSA 5000, Anton Paar) and the measured densities, as Figure 2.1 displays, match well with the simulated values.

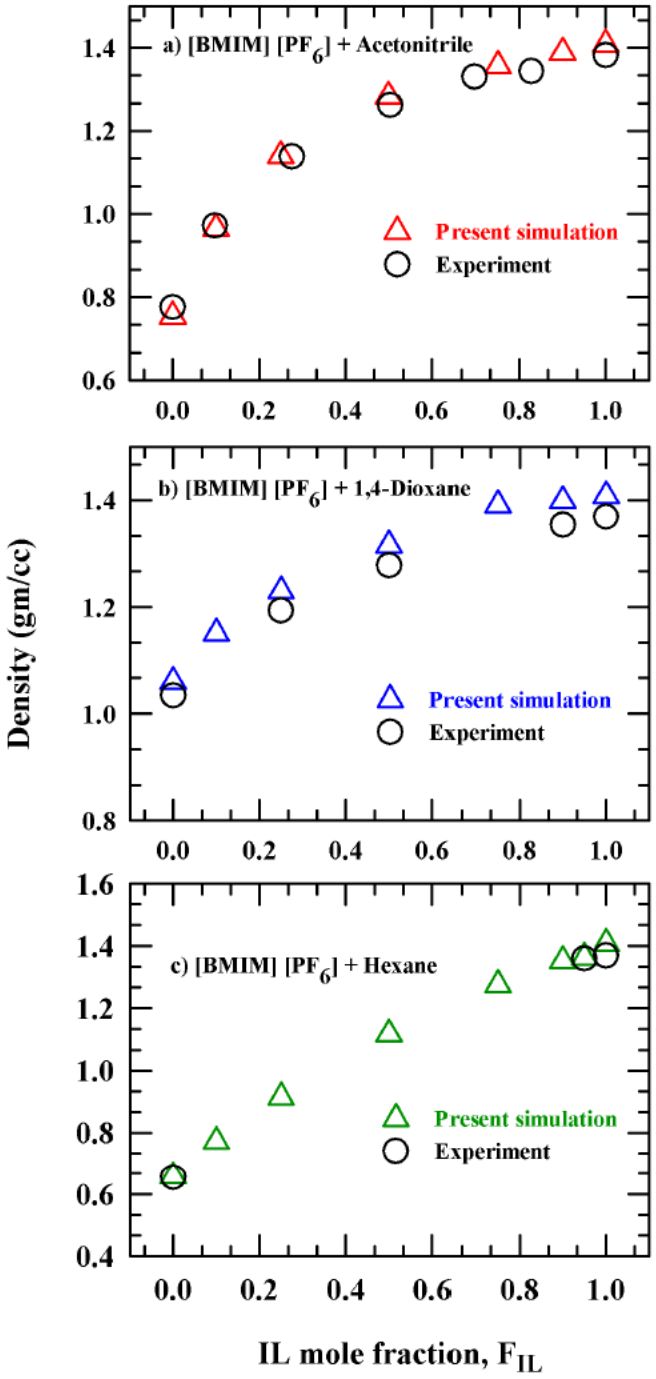

Figure 2.1: Comparison between simulated and experimental densities for the neat and the IL + cosolvent binary mixtures. Results are for 298 K. Open and filled symbols indicate respectively the densities from present simulations and experiments. The representations are color coded and the color codes are: pink, experimental density; red, ([BMIM] [PF_6] + acetonitrile); blue, ([BMIM][PF_6] + dioxane); green, ([BMIM][PF_6] + hexane).

Note an earlier experimental study [86] reported that [BMIM] [PF_6] is soluble in hexane only at mole fractions above F_{IL} = 0.8467 at temperatures higher than 340 K. We checked the solubility of [BMIM] [PF_6] and hexane for the mole fraction, F_{IL}=0.95 at 298 K (visually) and measured, as described for [BMIM] [PF_6] + dioxane binary mixtures, the density at this composition. Here also the agreement between the simulated and experimental densities, as displayed in Figure 2.1, is quite satisfactory.

We would like to mention here that in real experiments, [BMIM] [PF_6] + hexane binary mixture was found to macroscopically phase separate at $F_{IL} \leq 0.9$ at 298 K, and therefore densities for these binary mixtures at 298 K could not be measured for compositions $F_{IL} \leq 0.9$. However, the model potentials employed here to represent hexane and [BMIM] [PF_6] did not reproduce such a pronounced solubility gap and allowed simulations of the [BMIM] [PF_6] + hexane binary mixtures for compositions studied for the other two systems, although simulated radial and spatial distribution functions (presented later) clearly indicate increased clustering and non-uniform distribution of hexane, particularly at the lower mole fractions of [BMIM] [PF_6]. This suggests that these model potentials, although could not reproduce the composition dependence of the experimental solubility of hexane in [BMIM] [PF_6], they perhaps possess the right pieces of interaction parameters tweaking of which may produce the experimentally observed macroscopic phase separation.

2.3.2 Solution Structure of the Binary Mixtures: Insights from the Simulated Radial Distribution Functions (RDFs)

Because the first information on relative arrangements of particles in a condensed phase can be accessed via the radial distribution functions, a number of them that include both intra and inter-species have been computed for these binary mixtures at different compositions. As both polar and non-polar moieties exist in IL, we label the centre of the imidazoilum ring of the cation as “CR” which is considered as “head” (polar moiety) and the carbon atom “CT4” of the terminal methyl group of the alkyl chain as “tail” (non-polar moiety). This is indicated in Figure 2.A.2 (Appendix 2.A), along with a snap-shot of the equilibrated neat IL where segregation into polar and non-polar domains are clearly visible. One may obtain the RDFs involving these head and tail groups as well as the center-of-mass RDFs for investigating the preferred spatial arrangements and clustering.

2.3.2.1 Comparison of RDFs with earlier simulations

Figure 2.2 shows a comparison among the RDFs simulated in the present work and those reported earlier [22,53,87] for the neat [BMIM] [PF_6]. Note here that we have compared the center-of-mass anion-anion, cation-anion and cation-cation RDFs, and the atom-atom RDF between the H (H5) atom of the imidazolium ring of the cation and the fluorine atom of the anion. Clearly, the agreement between the present simulations and previous reports are quite satisfactory.

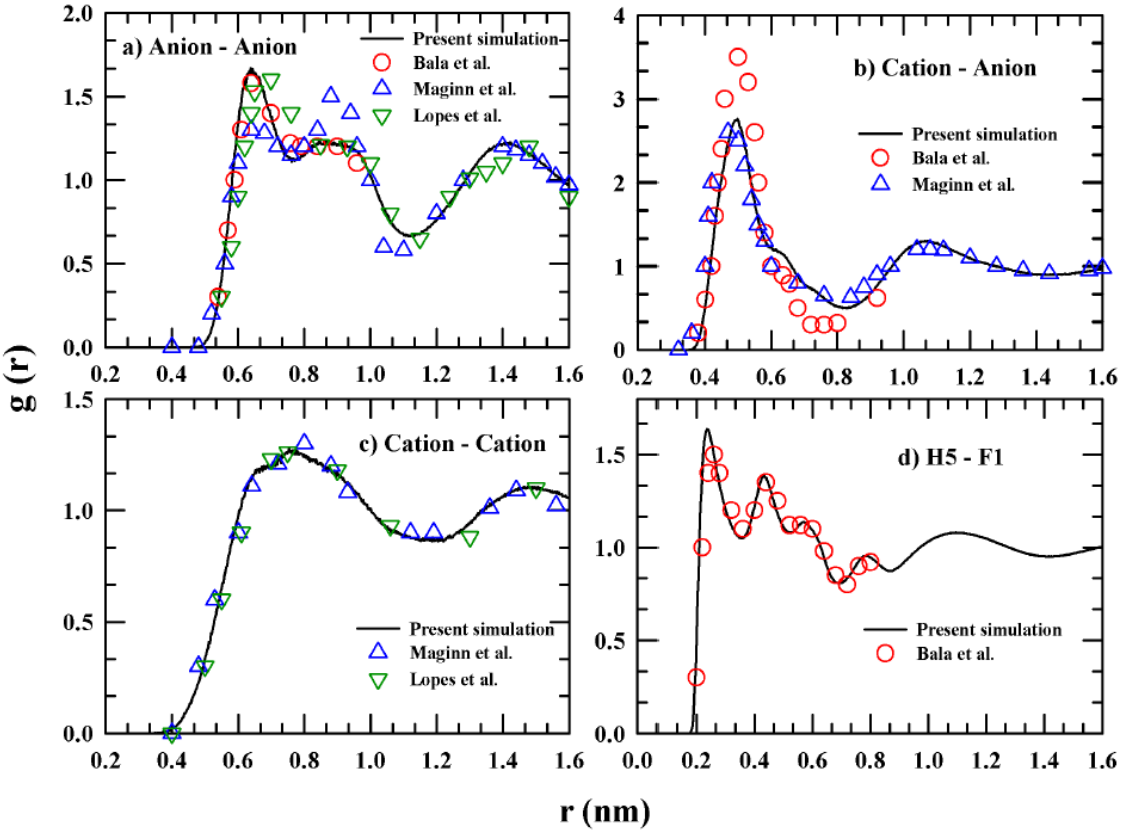

Figure 2.2: Comparison of simulated RDFs for anion-anion, cation-anion, cation-cation and H5 (H-atom of imidazolium ring of the cation)-F1 (fluorine atom of anion $[PF_6]^-$) of neat [BMIM] [PF_6] between the present simulations and those reported earlier [54,80]. Here, solid line represents results from the present simulations, whereas open symbols in blue, pink and green indicate the earlier simulated data. Note that "cation" here indicates the head group which is represented in the text as "CR".

2.3.2.2 Interaction of the cosolvent molecules with the Ionic Liquids

Because [BMIM] [PF_6] IL segregates into two polar and non-polar domains (shown in Figure 2.A.2, Appendix 2.A), the hosting of acetonitrile, dioxane and hexane in this IL will be guided by their interactions with these domains of [BMIM] [PF_6] according to their polarity [33,34]. For a representative study, we have monitored the interactions of these three cosolvents at a very dilute concentration through their different atoms with the different parts of the cation and the anion. Figure 2.3 depicts these interactions where the cosolvents are present as a minor component at F_{IL}=0.9.

As expected, the interaction of the IL with acetonitrile is the most pronounced among these three cosolvents of differing polarities. A detailed inspection of the individual RDFs suggests that the P atom of the anion is interacting more with different atoms of the acetonitrile molecule than the imidazolium ring containing part of the cation. This is also the observation for the interaction of dioxane with the IL ions. The interaction of hexane with these charge carrying parts of the IL is the weakest among these three cosolvents and this is the molecular level reflection of what we expect regarding their relative solubilities in this IL based on solvent polarity. Figure 2.A.3 (Appendix 2.A) depicts, via RDFs, the interactions of these cosolvents with the tail part (alkyl chain) of the IL cation. Notice in this figure that the interaction between dioxane and the tail part of the IL cation (CT4) is comparable to that between hexane and CT4. However, a relatively stronger interaction of dioxane with the ions (see Figure 2.3) than hexane permits a better miscibility of quadrupolar dioxane in this hydrophobic IL than non-polar hexane.

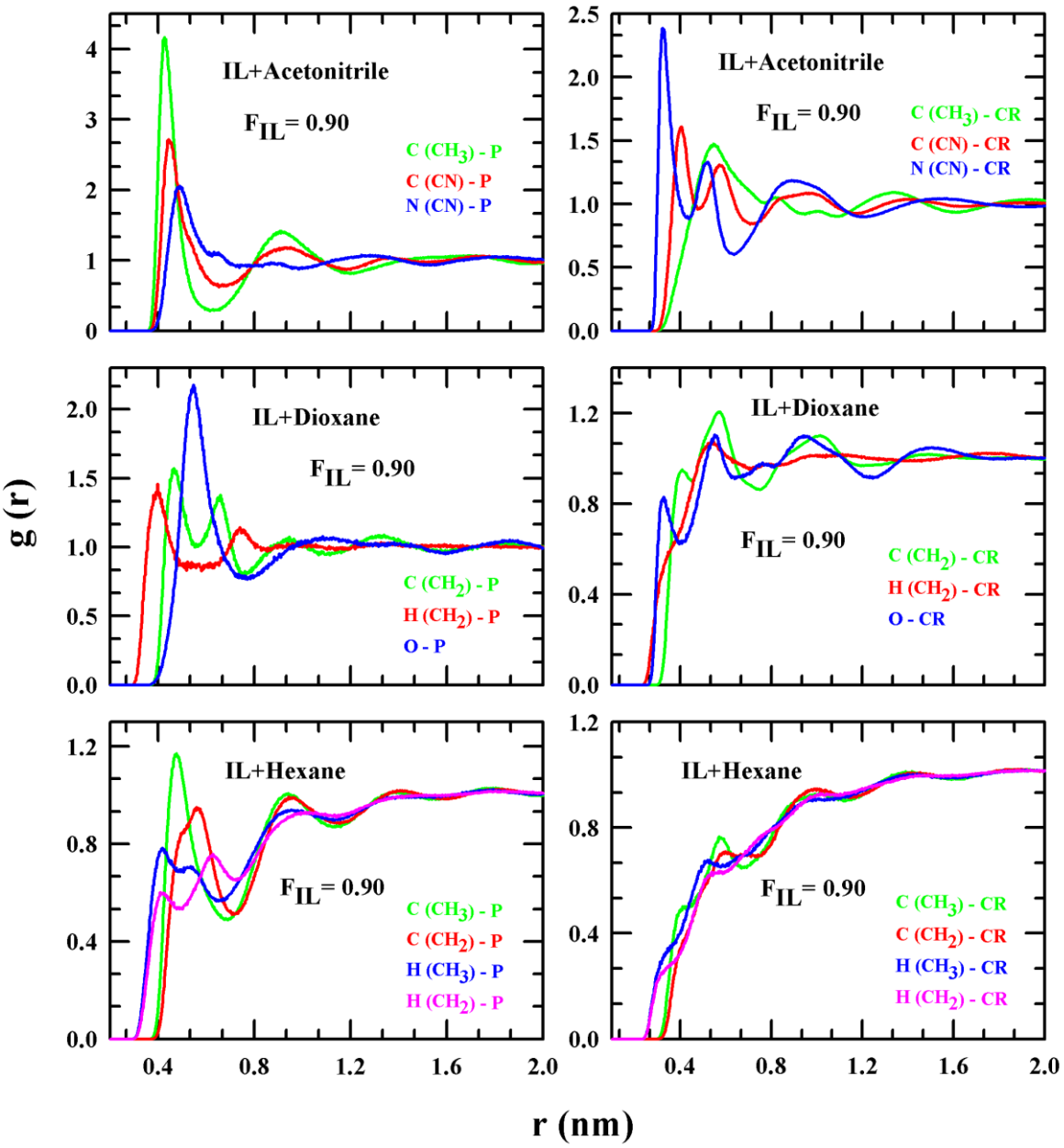

Figure 2.3: Simulated radial distribution functions (RDFs) between different atoms of the three cosolvents with different parts of the anion and the cation at mole fraction, F_{IL}=0.90, for the three different types of binary mixtures. Here, atomic pairs and their respective color codes are given in the inset of every panel. Note interactions are shown with the P and CR atoms (C-atom of the imidazolium ring attached to the two N-atoms) of the anion and cation respectively.

2.3.2.3 Ion-ion RDFs at low IL concentration: Debye screening length and break down for quadrupolar solvent

Figure 2.4 displays the simulated ion-ion and tail-tail RDFs for these three binary mixtures at F_{IL}=0.1. Note the peak heights of all the RDFs for [BMIM] [PF_6] + hexane binary mixture are the highest, while those for binary mixtures containing acetonitrile or dioxane are not too different from each other. The uncharacteristically large peak values of RDFs for dilute IL solutions in hexane indicate that the IL ions are not fully dispersed in hexane solution even at such a low concentration. This is a reflection of increased aggregation tendency of IL ions in low polar solvent, and can be understood in terms of Debye screening length (DSL):[88] $\kappa^{-1} = \sqrt{[\varepsilon_0 RT/2\rho F^2 I]}$ where R denotes the Boltzmann constant (k_B) times Avogadro number (N_A), T the absolute temperature, ρ the solution density, I the ionic strength and F the Avogadro number times the electronic charge (q). DSL is a continuum limit estimate of the lengthscale beyond which the field of an ion cannot be felt in an electrolyte solution, and increases with the$\sqrt{\varepsilon_0}$ at a given temperature and ionic strength. Quite clearly then the DSL would be very small in a non-polar solvent like hexane for which $\varepsilon_0 \sim 2$, allowing the ions to interact strongly with each other even in a solution of low ionic strength. This explains the very large peak heights for various RDFs in the hexane solution. A relatively large value of ε_0 also justifies the normal liquid-like heights of RDFs simulated for acetonitrile solution. What is counter-intuitive here is the similarity of RDF heights between the dioxane and acetonitrile solutions although the ε_0 value for dioxane is nearly the same as that for hexane. This can be attributed to the large quadrupole moment of dioxane which allows a better dissolution of the ions (relative to a non-polar solvent) via a stronger screening of the charge-charge interactions in a solution. This also reflects a break-down of the Debye-Huckel-Onsager theory of electrolyte solutions [88] in non-dipolar solvents where the effects of quadrupole moment on DSL have not been incorporated.

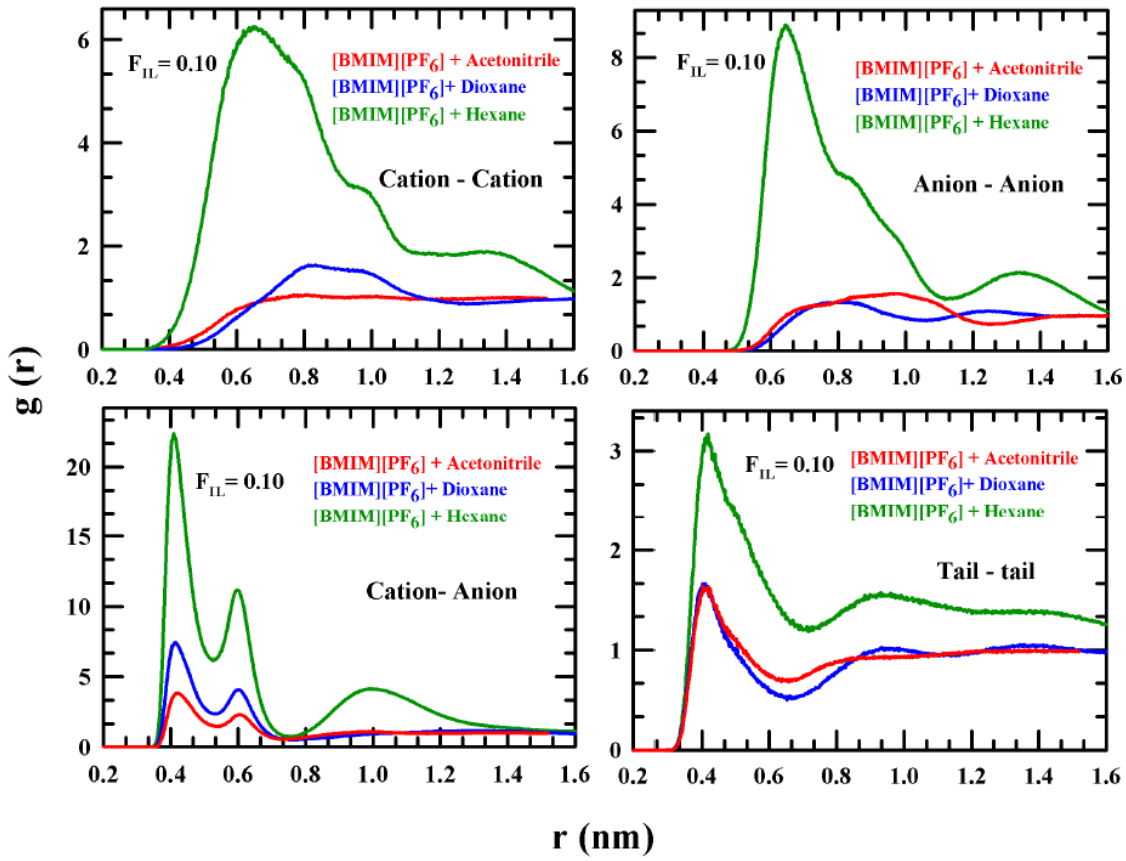

Figure 2.4: Simulated radial distribution functions (RDFs) for ion-ion (cation-cation, anion-anion, and cation-anion) and tail-tail for the three mixtures at F_{IL}=0.10. Various mixtures are color coded as shown in the insets of the figure. Note the cation-cation RDF represents the head-head interaction, and the tail-tail is between "CT4" atoms as represented in the text.

2.3.2.4 Impact of cosolvent polarity on solution structure: composition dependence of RDFs

We show in Figure 2.5 the composition dependent head-head and tail-tail RDFs for binary mixtures of [BMIM] [PF_6] with acetonitrile, dioxane and hexane. Note these head-head RDFs represent essentially the cation-cation RDFs because this head group is the cationic imidazolium group denoted as CR. The composition dependent anion-anion and cation-anion RDFs are provided in Figure 2.A.4 (Appendix 2.A).

Inspection of these RDFs is again a manifest of the polarity driven interactions of the IL ions with the cosolvent molecules at different concentrations. All ion-ion RDFs in acetonitrile and dioxane binary mixtures are comparable but differ from those for hexane binary mixtures. As already discussed, this difference originates from the relatively poor solvent screening of the IL ions in non-polar hexane. This relatively poor solvent screening is also the reason for somewhat larger heights of various RDFs in dioxane binary mixtures (particularly those at lower IL mole fractions) than the corresponding ones for acetonitrile solutions.

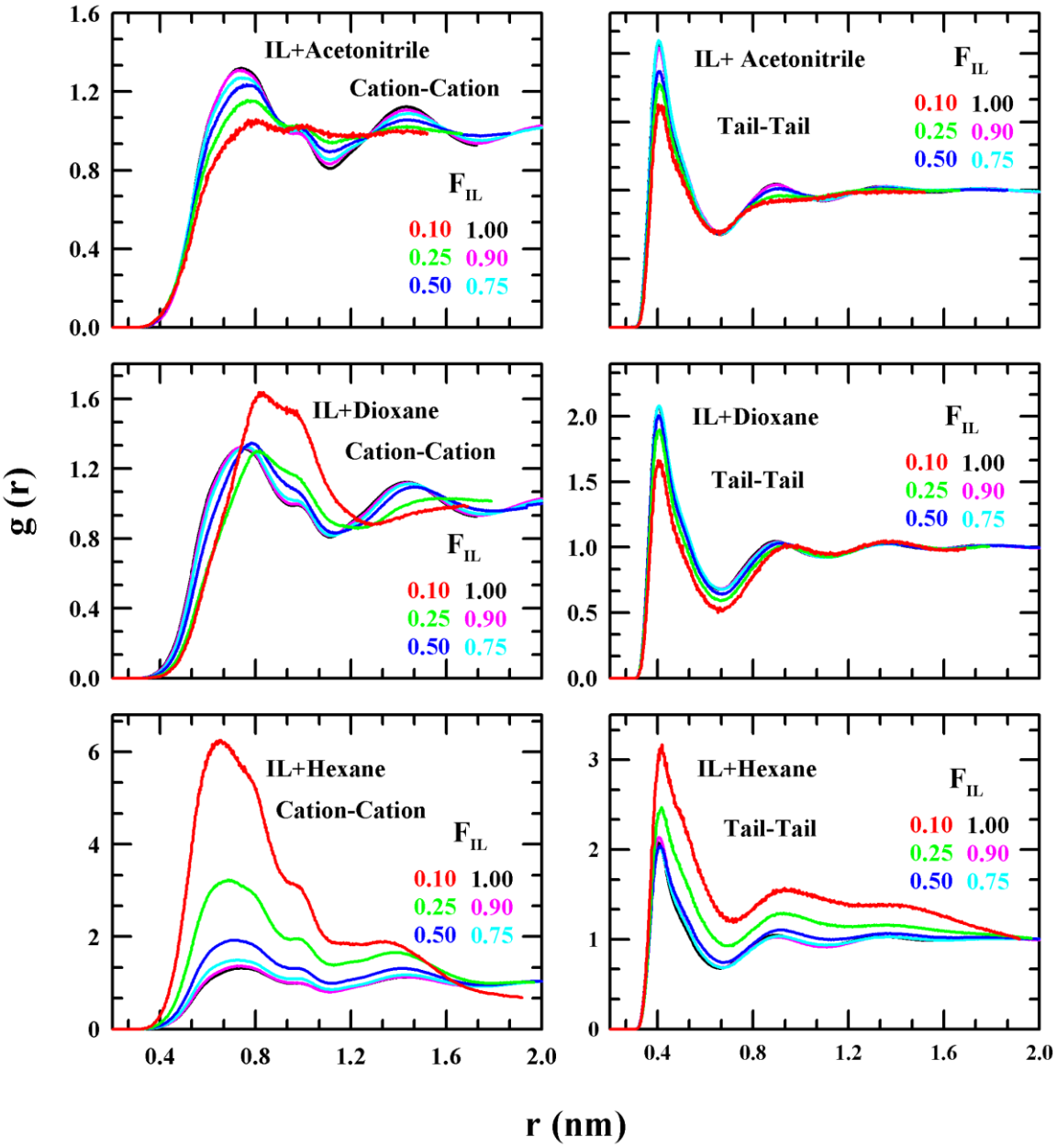

Figure 2.5: Simulated composition dependent radial distribution functions (RDFs) for cation-cation and tail-tail for the binary three mixtures. IL mole fractions are color coded.

Figure 2.6 presents simulation snapshots of these binary mixtures at a few representative IL mole fractions for a molecular view of IL ions in these cosolvents. These snapshots are complimentary to the RDFs and the discussion presented above assist in realizing the cosolvent polarity and mixture composition dependence of the solution structure. For clarity, molecular representations of the cosolvent molecules are not shown but the pictures are color-coded for different cosolvents.

At the highest IL mole fraction shown here (F_{IL}=0.9), the formation of polar and nonpolar domains and their distributions in binary mixtures of acetonitrile and dioxane remain nearly the same as that for the neat IL (see Figure 2.A.2, Appendix 2.A), whereas somewhat more pronounced clustering appears in the presence of hexane at this composition. This clustering and segregation into polar and non-polar domains enhance with the decrease in IL mole fractions in these binary mixtures and become the most pronounced for hexane mixture at F_{IL}=0.1. These snapshots, therefore, corroborate with the information provided by the two-dimensional-ion and tail-tail distribution functions presented earlier in Figure 2.5 and Figure 2.A.4 (Appendix 2.A), and strongly suggest that both cosolvent polarity and concentration critically affect the self-aggregation in IL. This is further supported by the representative snapshots for tail-tail interaction shown in Figure 2.A.5 (Appendix 2.A). Interestingly, similar enhancement of microscopic segregation and domain formation at low IL mole fractions have been found in experimental studies of aqueous binary mixtures of ILs with longer alkyl chains [13,89].

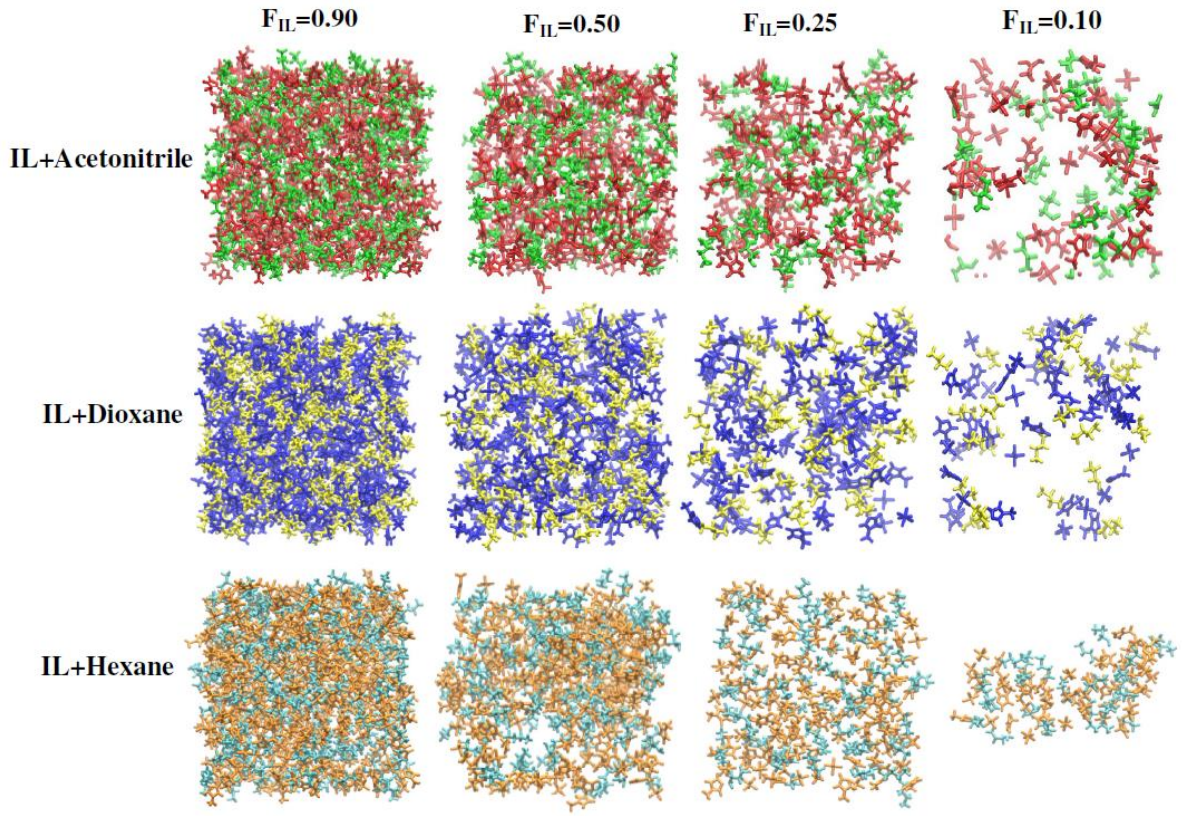

Figure 2.6: Snapshots from MD simulations for the three binary mixtures at IL mole fractions, F_{IL}=0.90, 0.50, 0.25, 0.10. For clarity, the co-solvent molecules are not shown and only the polar domain (comprised of the imidazolium ring along with the methyl chain of the cation and the anion) and the non-polar domain (includes the butyl chain of the cation) are shown. The color coding is defined as follows: (IL + acetonitrile) - red, polar domain; green, non-polar domain, (IL + dioxane) – blue, polar domain; yellow, non-polar domain, (IL+hexane) – brown, polar domain; cyan, non-polar domain.

Next, we present in Figure 2.7 the composition dependent solvent-solvent radial distribution functions for these binary mixtures in order to explore whether cosolvent clustering also occurs in these solutions particularly in the limit of high IL mole fractions. Interestingly again, RDF profiles shown in this figure indicate the strongest solvent clustering for hexane than for acetonitrile and dioxane at low cosolvent concentrations. Note also that the dioxane RDFs are nearly insensitive to the mixture composition while acetonitrile RDFs show a moderate increase in its height with the increase of IL mole fraction. However, the rate of increase of this height with the increase of IL mole fraction is much stronger for hexane than acetonitrile. It is therefore quite clear that the solution structure of these binary mixtures is dominated by the cosolvent clustering at higher IL mole fractions and segregation of IL into more pronounced polar and nonpolar domains in the limit of low IL concentrations, and these solution structural features depend strongly on cosolvent polarity.

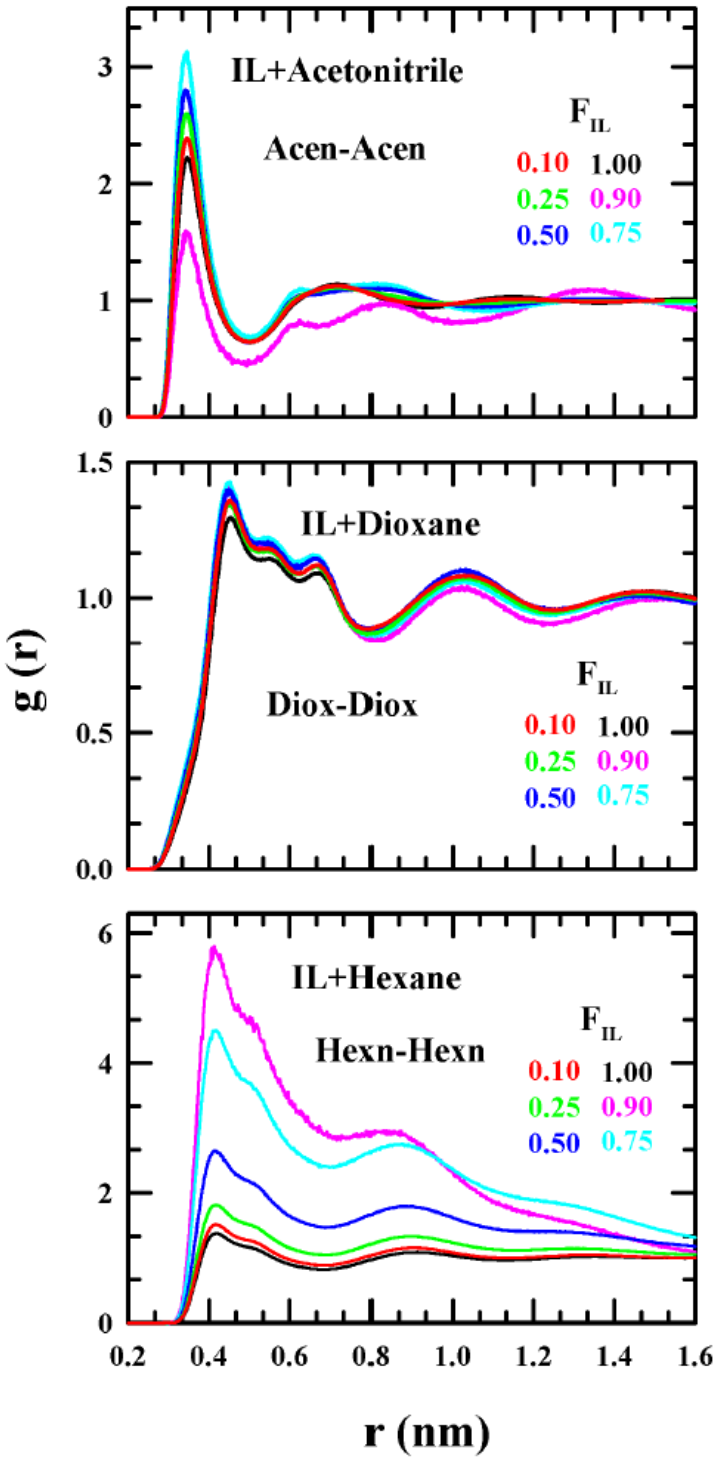

Figure 2.7: Simulated composition dependent solvent-solvent RDFs for the three binary mixtures. Here, the mole fractions are color coded as given in the inset of every panel. Note acetonitrile, dioxane and hexane are represented respectively as Acen, Diox and Hexn.

2.3.2.5 Coordination number (CN)

To get further insights into the solution structure, we have calculated the coordination number (CN) for the first solvation shell by using the relation, $CN = 4\pi\rho \int_0^{r_{shell}} dr\, r^2\, g(r)$, where r_{shell} denotes the distance where the first minimum of g(r) appears and ρ the bulk solution density. Note in these calculations r_{shell} is estimated from the first minimum of the corresponding RDFs shown before. For comparing our CN with earlier simulations for neat [BMIM] [PF_6] [87], r_{shell} has been determined from the center of mass RDFs. Table 2.B.15 (Appendix 2.B) presents the comparison with the present and the earlier [87] simulations and the agreement appears satisfactory.

The composition dependence of the coordination number (CN) for the first solvation shell in the three IL + cosolvent binary mixtures is presented in Figure 2.8. The coordination numbers correspond to number of cations around a cation (cation-cation), of anions around an anion (anion-anion) and of anions around a cation (cation-anion). Note the non-ideal increase of CN with IL mole fraction in all these three binary mixtures and the similarity between them for binary mixtures with dioxane and acetonitrile. Note also the higher CN for IL + hexane mixtures than those for the other two binary mixtures at lower IL mole fractions. This is a reflection of shorter DSL for solutions in the nonpolar hexane discussed earlier. For a better understanding, we show, in the right lower panel of this figure, the percentage of number of anions present around a cation. Data shown here indicate that the higher fraction of anions resides in the first solvation shell of the cation at the lower IL mole fractions, largest being for the IL + hexane binary mixtures.

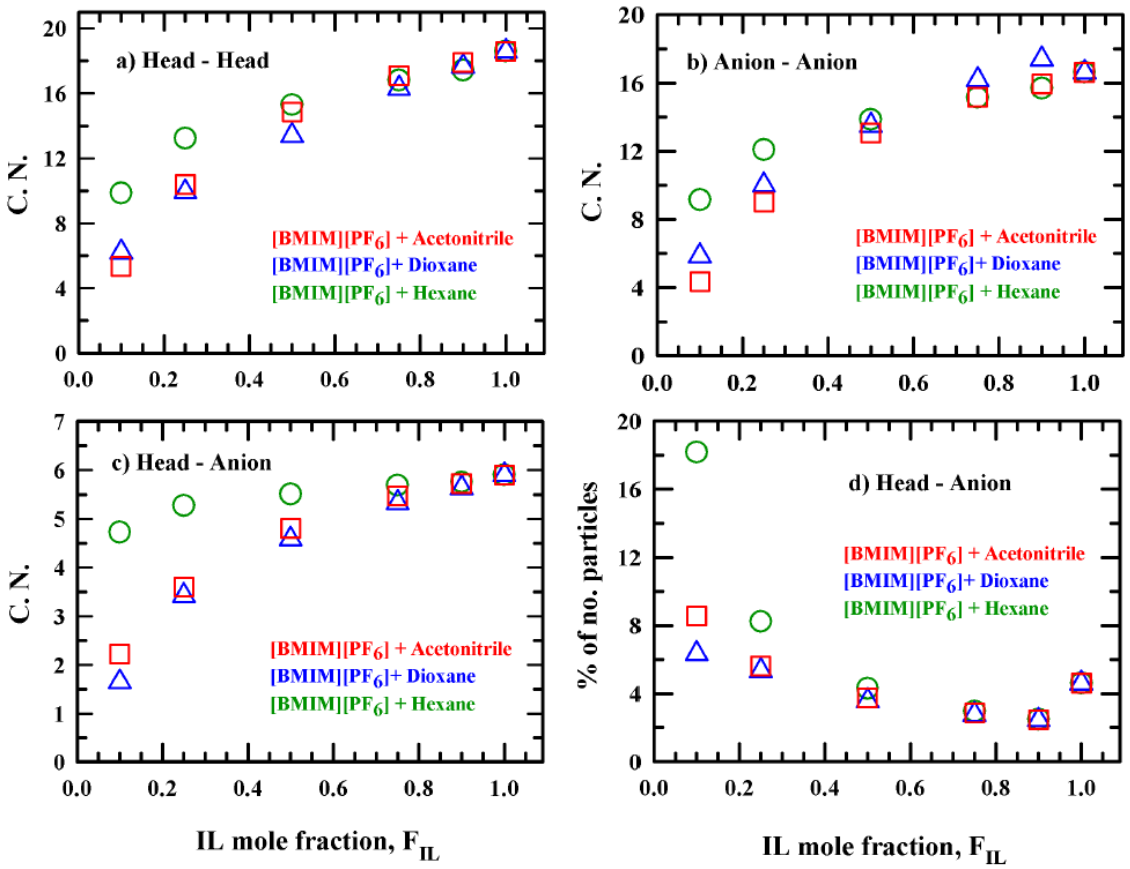

Figure 2.8: Composition dependent co-ordination numbers (CNs) for the cation-cation, anion-anion, cation-anion first solvation shells, and percentages of number of particles in the cation-anion first solvation shell for these three binary mixtures. Different mixtures are represented by open symbols; color coding are as follows: red square, (IL + acetonitrile); blue triangle, (IL+1, 4-dioxane); green circle, (IL+hexane).

2.3.2.6 Spatial distribution functions (SDFs)

For exploring the three-dimensional spatial arrangements of ions and cosolvent molecules in these binary mixtures at different compositions and to better understand the polarity impact on solution structure, we next obtain the composition dependent spatial distribution functions (SDFs) by selecting the $[BMIM]^+$ cation as reference molecule via the TRAVIS program [90]. The isovalues used to construct the SDF plots are available in Table 2.B.16 and Table 2.B.17 of Appendix 2.B. Note, for constructing the 3D iso-surface we choose that particular density value (isovalue), which represents the completion of first solvation shell.

The spatial distribution function of $[PF_6]^-$ ions around a $[BMIM]^+$ in the neat IL is presented in the upper panel of Figure 2.9, which shows that the anions are located above and below the imidazolium ring plane, where a significant anion density exists above the H5 atom with an isosurface of semi-circular shape. Also, anion densities can be noticed near the H4M-atom (closer to the methyl group) and the H4A-atom (closer to the butyl chain of the cation). The anion density near H4A atom appears relatively less and this may be due to the steric hindrance caused by the butyl chain. Because SDFs provide a three-dimensional view of the spatial arrangements of particles, these observations can be connected to the similar information provided for two-dimension by the corresponding RDFs. These RDFs (between different H-atoms and the P atom of the anion) are shown in the lower panel of this figure, which indicates a relatively larger peak height of g(r) for the H5-P than those for the H4M-P and the H4A-P radial distribution functions. The structure depicted by the SDFs of anion around the cation in the present simulations is comparable to earlier simulation reports [50,53,91]. Figure 2.A.6 (Appendix 2.A) shows this comparison. However, such an anion density near the H4A atom was missing in earlier study [53] and this can be connected to the slight disagreement of cation-anion RDFs between the present simulations and those reported earlier [53].

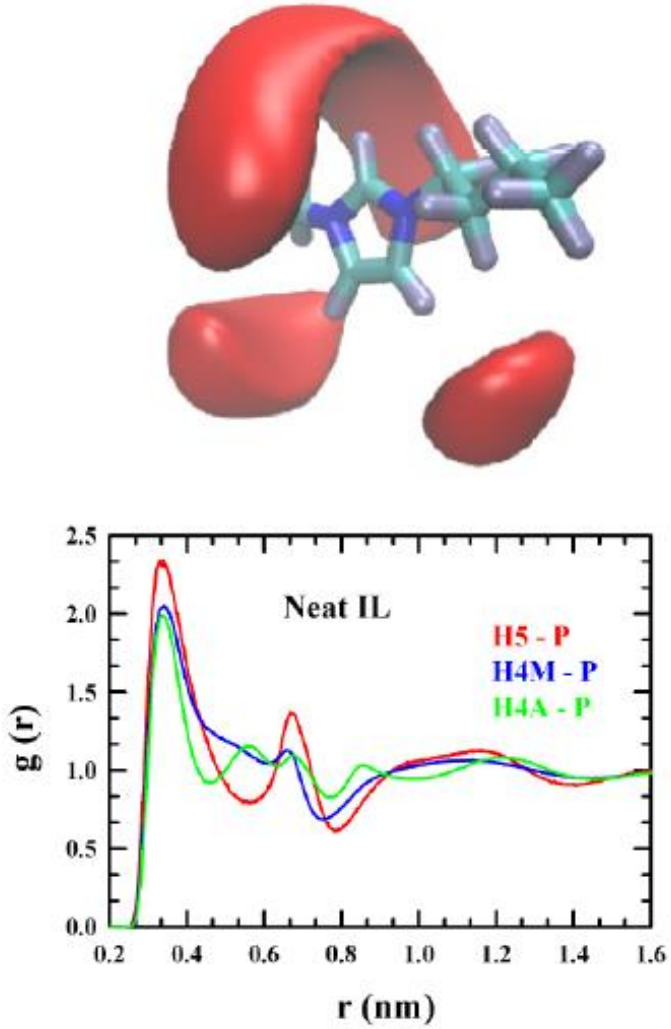

Figure 2.9: Spatial distribution functions, SDFs of the $[PF_6]^-$ anions (red, solid frame) around the cation $[BMIM]^+$ in neat IL, F_{IL}=1.0 (upper panel) and the simulated RDFs between various H-atoms attached to the imidazolium ring of the cation and the anion (lower panel).

The composition dependent SDFs for the anion and the three co-solvents acetonitrile, dioxane and hexane around the cation are depicted in Figure 2.10 for these three binary mixtures for F_{IL}=0.90, 0.50, 0.10. The following aspects can be noted from these SDFs. Both cosolvent polarity and concentration dependence are evident in this figure. For example, at any of the three representative IL mole fractions shown here, the anionic and cosolvent isodensity surfaces (or simply isosurfaces) differ significantly as one moves from polar to nonpolar solvent via the quadrupolar one. At higher IL mole fractions for IL + acetonitrile binary mixtures, the cosolvent isosurface accompanies the anion isosurface surrounding the cation but undergoes a depletion as IL becomes the minor component at F_{IL} =0.1. As expected, these cosolvent and anion isosurfaces are mostly around the cationic imidazolium ring, leaving out the butyl chain. As one replaces the dipolar acetonitrile as a cosolvent by the quadrupolar dioxane, the cosolvent isosurface does not appear immediately after the anion isosurface even at the highest F_{IL} considered; what we observe here is the expansion of the dioxane isosurface with the decrease of IL concentration which eventually provides a partial coverage to the butyl chain at F_{IL} =0.1. The most dramatic difference in the build-up of isosurfaces appear when the cosolvent is changed to nonpolar hexane. Note in this mixture that even at F_{IL} =0.9, the cosolvent and the anion isosurfaces appear as completely disjoint entities with the anion isosurface covering the cationic imidazolium ring and the hexane isosurface building up near the butyl chain. Upon increasing the hexane concentration further in this mixture, the cosolvent isosurface moves further away, indicating a clear microscopic phase separation between the IL and the cosolvent. These evidences were there in the composition dependent RDFs presented earlier but these SDFs have provided a vivid pictorial description of the microscopic solution structure in terms of ion and cosolvent distributions. We next explored the distributions of the anion and the cation in the three-dimensional solvation shell of the cosolvent molecules. Figure 2.11 shows the SDFs for the cation and the anion around the co-solvent molecules in these three binary mixtures at the mole fractions, F_{IL}=0.90, 0.50, 0.10. The SDFs around the acetonitrile molecule demonstrates that the anions are populated near the methyl (-CH_3) group and the cations near the N-atom of the nitrile (-CN) group of the acetonitrile molecule. RDFs shown in Figure 3 have already suggested such a spatial arrangement and the SDFs shown here confirm this microscopic picture in three-dimensions. Moreover, the composition dependence of the SDFs for this mixture suggests that the isodensity surfaces constructed by the cations and the anions surrounding the acetonitrile molecules gradually thins out with the further addition of acetonitrile in the IL + acetonitrile mixture.

The SDFs for the cation and the anion around the dioxane molecule indicates that anion densities are building up near the methylene (-CH_2 groups) on both sides of the oxygen axis, whereas the cation densities reside near the oxygen atoms, above and below, of the dioxane molecule. This has also been suggested by the corresponding RDFs shown already in Figure 2.3, although such a three-dimensional view was missing. As observed for IL + acetonitrile binary mixtures, the isodensity surfaces of anion and cation around the dioxane molecule decrease (not greatly though) upon further addition of dioxane in this binary mixture. There exists, however, a qualitative difference in the way these ion isodensity surfaces cover the acetonitrile and dioxane molecules in their respective binary mixtures with [BMIM] [PF_6]; this is a reflection of the difference in their polarities at the molecular level.

The difference in polarities and their reflection on ion isodensity surfaces appear dramatically when the ion isosurfaces are examined surrounding the hexane molecule in [BMIM] [PF_6] + hexane binary mixtures. At F_{IL}=0.9, the ion isosurfaces are closer, suggesting increased solubility of hexane only at higher IL mole fractions. At this IL concentration, hexane molecules interact with the alkyl chain of the cation. As hexane concentration is successively increased in the binary mixture, these isosurfaces move away because of the increased and more favorable interactions among hexane molecules. This then allows phase separation of the components which is seen as increased clustering of hexane molecules in Figure 2.10. Such a microscopic phase separation in the present simulations, as we will see in the next sub-section, can impose a barrier for qualitative analyses of the neck and void distributions in these binary mixtures.

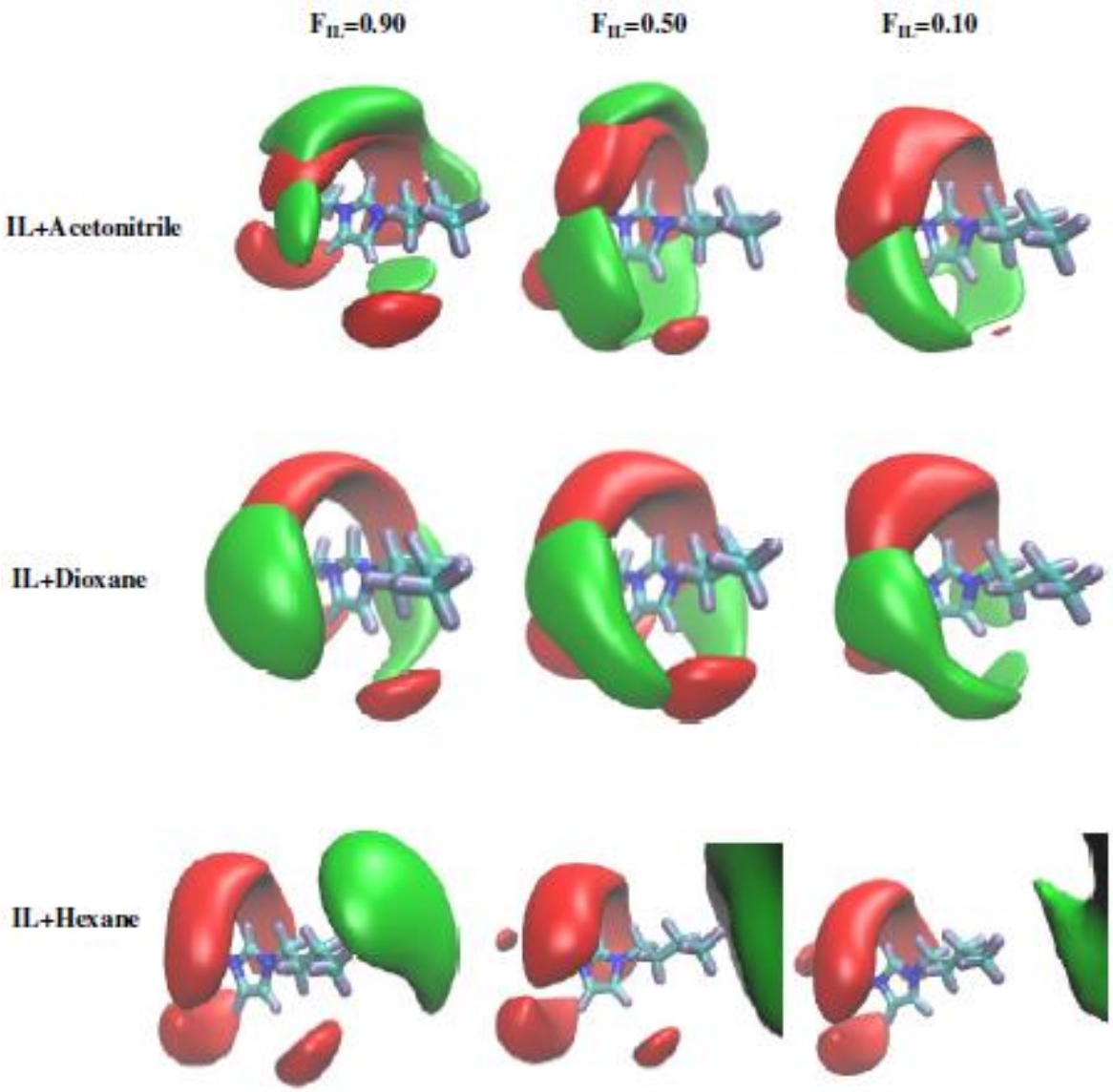

Figure 2.10: Composition dependent SDFs for the anion (red, solid frame) and the co-solvents (green, solid frame) around the cation for the three binary mixtures at F_{IL}=0.90, 0.50, 0.10. Note a few representative compositions are shown only to avoid clutter.

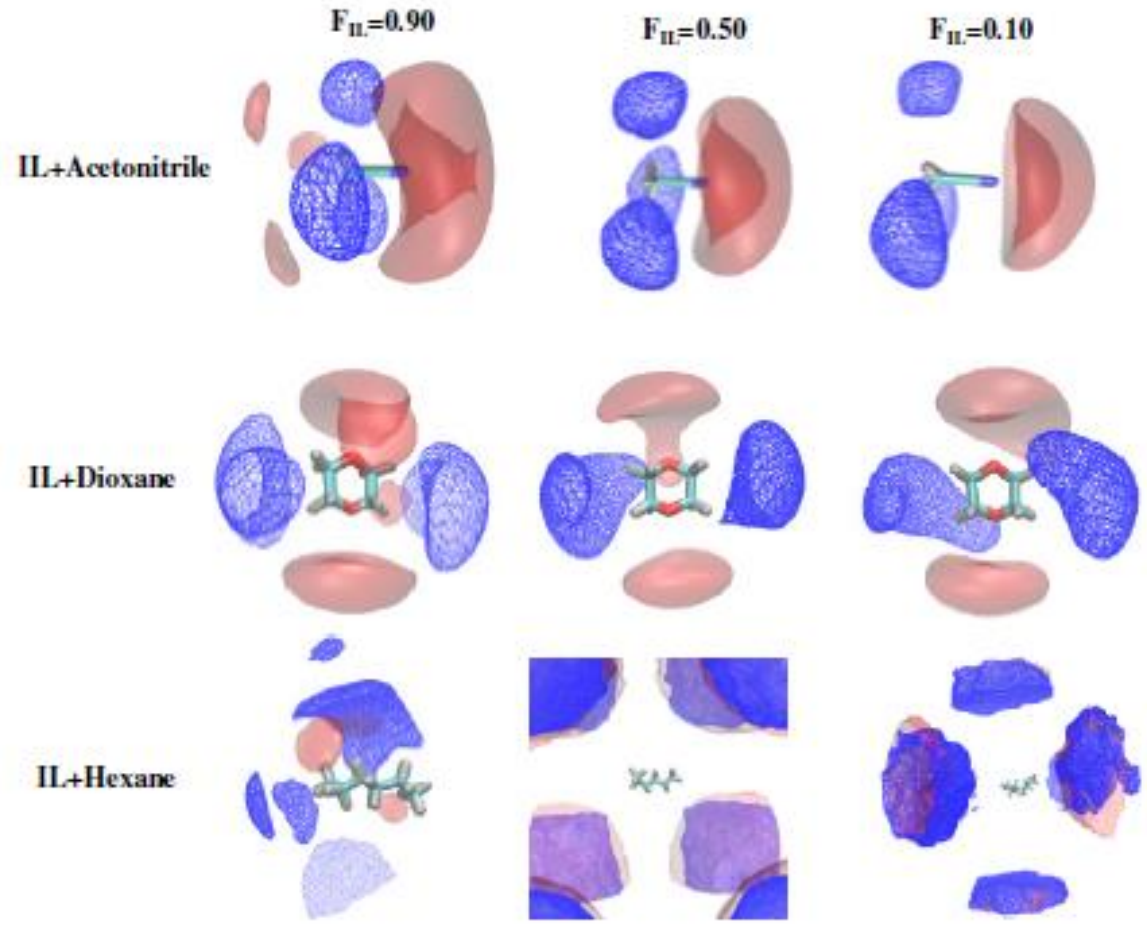

Figure 2.11: Composition dependent SDFs for the cation (red, transparent frame) and the anion (blue, wireframe) around the three cosolvents in the three binary mixtures for F_{IL}=0.90, 0.50, 0.10.

2.3.2.7 Voronoi Polyhedra analysis

We have computed the composition dependent void and neck distributions for [BMIM] [PF_6] + acetonitrile/dioxane/hexane binary mixtures to get further insight into the solution structure and their cosolvent polarity dependence. Distribution functions presented so far, namely the RDFs and the SDFs, depicted the relative spatial arrangements of ions or cosolvent molecules in these binary mixtures. Voids (arising from the excluded volumes) and necks (originating from the interconnections between voids) play an important role in solution structure as they might be connected to the particle mobilities in solutions [92-94]. Figure 2.12 displays the IL mole fraction dependent void and neck distributions respectively in these three different types of binary mixtures for both the ions. The corresponding distributions in the neat cosolvents are also shown in the same figure. Note here that the void and neck distributions mean the distributions of the radii of the voids and necks that are present in these solutions. Moreover, these voids are approximated as the spherical spaces separating the spherical ions in a fictitious solution mixture where other particles are completely ignored.

For all the three mixtures, the void distributions, g(r), peak around a lengthscale which is approximately the half of the ion diameters which shifts and spreads out to cover larger void radii upon successive dilution of the IL mixtures via the addition of cosolvents. This cosolvent concentration induced shift to larger radii is expected because the addition of cosolvent creates larger distances between neighbors. The subsequent spread out of the distributions suggests increased heterogeneity in the void radii upon cosolvent addition. In the case of dilute IL solutions in hexane, the pronounced phase separation does not allow calculations of void radius, making the visualization of the solution structure in terms of voids untenable. Another interesting feature of these distributions is that the distributions for mixtures are much broader than the neat components constituting these binary mixtures.

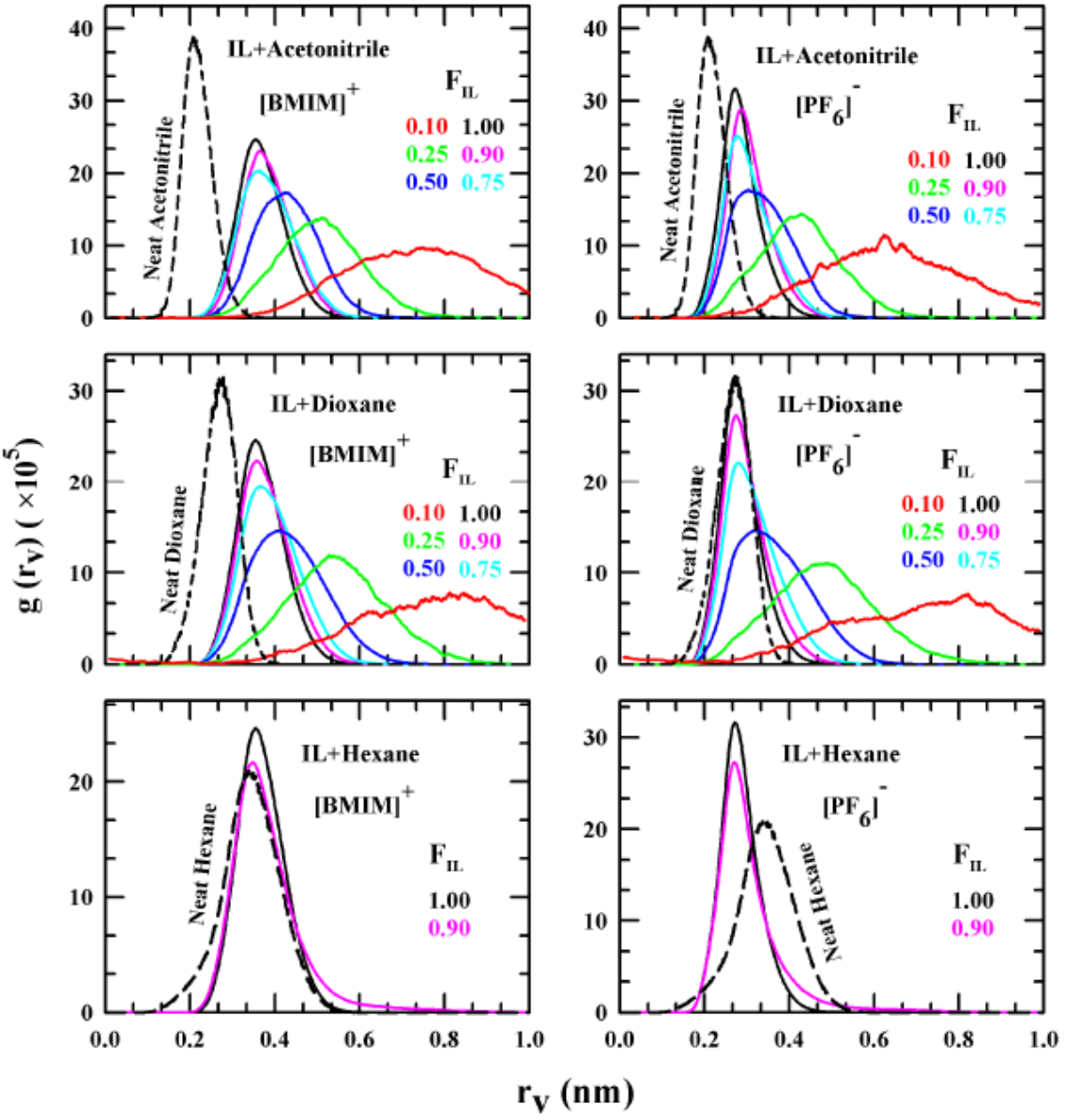

Figure 2.12*: Probability distributions of the void radius for $[BMIM]^+$ cation (left panels) and $[PF_6]^-$ anion (right panels) in the three binary mixtures at different F_{IL} along with the distributions for the corresponding neat cosolvents. Mole fractions are color coded as shown in the inset of each panel. Results for neat co-solvents are represented by the black dashed lines.

* Voronoi Polyhedra Analysis have been performed in collaboration with Prof. Pradip Kumar Ghorai (IISER Kolkata), India. It has been already published (Journal of Molecular Liquids 317 (2020) 113746)

A similar observation has been found also for the neck radius distributions and these results are shown in Figure 2.A.7 (Appendix 2.A). The full-width-at-half-maxima or simply the widths of these voids and necks are shown in Figure 2.13 as a function of IL mole fraction in these binary mixtures. Cosolvent widths are also shown for comparison. Clearly, both the neck and void distributions broaden as the IL is diluted with cosolvents, with the distributions being wider in dioxane binary mixtures than in the corresponding acetonitrile mixtures, particularly at the cosolvent-rich solutions. This is probably due to the polarity difference between these two cosolvents. The void and neck widths of the neat cosolvents also show a trend similar to that of cosolvent polarity dependence.

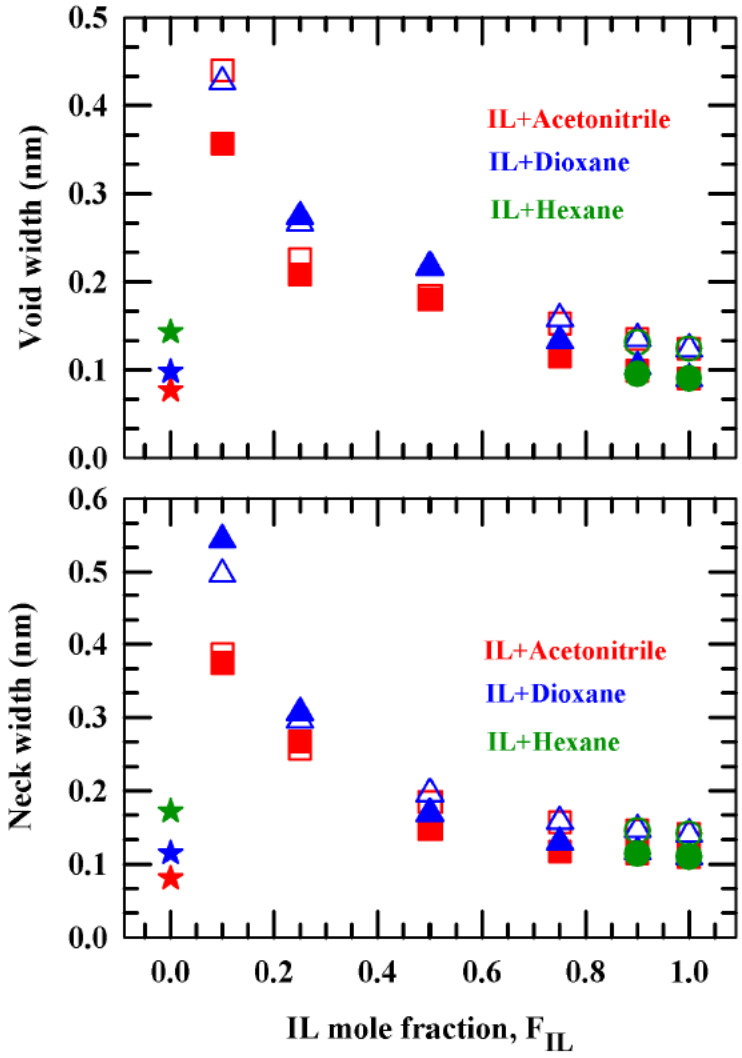

Figure 2.13: Void and neck widths obtained from the void and neck distributions of $[BMIM]^+$ and $[PF_6]^-$as a function F_{IL} in the three binary mixtures. Here, filled and open symbols represent respectively the data for $[BMIM]^+$ and $[PF_6]^-$. Void and neck widths for the co-solvents are also shown for comparison.

2.4 Concluding Remarks

In summary, the present simulation study reveals that the microscopic solution structures of [BMIM] [PF_6] + cosolvent binary mixtures at various compositions depend strongly on the cosolvent polarity. This conclusion is based on the following observations:

(a) The fact that the diameters of the cosolvent molecules do not differ greatly from each other, this interpretation of polarity impact on solution structure is not vitiated by the contributions arising from the separate sizes of the cosolvent molecules.

(b) The simulated composition dependent densities for these binary mixtures are in good agreement with those from experiments. This is true for the neat IL and the neat cosolvents as well. In addition, the RDFs from present simulations for the neat IL agree well with those reported earlier. All these provide the necessary validity to the present study.

(c) Both acetonitrile and dioxane interact more with the anion than with the cation; hexane's interaction with both the ions is the weakest. The interaction of the alkyl tail with hexane and dioxane is comparable. This makes dioxane more miscible in [BMIM] [PF_6] than hexane.

(d) The pronounced aggregation behavior of [BMIM] [PF_6] at low IL mole fraction in non-polar solvent is explained in terms of a relatively shorter Debye screening length (DSL). However, this explanation fails for a quadrupolar solvent like dioxane which has been found as good a host as acetonitrile (strongly dipolar) for this hydrophobic IL. This is reflected in the comparable heights of ion-ion RDFs in binary mixtures of this IL with these two cosolvents of widely differing polarities.

(e) Solution structure in these binary mixtures has been found to be dominated by the cosolvent clustering at the high IL mole fractions, and more pronounced segregation of the IL into polar and non-polar domains in the low IL concentrations. The extent of segregation depends on the polarity and concentration of the cosolvent present in these binary mixtures. This is further

supported by the presence of a larger fraction of the ions in the first solvation shell surrounding a given counter ion and a non-linear dependence of the coordination number.

(f) Isodensity surfaces show dramatic dependence on cosolvent polarity and clearly reflect phase segregation, particularly for hexane at low IL mole fractions. SDFs provide a vivid microscopic picture of these molecular length-scale arrangements in three-dimensions which were missing in the RDFs.

(g) Voronoi Polyhedra analyses indicate broader void and neck distributions relative to those in the neat IL and cosolvents, supporting the view of increased heterogeneity upon dilution of this IL with cosolvents.

Appendix 2.A

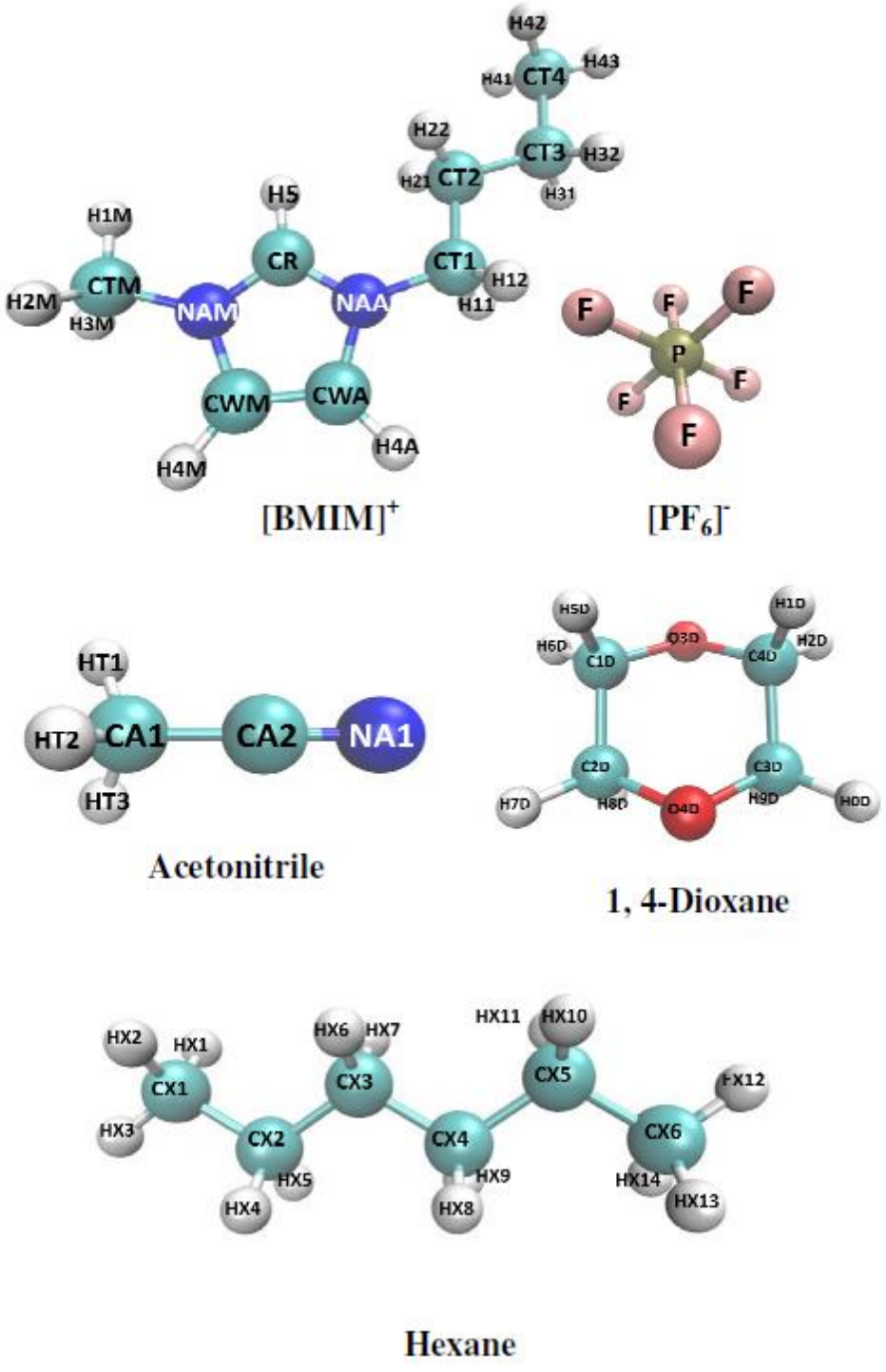

Figure 2.A.1: Chemical structures of $[BMIM]^+$, $[PF_6]^-$, acetonitrile, dioxane (1,4-dioxane) and hexane along with the representations that were used in the discussion of various simulation results.

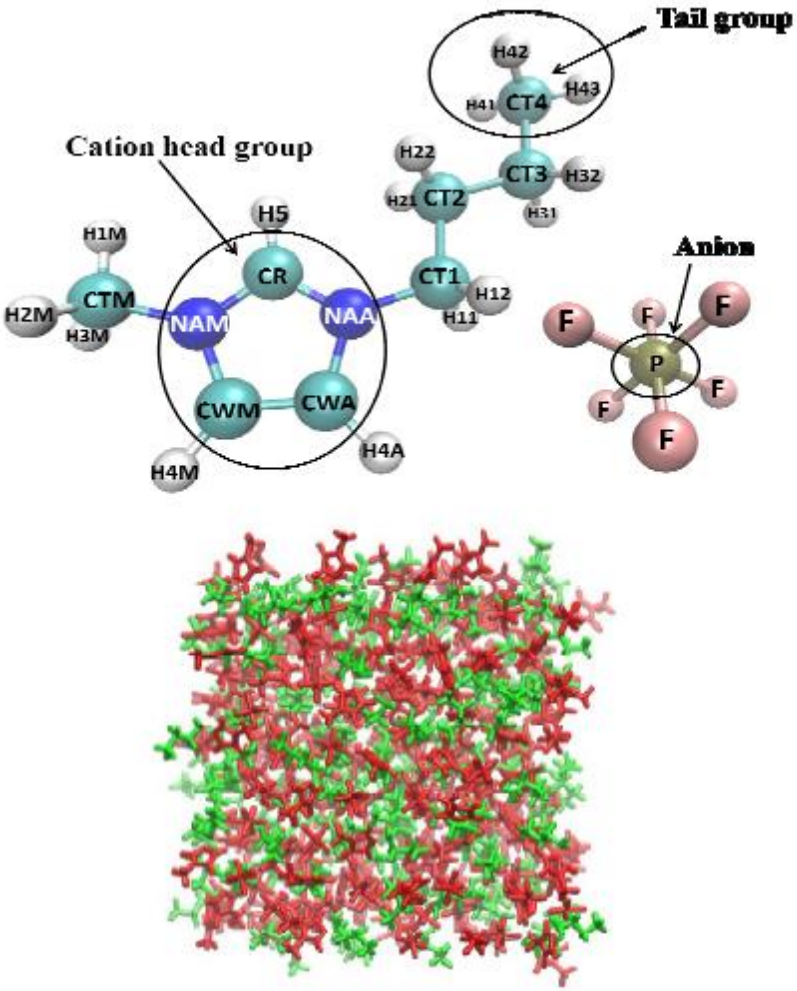

Figure 2.A.2: Structures of [BMIM] and [PF_6] showing the representation of head group, tail group and anion used in the calculation of RDFs (upper panel). Snapshot of the equilibrated neat [BMIM] [PF_6] IL, where the polar domain (imidazolium ring with the methyl group of the cation and the anion) and non-polar domain (alkyl chain of the cation) are colored in red and green respectively. (lower panel).

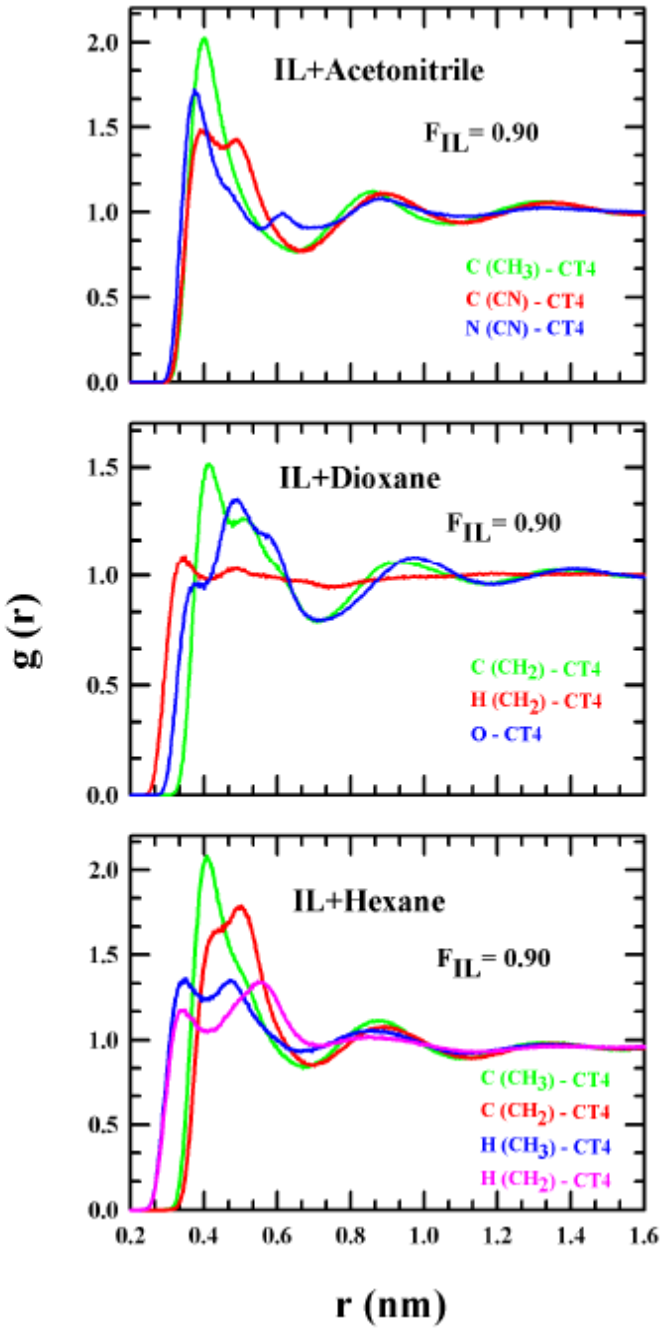

Figure 2.A.3: Simulated radial distribution functions (RDFs) between different atoms of the three cosolvents with tail part (alkyl chain) of the IL cation at F_{IL}=0.90 for the three binary mixtures. Here, atomic pairs and their respective color codes are given in the inset of every panel. Note interactions are shown with the CT4 atom (C-atom of the terminal methyl group of the alkyl chain) of the IL cation.

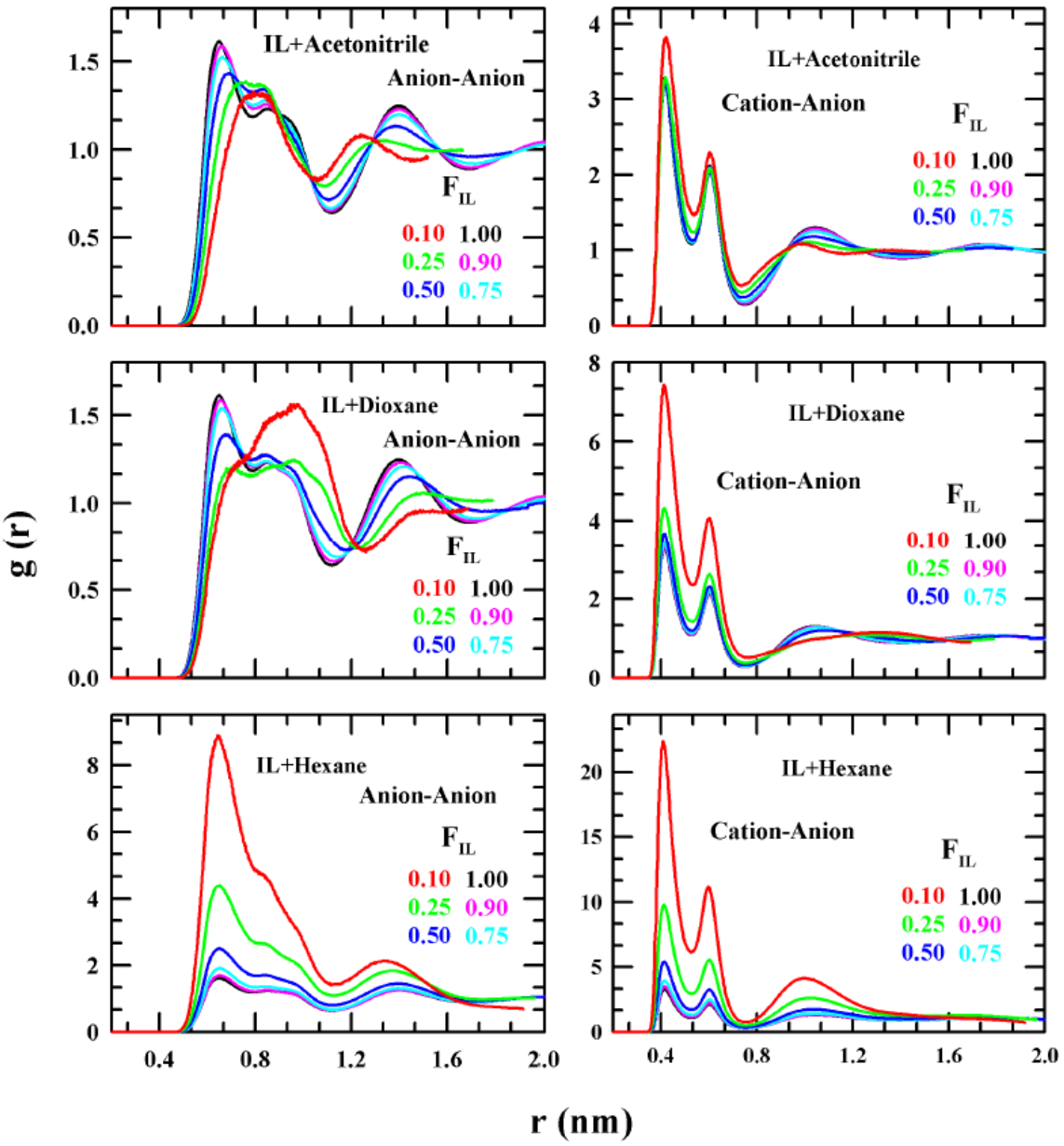

Figure 2.A.4: Simulated anion-anion and cation-cation radial distribution functions (RDFs) for the three binary mixtures. Here cation-cation RDF indicates the head-head interaction, which is calculated between the CR atoms of the imidazolium ring of the cation. Representations are color coded.

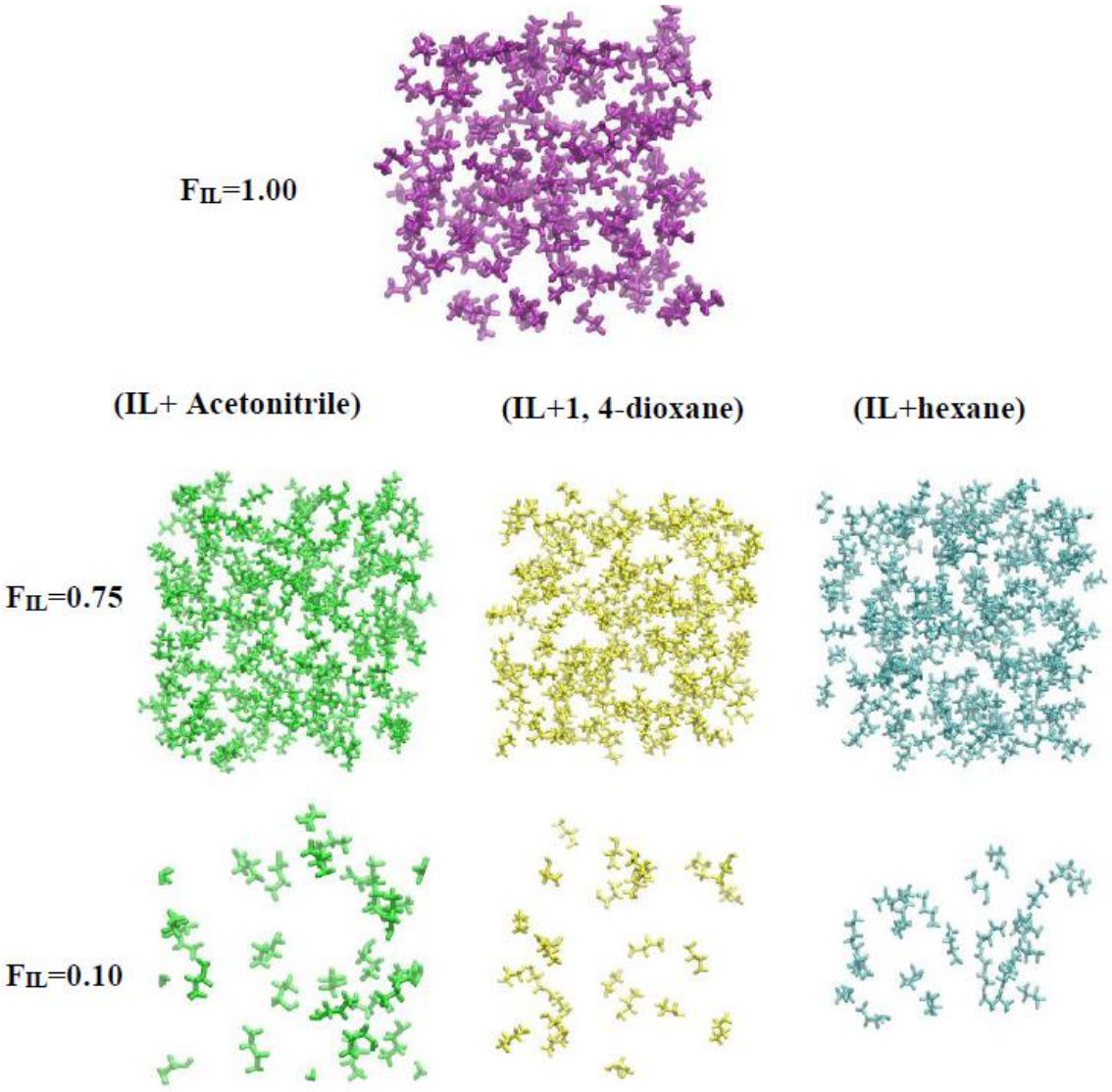

Figure 2.A.5: Simulation snapshots showing the effects of polarity on tail-tail interaction in the three binary mixtures at F_{IL}=1.0, 0.75, 0.10. Here, only the butyl chains of the cation are shown. Note the three binary mixtures and the neat IL are color coded, and 1,4-dioxane is simply dioxane.

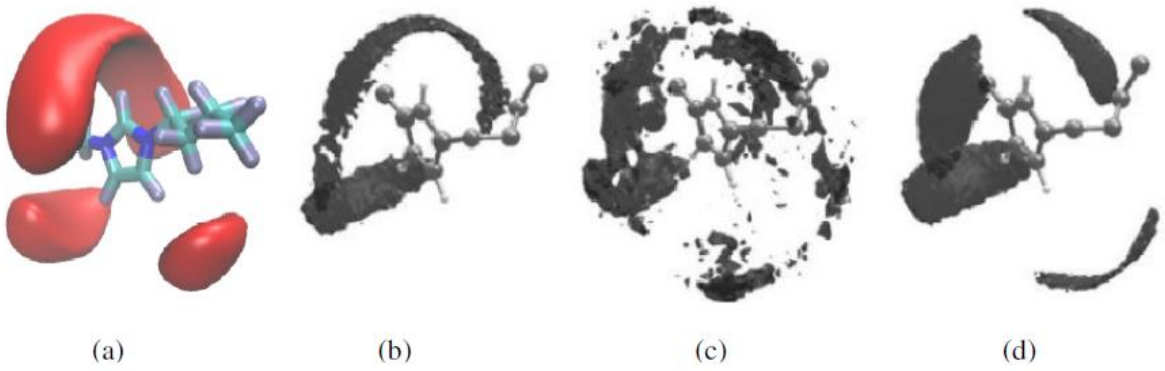

Figure 2.A.6: Comparison of spatial distribution functions, SDFs of the anion around the cation in the neat [BMIM][PF_6] between present simulations and earlier studies [50,53,91]. Note for SDFs in present simulations, anion is represented by the red solid frame.

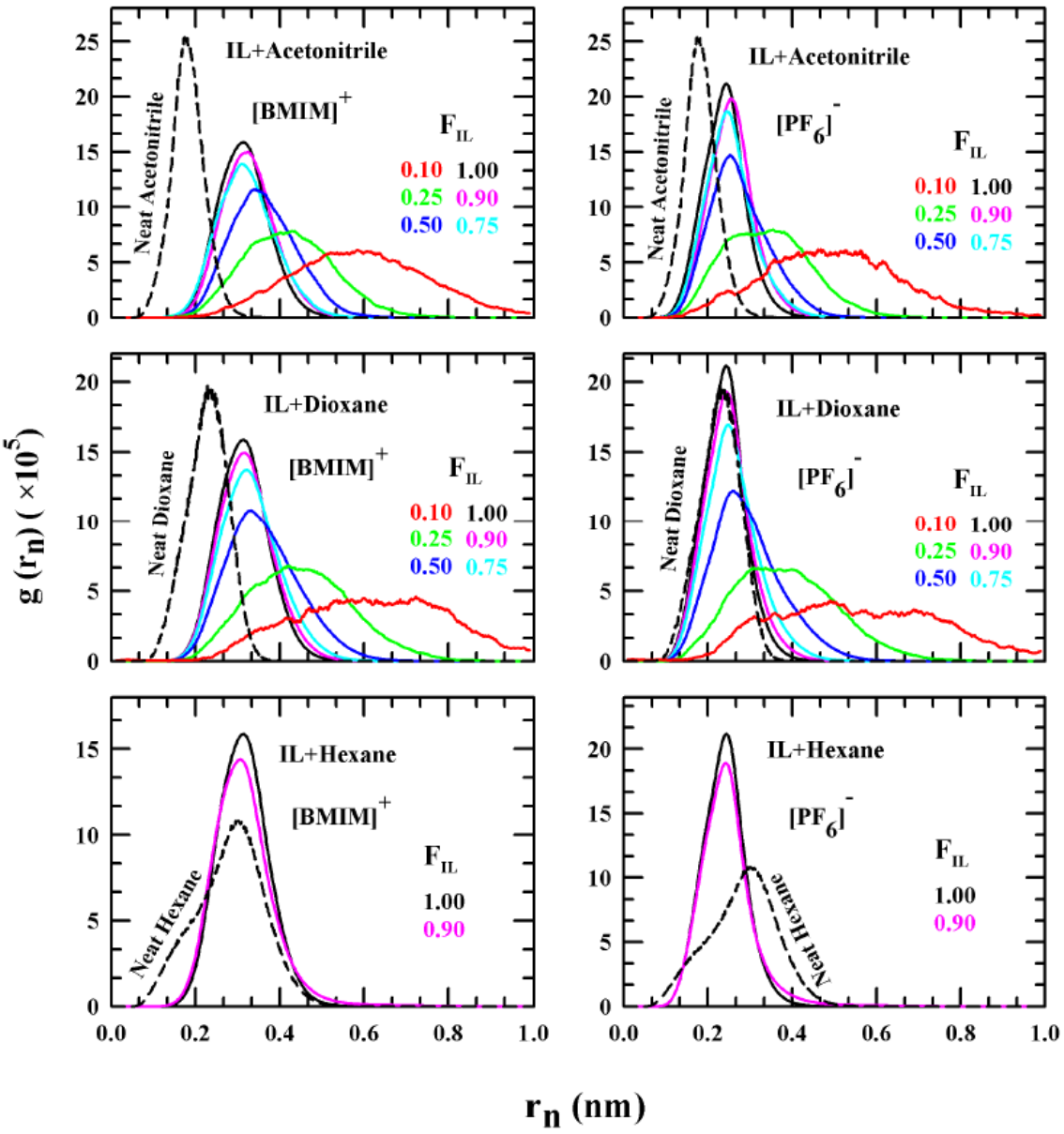

Figure 2.A.7: Probability distributions of the neck radius for $[BMIM]^+$ cation (left panels) and $[PF_6]^-$ anion (right panels) in the three binary mixtures at different IL mole fractions, F_{IL}, along with the distributions in the corresponding neat cosolvents. Mole fractions are color coded and the neat cosolvents are represented by the dashed black lines.

Appendix 2.B

Table 2.B.1: Partial atomic charges on each atom of $[BMIM]^+$ and $[PF_6]^-$

Atom	Partial charges, *e*
CR	0.060
NAM, NAA	0.052
CWM, CWA	-0.020
H5	0.096
H4M, H4A	0.096
CTM, CT1	-0.089
CT2, CT3	-0.038
CT4	-0.065
H1M, H2M, H3M, H11, H12	0.105
H21, H22, H31, H32, H41, H42, H43	0.026
P	0.580
F	-0.230

Table 2.B.2: Lennard Jones parameters of each atom of $[BMIM]^+$ and $[PF_6]^-$ ions

Atom	ε_{ij}, (kJ mol $^{-1}$)	σ_{ij}, (Å)
CR	0.292	3.55
NAM, NAA	0.711	3.25
CWM, CWA	0.292	3.55
H5	0.125	1.72
H4M, H4A	0.125	1.72
CTM, CT1, CT2, CT3, CT4	0.276	3.50
H1M, H2M, H3M, H11, H12	0.125	1.92
H21, H22, H31, H32, H41, H42, H43	0.125	2.50
P	0.836	3.94
F	0.255	3.118

Table 2.B.3: Bond lengths and bond force constants for $[BMIM]^+$ and $[PF_6]^-$

Bonds	r_{eq} (Å)	K_r (kJ $mol^{-1}Å^{-2}$)
CR-H5, CWM - H4M, CWA-H4A	1.08	constrained
CTM – HM (H1M, H2M, H3M), CT - H* [a]	1.09	constrained
CR - NA (NAM, NAA)	1.315	1996
CWM - NAM, CWA - NAA	1.378	1787
CWM - CWA	1.341	2176
NAM - CTM, NAA - CT1	1.466	1410
CT - CT	1.529	1121
P - F	1.6	1673

[a] CT represents the carbon (CT1, CT2, CT3 and CT4), H* represents the hydrogen (H11, H12, H21, H22, H31, H32, H41, H42, H43)

Table 2.B.4: Angle and angle force constants for $[BMIM]^+$ and $[PF_6]^-$

Angles	θ_{eq} (degree)	K_θ (kJ mol^{-1} rad^{-2})
CR-NAM-CWM, CR-NAA-CWA	108.0	292.60
CR-NAM-CTM, CR-NAA-CT1	126.4	292.60
CWM-CWA-NAA, CWA-CWM-NAM	107.1	292.60
NAM-CR-H5, NAA-CR-H5	125.1	146.3
NAM-CR-NAA	109.8	292.60
NAM-CWM-H4M, NAA-CWA-H4A	122.0	146.30
CWM-CWA-H4A, CWA-CWM-H4M	130.9	146.30
CWM-NAM-CTM, CWA-NAA-CT1	125.6	292.60
NAM-CTM-HM, NAA-CT-H*, CT-CT-H*	110.7	156.6
NAA-CT-CT, CT-CT-CT	112.7	418.4
HM-CTM-HM, H*-CT-H*	107.8	138.1
F-P-F	90.0	836.8

Table 2.B.5: Coefficients of Fourier series of dihedrals for $[BMIM]^+$ ion

Dihedrals	V_1 (kJ mol $^{-1}$)	V_2 (kJ mol $^{-1}$)	V_3 (kJ mol $^{-1}$)
X-NA-CR-X	0	19.46	0
X-CW-CW-X	0	44.98	0
X-NA-CW-X	0	12.55	0
CW-NA-CTM/CT1-HM	0	0	0.519
CR-NA-CTM/CT1-HM	0	0	0
CWA-NAA-CT1-CT2	-7.154	4.43	0.877
CR-NAA-CT1-CT2	-5.269	0	0
NAA-CT1-CT2-CT3	-7.480	-0.681	1.02
NA-CT1-CT2-H*	0	0	0
CT-CT-CT-H*	0	0	1.531
H*-CT-CT-H*	0	0	1.331
CT-CT-CT-CT	7.28	-0.657	1.167
X-NA-X-X[b]	0	8.37	0
X-CR/CW-X-X[b]	0	9.2	0

[b]X represents improper dihedral

Table 2.B.6: Partial charges and Lennard-Jones parameters for Hexane

Atoms	Partial charges, *e*	ε (kJ mol^{-1})	σ (Å)
CX1, CX6	-0.180	0.276	3.500
CX2, CX3, CX4, CX5	-0.120	0.276	3.500
HX	0.060	0.126	2.500

Table 2.B.7: Bond length and bond force constant values for Hexane

Bonds	r_{eq}(Å)	K_r (kJ $mol^{-1}Å^{-2}$)
CX-HX	1.09	1422.56
CX-CX	1.529	1121.31

Table 2.B.8: Angle and angle force constant values for Hexane

Angles	θ_{eq} (degree)	K_θ (kJ mol^{-1} rad^{-2})
HX-CX-HX	107.8	138.07
HX-CX-CX	110.7	156.90
CX-CX-CX	112.7	244.13

Table 2.B.9: Coefficients of Fourier series of dihedrals for Hexane

Dihedrals	V_1 (kJ mol^{-1})	V_2 (kJ mol^{-1})	V_3 (kJ mol^{-1})
HX-CX-CX-HX	0.00	0.00	0.318
HX-CX-CX-CX	0.00	0.00	0.366
CX-CX-CX-CX	1.740	-0.157	0.279

Table 2.B.10: Coordinate for 1, 4-Dioxane used in the simulation taken from an earlier study[55].

atom	x (Å)	y (Å)	z (Å)
C1D	0.085262	-0.001386	-0.006160
C2D	2.417071	0.000961	-0.005006
C3D	2.416775	1.516591	0.004953
C4D	0.084997	1.516167	0.003829
H5D	3.257125	-0.393001	0.554862
H6D	0.023445	-0.364800	-1.031591
H7D	-0.755193	-0.393741	0.552881
H8D	2.478546	1.880010	1.030382
H9D	3.257238	1.908967	-0.554066
H0D	0.022102	1.879562	1.029201
H1D	-0.755059	1.908247	-0.556005
H2D	2.480032	-0.364354	-1.030373
O3D	1.251088	2.005736	-0.604170
O4D	1.250952	-0.490575	0.602933

Table 2.B.11: Partial charges and Lennard-Jones parameters for 1, 4-Dioxane.

Atoms	Partial charges, *e*	ε (kJmol^{-1})	σ (Å)
C	0.140	33.233	3.50
H	0.030	15.106	2.50
O	-0.400	70.493	2.90

Table 2.B.12: Bond length values for 1, 4-dioxane.

Bonds	r_{eq}(Å)
C-O	1.400
C-C	1.520
C-H	1.085

Table 2.B.13: Angle and angle force constant values for 1, 4-dioxane.

Angle	θ_{eq} (degree)	K_θ (kJ mol^{-1} rad $^{-2}$)
C-O-C	112.3	502.08
O-C-C	110.2	418.40
H-C-O	108.5	418.40
H-C-C	110.4	418.40
H-C-H	108.8	292.88

Table 2.B.14: Coefficients of Fourier series of dihedrals for 1,4-dioxane.

Dihedrals	V_1 (KJ mol $^{-1}$)	V_2 (KJ mol $^{-1}$)	V_3 (KJ mol $^{-1}$)
O-C-C-O	-2.3012	0.0	0.0
C-O-C-C	2.7196	-1.0460	2.8032
H-C-O-C	0.0	0.0	3.1798
H-C-C-O	0.0	0.0	1.9582
H-C-C-H	0.0	0.0	1.2552

Table 2.B.15: Co-ordination numbers (CNs) in the first solvation shells calculated from the cation-anion, cation-cation and anion-anion center-of-mass RDFs in the neat [BMIM] [PF_6] IL. Comparison is made with an earlier work [87].

Pairs	Co-ordination number from Present simulation	Co-ordination number from Earlier study [87]
cation-anion	7.32	6.8
cation-cation	6.5	6.1
anion-anion	6.6	6.2

Table 2.B.16: Isovalues used in the SDF plots of anion and co-solvents around the cation for the three binary mixtures.

Mole Fraction, F_{IL}	Isovalues (nm^{-3}) around $[BMIM]^+$ cation					
	$[BMIM][PF_6]$ + acetonitrile		$[BMIM][PF_6]$ + 1,4-dioxane		$[BMIM][PF_6]$ + hexane	
	$[PF_6]^-$ [a]	acetonitrile [a]	$[PF_6]^-$ [a]	1,4-dioxane [a]	$[PF_6]^-$ [a]	hexane [a]
1.00	6.167	-	6.167	-	6.167	-
0.90	5.733	0.485	5.732	0.487	5.772	0.429
0.50	5.476	3.414	4.545	3.082	5.486	2.416
0.10	2.001	10.239	2.001	7.415	5.417	4.657

[a] is the surrounding species here.

Table 2.B.17: Isovalues used in the SDF plots of cation and anion around the co-solvents for the three binary mixtures.

Mole Fraction, F_{IL}	Isovalues (nm^{-3}) around Co-solvents					
	$[BMIM][PF_6]$ + acetonitrile		$[BMIM][PF_6]$ + 1,4-dioxane		$[BMIM][PF_6]$ + hexane	
	Around acetonitrile		Around 1,4-dioxane		Around hexane	
	$[BMIM]^+$ [b]	$[PF_6]^-$ [b]	$[BMIM]^+$ [b]	$[PF_6]^-$ [b]	$[BMIM]^+$ [b]	$[PF_6]^-$ [b]
1.00	-	-	-	-	-	-
0.90	3.708	6.019	3.947	4.285	3.452	3.105
0.50	3.264	4.285	2.954	3.123	1.814	1.849
0.10	1.094	1.600	0.838	1.012	0.487	0.496

[b] is the surrounding species here.

References

[1] E.W. Castner Jr, C.J. Margulis, M. Maroncelli, J.F. Wishart, Annu. Rev. Phys. Chem. **62**, 85-105 (2011).

[2] E.J. Maginn, J. Phys.: Condens. Matter **21**, 373101 (2009).

[3] J. Dupont, Acc. Chem. Res. **44**, 1223-1231 (2011).

[4] H. Niedermeyer, J.P. Hallett, I.J. Villar-Garcia, P.A. Hunt, T. Welton, Chem. Soc. Rev. **41**, 7780-7802 (2012).

[5] H. Liu, E. Maginn, A.E. Visser, N.J. Bridges, E.B. Fox, Ind. Eng. Chem. Res. **51**, 7242-7254 (2012).

[6] Y. Wang, W. Jiang, T. Yan, G.A. Voth, Acc. Chem. Res. **40**, 1193-1199 (2007).

[7] B. Gurkan, B. Goodrich, E. Mindrup, L. Ficke, M. Massel, S. Seo, T. Senftle, H. Wu, M. Glaser, J. Shah, J. Phys. Chem. Lett. **1**, 3494-3499 (2010).

[8] J.P. Hallett, T. Welton, Chem. Rev. **111**, 3508-3576 (2011).

[9] J.F. Wishart, Energy applications of ionic liquids, Energy Environ. Sci. **2**, 956-961 (2009).

[10] N.V. Plechkova, K.R. Seddon, Chem. Soc. Rev. **37**, 123-150 (2008).

[11] Y. Kohno, H. Ohno, Ionic liquid/water mixtures: from hostility to conciliation, Chem. Commun. **48**, 7119-7130 (2012).

[12] J. Jacquemin, P. Husson, A.A. Padua, V. Majer, Green. Chem. **8**, 172-180 (2006).

[13] A.L. Sturlaugson, K.S. Fruchey, M.D. Fayer, J. Phys. Chem. B **116**, 1777-1787 (2012).

[14] H. Shirota, R. Biswas, J. Phys. Chem. B **116**, 13765-13773 (2012).

[15] N. Yaghini, J. Pitawala, A. Matic, A. Martinelli, J. Phys. Chem. B **119**, 1611-1622 (2015).

[16] A. Sharma, P.K. Ghorai, J. Chem. Phys. **144**, 114505 (2016).

[17] A.A. Niazi, B.D. Rabideau, A.E. Ismail, J. Phys. Chem. B **117**, 1378-1388 (2013).

[18] W. Jiang, Y. Wang, G.A. Voth, J. Phys. Chem. B **111**, 4812-4818 (2007).

[19] S.D. Nickerson, E.M. Nofen, H. Chen, M. Ngan, B. Shindel, H. Yu, L.L. Dai, J. Phys. Chem. B **119**, 8764-8772 (2015).

[20] T. Pal, R. Biswas, J. Phys. Chem. B **119**, 15683-15695 (2015).

[21] S.M. Urahata, M.C. Ribeiro, J. Chem. Phys. **120**, 1855-1863 (2004).

[22] J.N. Canongia Lopes, A.A. Pádua, J. Phys. Chem. B **110**, 3330-3335 (2006).

[23] Y. Wang, G.A. Voth, J. Am. Chem. Soc. **127**, 12192-12193 (2005).

[24] Y. Wang, G.A. Voth, J. Phys. Chem. B **110**, 18601-18608 (2006).

[25] Z. Hu, C.J. Margulis, Proc. Natl. Acad. Sci. U. S. A. **103**, 831-836 (2006).

[26] H.V. Annapureddy, H.K. Kashyap, P.M. De Biase, C.J. Margulis, J. Phys. Chem. B **114**, 16838-16846 (2010).

[27] J. Habasaki, K. Ngai, J. Chem. Phys. **129**, 194501 (2008).

[28] T. Pal, R. Biswas, Theor. Chem. Acc. **132**, 1348 (2013).

[29] T. Pal, R. Biswas, J. Chem. Phys. **141**, 104501 (2014).

[30] D. Roy, N. Patel, S. Conte, M. Maroncelli, J. Phys. Chem. B **114**, 8410-8424 (2010).

[31] S. Das, B. Mukherjee, R. Biswas, J. Chem. Phys. **148**, 193839 (2018).

[32] K. Iwata, H. Okajima, S. Saha, H.-o. Hamaguchi, Acc. Chem. Res. **40**, 1174-1181 (2007).

[33] J.N. Canongia Lopes, M.F. Costa Gomes, A.A. Pádua, J. Phys. Chem. B **110**, 16816-16818 (2006).

[34] A.A. Pádua, M.F. Costa Gomes, J.N. Canongia Lopes, Acc. Chem. Res. **40**, 1087-1096 (2007).

[35] S. Saha, H.-o. Hamaguchi, J. Phys. Chem. B **110**, 2777-2781 (2006).

[36] R.M. Lynden-Bell, L. Xue, G. Tamas, E.L. Quitevis, J. Chem. Phys. **141**, 044506 (2014).

[37] M. Liang, S. Khatun, E.W.C. Jr., J. Chem. Phys. **142**, 121101 (2015).

[38] P. Yang, G.A. Voth, D. Xiao, L.G. Hines Jr, R.A. Bartsch, E.L. Quitevis, J. Chem. Phys. **135**, 034502 (2011).

[39] M.H. Kowsari, L. Tohidifar, J. Phys. Chem. B **120**, 10824-10838 (2016).

[40] B. Conway, C. Uitvlugt, M. Maroncelli, J. Phys. Chem. B **122**, 7385-7393 (2018).

[41] A. Paul, A. Samanta, J. Phys. Chem. B **112**, 947-953 (2008).

[42] D. Chakrabarty, A. Chakraborty, D. Seth, N. Sarkar, J. Phys. Chem. A **109**, 1764-1769 (2005).

[43] H.K. Kashyap, R. Biswas, J. Phys. Chem. B **114**, 16811-16823 (2010).

[44] S. Daschakraborty, R. Biswas, J. Chem. Phys. **140**, 014504 (2014).

[45] S. Daschakraborty, R. Biswas, J. Chem. Phys. **144**, 104505 (2016).

[46] A. Stoppa, J. Hunger, G. Hefter, R. Buchner, J. Phys. Chem. B **116**, 7509-7521 (2012).

[47] M. Khajehpour, J.F. Kauffman, J. Phys. Chem. A **104**, 9512-9517 (2000).

[48] P.W. Atkins, J. De Paula, J. Keeler, Atkins' physical chemistry. Oxford university press, 2018.

[49] D. van der Spoel, E. Lindahl, B. Hess, A. R. van Buuren, E. Apol, P. J. Meulenhoff, D. P. Tieleman, A. L. T. M. Sijbers, K. A. Feenstra, R. van Drunen, H. J. C. Berendsen, Gromacs User Manual 4.5.4, www.gromacs.org 2010.

[50] J.N. Canongia Lopes, J. Deschamps, A.A. Pádua, J. Phys. Chem. B **108**, 2038-2047 (2004).

[51] O. Borodin, G.D. Smith, R.L. Jaffe, J. Comput. Chem. **22**, 641-654 (2001).

[52] M. Allen, D. Tildesley, Oxford University Press; New York: 1987.

[53] B. Bhargava, S. Balasubramanian, J. Chem. Phys. **127**, 114510 (2007).

[54] W.L. Jorgensen, D.S. Maxwell, J. Tirado-Rives, J. Am. Chem. Soc. **118**, 11225-11236 (1996).

[55] G. Cinacchi, F. Ingrosso, A. Tani, J. Phys. Chem. B **110**, 13633-13641 (2006).

[56] C. Caleman, P.J. van Maaren, M. Hong, J.S. Hub, L.T. Costa, D. van der Spoel, J. Chem. Theory Comput. **8**, 61-74 (2012).

[57] K.A. Feenstra, B. Hess, H.J. Berendsen, J. Comput. Chem. **20**, 786-798 (1999).

[58] M. Frisch, M. Frisch, G. Trucks, K. Schlegel, G. Scuseria, M. Robb, J. Cheeseman, J. Montgomery, T. Vreven, K.-N. Kudin, Gaussian 03, revision D. 02, (2004).

[59] L. Martínez, R. Andrade, E.G. Birgin, J.M. Martínez, J. Comput. Chem. **30**, 2157-2164 (2009).

[60] B. Hess, H. Bekker, H.J. Berendsen, J.G. Fraaije, J. Comput. Chem. **18**, 1463-1472 (1997).

[61] U. Essmann, L. Perera, M.L. Berkowitz, T. Darden, H. Lee, L.G. Pedersen, J. Chem. Phys. **103**, 8577-8593 (1995).

[62] G. Bussi, D. Donadio, M. Parrinello, J. Chem. Phys. **126**, 014101 (2007).

[63] H.J. Berendsen, J.v. Postma, W.F. van Gunsteren, A. DiNola, J.R. Haak, J. Chem. Phys. **81**, 3684-3690 (1984).

[64] W. Humphrey, A. Dalke, K. Schulten, J. Mol. Graphics **14**, 33-38 (1996).

[65] M. Tanemura, T. Ogawa, N. Ogita, J. Comput. Phys. **51**, 191-207 (1983).

[66] D. Chakraborty, A. Chandra, J. Mol. Liquids **163**, 1-6 (2011).

[67] A. Sharma, P.K. Ghorai, J. Chem. Phys. **148**, 204514 (2018).

[68] D. Corti, P. Debenedetti, S. Sastry, F. Stillinger, Phys. Rev. E **55**, 5522 (1997).

[69] F.B. Usabiaga, D. Duque, Phys. Rev. E **79**, 046709 (2009).

[70] J.T. Fern, D.J. Keffer, W.V. Steele, J. Phys. Chem. B **111**, 3469-3475 (2007).

[71] N.N. Medvedev, A. Geiger, W. Brostow, J. Chem. Phys. **93**, 8337-8342 (1990).

[72] G. Palinkas, E. Hawlicka, K. Heinzinger, J. Phys. Chem. **91**, 4334-4341 (1987).

[73] M.E. van Leeuwen, B. Smit, J. Phys. Chem **99**, 1831-1833 (1995).

[74] N. Asahi, Y. Nakamura, J. Chem. Phys. **109**, 9879-9887 (1998).

[75] W.L. Jorgensen, J. Phys. Chem **90**, 1276-1284 (1986).

[76] C.J. Benmore, Y.L. Loh, J. Chem. Phys. **112**, 5877-5883 (2000).

[77] M. Diraison, G. Martyna, M. Tuckerman, J. Chem. Phys. **111**, 1096-1103 (1999).

[78] A. De Santis, A. Ercoli, D. Rocca, Phys. Rev. E **57**, R4871 (1998).

[79] A. Kalinichev, J.D. Bass, J. Phys. Chem. A **101**, 9720-9727 (1997).

[80] S.W. Siu, K. Pluhackova, R.A. Böckmann, J. Chem. Theory Comput. **8**, 1459-1470 (2012).

[81] H. Tokuda, K. Hayamizu, K. Ishii, M.A.B.H. Susan, M. Watanabe, J. Phys. Chem. B **108**, 16593-16600 (2004).

[82] Y. Marcus, The properties of solvents, (1998).

[83] D. Linde, CRC Handbook of Chemistry and, Physics, 73rd Ed., CRC, Boca Raton 9-51 (1992).

[84] T. Aminabhavi, V. Patil, M. Aralaguppi, H. Phayde, J. Chem. Eng. Data **41**, 521-525 (1996).

[85] M.T. Zafarani-Moattar, H. Shekaari, J. Chem. Eng. Data **50**, 1694-1699 (2005).

[86] U. Domańska, A. Marciniak, J. Chem. Eng. Data **48**, 451-456 (2003).

[87] T.I. Morrow, E.J. Maginn, J. Phys. Chem. B **106**, 12807-12813 (2002).

[88] S. Glasstone, An Introduction to Electrochemistry 1942. D. Van Nostrand, 1942.

[89] R. Biswas, A. Das, H. Shirota, J. Chem. Phys. **141**, 134506 (2014).

[90] M. Brehm, B. Kirchner, J. Chem. Inf. Model. **51**, 2007-2023 (2011).

[91] B. Bhargava, S. Balasubramanian, J. Phys. Chem. B **111**, 4477-4487 (2007).

[92] B. JO'm, A.K. Reddy, Modern Electrochemistry: An Introduction to an interdisciplinary area. Plenum Press, 1970.

[93] A. Kumar, J. Am. Chem. Soc. **115**, 9243-9248 (1993).

[94] A.P. Abbott, D. Boothby, G. Capper, D.L. Davies, R.K. Rasheed, J. Am. Chem. Soc. **126**, 9142-9147 (2004).

Chapter 3

Heterogeneous Dynamics in [BMIM][PF_6] + Cosolvent Binary Mixtures: Does It Depend Upon Cosolvent Polarity?

3.1 Introduction

Heterogeneous dynamics means relaxations of particles in a given system with different rates. These relaxation rates may be well separated from each other or can involve multiple relaxation timescales so thinly separated as to appear as being continuous. While the relaxations with well-separated multiple timescales correspond to hierarchical relaxations (fast is first), relaxations with continuously varying timescales relate to distributed kinetics [1,2]. This concept of dynamically heterogeneous relaxations or simply 'dynamic heterogeneity' (DH) has originated from the study of dynamics in deeply supercooled liquids near glass transition and has attracted attention over the years of theoreticians and experimentalists alike. The origin of DH may or may not be connected to spatial heterogeneity of a given system. As a result, the identification of DH with 'spatially varying relaxation rates' may not be valid always; the inherent non-exponentiality in particle relaxations in an otherwise homogeneous system can also lead to experimental observation of over-all non-exponential relaxation. Such an observation should not be misconstrued as an evidence for heterogeneous relaxations arising from spatial inhomogeneity, although time correlation functions involving random stochastic time-dependent variables are supposed to decay exponentially with time once the diffusive limit is reached [3].

Time-dependent fluorescence Stokes shift (TDFSS) and anisotropy measurements, and dielectric relaxation (DR) experiments with several neat ILs have revealed heterogeneous dynamics[4–11]. Fluorescence correlation spectroscopic studies have provided further support via the observation of heterogeneous diffusive dynamics for the centre-of-mass motion of a dissolved fluorescent probe solute [12,13]. Relevant theoretical studies of solvation dynamics in neat ILs have also supported the view of heterogeneous collective orientational polarization

density relaxation of ILs in response to a sudden alteration of the equilibrium charge distribution of a laser-excited dissolved solute [14–22]. Subsequently, heterogeneous relaxation dynamics have been reported by TDFSS and DR measurements for binary mixtures of ILs with small molecular solvents [19,21,23–26]. All these experiments, however, measure the solvent polarization response at the collective wavevector ($k \to 0$) limit and as a result, information regarding relaxations at the molecular length-scales has remained largely inaccessible. To be specific, these measurements cannot separate out the component dynamics and therefore one does not know how the inherent dynamics of the neat components are mutually influenced.

One attempt toward this direction has been initiated several years ago which examined, through molecular dynamics simulations, the composition dependence of heterogeneity in the relaxations of individual components of (IL+water) binary mixtures [27]. This simulation study has indeed found a considerable mixture composition dependence of heterogeneous relaxations of both the components. However, no study on cosolvent dependence has been reported so far. The present simulation study is designed to provide such a study where cosolvent polarity dependence of heterogeneous relaxation dynamics at various mixture compositions has been explored thoroughly by keeping the van der Waal's radii of the different cosolvent specie approximately the same. The cosolvents chosen for this purpose are acetonitrile (dipolar), dioxane (quadrupolar) and hexane (nonpolar). The structural aspects of these binary mixtures and their cosolvent polarity dependencies have already been reported [28]. The numerical values of the static dielectric constants, dipole and quadrupole moments, van der Waal's radii and viscosities of the neat systems employed here are summarized in Table 3.1 [14,16,25,26,29–31].

Table 3.1: Physicochemical properties of [BMIM] [PF_6] IL and three cosolvents.

Solvent	ε_0	μ (D)	$< Q >$ (DÅ)	van der Waals' radii (Å)	Viscosity, η (cP)
[BMIM] [PF_6]	16	$[BMIM]^+$: ~4	N/A	$[BMIM]^+$: 3.4 $[PF_6]^-$: 2.7	310
acetonitrile	35.9	3.92	2.49	2.75	0.34

1,4-dioxane	2.2	0	11.68	3.2	1.18
Hexane	1.88	0	0.6	3.75	0.3

In this present study, a total of seven mixture compositions (F_{IL}=1.00, 0.90, 0.75, 0.50, 0.25, 0.10, 0.00) have been considered including the neat liquids. Cosolvent polarity and composition dependencies of several dynamic heterogeneity parameters such as non-Gaussian (NG) and new non-Gaussian (NNG) parameters, single particle displacement distributions, self-intermediate scattering functions, four-point dynamic susceptibilities and overlap functions have been computed. These DH parameters provide insights into the polarity driven interaction between the IL and different cosolvents and their role in the modification of the inherent motional features of the molecular ions constituting the IL, ([BMIM] [PF_6]), and those of the three different cosolvent molecules.

3.2 Computational Details

Molecular dynamics simulations of [BMIM][PF_6] + acetonitrile/dioxane/hexane) binary mixtures were performed using the GROMACS 4.5.6 package [32–34] at 298 K. A total of 256 particles were simulated. Charge neutrality was ensured by choosing equal numbers of cation and anion. Table 3.B.1 (Appendix 3.B) summarizes the number of component particles employed to form the simulated binary mixtures at each of the seven compositions considered. The chemical structures of IL ions and cosolvents are shown in Figure 3.A.1 of the Appendix 3.A.

The potential energy functional form for the IL and hexane is as follows [35,36],

$$U(R) = \sum_{bonds} K_r(r - r_{eq})^2 + \sum_{angles} K_\theta(\theta - \theta_{eq})^2 + \sum_{dihedrals} \left[\frac{V_1}{2}(1 + cos\varphi) + \frac{V_2}{2}(1 - cos2\varphi) + \frac{V_3}{2}(1 + 3cos\varphi)\right] + \sum_{i<j}^{atoms} \left(\frac{A_{ij}}{R_{ij}^{12}} - \frac{B_{ij}}{R_{ij}^{6}}\right) + \sum_{i<j}^{atoms} \frac{q_i q_j}{4\pi\varepsilon_0 R_{ij}}) \quad (3.1)$$

K_r and K_θ in the above equation represent the bond and angle force constants respectively, r_{eq} the equilibrium bond distance, θ_{eq} the equilibrium angle. V_1, V_2 and V_3 are the coefficients of

Fourier series and φ denote the dihedral angle. R_{ij} is the distance between the atoms i and j, ε_0 the permittivity of the vacuum. q_i and q_j represent partial charges.

Moreover, the following potential energy function is used for 1,4-dioxane [37],

$$U(r) = \sum_{bonds} K_r(r - r_0)^2 + \sum_{angles} K_\theta(\theta - \theta_0)^2 + \sum_{dihedrals} \left[\frac{V_1}{2}(1 + cos\varphi) + \frac{V_2}{2}(1 - cos2\varphi) + \frac{V_3}{2}(1 + cos3\varphi)\right] + \left[\sum_{i<j}^{atoms} \left\{4\varepsilon_{ij}\left[\left(\frac{\sigma_{ij}}{r_{ij}}\right)^{12} - \left(\frac{\sigma_{ij}}{r_{ij}}\right)^{6}\right] + \frac{q_i q_j}{4\pi\varepsilon_0 r_{ij}}\right\}\right] \quad (3.2)$$

where, σ_{ij} denotes the van der Waals radius, ε_{ij} the well depth and the rest represent the same as discussed above.

The interaction parameters for the $[BMIM]^+$ and $[PF_6]^-$ ions were taken from earlier works [38,39]. In addition, the partial charges of the IL ions were reduced to $\pm 0.8e$ and modified Lennard-Jones parameters used [35] in the present simulations. The potential energy parameters for acetonitrile, dioxane and hexane were taken from the existing literature [36,37,40]. Also, molecular geometries of acetonitrile molecule displayed in a webpage (http://virtualchemistry.org/gmld.php) were considered. Note for acetonitrile, to keep the nitrile group perfectly linear [41], the moment of inertia and the total mass of the molecule were maintained by adding a virtual construction site to the topologies.

Simulations were carried out in a cubic box with periodic boundary conditions. $[BMIM]^+$ cation, $[PF_6]^-$ anion and hexane molecules were optimized via ab-initio calculations in the Gaussian03 program [42] by using the HF/6-31 + G(d) basis set, whereas the optimized structures of acetonitrile and dioxane were taken from Refs. [37,40], respectively. The starting configurations of the system were built in the Packmol software [43]. After energy minimization in the GROMACS package, the system was initially equilibrated at 450 K and 1 atm pressure in the NPT ensemble using the velocity rescaling thermostat [44] and the Berendsen barostat [45] with coupling constants 0.5 ps and 2.0 ps, respectively. The system was then brought down to 298 K with a step size of 50 K and each step was run for a duration of 100 ps. After that, the

system was further equilibrated in the NPT ensemble for 4 ns to ensure the proper equilibration, which was followed by 2ns equilibration run in the NVT ensemble.

In these simulations, the equation of motion was integrated by using the leap-frog algorithm [46] with a time step of 2 fs. The cut off radius was set to 15 Å and the particle mesh Ewald (PME) summation [47] was used for the long-range electrostatic interactions. Bonds were kept constrained throughout the simulations using the LINCS algorithm [48]. The production run was for 100 ns, where the trajectories were saved after every 0.1 ps for analyses. Visual Molecular Dynamics (VMD) software [49] was used for visualization of the molecules at different stages of the simulations.

3.3 Fidelity Check of Force Field

For the fidelity check of the force fields employed in the simulations of the IL and the three cosolvents, we have compared, in Table 3.2 & 3.3, the translational diffusion co-efficients (D) of the ions and the cosolvents with those obtained from earlier simulations[35,37,50,51] and experiments. [52–56] Table 3.2 provides the diffusion co-efficient values of $[BMIM]^+$ and the $[PF_6]^-$ ions in the neat IL along with the corresponding β values (given in the parentheses). The D values of $[BMIM]^+$ and $[PF_6]^-$ ions have been obtained from the slopes of the respective mean square displacements (MSDs) in the long-time limit where β is equal or nearly equal to unity ($\beta \cong 1$) (see Figure 3.A.2 in Appendix 3.A). Data in Table 3.2 indicate that D values for the cation and the anion estimated from the present simulations are lower than those from experiments [52] and previous simulations[35]. In the earlier simulation study [35], the estimated diffusion co-efficients of the ions agreeing to the experimental values better than to our simulated values. Interestingly, D values in the previous simulation study [35] were estimated from MSDs at long-time for a duration of ~400-500 ps (from a production run of 4ns). However, the associated β values have not been reported. The diffusion co-efficients for the three cosolvents, provided in Table 3.3, agree well with earlier simulations [37,50,51] and experimental results [53–56]. Also, the simulated densities of all the binary mixtures are in well agreement with the available experimental data (shown in Figure 3.A.3 of Appendix 3.A).

Table 3.2: Comparison of self-diffusion co-efficients, D in 10^{-12} m^2sec^{-1} of IL cation and anion obtained from present simulation with those from experiment and earlier simulation. The corresponding β values are given in the parentheses.

Present simulation Production run=100 ns		Present simulations Production run=4 ns		Earlier simulations Production run=4 ns		Experiments (PFG-NMR)	
$[BMIM]^+$	$[PF_6]^-$	$[BMIM]^+$	$[PF_6]^-$	$[BMIM]^+$	$[PF_6]^-$	$[BMIM]^+$	$[PF_6]^-$
3.81 (0.87)	2.53 (0.82)	6.11 (0.69)	5.5 (0.66)	6.7 (unknown)	4.7 (unknown)	8.0	5.9

Table 3.3: Self-diffusion co-efficients (D), of the three cosolvents – acetonitrile, 1,4-dioxane and hexane are compared with earlier simulations and experiments.

Cosolvent	Present simulations m^2sec^{-1} (298 K)	Earlier simulations m^2sec^{-1}	Experiments m^2sec^{-1}
acetonitrile	4.43×10^{-9}	$4.4\pm0.2\times10^{-9}$ (298 K)	4.31×10^{-9} (298.2 K) (NMR)
1, 4-dioxane	0.91×10^{-9}	0.78×10^{-9} (291K)	1.089×10^{-9} (298 K) (0.89×10^{-9}, 288 K) (PFG-NMR)
hexane	3.119×10^{-9}	2.99×10^{-9} (298.15K)	4.21×10^{-9} (298.15 K, NMR) 3.1×10^{-9} (250 K, neutron scattering)

3.4 Results and Discussion

3.4.1 Composition Dependent Mean Square Displacements (MSDs) and Diffusion Co-efficients: Impact of Cosolvent Polarity

We have calculated the centre-of-mass MSDs for the ions and the cosolvent molecules in binary mixtures of ([BMIM] [PF_6] + acetonitrile/1,4-dioxane/hexane) at various mole fractions from their time dependent positions via the following equation [27,57,58],

$$\langle \delta r^2(t) \rangle = \langle N^{-1} \sum_{i=1}^{N} |\Delta r_i^c(0,t)|^2 \rangle \quad (3.3)$$

where r_i^c denotes the center-of-mass of particle i. These simulated MSDs show $\langle \delta r^2(t) \rangle \propto t^{\beta}$ behaviour with β =2 (inertia-dominated short-time regime), β <1 (sub-diffusive regime at intermediate times) and β =1 (diffusion-dominated long-time regime). This kind of complex time dependence is the characteristic of supercooled liquids [59], ionic glasses [60] and room temperature ionic liquids [61]. The sub-diffusive regime arises because of the rattling (no appreciable displacement of particles with time) motion of particles in a cage [8,59,60,62] formed by its surrounding neighbours, and this rattling persists for a significant duration. The composition-dependence of MSDs for cation (upper panel), anion (middle panel) and the cosolvent (lower panel) in these binary mixtures are shown via a representative plot in Figure 3.A.4 (Appendix 3.A). It shows the substantial reduction of the extent of sub-diffusive flat regime upon the addition of the cosolvents, which is an indication of cage softening by the presence of cosolvent molecules. The effects of cosolvent polarity on the centre-of-mass motion of the particles in these IL mixtures are shown in Figure 3.1. The approximate diffusion on-set time scales are indicated by bullet marks on the MSD curves with numerical values of the corresponding timescales summarized in Table 3.B.2 (Appendix 3.B). It shows that the steepest slope of the MSDs occurs for mixtures at the lowest IL mole fractions studied (F_{IL}=0.10), the impact being the maximum for acetonitrile.

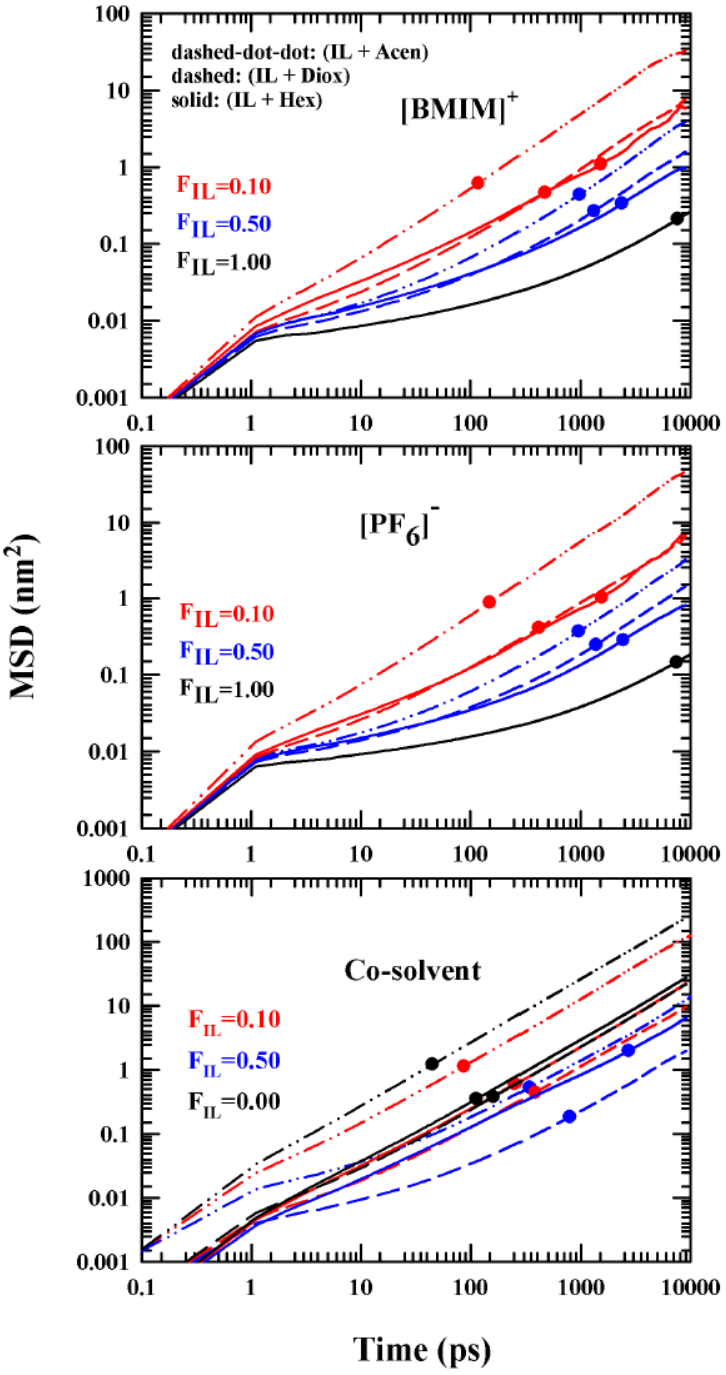

Figure 3.1: Simulated mean square displacements (MSDs) for both the ions $[BMIM]^+$ (upper panel), $[PF_6]^-$ (middle panel) and cosolvents (lower panel) in three binary mixtures. Here, dashed-dot-dot, dashed and solid lines represent the (IL+Acen), (IL+Diox) and (IL+Hex) binary mixtures respectively. Acen, Diox and Hex represent acetonitrile, 1,4-dioxane and hexane respectively. Note only four IL mole fractions F_{IL}=0.00, 0.10, 0.50, and 1.00 are shown here. Bullet marks indicate the approximate diffusion onset time scales.

Next, the translational diffusion coefficients of the ions of [BMIM] [PF_6] IL and the cosolvent molecules at all the mole fractions have been calculated by using the Einstein relation [58],

$$D = \left[\frac{1}{6t}(\langle \delta r^2(t) \rangle)\right]_{t\to\infty} \quad (3.4)$$

We have estimated the self-diffusion coefficients of all the particles from the slopes of the respective MSDs in the long-time diffusive regime. For this, we have used 100ns trajectories to verify whether $\beta \cong 1$ at long time. The corresponding plots of β as a function of time are shown in Figure 3.A.5 (Appendix 3.A) to visually detect the diffusive regime. Figure 3.2 presents the composition dependence of self-diffusion coefficients of both the ions and the three cosolvents- acetonitrile, 1, 4-dioxane and hexane- in their respective binary mixtures. The estimated self-diffusion coefficient of each of the components in the binary mixtures decreases with increasing F_{IL}, which is a consequence of increase in viscosity with IL mole fraction in the binary mixtures. Similar trend of self-diffusion coefficients in [C_6mim] [FSI] + Acetonitrile mixtures have also been reported in an earlier work[63]. Note the increase of diffusion coefficients of ions is the largest in the presence of acetonitrile and the smallest in the presence of hexane in these (IL+cosolvent) binary mixtures.

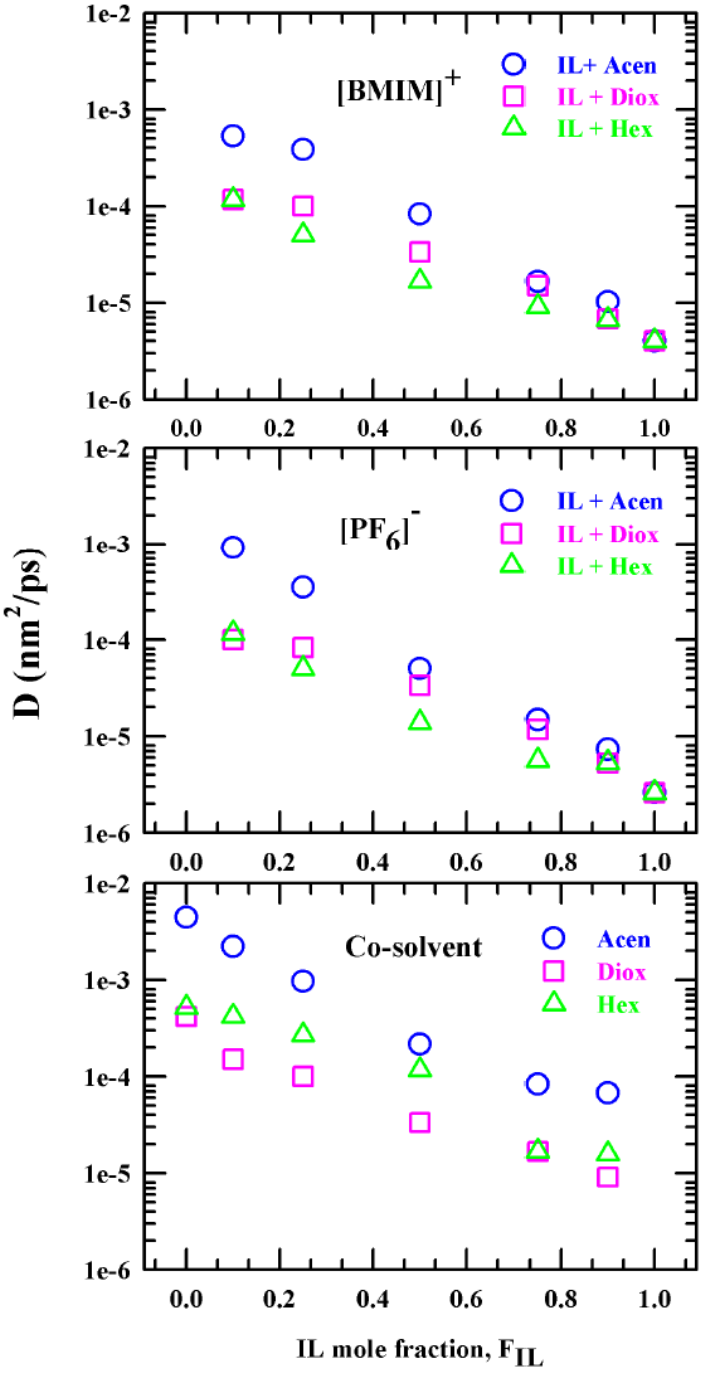

Figure 3.2: Composition dependence of diffusion coefficients of the $[BMIM]^+$ (upper panel), $[PF_6]^-$ (middle panel) and cosolvent (lower panel) in three binary mixtures (IL+Acen), (IL+Diox) and (IL+Hex).

3.4.2 Composition Dependent Dynamic Heterogeneity (DH) Parameters: Impact of Cosolvent polarity on Non-Gaussian (NG) and New Non-Gaussian (NNG) Parameters

So far, we have investigated the effects of cosolvent polarity on self-diffusion coefficients of ions and cosolvent molecules in these binary mixtures at different IL mole fractions. Because the diffusion coefficients have been obtained from the slopes of the respective MSDs, the numerical values cannot reflect the underlying displacement distributions. In a homogeneous liquid where particle interactions are largely governed by the excluded volume effect and allowing the particles to execute temporally uncorrelated completely random moves fuelled by the thermal energy, the particle displacements are expected to follow the Central Limit Theorem to produce Gaussian distribution of displacements. This consideration provides an avenue for a quick check of heterogeneous particle dynamics via examining the deviation of the underlying displacement distributions from being Gaussian. In a system with anomalous motional features, particles can execute displacements both larger and smaller than those predicted by the Gaussian distribution for a homogeneous system. The larger displacements associate with the more mobile particles and thus with faster timescales than the particles with smaller displacements. Therefore, two additional timescales appear in the system which are different from the normal collisional and diffusion timescales. The faster timescale arising from the larger displacements is known as the non-Gaussian timescale (τ_{NG}) and can be estimated from the peak position of a curve showing the time dependence of a quantity, $\alpha_2(t)$. [59,64] The other slower timescale associated with the smaller displacements (relatively less mobile particles) can be obtained similarly from the time dependence of the new non-Gaussian parameter, $\gamma(t)$). [57,65] This slower timescale is known as the new non-Gaussian timescale (τ_{NNG}). These two quantities, $\alpha_2(t)$ and $\gamma(t)$, are linked to the mean squared displacements (MSDs) as follows [57,59,64,65]:

$$\alpha_2(\mathrm{t}) = \frac{3\langle \delta \mathrm{r}^4(\mathrm{t})\rangle}{5\langle \delta \mathrm{r}^2(\mathrm{t})\rangle^2} - 1 \tag{3.5}$$

$$\gamma(\mathrm{t}) = \frac{1}{3}\langle \delta \mathrm{r}^2(\mathrm{t})\rangle \left\langle \frac{1}{\delta \mathrm{r}^2(\mathrm{t})} \right\rangle - 1 \tag{3.6}$$

where $\langle \delta \mathrm{r}^2(\mathrm{t})\rangle = \langle \mathrm{N}^{-1} \sum_{\mathrm{i}=1}^{\mathrm{N}} |\Delta \mathrm{r}_\mathrm{i}(0,\mathrm{t})^2| \rangle$ and $\langle \delta \mathrm{r}^4(\mathrm{t})\rangle = \langle \mathrm{N}^{-1} \sum_{\mathrm{i}=1}^{\mathrm{N}} |\Delta \mathrm{r}_\mathrm{i}(0,\mathrm{t})^4| \rangle$.

Here, $\Delta r_i(0,t) = r_i(t) - r_i(0)$ describes the displacement vector for the i^{th} particle in a system containing N particles and δr is the distance over which a particle moved in time t.

The simulated $\alpha_2(t)$ and $\gamma(t)$ for the neat IL (upper panel) and the neat cosolvents (lower panel) are shown in Figure 3.3. The NG (τ_{NG}) and NNG (τ_{NNG}) timescales obtained for both the $[BMIM]^+$ and $[PF_6]^-$ ions (upper panel) are respectively 0.5-1.0 ns and 2-4 ns and the corresponding $\alpha_2(t)$ peak heights are higher than the peak height predicted for the homogeneous liquid (~ 0.2) [59]. Moreover, the time scales obtained for the three cosolvents, acetonitrile, 1, 4-dioxane and hexane, lies in the range 1-10 ps along with the $\alpha_2(t)$ peak height <0.2, which indicates that the pure IL is far more dynamically heterogeneous than the neat cosolvents.

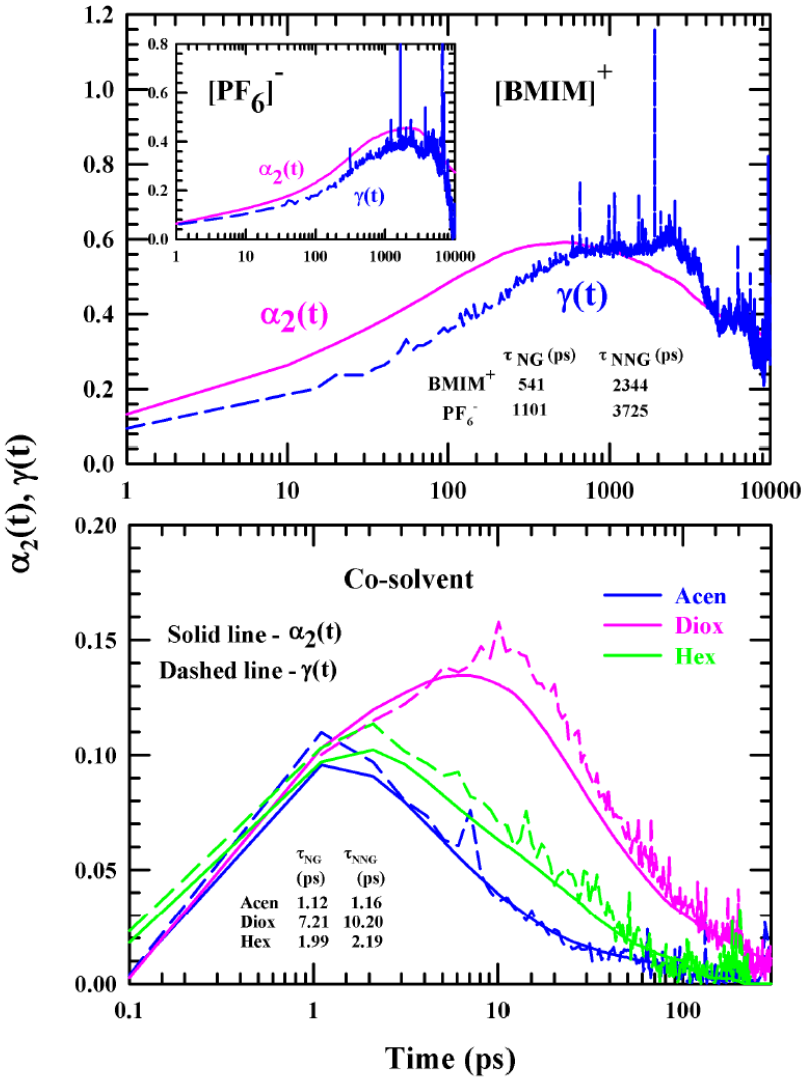

Figure 3.3: Simulated NG ($\alpha_2(t)$) and NNG ($\gamma(t)$) for both the ions $[BMIM]^+$ (upper panel) and $[PF_6]^-$ (in the inset of upper panel) in neat [BMIM][PF_6] IL and the neat three cosolvents – acetonitrile, 1,4-dioxane and hexane (lower panel). Here, solid lines and dashed lines represent the $\alpha_2(t)$ and $\gamma(t)$ respectively. Approximate NG and NNG peak times are shown in the inset.

Next, we explore the impact of cosolvent polarity on τ_{NG} and τ_{NNG}. The cosolvent polarity dependencies of $\alpha_2(t)$ and $\gamma(t)$ at four representative mole fractions, F_{IL}=1.00, 0.50, 0.10, 0.0 are presented in Figure 3.4 (left panels) and Figure 3.A.6 (Appendix 3.A). For clarity, data for all mole fractions studied are not shown. The $\alpha_2(t)$ and $\gamma(t)$ at all these mole fractions for the (IL + acetonitrile) binary mixture are given in Figure 3.A.7 & 3.A.8 (Appendix 3.A). The right panels of Figure 3.4 depict the composition dependence of τ_{NG} (also summarized in Table 3.4) for both the ions and the cosolvent in these three (IL+cosolvent) binary mixtures. A strong composition dependence is clear from the data in left and right panels of Figure 3.4. The NG peak heights and the timescales for the cation and anion drastically decrease as the IL is successively diluted by adding cosolvent in the mixture. For the cosolvents, on the other hand, τ_{NG} increases with increase of F_{IL} as the system changes from neat cosolvents to concentrated IL solution. Here, shortening of τ_{NG} for the ions (~540 ps to ~4 ps for $[BMIM]^+$ and ~1100 ps to ~50 ps for $[PF_6]^-$) occurs upon changing the composition from F_{IL}=1.00 to F_{IL}=0.10. For the cosolvents, the timescale slows down from a few ps in the neat system to sub-nanosecond in solutions with F_{IL}=0.9. A close examination of the data in right panels of Figure 3.4 reveals that τ_{NG} for $[BMIM]^+$ becomes the fastest in solution when the cosolvent is acetonitrile. τ_{NG} for $[BMIM]^+$ remains faster in solutions with 1,4-dioxane than with hexane for most of the IL concentration regime. τ_{NG} for $[PF_6]^-$ remains the fastest in presence of acetonitrile but the trend observed for the cation in the other two binary mixtures reverses for the anion. This reflects both polarity impact on τ_{NG} as well as the variations in interactions with the added cosolvent of differing polarities for cation and anion because of their differences in ionic charge and molecular size. This complexity in interactions also impact the DH timescales for cosolvent in these binary mixtures (right lower panel, Figure 3.4) where τ_{NG} for acetonitrile has been found to be the fastest for acetonitrile and the slowest for hexane.

Next, composition dependent $\gamma(t)$ profiles, presented in Figure 3.A.6 (Appendix 3.A), suggest considerable impact of cosolvent polarity. The composition dependent peak times, τ_{NNG}, shown in Figure 3.5 (also summarized in Table 3.4), reveal this polarity effect more clearly. As in the case of τ_{NG}, both the ions show the fastest NNG timescales in IL binary mixtures with acetonitrile. One can also differentiate in τ_{NNG} for the IL ions between the IL binary mixtures containing dioxane and hexane. The difference in polarities is also clearly visible in τ_{NNG} for cosolvents in these (IL + cosolvent) binary mixtures.

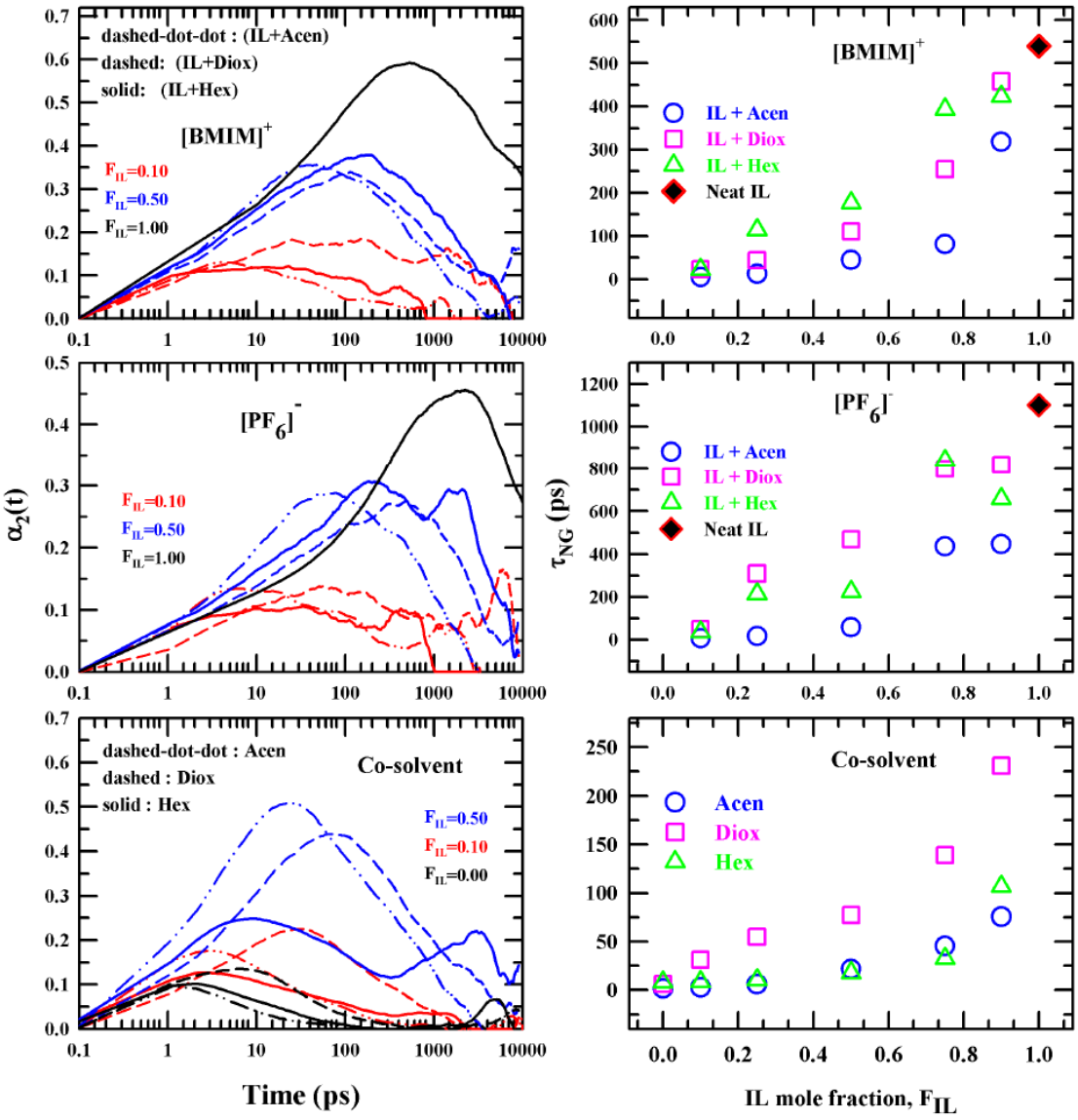

Figure 3.4: Cosolvent polarity dependence of $\alpha_2(t)$ parameters for both the ions $[BMIM]^+$ (left upper panel), $[PF_6]^-$ (left middle panel) and the cosolvents (left lower panel) in three binary mixtures. Right panels show the composition dependent τ_{NG} for both ions (upper & middle) and cosolvents (lower) in these mixtures. All data are color coded.

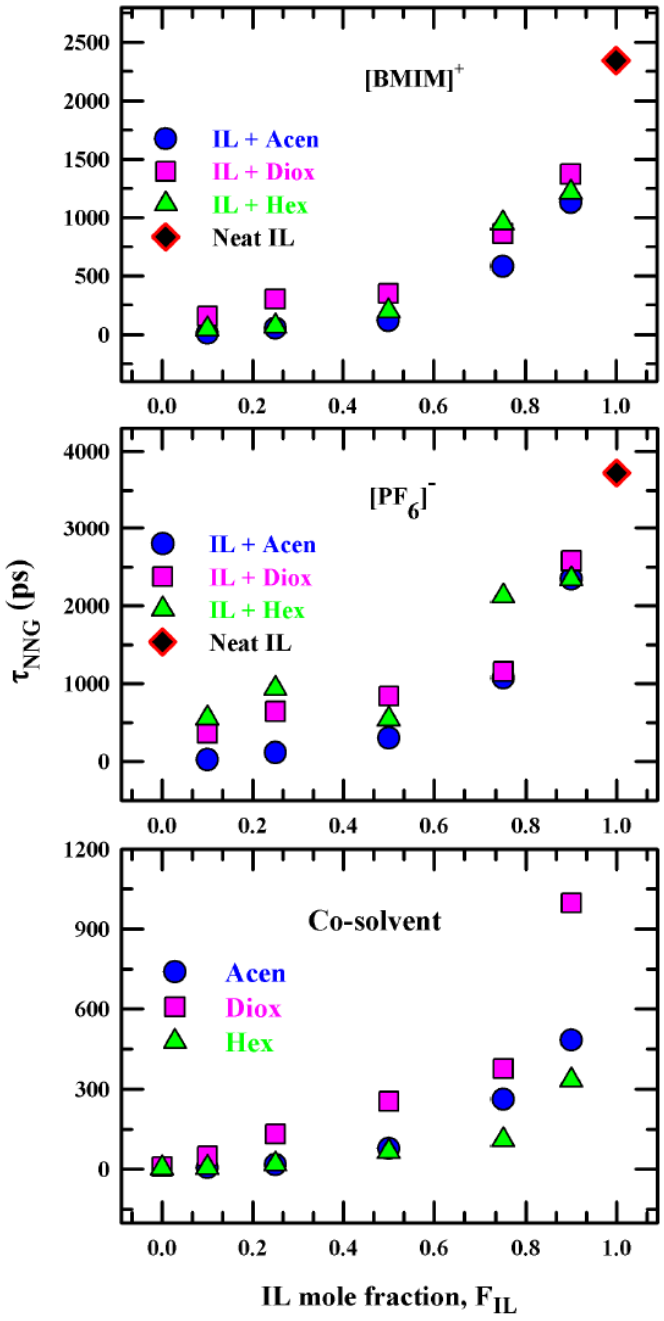

Figure 3.5: Composition dependent τ_{NNG} for $[BMIM]^+$ (upper panel), $[PF_6]^-$ (middle panel) and the cosolvents (lower panel) in the three binary mixtures. Data for different mixtures are color coded.

Table 3.4: Comparison of time scales obtained from various simulated DH parameters in the three binary mixtures at different IL mole fraction (F_{IL}).

	τ_{NNG}	τ_α	τ_Q	t_4^{max}	τ_{NNG}	τ_α	τ_Q	t_4^{max}	τ_{NNG}	τ_α	τ_Q	t_4^{max}
IL+Acen	**[BMIM]$^+$** (ps)				**[PF$_6$]$^-$** (ps)				**Cosolvent** (ps)			
1.00	2344	3235	3810	5294	3725	3150	2580	7089	-	-	-	-
0.90	1127	1235	1228	3270	2344	1199	745	3557	484	46	187	145
0.75	584	591	555	1084	1073	559	333	1374	262	9	85	32
0.50	120	181	152	385	302	154	88	321	77.5	4	28	10
0.25	52.3	42	33	52	114	38	17	60	17.6	2	7	4
0.10	8.84	16	12	39	25.1	15	6.2	41	6.72	1	3	2
0.00	-	-	-	-	-	-	-	-	1.5	1	1.1	1
IL+Diox	**[BMIM]$^+$**				**[PF$_6$]$^-$**				**Cosolvent**			
1.00	2344	3235	3810	5294	3725	3150	2580	7089	-	-	-	-
0.90	1372	1777	1705	3868	2580	1670	1070	5721	998	435	1399	449
0.75	864	929	820	2852	1156	302	484	2124	377	228	718	403
0.50	350	448	346	779	841	345	192	690	255	121	396	326
0.25	302	157	110	304	644	112	57	211	132	45.1	148	74
0.10	157	87	57	357	367	60.1	27.4	700	49.8	23.1	145	37
0.00	-	-	-	-	-	-	-	-	9.9	13.3	31	33
IL+Hex	**[BMIM]$^+$**				**[PF$_6$]$^-$**				**Cosolvent**			
1.00	2344	3235	3810	5294	3572	3150	2580	7089	-	-	-	-
0.90	1214	1617	1255	5400	2344	1551	810	5920	334	107	202	286
0.75	952	1151	1220	2900	2125	1238	779	3960	109	33	49	78
0.50	200	423	433	370	543	427	263	778	65.3	18	24	47
0.25	71.9	135	153	88	937	152	148	89	18.8	10	13	22
0.10	44.1	32	42	29	557	41	25.7	34	7.0	9	11	13
0.00	-	-	-	-	-	-	-	-	3.42	7	8	12

3.4.3 Single Particle Displacement Distributions

Single particle displacement distribution quantifies the DH signatures via the deviation from the Gaussian displacement distribution predicted for homogeneous liquids [58], and it can be calculated via the simulated self-part of the van Hove correlation function, $G_s(r,t)$ [66–70] by using the following expression,

$$P[\log_{10}(\delta r); t] = \ln(10)\, 4\pi\delta r^3 G_s(\delta r, t) \quad (3.7)$$

For a Gaussian $G_s(r,t)$, $P[\log_{10}(\delta r); t]$ becomes independent of time[66] with a peak height of ~ 2.13 and deviations from this peak height suggests presence of heterogeneous dynamics.

Figure 3.6 shows the simulated $P[\log_{10}(\delta r); t]$ at $t = \tau_{NG}$ for the $[BMIM]^+$, $[PF_6]^-$ ions and the cosolvents at F_{IL}=1, 0.50, 0.10 and 0. Note the peak heights in these binary mixtures for both the ions and the three cosolvents remain below the homogeneous limit, suggesting underlying non-Gaussian displacement distributions. Interestingly, $P[\log_{10}(\delta r); \tau_{NG}]$ for $[BMIM]^+$ indicates dilution of IL by cosolvents permits $[BMIM]^+$ accessing larger displacements but increase in cosolvent polarity does the reverse. $P[\log_{10}(\delta r); \tau_{NG}]$ for $[PF_6]^-$, on the other hand, suggests accessing of larger displacements with both dilution of IL by cosolvent and increase of cosolvent polarity. For neat cosolvents, increase of polarity allows accessing larger displacements. In binary mixtures, with successive addition of IL $P[\log_{10}(\delta r); \tau_{NG}]$ shifts toward larger displacements for hexane and moves to opposite direction for dioxane with the least impact on displacement lengthscales sampled by acetonitrile.

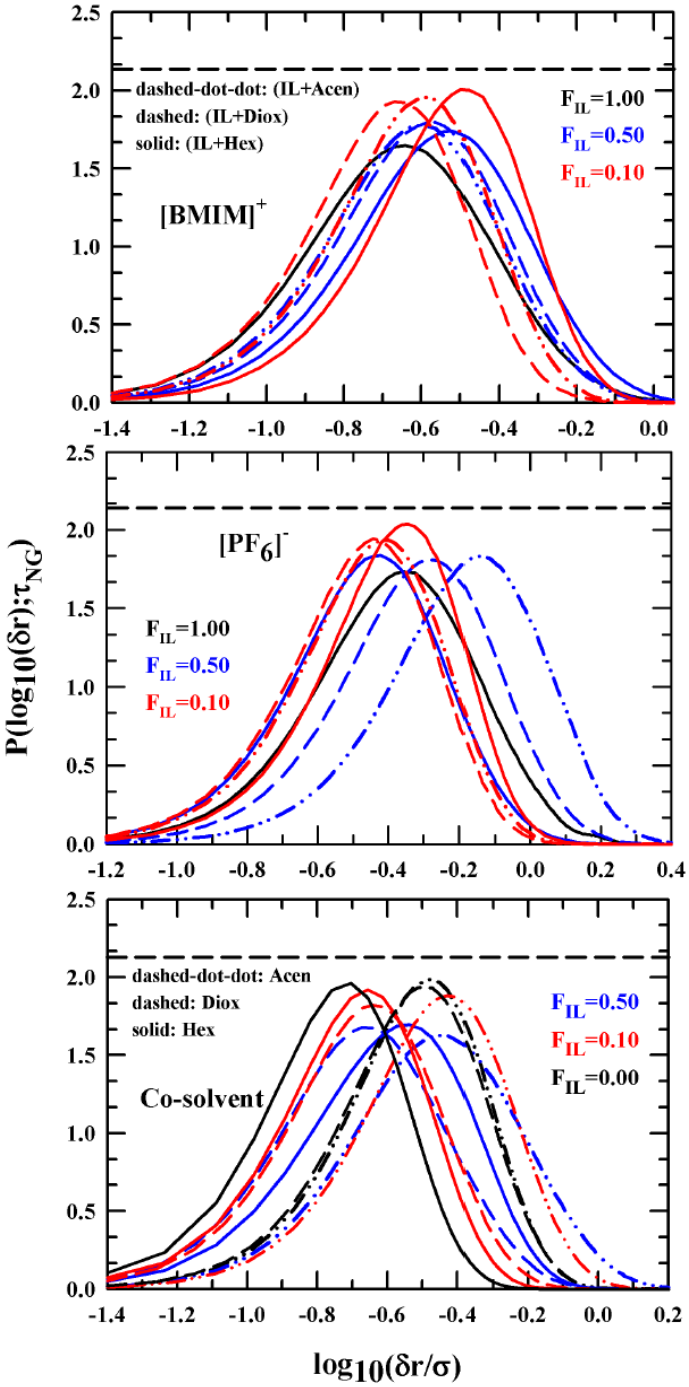

Figure 3.6: Cosolvent polarity dependence of simulated single particle displacement distributions, $P[log_{10}(\delta r); t = \tau_{NG}]$ for the IL ions $[BMIM]^+$ (upper panel), $[PF_6]^-$ (middle panel) and cosolvents (lower panel) in the three binary mixtures at F_{IL}=1.0, 0.50, 0.10, 0.0. Here, horizonal black line denotes the peak height (~2.13) for Gaussian distribution of particle displacements.

The simulated $P[\log_{10}(\delta r);\ \tau_{NNG}]$, shown in Figure 3.A.9 (Appendix 3.A), suggests relatively stronger cosolvent polarity impact on $[PF_6]^-$ displacements than on those for $[BMIM]^+$ where the effect of dilution is weaker for polar binary mixtures than in the non-polar ones. In addition, at $t = \tau_{NNG}$, displacements accessed by the neat solvent molecules increases with the increase of cosolvent polarity. Interestingly, for both the three cosolvents, increase of IL concentration in binary mixture allows sampling of larger displacements with the maximum effect for hexane and minimum for dioxane. All these observations, therefore strongly suggest that cosolvent polarity indeed contributes to the heterogeneous relaxations of molecules and molecular ions in these complex binary mixtures.

3.4.4 Self-Intermediate Scattering Function: Mixture Composition and Cosolvent Polarity Dependence

The self-intermediate scattering function, $F_s(k,t)$, which tracks the time evolution of density at a given space point, can be simulated from the real part of the incoherent scattering function [58,65,71], $F_s(k,t) = N^{-1}\sum_i\langle \cos k \times [r_i(t) - r_i(0)]\rangle$ in the limit of the nearest neighbour wavenumber ($k\sigma \rightarrow 2\pi$, σ being the diameter). The 1/e decay time of the self-dynamic structure factor, $F_s(k\sigma \rightarrow 2\pi, t)$, provides an approximate estimate of the α-relaxation (structural relaxation) time scale, τ_α. To study the cosolvent polarity dependence on structural relaxation, the simulated $F_s(k\sigma \rightarrow 2\pi, t)$ profiles for the IL ions and the cosolvents in these binary mixtures at various compositions have been monitored. The simulated results are presented in Figure 3.7, where the corresponding 1/e decay time are indicated as bullet marks and also these values are provided in Table 3.4. A representative plot showing the decay of $F_s(k\sigma \rightarrow 2\pi, t)$ for all the IL mole fractions studied are presented in Figure 3.A.10 (Appendix 3.A). It is clear from this figure that the relaxations of $F_s(k\sigma \rightarrow 2\pi, t)$ for both the ions are the fastest in acetonitrile containing binary mixtures among the three different binary mixtures considered. In addition, the IL concentration effect on the self-dynamic structure factor relaxation is also the strongest for acetonitrile containing IL mixtures. Interestingly, the relaxation of the acetonitrile self-dynamic structure factor in these ionic liquid solutions is the fastest among the three cosolvents considered here. This is a reflection of strong polarity impact on the relaxation of self-dynamic structure factor in ($[BMIM]^+[PF_6]^-$ + acetonitrile/dioxane/hexane) binary mixtures.

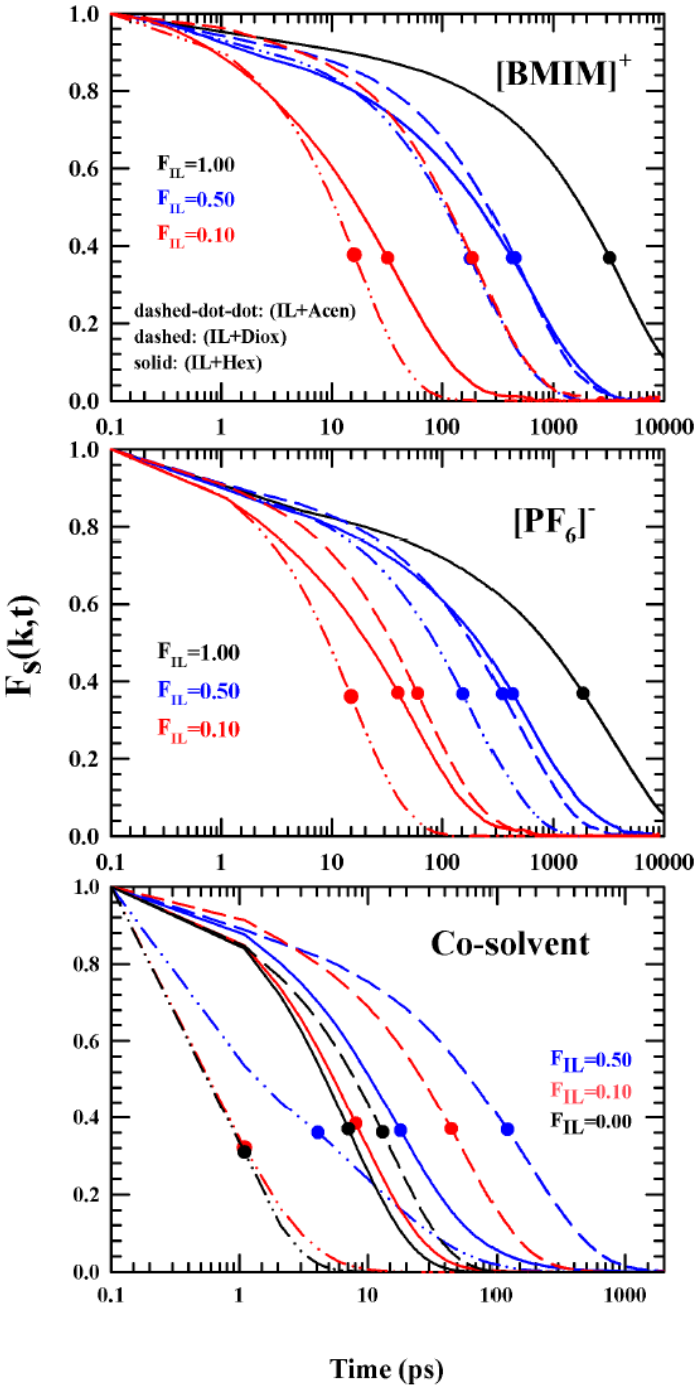

Figure 3.7: Cosolvent polarity dependent normalized self-part of the intermediate scattering function at the nearest neighbor ($k\sigma \rightarrow 2\pi$), $F_s(k,t)$ for the three binary mixtures at mixture compositions, F_{IL}=1.0, 0.50, 0.10, 0.0. Here, bullet marks indicate the respective 1/e decay times,τ_α.

Next, we show in Figure 3.8 the IL mole fraction dependence of the diffusion on-set timescales obtained from the simulated relaxations of the self-dynamic structure factors and the MSDs (left panels), and the correlation between them at different IL mole fractions (right panels). The diffusion on-set timescale for MSDs ($\tau_{MSD,\beta}$) can be approximately identified as the time when $\beta \cong 1$ in the relation, $\langle \delta r^2 \rangle \propto t^{\beta}$. This is already shown in Figure 3.1 by bullet marks. For the self-dynamic structure factor, the diffusion on-set timescale (τ_{α}) can be approximated as the time by which the decay of the normalized $\mathrm{F_s}(\mathrm{k}\sigma \to 2\pi, \mathrm{t})$ has reached e^{-1} or nearly 63%. The remaining portion of the total decay (~37%) is believed to be carried out by the diffusive motion of the particles alone via the centre-of-mass structural rearrangement, $(\mathrm{F_s}(\mathrm{k}\sigma \to 2\pi, \mathrm{t}) = \mathrm{F_s}(\mathrm{k}\sigma \to 2\pi, \mathrm{t} = 0)\exp\left[-\mathrm{D}(k\sigma)^2 t\right]$. Clearly, the structural relaxation and MSD at long time are governed by the same solvent translational rearrangement in a homogeneous solvent, a linear correlation between them is expected. Any non-linearity in that correlation may therefore be interpreted as a signature of heterogeneous relaxation dynamics. The IL mole fraction dependent $\tau_{MSD,\beta}$ and τ_{α}, shown in the left panels of this figure, suggest that both the timescales show sharp rise as F_{IL} approaches unity. Moreover, τ_{α} is uniformly larger than $\tau_{MSD,\beta}$ across the compositions studied for these binary mixtures. The right panels show that these two timescales not only deviate from a 1:1 correlation between them but also show a mutual non-linear dependence. This provides a further support to the view of solution heterogeneous dynamics. Again, the extent of deviation is the minimum for ions in acetonitrile solutions, suggesting a polarity dependence of the underlying heterogeneous relaxation dynamics.

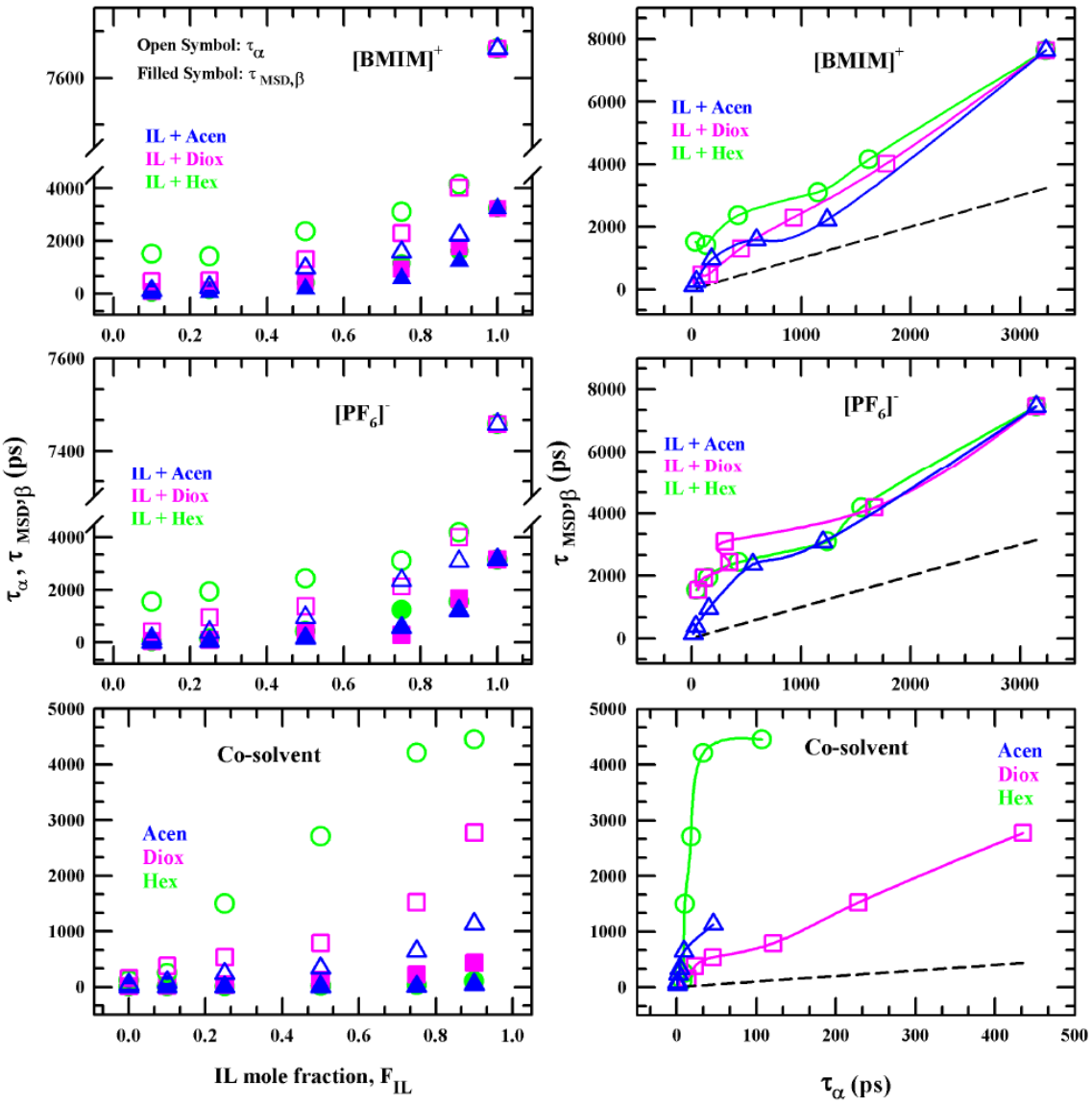

Figure 3.8: IL mole fraction dependence of diffusion on-set time scales obtained from the simulated $F_s(k,t)$, (τ_α) and MSDs, $(\tau_{MSD,\beta})$ for both the ions, $[BMIM]^+$(left upper panel), $[PF_6]^-$ (left middle panel) and cosolvents (left lower panel) in these three binary mixtures. The right panels depict the correlations between τ_α and $\tau_{MSD,\beta}$ for IL ions (right upper & middle panel) and cosolvents (right lower panel) at various IL mole fractions in these binary mixtures.

3.4.5 Overlap function

The overlap function tracks the density fluctuations at smaller length-scale (0.3σ, σ being the particle diameter) than $F_s(k\sigma \rightarrow 2\pi, t)$, and is defined as,[72–74]

$$Q(t) = \sum_{i=1}^{N} W_i(a,t)\exp[ik.r_i(0)] \quad (3.8)$$

In the above equation, $W_i(a,t)$ is a Heaviside step function and defined as, $W_i(a,t) = \Theta(a - |r_i(t) - r_i(0)|)$, where a=0.3σ following an earlier suggestion. [73] The condition a=0.3σ is to ensure that the nearest neighbour particles are not firmly occupying positions as in a crystal lattice but in a molten disordered state satisfying grossly the Lindemann criterion [75,76] after accounting for the anharmonicity and the cooperative effects. The need of monitoring Q(t) relaxations arises for ensuring that $F_s(k\sigma \rightarrow 2\pi, t)$ is not tracking the relaxation due to nearest neighbour vibrations but in fact involves particle translations. It is therefore natural to expect that $Q(t)$ decays would resemble $F_s(k\sigma \rightarrow 2\pi, t)$ relaxations and the corresponding e^{-1}decay times (τ_Q and τ_α) correlate better to each other.

Figure 3.9 presents the polarity dependence of Q(t) decays for $[BMIM]^+$, $[PF_6]^-$ and cosolvents in these binary mixtures at various mole fractions (left panels) and the correlations between τ_Q and τ_α (right panels). As before, the e^{-1}decay times (τ_Q) are represented by the bullet marks on the individual decays. τ_Q values are summarized in Table 3.4. Data in this table show that timescales obtained from various dynamic heterogeneity parameters, namely, τ_{NNG}, τ_α and τ_Q, becomes faster upon adding the cosolvents and show substantial cosolvent polarity dependence. Note in the right panels that the correlation between τ_Q and τ_α is significantly better than what we have seen between τ_α and $\tau_{MSD,\beta}$ in Figure 3.8 (right panels).

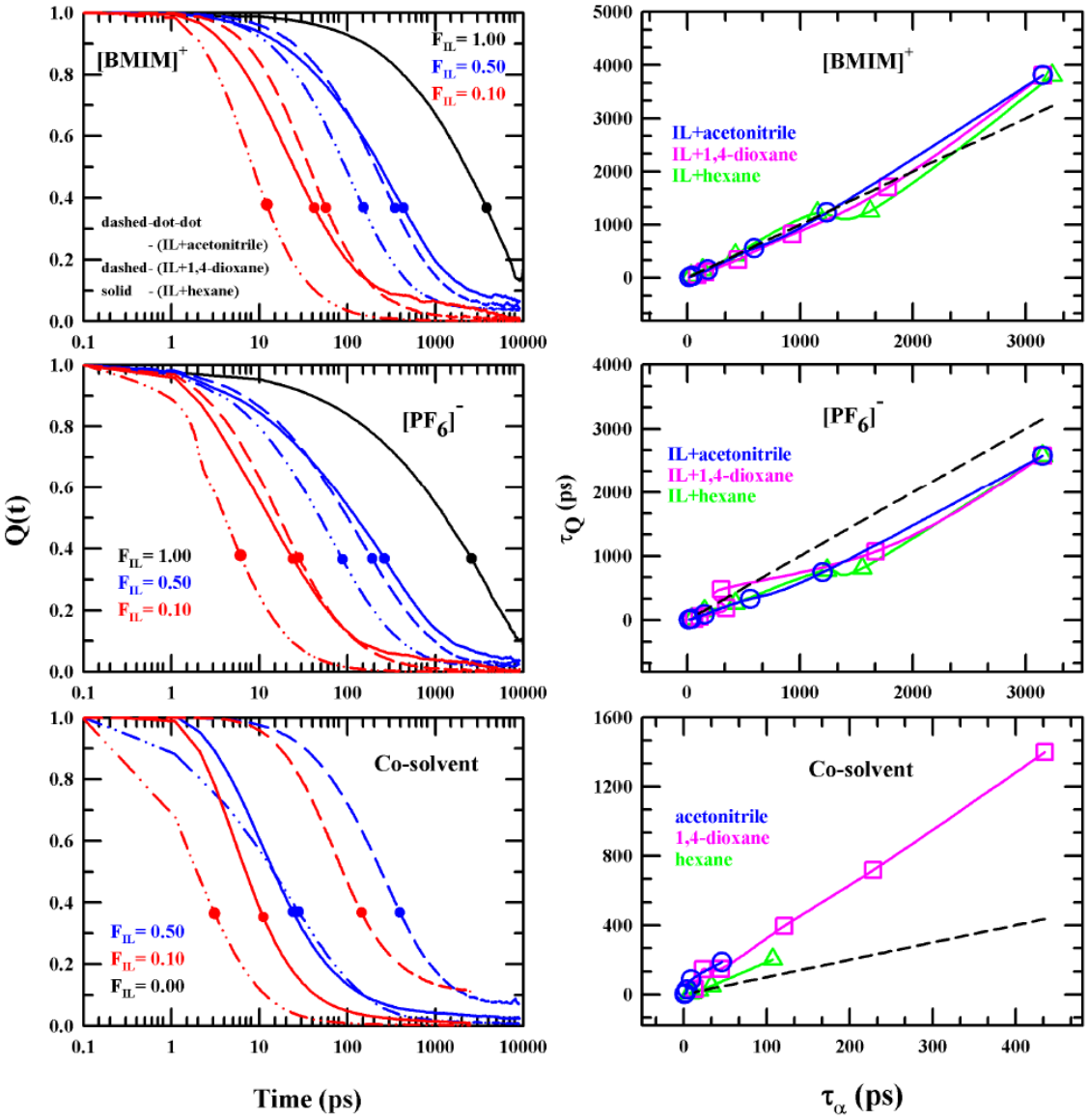

Figure 3.9: Cosolvent polarity dependent simulated overlap function, $Q(t)$, for both the IL ions and cosolvents in the three binary mixtures at 298 K are presented in the left panels, where bullet marks indicate the respective e^{-1} decay times, τ_Q. The right panels show the correlations between e^{-1} decay times obtained from $Q(t)$ (τ_Q) and $F_s(k,t)$ relaxations (τ_α) at various IL mole fractions of these IL mixtures.

3.4.6 Four-Point Correlations: Composition and Cosolvent Polarity Dependence

In slow highly viscous systems, the mobilities of particles over a length-scale may remain the same for a particular duration. This is akin to stating that (i) up to what lengthscale particles are relaxing with the same or similar rates?, and (ii) for what time-duration these particles relax with the same or similar rates? While the former question connects to correlated lengthscales, the other relates to correlated timescales. Four-point correlation function, $\chi_4(k,t)$, tracks the temporal correlations of the local mobilities at two different space points over a certain period of time. $\chi_4(k,t)$ can be approximated by the fluctuation (variance) of the self-dynamic structure factor, $F_s(k,t)$, [72,73,77–79] via the following equation,

$$\chi_4(k,t) = N[\langle F_s(k,t)^2\rangle - \langle F_s(k,t)\rangle^2] \quad (3.9)$$

The maximum time over which the mobility fluctuations remain correlated is designated as, t_4^{max} , which can be obtained from the peak position of $\chi_4(k,t)$ versus t profiles. The composition dependent $\chi_4(k \to 2\pi, t)$ for the ions and the three cosolvents in all these (IL+cosolvent) binary mixtures are shown in Figure 3.10 for the two representative compositions, F_{IL}=0.50, 0.10 along with those for the three neat cosolvents. The corresponding peak times, t_4^{max} , are indicated by the dashed vertical lines. It is clear from this figure that $\chi_4(k \to 2\pi, t)$ responds to both cosolvent polarity and IL mole fraction. The cosolvent polarity and IL mole fraction dependencies of the correlated timescale, t_4^{max}, are presented in Figure 3.11. It is interesting to note in this figure that t_4^{max} for even for neat cosolvents depends on the solvent polarity, and bears the signature of quadrupolar nature of dioxane. In binary mixtures with IL, t_4^{max} is the fastest for acetonitrile containing solutions among these three mixtures.

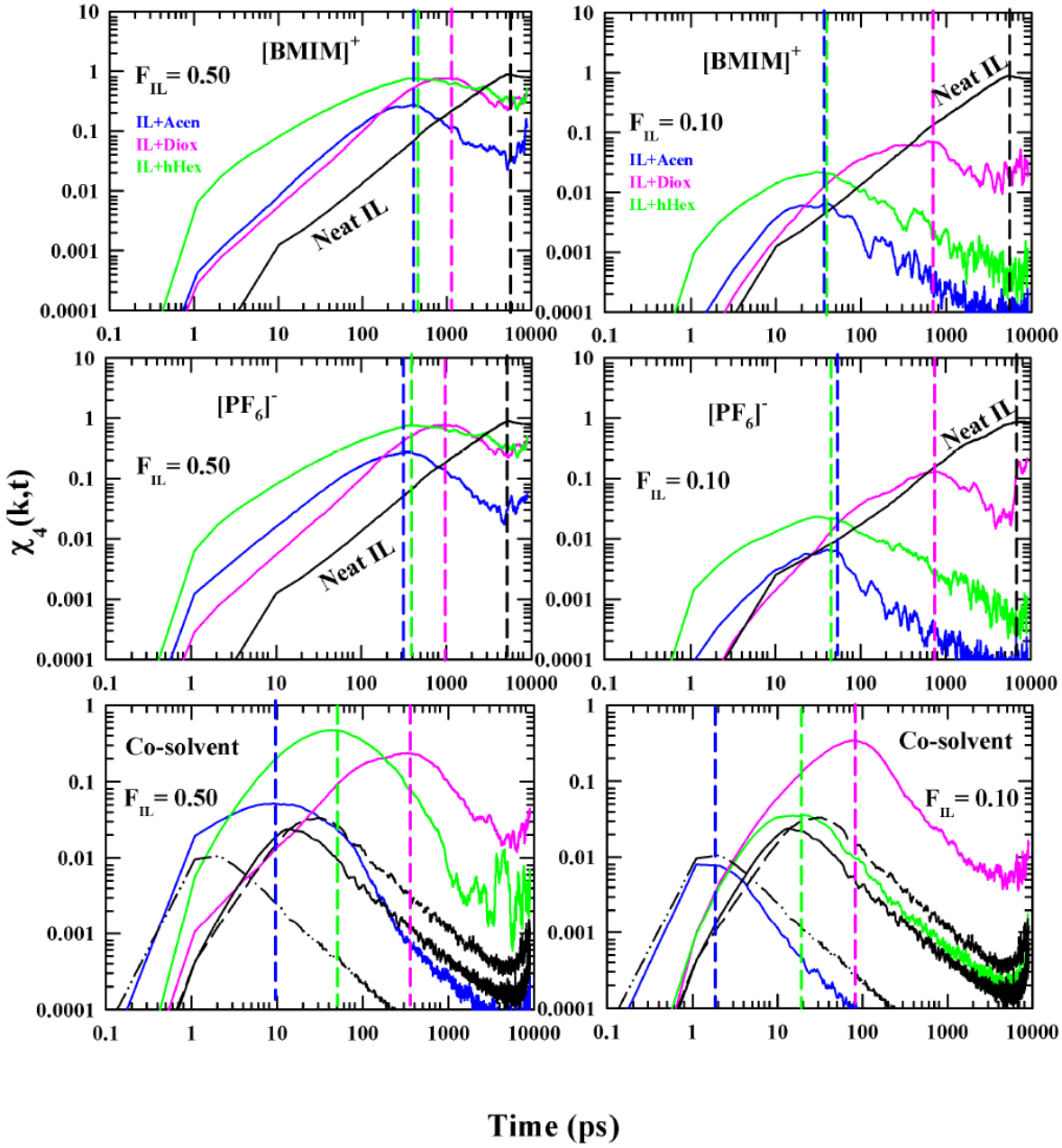

Figure 3.10: Simulated four-point dynamic susceptibility, $\chi_4(k,t)$ for ions and cosolvents at two representative mole fractions F_{IL}=0.50 (left panels), 0.10 (right panels) along with those for neat IL and cosolvents. The vertical lines represent the approximate peak times.

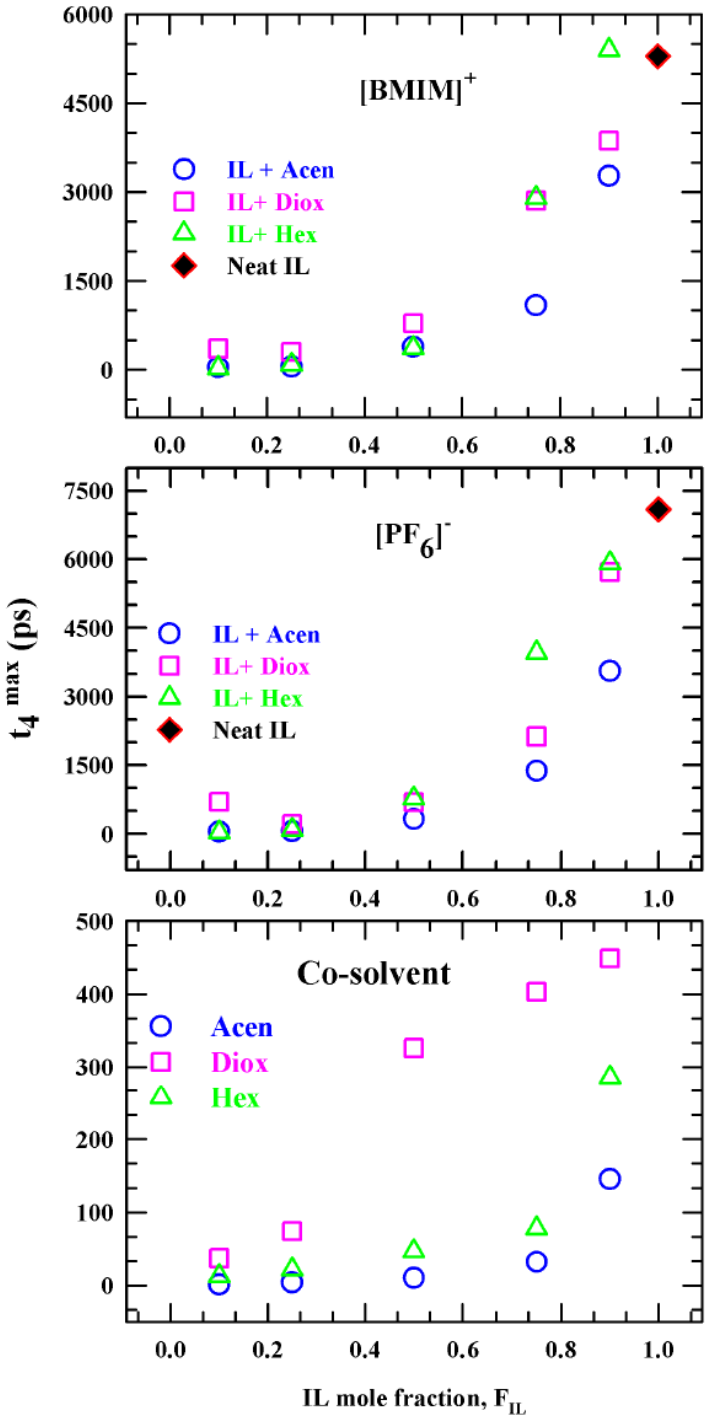

Figure 3.11: IL mole fraction dependence of the correlated time scales, t_4^{max}, obtained from $\chi_4(k,t)$ as a function of IL mole fraction (F_{IL}) for ions and cosolvents in three binary mixtures.

3.5 Conclusion

In summary, the present study finds a significant cosolvent polarity dependence for the dynamics of ([BMIM] [PF_6] + cosolvent) binary mixtures, and identifies the quantities that characterize the heterogeneous relaxation dynamics of individual components in these complex binary mixtures. The heterogeneity signatures become more pronounced at higher IL concentrations and for solutions with less polar cosolvents. Simulated mean square displacements (MSDs) for both the ions and the cosolvents indicate the cage softening upon successive addition of the cosolvents into IL, leading to higher mobilities for ions in solutions with more polar solvents. DH time scales and the peak heights obtained from NG and NNG parameters show both the composition and polarity dependencies. These time scales become faster in presence of the cosolvents in the IL mixtures and the fastest time scales have been obtained for the (IL + acetonitrile) mixtures. In addition, the NG and NNG peak height undergo a dramatic decrease when the system changes from neat IL (F_{IL}=1.00) to dilute IL solutions (F_{IL}=0.10). Composition dependent single particle displacement distributions show that in dilute IL solutions the displacement distributions are moderately deviated from being Gaussian. Relaxation time scales from self-intermediate scattering function and overlap function become significantly faster in binary mixtures of IL with cosolvents and these relaxation times respond significantly to the cosolvent polarity. The temporal correlation between relaxation dynamics at two different space points, quantified by t_4^{max} through the calculations of $\chi_4(k,t)$, become the shortest for IL solutions with acetonitrile. All in all, the study reveals that dynamic heterogeneity of [BMIM][PF_6] changes significantly upon dilution with cosolvents and the extent of modification depends strongly on cosolvent polarity.

Appendix 3.A

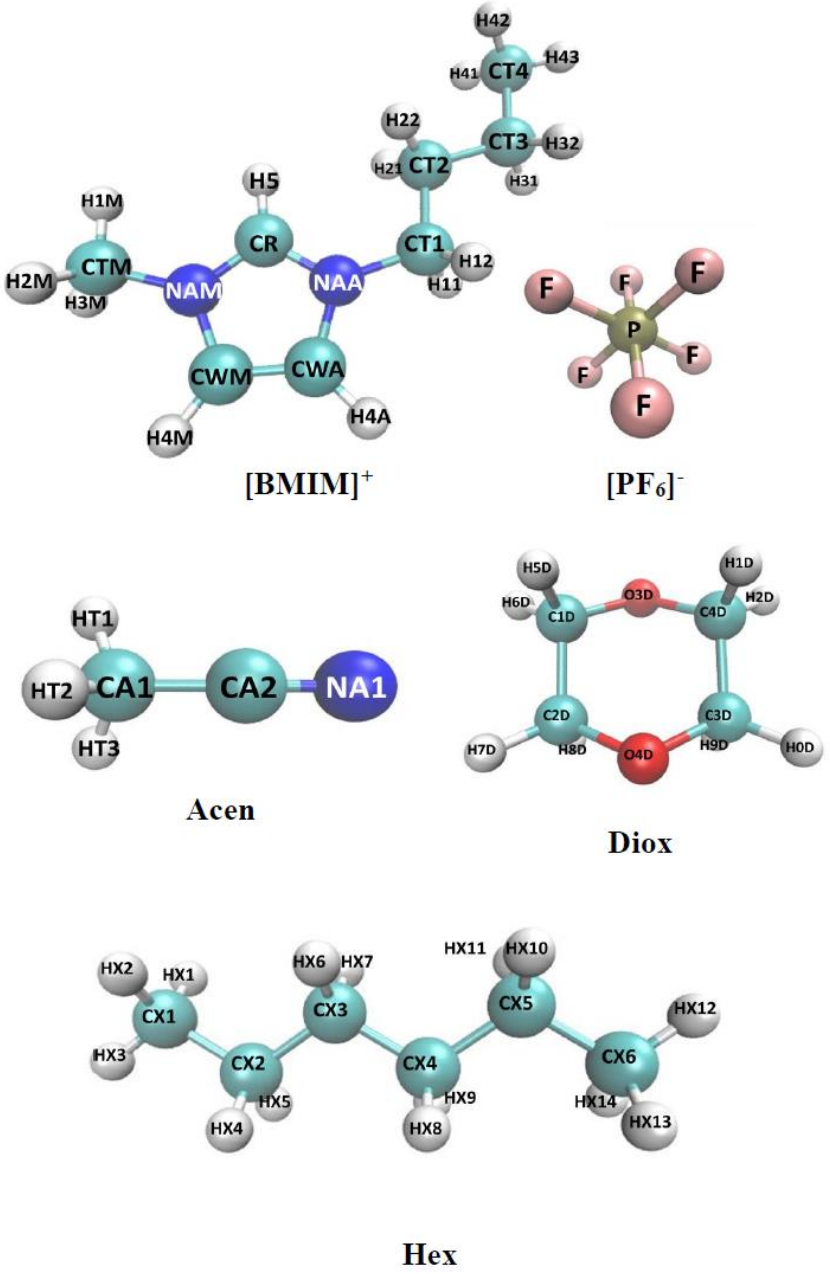

Figure 3.A.1: Chemical structures of $[BMIM]^+$, $[PF_6]^-$, acetonitrile (Acen), 1,4-dioxane (Diox) and hexane (Hex) along with the representations, which were used in the discussion of various simulated properties.

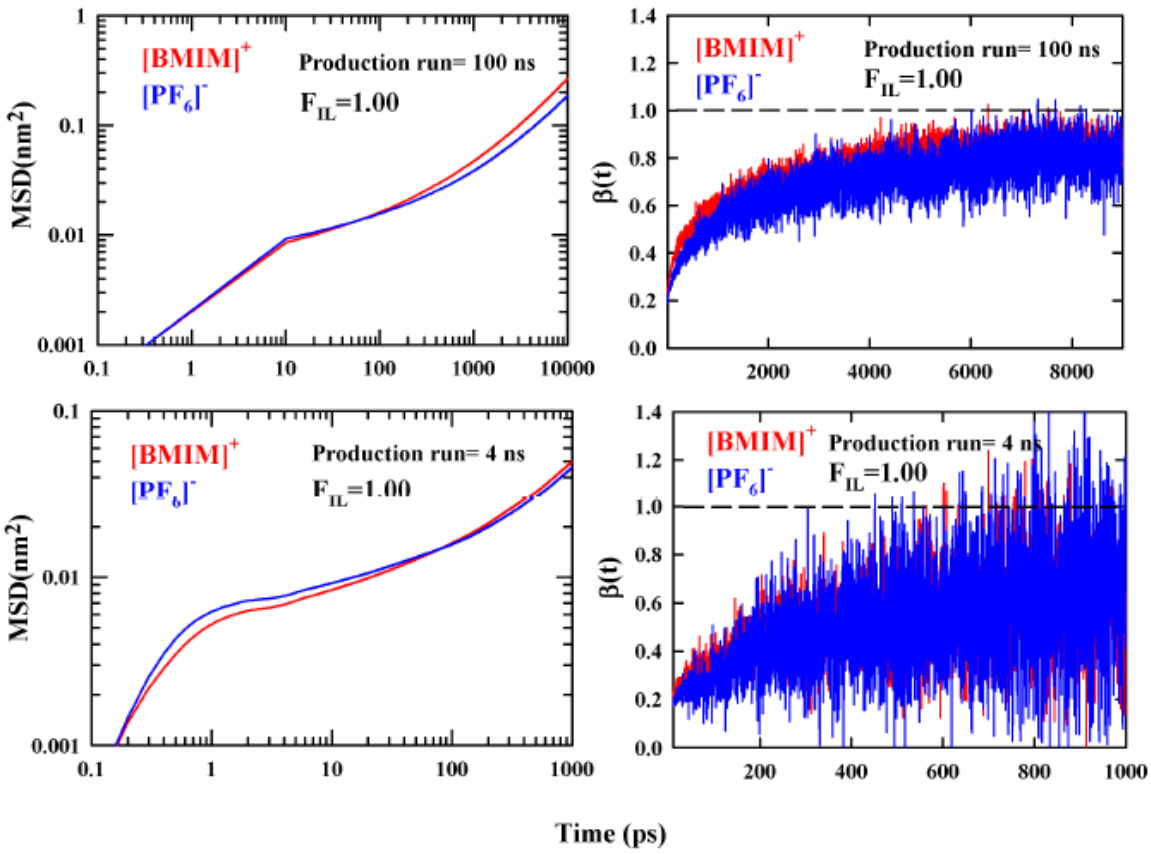

Figure 3.A.2: Mean square displacements (MSDs) for $[BMIM]^+$ cation and $[PF_6]^-$ anion in neat IL (F_{IL}=1.00) for 100 ns (upper left panel) and 4 ns production run (lower left panel) and their corresponding β (t) plots for 100 ns (upper right panel) and 4ns production run (lower right panel).

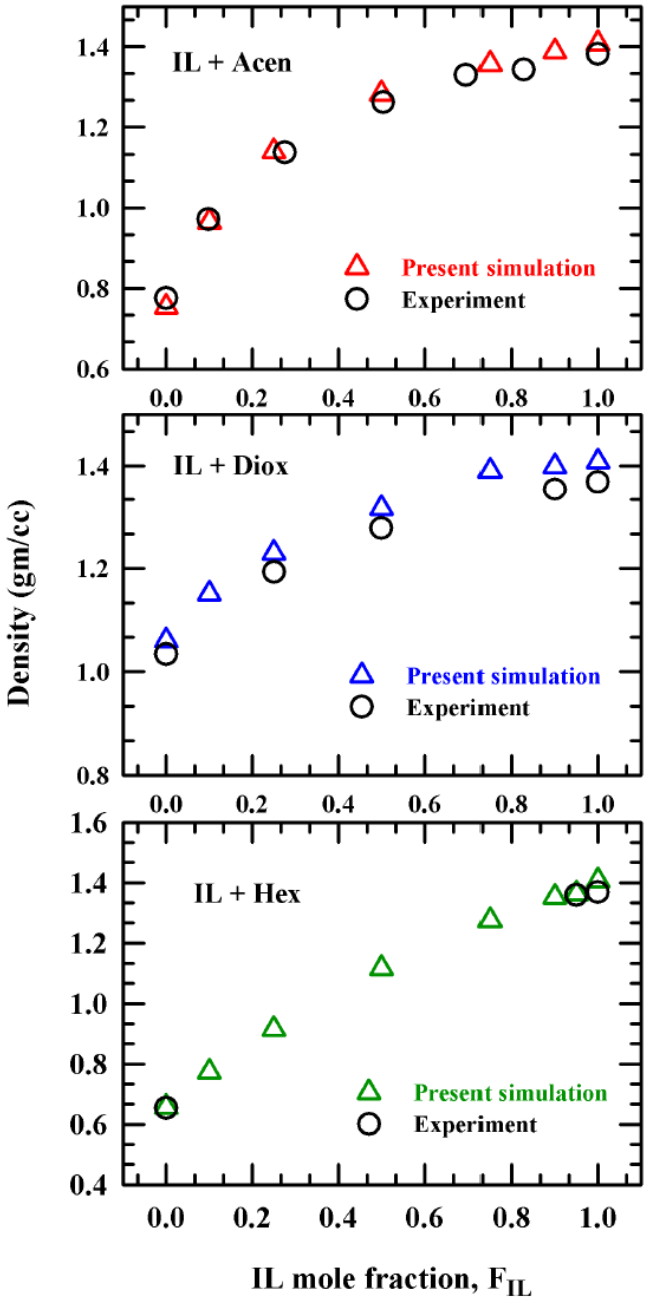

Figure 3.A.3: Composition dependent simulated densities from present simulation and experiments for the three binary mixtures at 298 K. The triangles and circles indicate the densities from present simulations and experiments respectively. Different binary mixtures are represented by color coding as: red, (IL+Acen); blue, (IL+Diox); green, (IL+Hex).

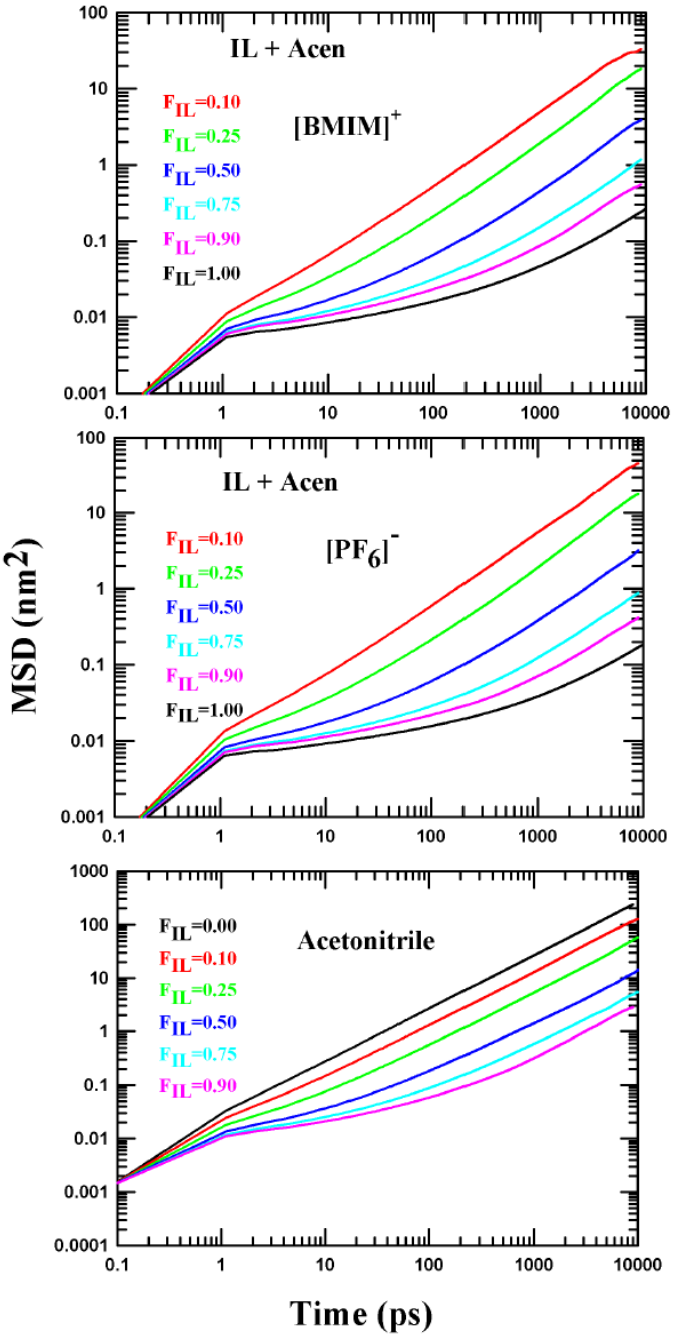

Figure 3.A.4: Composition-dependent translational mean squared displacements (MSDs) for $[BMIM]^+$ cation, $[PF_6]^-$ anion and acetonitrile at 298 K for the binary mixture (IL+Acen).

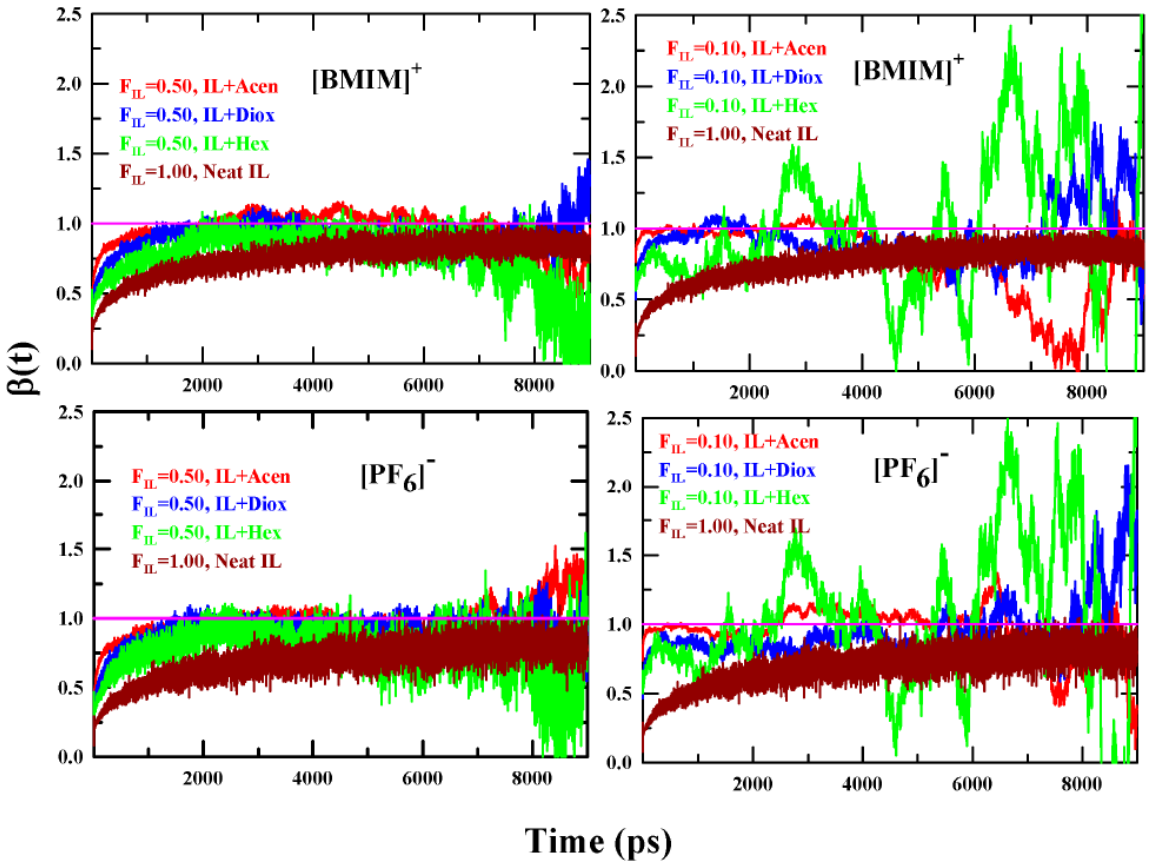

Figure 3.A.5: β (t) plots for the $[BMIM]^+$ cation at F_{IL}=0.50 (upper left panel), F_{IL}=0.10 (upper right panel) and for the $[PF_6]^-$ anion at F_{IL}=0.50 (lower left panel), F_{IL}=0.10 (lower right panel). Note β (t) plots are given for the three binary mixtures along with the pure IL, where color coding are as follows (IL+Acen), red; (IL+Diox), blue; (IL+Hex), green and pure IL, dark red.

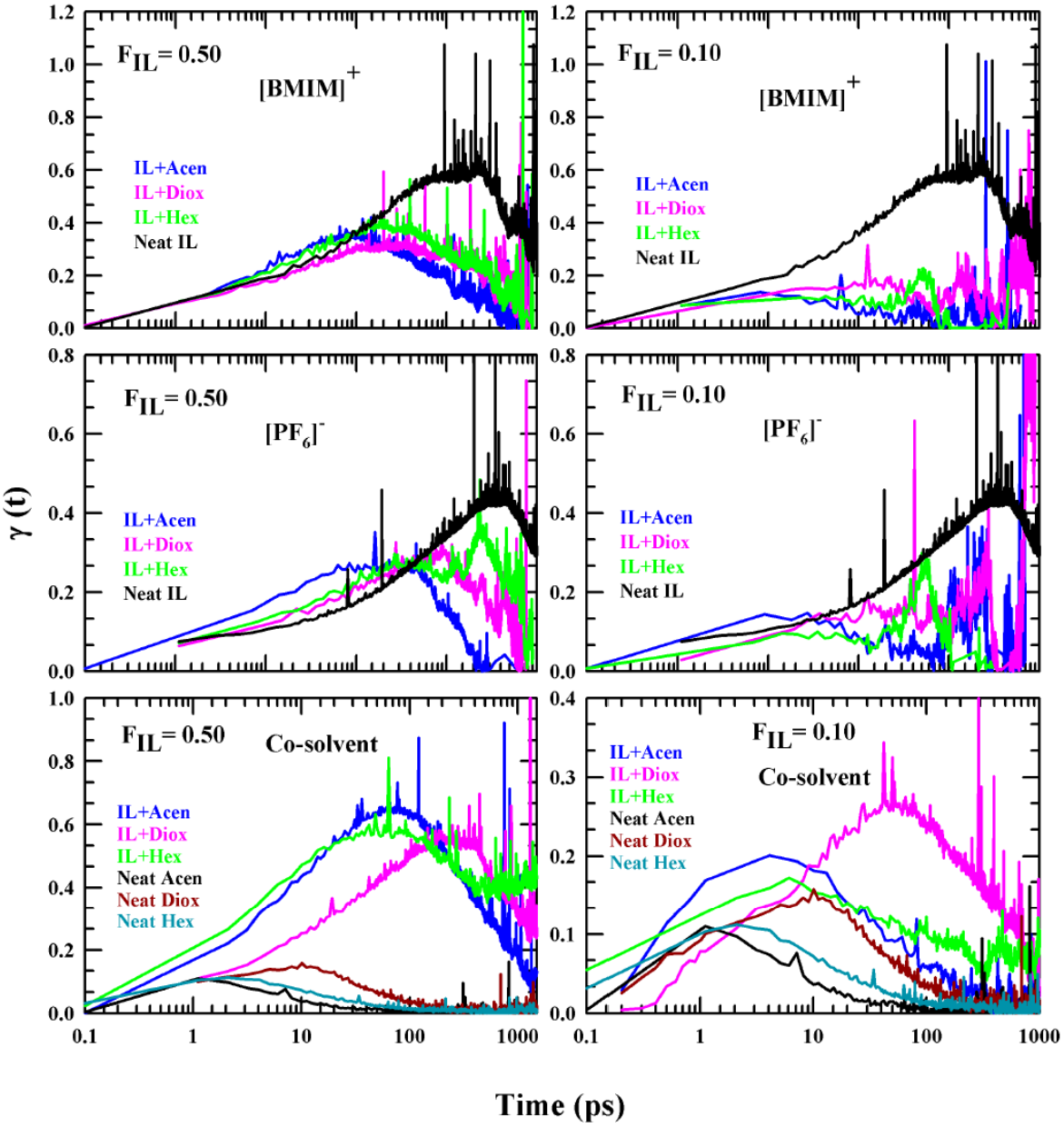

Figure 3.A.6: Cosolvent polarity dependent $\gamma(t)$ for both the ions $[BMIM]^+$ (upper panel), $[PF_6]^-$ (middle panel) and the cosolvent (lower panel) in the three binary mixtures at two compositions F_{IL}=0.50 (left panels) and 0.10 (right panels) along with the corresponding neat systems. Different systems and the corresponding neat solvents are color coded.

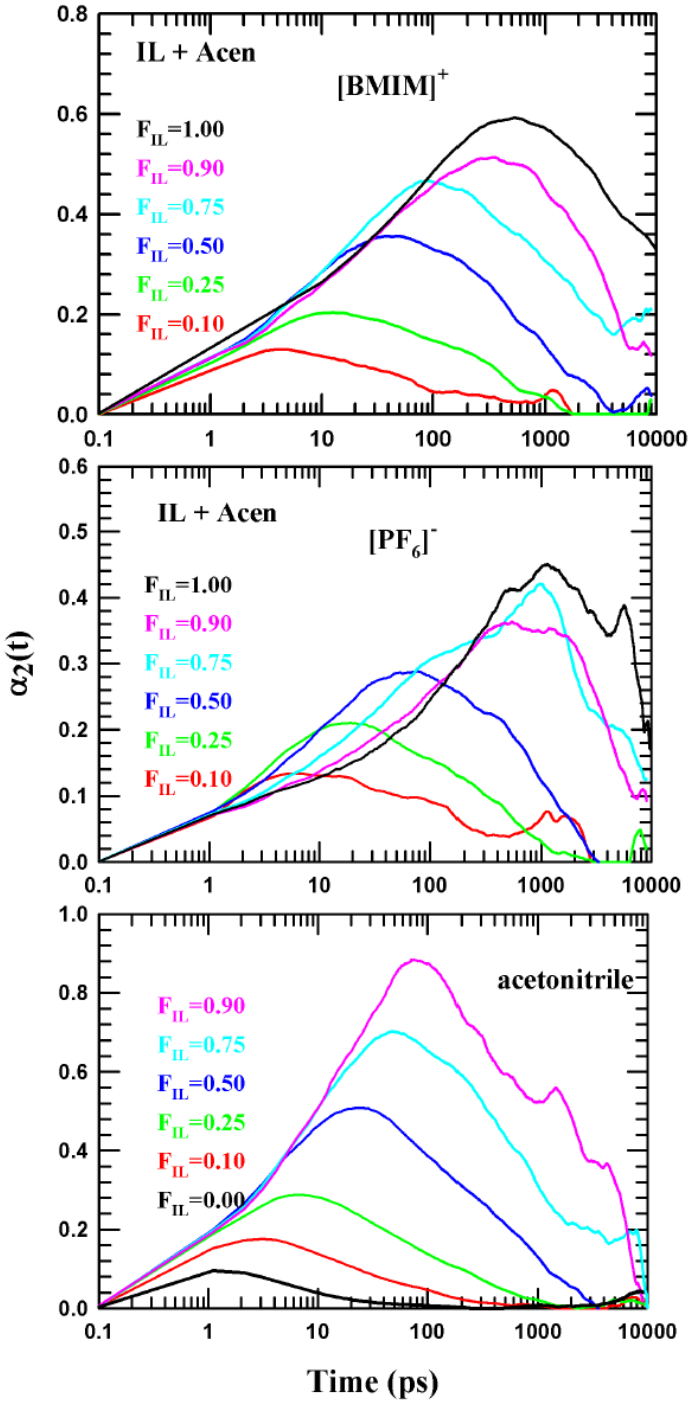

Figure 3.A.7: Composition dependent $\alpha_2(t)$ for $[BMIM]^+$, $[PF_6]^-$ and the three cosolvents in the binary mixture of (IL+Acen).

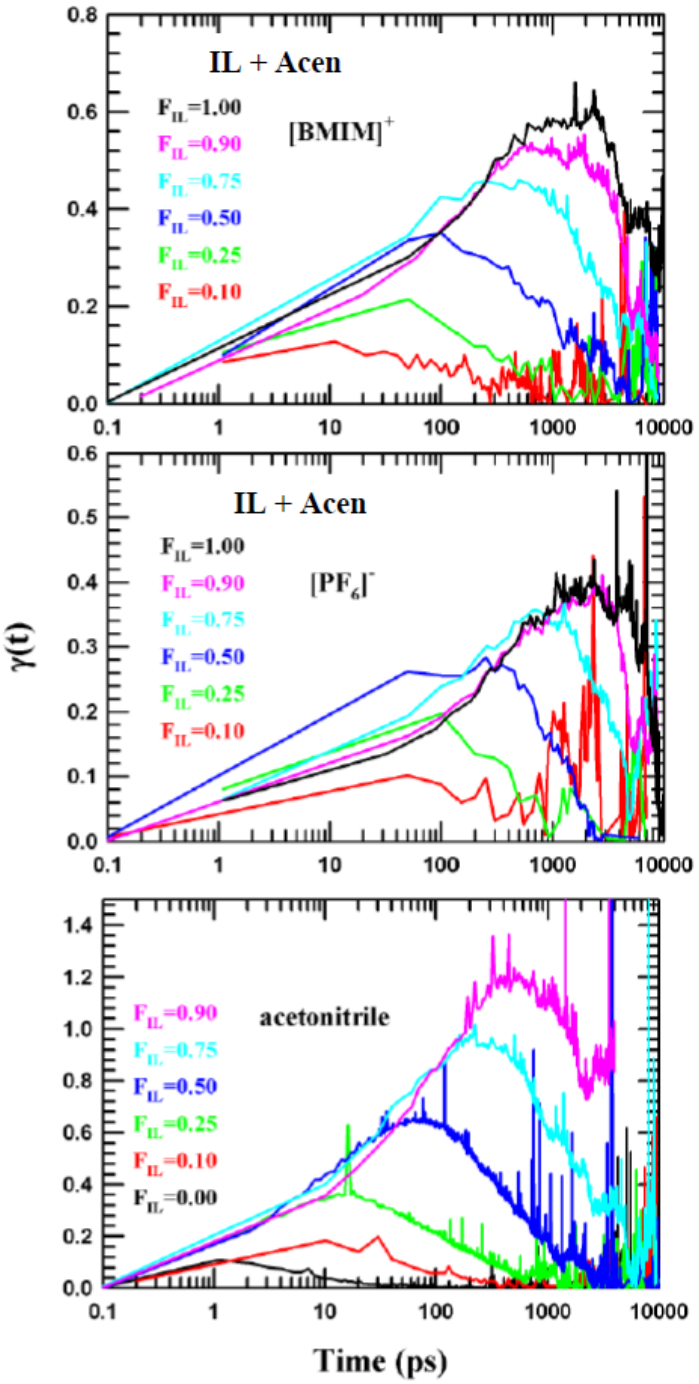

Figure 3.A.8: Composition dependent $\gamma(t)$ for $[BMIM]^+$, $[PF_6]^-$ and the three cosolvents in the binary mixture of (IL+Acen).

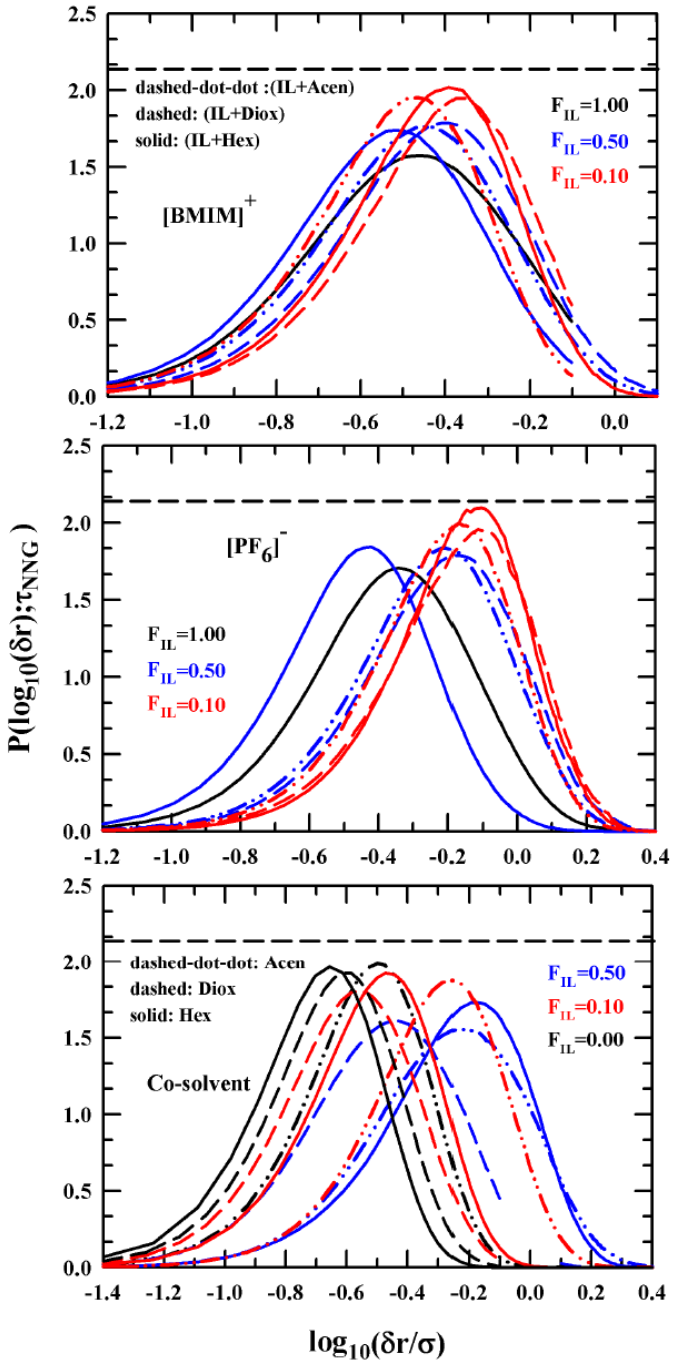

Figure 3.A.9: Cosolvent polarity dependence of simulated single particle displacement distribution, $P[log_{10}(\delta r); t = \tau_{NNG}]$ for the IL ions $[BMIM]^+$ (upper panel), $[PF_6]^-$ (middle panel) and three cosolvents (lower panel) in the three binary mixtures. Horizonal black line denotes the peak height (~2.13) for the Gaussian distribution of particle displacements.

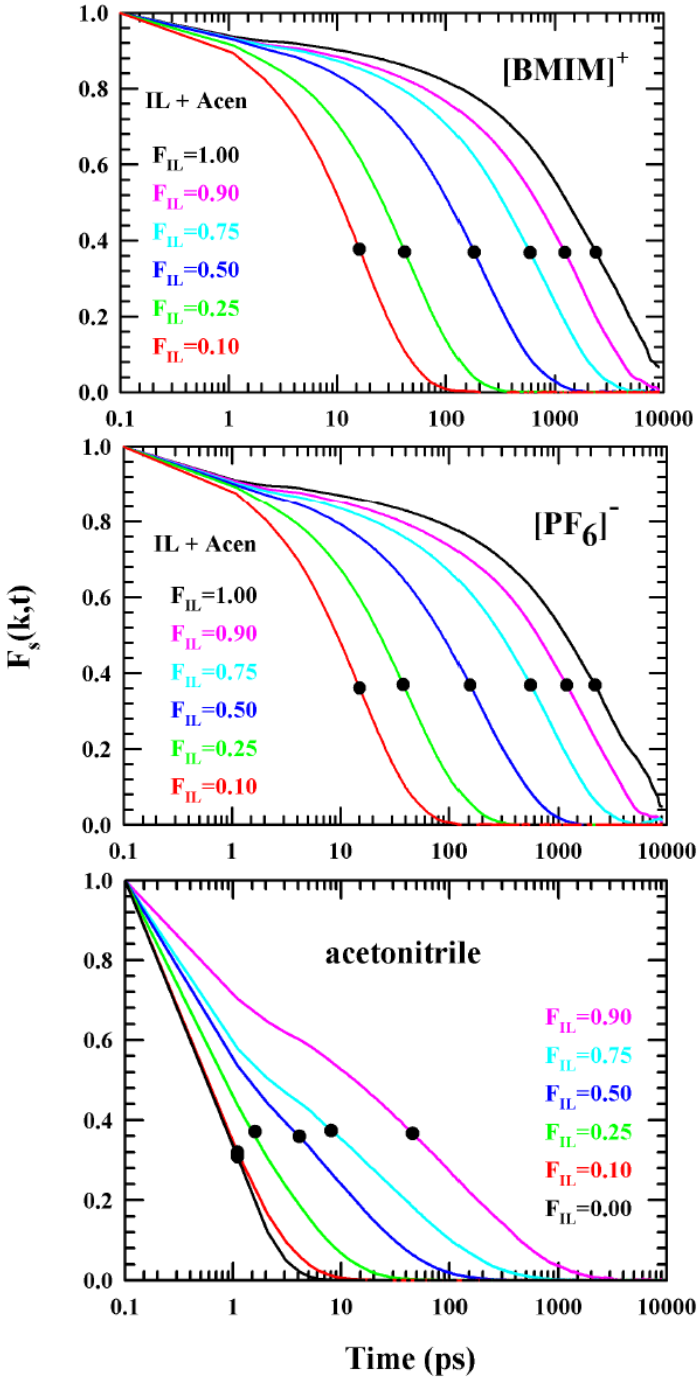

Figure 3.A.10: Composition dependent $F_s(k,t)$ for ions and cosolvents in (IL+Acen) mixture, various mole fractions are color coded. Note, k value corresponds to the nearest neighbor wave vector

Appendix 3.B

Table 3.B.1: Number of ion pairs and cosolvent molecules used in the simulation at different IL mole-fractions (F_{IL}).

F_{IL}	$[BMIM]^+$	$[PF_6]^-$	Cosolvent molecules
1.00	128	128	0
0.90	230	230	26
0.75	192	192	64
0.50	128	128	128
0.25	64	64	192
0.10	26	26	230
0.00	0	0	256

Table 3.B.2: Diffusion on-set time scales for the three binary mixtures at IL mole fraction F_{IL}=1.0, 0.50, 0.10, 0.0.

F_{IL}	$[BMIM]^+$ (ps)			$[PF_6]^-$ (ps)			Cosolvent (ps)		
	IL+Acen	**IL+Diox**	**IL+Hex**	**IL+Acen**	**IL+Diox**	**IL+Hex**	**IL+Acen**	**IL+Diox**	**IL+Hex**
1.0	7642	7642	7642	7458	7458	7458	-	-	-
0.5	966	1314	2366	955	1374	2433	337	789	2708
0.1	118	469	1512	150	414	1550	87	381	253
0.0	-	-	-	-	-	-	45	161	113

References

[1] M.D. Ediger, Annu. Rev. Phys. Chem. **51**, 99 (2000).

[2] R.S. Stein and H.C. Andersen, Phys. Rev. Lett. **101**, 267802 (2008).

[3] J.L. Doob, Ann. Math. 351 (1942).

[4] J. Hunger, A. Stoppa, S. Schrödle, G. Hefter, and R. Buchner, Chem. Phys. Chem. **10**, 723 (2009).

[5] A. Stoppa, J. Hunger, R. Buchner, G. Hefter, A. Thoman, and H. Helm, J. Phys. Chem. B **112**, 4854 (2008).

[6] O. Zech, J. Hunger, J.R. Sangoro, C. Iacob, F. Kremer, W. Kunz, and R. Buchner, Phys. Chem. Chem. Phys. **12**, 14341 (2010).

[7] X.-X. Zhang, M. Liang, N.P. Ernsting, and M. Maroncelli, J. Phys. Chem. B **117**, 4291 (2013).

[8] D. Roy, N. Patel, S. Conte, and M. Maroncelli, J. Phys. Chem. B **114**, 8410 (2010).

[9] H. Jin, X. Li, and M. Maroncelli, J. Phys. Chem. B **111**, 13473 (2007).

[10] J. Ingram, R. Moog, N. Ito, R. Biswas, and M. Maroncelli, J. Phys. Chem. B **107**, 5926 (2003).

[11] S. Arzhantsev, H. Jin, G.A. Baker, and M. Maroncelli, J. Phys. Chem. B **111**, 4978 (2007).

[12] A. Adhikari, K. Sahu, S. Dey, S. Ghosh, U. Mandal, and K. Bhattacharyya, J. Phys. Chem. B **111**, 12809 (2007).

[13] D.K. Sasmal, A.K. Mandal, T. Mondal, and K. Bhattacharyya, J. Phys. Chem. B **115**, 7781 (2011).

[14] H.K. Kashyap and R. Biswas, J. Phys. Chem. B **112**, 12431 (2008).

[15] H.K. Kashyap and R. Biswas, J. Phys. Chem. B **114**, 254 (2010).

[16] H.K. Kashyap and R. Biswas, J. Phys. Chem. B **114**, 16811 (2010).

[17] S. Daschakraborty and R. Biswas, Chem. Phys. Lett. **510**, 202 (2011).

[18] S. Daschakraborty and R. Biswas, Chem. Phys. Lett. **545**, 54 (2012).

[19] S. Daschakraborty and R. Biswas, J. Phys. Chem. B **118**, 1327 (2014).

[20] S. Daschakraborty, T. Pal, and R. Biswas, J. Chem. Phys. **139**, 164503 (2013).

[21] S. Daschakraborty and B. Ranjit, J. Phys. Chem. B **115**, 4011 (2011).

[22] T. Pal and R. Biswas, J. Chem. Phys. **141**, 164502 (2014).

[23] X.-X. Zhang, M. Liang, J. Hunger, R. Buchner, and M. Maroncelli, J. Phys. Chem. B **117**, 15356 (2013).

[24] M. Liang, X.-X. Zhang, A. Kaintz, N.P. Ernsting, and M. Maroncelli, J. Phys. Chem. B **118**, 1340 (2014).

[25] A. Stoppa, J. Hunger, G. Hefter, and R. Buchner, J. Phys. Chem. B **116**, 7509 (2012).

[26] S. Daschakraborty and R. Biswas, J. Chem. Phys. **144**, 104505 (2016).

[27] T. Pal and R. Biswas, J. Phys. Chem. B **119**, 15683 (2015).

[28] J. Rajbangshi, S. Banerjee, P.K. Ghorai, and R. Biswas, J. Mol. Liq. **317**, 113746 (2020).

[29] A. Paul and A. Samanta, J. Phys. Chem. B **112**, 947 (2008).

[30] S. Daschakraborty and R. Biswas, J. Chem. Phys. **140**, 014504 (2014).

[31] M. Khajehpour and J.F. Kauffman, J. Phys. Chem. A **104**, 9512 (2000).

[32] M.J. Abraham, T. Murtola, R. Schulz, S. Páll, J.C. Smith, B. Hess, and E. Lindahl, SoftwareX **1**, 19 (2015).

[33] S. Páll, M.J. Abraham, C. Kutzner, B. Hess, and E. Lindahl, in (Springer, 2014), pp. 3–27.

[34] H. Bekker, H. Berendsen, E. Dijkstra, S. Achterop, R. Van Drunen, D. Van der Spoel, A. Sijbers, H. Keegstra, B. Reitsma, and M. Renardus, in (World Scientific Singapore, 1993), pp. 252–256.

[35] B. Bhargava and S. Balasubramanian, J. Chem. Phys. **127**, 114510 (2007).

[36] W.L. Jorgensen, D.S. Maxwell, and J. Tirado-Rives, J. Am. Chem. Soc. **118**, 11225 (1996).

[37] G. Cinacchi, F. Ingrosso, and A. Tani, J. Phys. Chem. B **110**, 13633 (2006).

[38] J.N. Canongia Lopes, J. Deschamps, and A.A. Pádua, J. Phys. Chem. B **108**, 2038 (2004).

[39] O. Borodin, G.D. Smith, and R.L. Jaffe, J. Comput. Chem. **22**, 641 (2001).

[40] C. Caleman, P.J. van Maaren, M. Hong, J.S. Hub, L.T. Costa, and D. van der Spoel, J. Chem. Theory Comput. **8**, 61 (2012).

[41] K.A. Feenstra, B. Hess, and H.J. Berendsen, J. Comput. Chem. **20**, 786 (1999).

[42] M. Frisch, G. Trucks, H. Schlegel, G. Scuseria, M. Robb, J. Cheeseman, J. Montgomery Jr, T. Vreven, K. Kudin, and J. Burant, *Gaussian. Inc* Wallingford CT (2004).

[43] L. Martínez, R. Andrade, E.G. Birgin, and J.M. Martínez, J. Comput. Chem. **30**, 2157 (2009).

[44] G. Bussi, D. Donadio, and M. Parrinello, J. Chem. Phys. **126**, 014101 (2007).

[45] H.J. Berendsen, J. van Postma, W.F. van Gunsteren, A. DiNola, and J.R. Haak, J. Chem. Phys. **81**, 3684 (1984).

[46] R.W. Hockney, S. Goel, and J. Eastwood, J. Comput. Phys. **14**, 148 (1974).

[47] U. Essmann, L. Perera, M.L. Berkowitz, T. Darden, H. Lee, and L.G. Pedersen, J. Chem. Phys. **103**, 8577 (1995).

[48] B. Hess, H. Bekker, H.J. Berendsen, and J.G. Fraaije, J. Comput. Chem. **18**, 1463 (1997).

[49] W. Humphrey, A. Dalke, and K. Schulten, J. Mol. Graph. **14**, 33 (1996).

[50] Y. Hirata, J. Phys. Chem. A **106**, 2187 (2002).

[51] S.W. Siu, K. Pluhackova, and R.A. Böckmann, J. Chem. Theory Comput. **8**, 1459 (2012).

[52] H. Tokuda, K. Hayamizu, K. Ishii, M.A.B.H. Susan, and M. Watanabe, J. Phys. Chem. B **108**, 16593 (2004).

[53] R.L. Hurle and L.A. Woolf, J. Chem. Soc. Faraday Trans. 1 Phys. Chem. Condens. Phases **78**, 2233 (1982).

[54] M. Holz, S.R. Heil, and A. Sacco, Phys. Chem. Chem. Phys. **2**, 4740 (2000).

[55] K.R. Harris, J. Chem. Soc. Faraday Trans. 1 Phys. Chem. Condens. Phases **78**, 2265 (1982).

[56] T. Hofmann, D. Wallacher, M. Mayorova, R. Zorn, B. Frick, and P. Huber, J. Chem. Phys. **136**, 124505 (2012).

[57] T. Pal and R. Biswas, J. Chem. Phys. **141**, 104501 (2014).

[58] J.-P. Hansen and I.R. McDonald, *Theory of Simple Liquids* (Elsevier, 1990).

[59] F. Faupel, W. Frank, M.-P. Macht, H. Mehrer, V. Naundorf, K. Rätzke, H.R. Schober, S.K. Sharma, and H. Teichler, Rev. Mod. Phys. **75**, 237 (2003).

[60] J. Habasaki and K. Ngai, J. Non-Cryst. Solids **352**, 5170 (2006).

[61] T. Pal and R. Biswas, Theor. Chem. Acc. **132**, 1348 (2013).

[62] J.D. Eaves and D.R. Reichman, Proc. Natl. Acad. Sci. **106**, 15171 (2009).

[63] M.H. Kowsari and L. Tohidifar, J. Phys. Chem. B **120**, 10824 (2016).

[64] M.S. Shell, P.G. Debenedetti, and F.H. Stillinger, J. Phys. Condens. Matter **17**, S4035 (2005).

[65] K. Kim and S. Saito, J. Chem. Phys. **133**, 044511 (2010).

[66] E. Flenner and G. Szamel, Phys. Rev. E **72**, 011205 (2005).

[67] J.-P. Hansen, Phys. Stat. Mech. Its Appl. **201**, 138 (1993).

[68] D.R. Reichman, E. Rabani, and P.L. Geissler, J. Phys. Chem. B **109**, 14654 (2005).

[69] A.M. Puertas, M. Fuchs, and M.E. Cates, J. Chem. Phys. **121**, 2813 (2004).

[70] W.P. Krekelberg, V. Ganesan, and T.M. Truskett, J. Chem. Phys. **132**, 184503 (2010).

[71] G. Szamel and E. Flenner, Phys. Rev. E **74**, 021507 (2006).

[72] K. Kim and S. Saito, J. Chem. Phys. **138**, 12A506 (2013).

[73] N. Lačević, F.W. Starr, T. Schrøder, and S. Glotzer, J. Chem. Phys. **119**, 7372 (2003).

[74] S.C. Glotzer, J. Non-Cryst. Solids **274**, 342 (2000).

[75] C. Alba-Simionesco, B. Coasne, G. Dosseh, G. Dudziak, K. Gubbins, R. Radhakrishnan, and M. Sliwinska-Bartkowiak, J. Phys. Condens. Matter **18**, R15 (2006).

[76] F. Lindemann, Z Phys **11**, 609 (1910).

[77] S. Franz and G. Parisi, J. Phys. Condens. Matter **12**, 6335 (2000).

[78] C. Donati, S. Franz, S.C. Glotzer, and G. Parisi, J. Non-Cryst. Solids **307**, 215 (2002).

[79] C. Toninelli, M. Wyart, L. Berthier, G. Biroli, and J.-P. Bouchaud, Phys. Rev. E **71**, 041505 (2005).

Chapter 4

Heterogeneous Orientational Relaxations and Translation-Rotation Decoupling in (Choline Chloride + Urea) Deep Eutectic Solvents: Investigation Through Molecular Dynamics Simulations and Dielectric Relaxation Measurements

4.1 Introduction

Research studies carried out in the last couple of decades focussing on environmentally friendly yet efficient reaction media have suggested that ionic liquids (ILs)[1,2] and deep eutectic solvents (DESs)[2–9] possess appropriate physico-chemical properties for large-scale industrial applications, replacing a large body of common and hazardous organic solvents. DESs appear to have an edge over the ILs because of their less expensive, favourable handling and easy-to-transport features.[4,5,8,10] Application of deep eutectic solvents (DESs) in synthetic chemistry[11,12] and electrochemistry[13–15] as reaction media is increasing for their less toxicity, low vapor pressure and other desirable solvent features. Search for biodegradable reaction media[16] and therapeutic solvent matrices[17] have led to the generations of several important DESs. DESs are multi-component melts, providing a stable liquid phase at temperatures much below the melting temperatures of the individual components. These components are often organic compounds and inorganic salts and therefore, DESs can be either ionic[4,18–21] or nonionic,[22] depending upon the choice of the constituent components. This allows a wide window of choice for selecting components for engineering task-specific liquid solvents, ushering delight providing the much needed flexibility for engineering task-specific liquid solvents for carrying out reactions yielding tailored products. DESs are, therefore, not only capable of successfully addressing many of the critical environmental issues, but can also usher delight to the synthetic chemists for being able to create at will the required polarity and viscosity for carrying out reactions to yield the desired products. These systems are also rich and diverse in basic scientific aspects because of the ‘metastability’ arising from being in the liquid phase at temperatures lower than the melting temperatures of the individual components.

The signature of metastability has probably been reflected via the pronounced fractional viscosity dependence of relaxation rates at temperatures ~50-150 K above the respective thermodynamic glass transition temperatures for a variety of DESs.[18–36] This is striking because such a strong viscosity decoupling of relaxation rates is known to occur for deeply supercooled liquids near glass transition where spatial inhomogeneity is believed to characterize the liquid structure at such low temperatures.

In the class of ionic deep eutectics, a new set of DESs have been prepared by melting mixtures of appropriate mole or weight fractions of quaternary ammonium salts and neutral hydrogen bond donors. The biodegradable[37] and readily available nature of choline chloride ($OHCH_2CH_2N(CH_3)_3Cl$), a quaternary ammonium salt possessing similarities to the vitamin B complex-group, turns these particular systems quite promising for selection as one of the preferred constituent elements for the preparation of environmentally-benign DESs. As choline chloride based DESs,[8,9] have been already accepted as the green solvent systems,[38,39] they are extensively used in the field of organic synthesis,[40,41] gas absorption,[42] selective metal extraction[43] and electrochemistry.[44] Although there are many combinations available,[45–57] the most frequently studied DESs are composed of choline chloride and urea ($CH_3CO(NH_2)_2$).[9,31] The choline chloride based DESs has the melting temperature of 285 K, which is much lower than the individual melting temperatures of the constituents (choline chloride – 575 K and urea – 406 K).[31,39] This DES may therefore be called as a room temperature DES. The biocompatible choline chloride is an important ingredient in animal and poultry food industry.[58,59] Urea, on the other hand, is an important ingredient in fertilizer industry[60] and also plays an important role in microbial metabolism in aquatic systems.[61]

Although several physico-chemical properties, such as densities,[47] viscosities,[39,47,62] conductivity values[39] and molar heat capacities[63] of these chlorine chloride based DESs at various temperatures have already been reported, the interaction and dynamics of (choline chloride + urea) DESs have not been extensively explored yet. Structural analysis of choline chloride and urea DESs performed via molecular dynamics simulations has suggested stronger interaction between the hydrogen bond donor and chloride ion than the choline ion[64]. Several properties such as density, viscosity and surface tension have been reproduced for these DESs by using a new set of non-polarizable OPLS-AA interaction parameters.[65] Interestingly, the

pulsed field gradient NMR spectroscopic study[66] in choline chloride based DESs have proposed that the molecular diffusions do not follow the random walk model. Rather, they follow a jump mechanism which is expected for some DESs[33,34] and ionic liquids.[67–69] In addition, dynamic Stokes' shift and fluorescence anisotropy measurements[31] of (choline chloride + urea) DESs at various temperatures has suggested a departure from hydrodynamic viscosity dependence of solute solvation and rotation times, suggesting presence of dynamic heterogeneity in these DESs. This and the presence of spatial heterogeneity suggested by the excitation wavelength-dependence of steady state fluorescence emissions[31,70] strongly indicate the spatio-temporally heterogeneous nature of (choline chloride + urea) DESs.

However, the above inference on spatio-temporal heterogeneity of (choline chloride + urea) DESs is entirely based on steady state and time-resolved fluorescence measurements which require an external probe molecule as a reporter. Therefore, the real solution heterogeneity status may be different from what is being reported as both the heterogeneity length- and time-scales could be significantly modified by the diameter of the fluorescent probe molecule and its average excited state lifetime.[71–73] In such a situation, one either resorts to computer simulations for generating information on structure and dynamics of the system by employing model interaction potentials and makes an attempt to better understand the fluorescence spectroscopic data, or performs different but complementary experiments which do not require a foreign probe solute. Dielectric relaxation (DR)[74] measurements can directly probe the inherent orientational dynamics of the medium and thus can be used, in conjunction with viscosity measurements and hydrodynamic theory on rotational motion, to infer the structural and dynamical complexities of the system under study. DR measurements carried out earlier for several ionic acetamide DESs in the frequency window, $0.2 \leq \nu/GHz \leq 50$, have suggested a strong presence of dynamic heterogeneity.[27] Hence, we have first carried out molecular dynamics simulations of choline chloride and urea deep eutectic solvents (DESs) of general composition [f choline chloride + (1-f) urea] for f = 0.33 and 0.40 at six different temperatures in the temperature range $298 \leq T/K \leq 333$ for scrutinizing our earlier conclusions on this DES based on time-resolved fluorescence measurements. This simulation study is then followed up by performing DR measurements in the frequency window, $0.2 \leq \nu/GHz \leq 50$. Note this accessible frequency window does not allow us to discuss confidently about dynamics with timescales slower than a nanosecond and faster than a few picoseconds. Computer simulations, however, do not suffer from this lacunae, although the use of course-

grained model interaction potentials can generate, at best, a qualitative understanding of the relevant experimental data in terms of microscopic structure and dynamics.

4.2 Force Field and Simulation Details

All-atom molecular dynamics simulations of (choline chloride + urea) DESs at six different temperatures within the temperature regime $293 \leq T/K \leq 333$ at 0.33 mole fraction of urea were performed using GROMACS version 4.5.4.[75–77] To obtain the mole fraction f = 0.33 for the general composition, $[f\ \text{choline chloride} + (1-f)\ \text{urea}]$, 500 choline chloride pairs mixed with 1000 urea molecules were simulated. Here, the molecules interacted via the following OPLS-AA[65] interaction potential:

$$E_{bonds} = \sum_i k_{b,i}(r_i - r_{0,i})^2 \tag{4.1}$$

$$E_{angles} = \sum_i k_{\theta,i}(\theta_i - \theta_{0,i})^2 \tag{4.2}$$

$$E_{torsion} = \sum_i \left[\frac{1}{2}V_{1,i}(1 + cos\varphi_i) + \frac{1}{2}V_{2,i}(1 - cos2\varphi_i) + \frac{1}{2}V_{3,i}(1 + cos3\varphi_i) + \frac{1}{2}V_{4,i}(1 - cos4\varphi_i)\right] \tag{4.3}$$

$$E_{nonbond} = \sum_i \sum_{j>1} \left\{\frac{q_i q_j e^2}{r_{ij}} + 4\varepsilon_{ij}\left[\left(\frac{\sigma_{ij}}{r_{ij}}\right)^{12} - \left(\frac{\sigma_{ij}}{r_{ij}}\right)^{6}\right]\right\} \tag{4.4}$$

Here, the intramolecular bonded interactions include harmonic terms for bond stretching (with bond distance, r; equilibrium bond distance, r_0; bond force constant, k_b), angle stretching (with bond angle, θ; equilibrium bond angle, θ_0; angle force constant, k_θ), and V_1, V_2 and V_3 represent the Fourier coefficients. φ denotes the dihedral angle. The non-bonded interactions consist of Lennard-Jones (LJ) and Coulomb interactions, where LJ radii, potential well depth and the distance between the atoms are represented as σ_{ij}, ε_{ij} and r_{ij} respectively. q_i and q_j represent partial charges. In our simulations, the geometric combination rules have been employed for the Lennard-Jones coefficients, $\sigma_{ij} = \left(\sigma_{ii}\sigma_{jj}\right)^{1/2}$ and $\varepsilon_{ij} = \left(\varepsilon_{ii}\varepsilon_{jj}\right)^{1/2}$. The interaction parameters for choline chloride and urea molecules were taken from the OPLS-AA force field[65] parameters, which were employed to reproduce various experimental quantities like densities, heat capacities, surface tensions, and viscosities. The partial charges and

Lennard-Jones parameters of choline and urea are provided in Tables 4.B.1 and 4.B.2 (Appendix 4.B) respectively.

The initial configurations were built using the Packmol software[78] and energy minimized in GROMACS via using the steepest decent algorithm. Simulations were carried out in a cubic box employing the periodic boundary conditions. The cut-off radius for short-ranged interaction was set for 1.6 nm and the long-ranged electrostatic interaction was treated with Particle-Mesh Ewald (PME) summation.[79] Throughout the simulations, all the covalently bonded H-atoms were kept constrained using the LINCS algorithm[80] with order of 8. The energy optimized configurations were then equilibrated in the NPT ensemble for 15 ns at 1.0 bar pressure using a velocity rescaling thermostat[81] and Berendsen ensemble[82] with the relaxation times of 0.5 ps and 2.0 ps respectively. Equations of motions were solved by using the leapfrog algorithm[83] with a time step of 1 fs and the production run for all the simulations was for 100 ns in the NVT ensemble. The simulated trajectories were saved every after 0.1 ps for data analyses. For the calculations of continuous H-bond relaxation dynamics, separate trajectories were generated using the same ensemble with the pre-equilibrated trajectories and in this case, the trajectories were saved at a regular interval of 0.01 ps. For the visualization of the molecules during the simulation process, Visual Molecular Dynamics (VMD)[84] software was used.

For the fidelity check of the force field, we have compared the simulated densities of $[f\ \text{choline chloride} + (1-f)\ \text{urea}]$ DES at various temperatures with those obtained from experiments[85] and earlier simulations.[65] These comparisons are presented in Figure 4.A.1 (Appendix 4.A). It shows that the simulated densities agree well with the experimental values and predictions from earlier simulations[65] with the maximum deviation of ~ 4 %.

4.3 Experimental Details

4.3.1 Materials and Method

Choline chloride (≥99%, Sigma-Aldrich) and urea (≥99%, SRL) were vacuum-dried at room temperature for 48 h before use. Samples were prepared and relevant experiments were done in a tightly humidity-controlled environment. Further details regarding sample preparation could be found elsewhere as these DESs were already studied via fluorescence measurements.[58] Briefly, the sample vessels were sealed and heated slowly to ~340 K until it formed a clear melt. Then the DR measurements were carried out after allowing the samples to reach the desired temperatures.

4.3.2 DR Measurement Details*

The frequency dependent relative permittivity, $\varepsilon^*(\nu)$ can be represented by the following relation[86,87]

$$\varepsilon^*(\nu) = \varepsilon'(\nu) - \left[i\varepsilon''(\nu) + \frac{i\kappa}{2\pi\varepsilon_p\nu}\right] \tag{4.5}$$

Here, κ corresponds to the dc conductivity of the medium, and ε_p is the permittivity of free space. $\varepsilon'(\nu)$ represents the real part of the complex permittivity whose zero-frequency limit $\varepsilon_0 = \varepsilon(\nu \to 0)$ is the static dielectric constant of the medium. The permittivity at infinite frequency $\varepsilon_\infty = \varepsilon(\nu \to \infty)$ represents the contributions derived from intermolecular vibrations and intramolecular polarizability, which is occurred at the high frequency regime. As our present measurement is only accessible to the frequency 50 GHz, we are not allowed to probe separately the high frequency response arising from intramolecular polarizability and intermolecular vibrations. The reported ε_∞ includes this high frequency relaxation contributions, and it is larger than n_D^2 (n_D is refractive index). Note that in complete DR measurements, $\varepsilon_\infty \approx n_D^2$.

*Dielectric relaxation (DR) measurements have been done by Dr. Kallol Mukherjee at S N Bose National Centre for Basic Sciences, Kolkata, India. This is a part of our submitted paper in J. Rajbangshi, K. Mukherjee, and R. Biswas J. Phys. Chem. B (2021).

Approximately 8 mL of each mixture were subjected to DR measurements after proper thermal equilibration in an appropriately humidity-controlled environment. Temperature dependent DR measurements for these DESs were carried out by using a heating plate (MS-H-Pro from SCILOGEX, USA). We used a thermometer which was set at the same plane of the probe end to estimate the temperature more accurately and to avoid the misinterpretation of sample temperature which can arise from temperature gradient because of using a heating plate. During all measurements, desired experimental temperatures were sufficiently stable for conducting repeat (at least three) data acquisition.

4.4 Simulation Data Analyses: Statistical Mechanical Relations

The normalized reorientational time correlation function, $C_l(t)$[88] is defined as follows,

$$C_l(t) = \frac{\langle P_l[\vec{u}_i(t).\vec{u}_i(0)]\rangle}{\langle P_l[\vec{u}_i(0).\vec{u}_i(0)]\rangle} \quad (4.6)$$

where, P_l denotes the Legendre polynomial of rank l and $\vec{u}$ is the unit vector. For choline ion, the unit vector joins the O – H (-OH) atoms, and for urea it connects the N-atoms of the -NH_2 groups. According to the Debye's model of diffusive reorientation,[89,90] the reorientation correlation time for homogeneous systems is given by,

$$\tau_l = [l(l+1)D_R]^{-1} \quad (4.7)$$

where, D_R denotes the rotational diffusion co-efficient. If the angular diffusion occurs through Debye rotation, then $\langle\tau_1\rangle/\langle\tau_2\rangle = 3$ [89,90] suggests stochastic random orientational diffusion and the validity of the $l(l+1)$ law. However, a deviation from $\langle\tau_1\rangle/\langle\tau_2\rangle = 3$ may suggest presence of the orientational dynamic heterogeneity, which may be observed in slow viscous liquid systems.[91–94]

Because these DESs support formation of extensive intra- and inter-species H-bonding, the reorientational relaxation would surely involve breakage and formation of H-bonds. For this, the H-bond fluctuation dynamics has been monitored via two different H-bond relaxation functions; they are the continuous H-bond relaxation function, $S_{HB}(t)$, and the structural H-

bond relaxation function, $C_{HB}(t)$. The $S_{HB}(t)$[95–100] and $C_{HB}(t)$[95,96,98,100] are defined as follows,

$$S_{HB}(t) = \frac{\langle h(0)H(t)\rangle}{\langle h\rangle} \tag{4.8}$$

and, $$C_{HB}(t) = \frac{\langle h(0)h(t)\rangle}{\langle h\rangle} \tag{4.9}$$

Here, $H(t) = 1$ if the tagged pair of particles, for which $h(0)$ is calculated, remains continuously H-bonded until time t, or else zero. $S_{HB}(t)$ therefore, describes the probability of two participating molecules remaining H-bonded continuously for the duration t. when H-bonding between the participating molecules breaks down, it becomes zero. $C_{HB}(t)$, on the other hand, provides the time scale of reformation of H-bond (after being severed from the previous partner) after structural rearrangement through diffusion. As a result, $C_{HB}(t)$ is associated with structural relaxation and a translational diffusion timescale always associates with H-bond relaxation dynamics.

Translational motion of particles can be obtained from the center-of-mass mean square displacements (MSDs) via the following equation,[88,101,102]

$$\langle \delta r^2(t)\rangle = \langle N^{-1}\sum_{i=1}^{N}|\Delta r_i^c(0,t)|^2\rangle \tag{4.10}$$

Here, r_c^i represents the center-of-mass vector of particle i. The time dependencies of MSDs can be expressed as, $MSD \propto t^{\beta(t)}$, with

$$\beta(t) = \frac{d}{d[\ln(t)]}[ln\langle \Delta r^2(t)\rangle] \tag{4.11}$$

Simulated MSDs exhibit different regime. For example, the inertia-dominated regime at short time corresponds to $\beta = 2$, the sub-diffusive regime at intermediate time to $\beta < 1$, and diffusive regime at long time to $\beta = 1$.

The normalized velocity autocorrelation function (VACFs)[103,104], $C_v^N(t)$, is defined as

$$C_v^N(t) = \frac{\langle v(t).v(0)\rangle}{\langle v(0).v(0)\rangle} \tag{4.12}$$

which has been monitored for all the species to detect caging motion. This is important particularly for the chloride (Cl^-) ion as it may be involved interacting simultaneously with the choline cation and the urea molecules and remain caged for a duration longer than a neutral particle diffusing through a liquid medium. In addition, diffusion coefficient can be independently obtained from the simulated VACF via the relation,[88] $D = A\int_0^\infty dt\, C_v^N(t)$, with $A = \frac{k_B T}{m}$. This relation provides an alternative and useful route to estimate diffusion coefficients for high viscous systems where MSDs do not reach the diffusive regime ($\beta = 1$) at long time.

The translational component of the dynamic heterogeneity (DH) in slow viscous systems can be tracked via the calculations of the non-Gaussian ($\alpha_2(t)$)[105,106] and the new non-Gaussian ($\gamma(t)$)[101,107] parameters defined as,

$$\alpha_2(t) = \frac{3\langle \delta r^4(t)\rangle}{5\langle \delta r^2(t)\rangle^2} - 1 \tag{4.13}$$

and $$\gamma(t) = \frac{1}{3}\langle \delta r^2(t)\rangle \left\langle \frac{1}{\delta r^2(t)} \right\rangle - 1 \tag{4.14}$$

where, $\langle \delta r^2(t)\rangle = \left\langle \frac{1}{N}\sum_{i=1}^N |\Delta r_i(t)|^2 \right\rangle$ and $\left\langle \frac{1}{\delta r^2(t)} \right\rangle = \left\langle \frac{1}{N}\sum_{i=1}^N \frac{1}{|\Delta r_i(t)|^2} \right\rangle$. $\Delta r_i(t)$ is the displacement of i-th particle at time duration t from any arbitrary time origin. $\alpha_2(t)$ tracks those particles which execute displacements larger than those predicted from the Gaussian distribution of particle displacements, whereas the ($\gamma(t)$) connects to the particles that are associated with displacements smaller than the Gaussian prediction. The presence of $\left\langle \frac{1}{\delta r^2(t)} \right\rangle$ in the expression of $\gamma(t)$ ensures this and paves the way for emergence of an additional timescale much slower than the corresponding diffusion timescale.

The signature of the translational DH is then explored via simulating the self-intermediate scattering function,[88,107,108] $F_s(k,t)$, in the limit of nearest wavenumber ($k\sigma \rightarrow 2\pi, \sigma$ being the diameter):

$$F_s(k,t) = N^{-1}\sum_i \langle \cos k \times [r_i(t) - r_i(0)] \rangle \quad (4.15)$$

The 1/e decay time of $F_s(k,t)$ decay profile is connected to the α-relaxation time scale which associates with structural relaxation.

Four-point dynamic susceptibility, $\chi_4(k,t)$, provides information regarding the temporal correlations among the particles having similar mobility at two space points over a certain duration of time. $\chi_4(k,t)$[109–113] can be estimated from the fluctuations of $F_s(k \rightarrow 2\pi, t)$

$$\chi_4(k \rightarrow 2\pi, t) = N[\langle F_s(k \rightarrow 2\pi, t)^2 \rangle - \langle F_s(k \rightarrow 2\pi, t) \rangle^2] \quad (4.16)$$

Since the $\chi_4(k,t)$ tracks the correlation among particles with similar mobility for a certain duration of time, the maximum time over which the particles remain correlated can be designated as t_4^{max} and can be estimated from the time profile of the simulated $\chi_4(k,t)$.

4.5 Results and Discussion

4.5.1 Simulation Results

4.5.1.1 Reorientational Relaxations: Heterogeneity signatures and Translation-Rotation Decoupling

The simulated temperature dependent reorientational correlation functions, $C_1(t)$ and $C_2(t)$ for the choline ion (upper panel) and urea (lower panel) are shown respectively in Figure 4.1 and Figure 4.2. Also, representative comparison among different fit functions for both the decays $C_1(t)$ and $C_2(t)$ at T = 333K are provided in Figure 4.A.2 and Figure 4.A.3 (Appendix 4.A) respectively. These fits suggest that a sum of four exponentials are required to adequately describe these simulated reorientational correlation functions. Decay fit parameters summarized Table 4.1 and Table 4.2 suggest that these decays are spread over a wide range of timescales, covering from sub-picosecond to a few tens of nanoseconds time regimes.

In addition, average relaxation times in these tables indicate that both $C_1(t)$ and $C_2(t)$ decays are uniformly faster for the choline ions than for the neutral urea molecules at all the temperatures studied. As expected, (and also shown representatively in Figure 4.A.4 of Appendix 4.A), the $C_2(t)$ decays are faster than the $C_1(t)$ decays for both choline and urea. The temperature dependence follows the same trend as that of viscosity (see Table 4.B.3 of Appendix 4.B). Note that the simulated $C_1(t)$ relaxations at temperatures below 300 K account for nearly half of the total decays (within the 10 ns time window), suggesting the presence of a large slow component with timescales in the several tens of nanoseconds. The corresponding $C_2(t)$ relaxations within this time window account for ~60-70%, indicating the presence of a similar nanosecond component in these decays as well. Interestingly, such a slow component has also been observed in the simulated $C_l(t)$ decays for $[BMIM]^+$ in $[BMIM][PF_6]$ IL.[104]

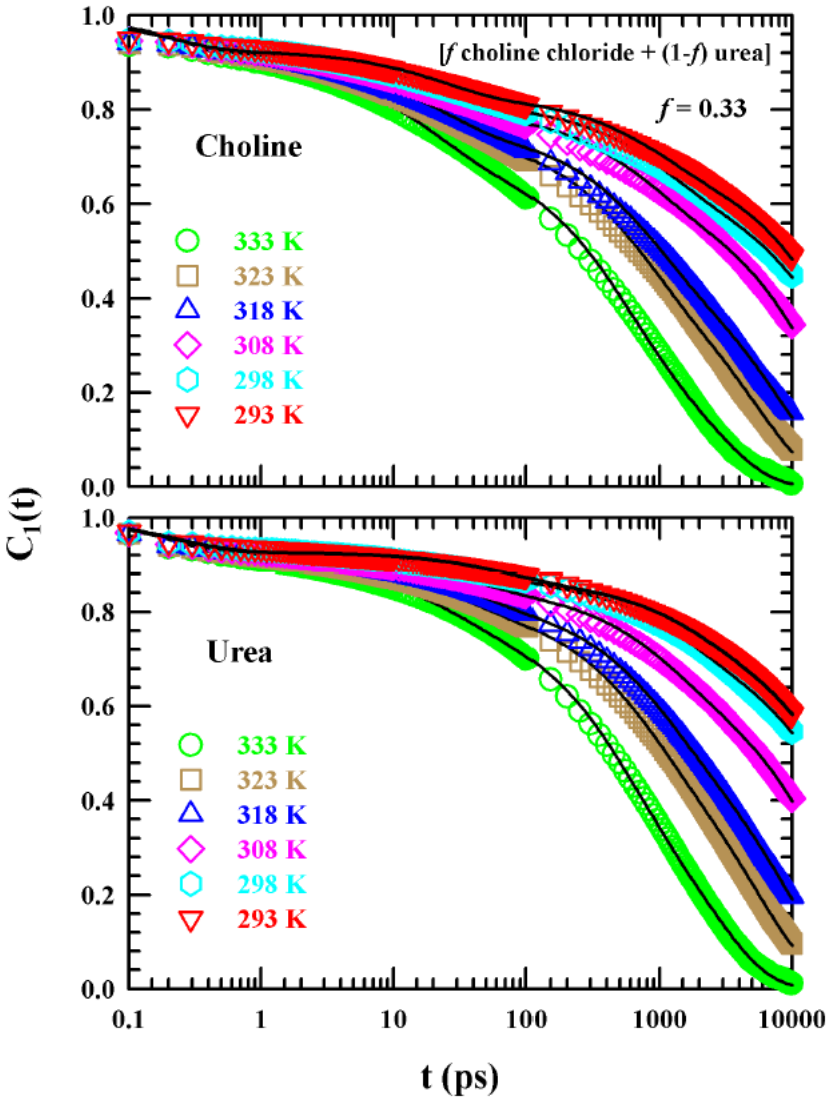

Figure 4.1: Temperature dependent simulated first rank (l=1) reorientational correlation functions, $C_1(t)$, for choline (upper panel) and urea (lower panel) in [f choline chloride + (1-f) urea] DES at f = 0.33. The lines going through the simulated data denote multi-exponential fits. Data for different temperatures are color coded.

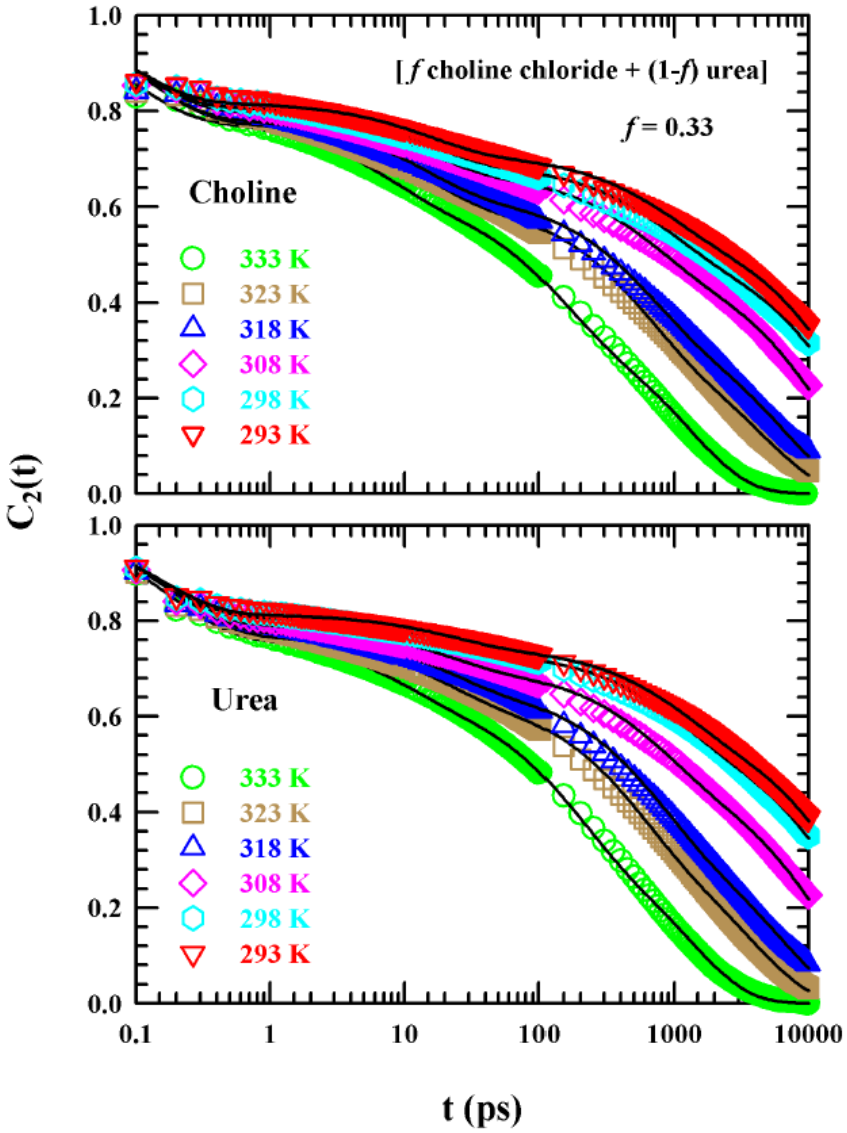

Figure 4.2: Temperature dependence of the simulated second rank (l=2) reorientational correlation functions, $C_2(t)$, for choline (upper panel) and urea (lower panel) in [f choline chloride + (1-f) urea] DES at f = 0.33. As before, the lines going through the simulated data represent multi-exponential fits. Data for different temperatures are color coded.

Multi-exponential fit parameters summarized in Table 4.1 and Table 4.2 show that the temperature dependent $C_l(t)$ decays for choline and urea are associated with four well-separated relaxation timescales - ~ 0.1-0.4 ps, ~ 10–70 ps, ~ 0.1 – 2 ns and ~ 1 – 40 ns. The sub-picosecond timescale is a typical signature of inertial collective dynamics of H-bonded systems at short times,[27,94] whereas the slow long-time decay with time constant of several tens of nanoseconds reflects a combined influence of high viscosity and H-bonding interactions.[27] The latter can be understood if we consider that the average reorientational correlation times become faster by a factor of ~20-30 for increasing the solution temperature from 293 K to 333 K while the DES viscosity decreases by a factor of ~12 for the same temperature change. The simultaneous participation of H-bonding in slowing down the reorientation dynamics is further reflected in the observation that the average reorientation times for urea is shortened by ~25-30 times in contrast to a decrease of ~20-25 times for choline. However, these two ultrafast and ultraslow timescales would not feature in the experimental DR data presented later in this chapter because of the limitation in the measurement window $(0.2 \leq \nu/GHz \leq 50)$. These timescales may appear when we explore the role of H-bond relaxation in the single particle collective reorientational dynamics through the simulations of the continuous and structural H-bond relaxation dynamics. In addition, we would like to mention here that a slow decay component with a time constant of a few tens of nanoseconds have been found earlier in the simulated reorientational relaxation in [BMIM] [PF_6] ionic liquid,[104] dynamic fluorescence anisotropy measurements employing a neutral dipolar solute in (acetamide + electrolyte) DESs[19] and in several ILs.[114] The presence of the other two reorientational relaxation time constants, ~ 10–70 ps and ~ 0.1 – 2 ns, may appear in our DR measurements as they are likely to be detected in the measurement window employed. This experimental verification is critically important for verification of the model potentials to represent the DES components in the present simulation study.

Table 4.1: Multi-exponential fit parameters for the first rank (l=1) $C_1(t)$, for choline and urea in the [f choline chloride + (1-f) urea] DESs for f = 0.33 at various temperatures.

T(K)	a_1	τ_1 (ps)	a_2	τ_2 (ps)	a_3	τ_3 (ps)	a_4	τ_4 (ps)	$\langle\tau\rangle$ (ps)[a]
Choline									
293	0.08	0.2	0.09	23	0.15	909	0.68	29295	20038
298	0.08	0.2	0.11	23	0.18	1000	0.63	28083	17971
308	0.08	0.3	0.12	21	0.18	769	0.62	16773	10405
318	0.10	0.3	0.14	21	0.27	769	0.49	10000	5090
323	0.10	0.3	0.15	20	0.28	625	0.47	5000	2513
333	0.11	0.4	0.19	19	0.34	454	0.36	2500	1057
Urea									
293	0.07	0.2	0.06	69	0.12	1667	0.75	39479	29823
298	0.08	0.2	0.05	47	0.15	1429	0.72	35185	25606
308	0.08	0.3	0.07	39	0.19	1111	0.66	19751	13259
318	0.09	0.3	0.09	39	0.26	909	0.56	10000	5863
323	0.09	0.3	0.10	30	0.26	714	0.55	5000	2925
333	0.10	0.3	0.11	24	0.33	435	0.46	2500	1294

[a] Average reorientational correlation time, $\langle\tau\rangle = \sum_i a_i\tau_i$ with $\sum_i a_i = 1$.

Table 4.2: Multi-exponential fit parameters describing the simulated second rank (*l*=2) reorientation correlation functions, $C_2(t)$, for choline and urea in the [*f* choline chloride + (1-*f*) urea] DESs for *f* = 0.33 at various temperatures.

T(K)	a_1	τ_1 (ps)	a_2	τ_2 (ps)	a_3	τ_3 (ps)	a_4	τ_4 (ps)	$\langle\tau\rangle$ (ps)[b]
Choline									
293	0.18	0.1	0.11	15	0.16	833	0.55	21027	11754
298	0.19	0.1	0.12	14	0.18	833	0.51	19750	10364
308	0.20	0.1	0.13	14	0.19	625	0.48	12684	6223
318	0.21	0.1	0.16	14	0.27	588	0.36	5000	1963
323	0.22	0.1	0.17	13	0.29	555	0.32	5000	1772
333	0.22	0.1	0.16	7	0.26	127	0.36	1250	484
Urea									
293	0.19	0.2	0.07	22	0.17	1111	0.58	24090	14082
298	0.19	0.2	0.07	20	0.18	1000	0.56	20879	11794
308	0.20	0.2	0.09	19	0.22	769	0.49	12479	6229
318	0.22	0.2	0.12	20	0.29	667	0.37	5000	2042
323	0.23	0.2	0.13	17	0.29	476	0.35	3333	1319
333	0.23	0.2	0.13	9	0.29	159	0.35	1250	489

[b] Average reorientational correlation time scale, $\langle\tau\rangle = \sum_i a_i\tau_i$ with $\sum_i a_i = 1$.

Next, we investigate the translation-rotation decoupling in this DES. The celebrated translation-rotation decoupling is known to occur in deeply supercooled systems where translational diffusion decouples from the medium viscosity much earlier than the rotational diffusion. This decoupling in supercooled liquids, however, take place at viscosity values that are several orders of magnitudes higher than the viscosity range ($1500 > \eta/cP > 50$) covered by the present DES at the temperatures studied, $293 \leq T/K \leq 333$ (see Table 4.B.3, Appendix 4.B). The dynamical heterogeneity in the simulated reorientational relaxations is suggested by the violation of the Debye's $l(l+1)$ law[115,116] through the prediction of $\langle\tau_1\rangle/\langle\tau_2\rangle < 3$ for angular displacements of both the choline ions and the urea molecules at each of the temperatures studied (see Table 4.B.4, Appendix 4.B). For investigating the heterogeneity in more detail, we examined the translation-rotation decoupling for which we needed to simulate the translational diffusion coefficients for both choline and urea. It was found earlier[65] that translational diffusion coefficients estimated from the simulated MSDs were not reliable, particularly at lower temperatures (higher solution viscosities), because those MSDs did not (as also in the present study shown later) achieve the desired linear time dependence (that is, $\beta = 1$ for MSD $\propto t^{\beta}$) at long time. We have therefore calculated the translational diffusion coefficients through the VACF route. The predicted diffusion coefficients are shown in Table 4.3 and the simulated VACFs are provided in Figure 4.A.5 (Appendix 4.A). A comparison between the simulated values and those from the pulsed field gradient nuclear magnetic resonance (PFGNMR) measurements[66] (see Table 4.3) suggests qualitative agreement between simulations and experiments although one should keep in mind that inelastic neutron scattering measurements may report diffusion coefficient values smaller than those from the PFGNMR experiments.[117,118]

Table 4.3: Comparison of translational diffusion co-efficients between the simulated values (via the VACF route) and those from PFGNMR measurements for choline, chloride and urea in [*f* choline chloride + (1-*f*) urea] DESs for *f*=0.33 at various temperatures. Measured diffusion co-efficient values are provided in parentheses. The ratio between the experimental and simulated D values indicate the quality of agreement.

T(K)	D_{CHOL^+} $(\times 10^{-11} m^2/s)$	D_{Cl^-} $(\times 10^{-11} m^2/s)$	D_{urea} $(\times 10^{-11} m^2/s)$	$\frac{D_{Exp}}{D_{Simu}}$	
				Choline	Urea
293	0.45 (0.26 [b])	1.38	0.78 (0.49 [b])	0.58	0.63
298	0.48 (0.35 [a])	1.45	0.84 (0.66 [a])	0.73	0.78
308	0.43 (0.70 [a])	1.38	0.81 (1.24 [a])	1.63	1.53
318	0.55 (1.25 [a])	1.52	0.92 (2.16 [a])	2.27	2.34
323	0.57 (1.64 [a])	1.55	0.95 (2.73 [a])	2.87	2.87
333	0.60 (2.89 [b])	1.61	0.97 (4.62 [b])	4.82	4.76

[a] Experimental diffusion co-efficients from PFGNMR measurements.

[b] Diffusion co-efficients obtained from linear fitting of the PFGNMR data.

In Figure 4.3 we show the ratio of for homogeneous liquids where the hydrodynamic relations are valid for both the rotational and the translational diffusions of a particle, the rank (l) dependence of the translation-rotation decoupling can be expressed as,

$$\frac{\langle \tau_l \rangle}{\tau_{trans}} = \frac{fc}{3 \times l(l+1)} \tag{4.17}$$

employing $\tau_{trans} = 4r^2/D_{trans}$, $\langle \tau_l \rangle = 1/[l(l+1) \times D_{rot}]$, $D_{trans} = k_B T/6\pi\eta r$, $D_{rot} = k_B T/8\pi\eta r^3 fc$, with $k_B T$ denoting the Boltzmann constant times the absolute temperature and r the radius of the diffusor. f and c represent respectively the shape factor and coupling parameter for aspherical particles. For spherical diffusor, f and c are taken as unity. Notice that $\langle \tau_l \rangle/\tau_{trans}$ is independent of both the diffusor radius and the viscosity of the diffusing medium, and becomes equal to 0.167 for $l = 1$ and 0.055 for $l = 2$ for spherical diffusors. Figure 4.3 shows the simulated ratio, $\langle \tau_l \rangle/\tau_{trans}$, for both choline and urea at different temperatures considered. As expected, the extent of decoupling is larger at lower temperatures (higher viscosities) for both the ranks. Interestingly, the first rank ($l = 1$) reorientations of both urea and choline exhibit stronger decoupling compared to their second rank ($l = 2$) reorientations. This can be understood by considering that the first rank reorientation relaxations correspond to an angular displacement of 90º and are therefore exposed to stronger medium frictional resistance than that experienced by the second rank ($l = 2$) reorientation dynamics which correspond to an angular diffusion of ~55º. As the solution viscosity decreases upon rising the temperature, the extent of decoupling reduces and the ratio, $\langle \tau_l \rangle/\tau_{trans}$, finally achieves the corresponding hydrodynamic limiting values, $1/6$ for $l = 1$ and $1/18$ for $l = 2$. Figure 4.A.6 (Appendix 4.A) shows that both urea and choline can be approximated as oblate spheroids with f = 0.61 and 0.64 and c = 0.78 and 0.6, respectively. [119–121] Inclusion of shape factors and coupling parameters for choline and urea in the above equation then modifies the hydrodynamic limiting values for spherical rotors for both the ranks. Consequently, the simulated values of $\langle \tau_l \rangle/\tau_{trans}$ at 333K agree quite well to the modified theoretical predictions.

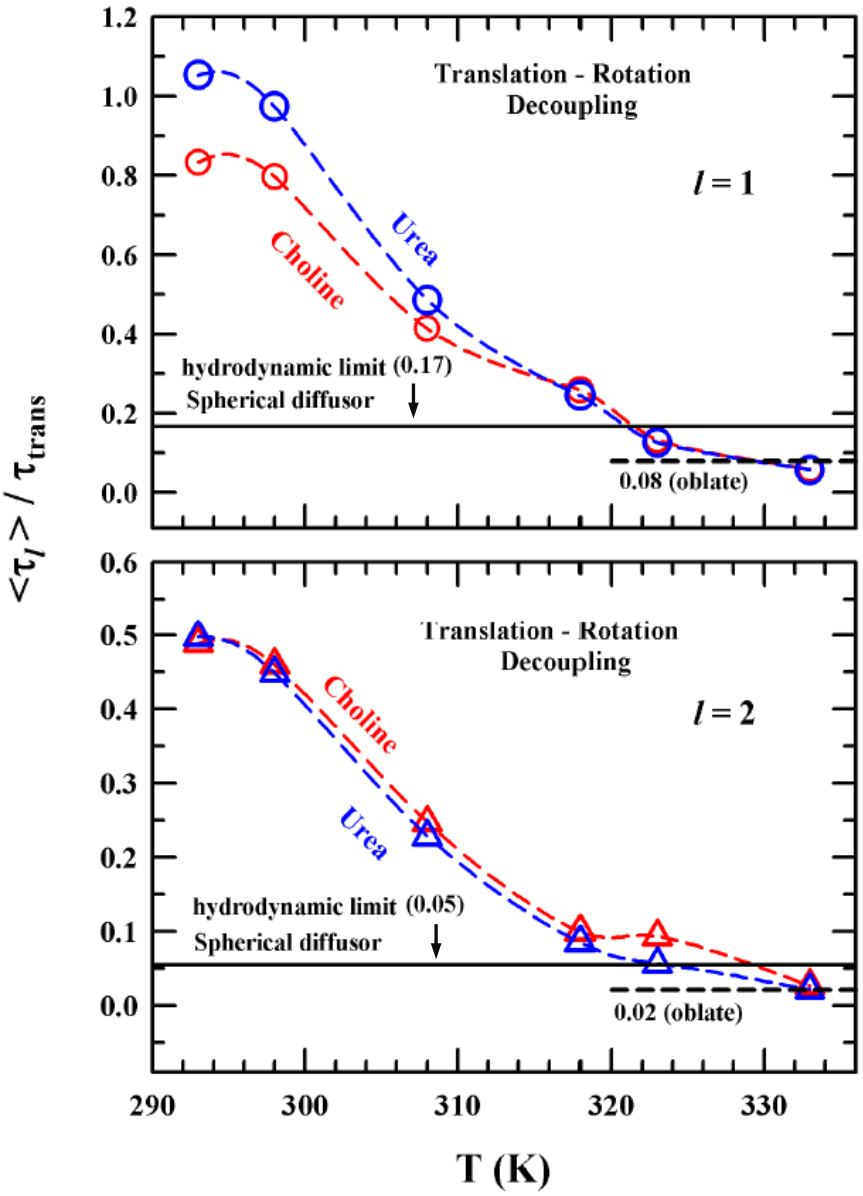

Figure 4.3: Ratio between the average rank dependent reorientation times ($\langle\tau_l\rangle$) and the translational diffusion time scales (τ_{trans}), $\frac{\langle\tau_l\rangle}{\tau_{trans}}$, for choline and urea are shown as a function of temperature. Results for both the ranks, l = 1 and 2, are shown. Note the hydrodynamic limit for a spherical diffusor is indicated by the black solid line, whereas that for an oblate particle is indicated by black broken line. Also, the limiting values are mentioned.

4.5.1.2 H-bonding Relaxations: Connection to Reorientational Relaxations

It is expected that the reorientational relaxations in (choline chloride + urea) DES would involve H-bond relaxations because this system supports extensive inter-species H-bonding. This allows the H-bond relaxations, particularly the structural H-bond relaxations, to possess relaxation timescales similar to those already found in reorientational relaxations. We have followed here both the continuous (S_{HB} (t)) and the structural (C_{HB} (t)) H-bond relaxations for the choline-chloride and chloride-urea pairs. Note here that we have monitored the fluctuation dynamics of the H-bond that had formed between the chloride ion and the hydroxyl hydrogen of the -CH_2OH group of the choline ion, and that between the chloride ion and the amide hydrogens (-NH_2) of the urea molecule. The temperature dependent S_{HB} (t) decays are shown in Figure 4.A.7 (Appendix 4.A) and the corresponding multi-exponential fit parameters summarized in Table 4.B.5 (Appendix 4.B). It is evident from Table 4.B.5 that the average continuous H-bond lifetimes do not show any temperature dependence and are in the sub-picosecond regime. In addition, the continuous H-bond lifetime for choline and chloride pair is nearly twice as long as that between urea and chloride pair. The structural H-bond relaxation dynamics (C_{HB} (t)), on the other hand, is much slower and spread over sub-picosecond to several tens of nanoseconds. This is shown in Figure 4.4 and the corresponding multi-exponential fit parameters are provided in Table 4.4. A representative comparison of various fit functions for the $C_{HB}(t)$ relaxation of chloride-choline H-bond pair is provided in Figure 4.A.8 (Appendix 4.A**)**, which suggests that these $C_{HB}(t)$ decays require multi-exponential fits for adequate descriptions. Interestingly, the sub-100 ps and sub-nanosecond timescales appearing here have also been found in the corresponding $C_l(t)$ decays. This is natural because in extensively H-bonded systems such as this one, reorientation dynamics involves breakage and reformation of multiple H-bonds. The extremely slow relaxation timescale that, depending upon DES temperature, vary between a few nanoseconds to a few tens of nanoseconds is connected to the particle centre-of-mass diffusion. This can be verified by estimating the translational diffusion timescale, τ_{trans}, for any of the molecules in these H-bonded pairs. For example, τ_{trans} for choline and urea at 293 K respectively are ~ 24 ns, and ~28 ns, using the respective molecular diameters summarized in Table 4.B.6 (Appendix 4.B) and the simulated translational diffusion coefficients (see Table 4.3). These values correspond well with the slowest timescales (~30 - 40 ns) associated with the C_{HB} (t) decays. A similar observation was made earlier for other DESs as well.[28,122]

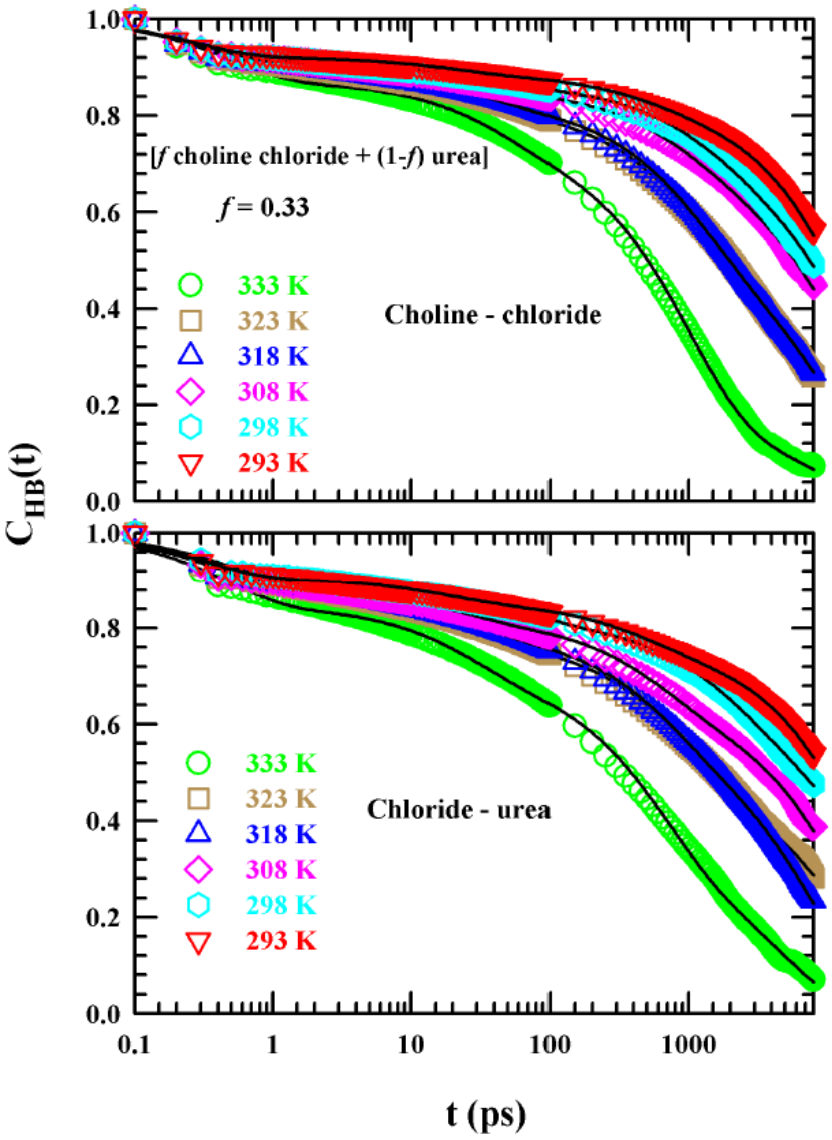

Figure 4.4: Temperature dependence of the **s**imulated decays of the structural H-bond relaxation functions, $C_{HB}(t)$, for choline – chloride (upper panel) and chloride – urea (lower panel) H-bonds in [*f* choline chloride + (1-*f*) urea] DES at *f*=0.33. Here, the symbols and solid lines denote the simulations and the fits respectively.

Table 4.4: Multi-exponential fit parameters for the simulated H-bond relaxations, $C_{HB}(t)$, for choline - chloride and chloride - urea pairs in [*f* choline chloride + (1-*f*) urea] DESs for $f = 0.33$ at various temperatures.

T(K)	a_1	τ_1 (ps)	a_2	τ_2 (ps)	a_3	τ_3 (ps)	a_4	τ_4 (ps)	$\langle\tau\rangle$ (ps)[a]
Choline - chloride									
293	0.08	0.3	0.03	19.3	0.06	526	0.83	19853	16510
298	0.09	0.3	0.05	31.2	0.13	1429	0.73	19755	14608
308	0.09	0.3	0.05	30.4	0.15	1000	0.71	16830	12101
318	0.1	0.4	0.07	32.5	0.29	1111	0.54	11387	6473
323	0.11	0.4	0.08	35.3	0.26	1000	0.55	10255	5903
333	0.13	0.5	0.13	42.7	0.57	1000	0.17	10000	2276
Chloride - urea									
293	0.1	0.3	0.05	17.5	0.09	454	0.76	22055	16838
298	0.1	0.5	0.08	59.9	0.19	2000	0.63	27980	18012
308	0.1	0.4	0.08	20.7	0.18	588	0.64	15165	9813
318	0.12	0.5	0.09	24.5	0.21	667	0.58	10000	5942
323	0.13	0.5	0.1	31	0.28	909	0.49	14830	7524
333	0.15	0.5	0.14	26.3	0.38	588	0.33	5000	1877

[a] Average reorientational correlation time scale, $\langle\tau\rangle = \sum_i a_i\tau_i$ with $\sum_i a_i = 1$

4.5.1.3 Mean Square Displacements (MSDs): First Indication of Translational Heterogeneity

Translational motions of all the particles in the [*f* choline chloride + (1-*f*) urea] DES at $f = 0.33$ were tracked via the center-of-mass MSDs, $\langle|\Delta r(t)|^2\rangle$, at various temperatures. Representative simulation data are shown in the upper panel of Figure 4.5. What strikes most in this panel is that the average displacement $\sqrt{\langle|\Delta r(t)|^2\rangle}$ executed by any of these species (urea, choline or chloride) at 293 K is $\leq$ 1 Å even after a nanosecond. This amounts to ~15-25% of their respective diameters and suggests 'rattling-in-a-cage' motion. What is even more interesting is that the simulated MSDs at 293 K for none of these species have reached the diffusive limit ($\langle|\Delta r(t)|^2\rangle \propto t^{\beta(t)}, \beta = 1$ at $t \to \infty$) even after ~10 ns. Note also that chloride is the slowest among these three different species and has executed ~1 Å average displacement in ~10 ns. This prolonged sub-diffusive behaviour ($\beta < 1$) is an indication of heterogeneous translational dynamics in this DES which, upon increasing temperature, undergoes partial homogenization. This is demonstrated in the second panel where $\beta(t)$ obtained from Eq. 4.11 is shown as a function of time for these three species. Clearly, $\beta \neq 1$ even after 50 ns for any of these species at 293 K. The span of the sub-diffusive region is substantially reduced at 333K, reflecting temperature-induced partial removal of solution heterogeneity.

This dramatic slowdown of chloride, urea and choline originates from the extensive interspecies interactions. This can be visualized, for example, from the three-dimensional arrangement of choline and chloride ion densities around a urea molecule in this DES by looking at the spatial distribution functions (SDFs). This is shown in Figure 4.A.9 (Appendix 4.A). Also, the simulated $C_v^N(t)$ for urea, choline and chloride ions at two temperatures 293 K and 333 K already presented in Figure 4.A.5 (Appendix 4.A) clearly indicate that the VACFs for chloride ion are different from those for choline ion and urea molecule, and the chloride VACFs enter into the negative region much earlier compared to the other particles. In addition, the chloride VACFs are more structured with relatively larger negative amplitudes than the VACFs for the other two species. The larger negative amplitude may be interpreted as more pronounced rattling in cage,[88,123] making the DES dynamics even more heterogeneous.

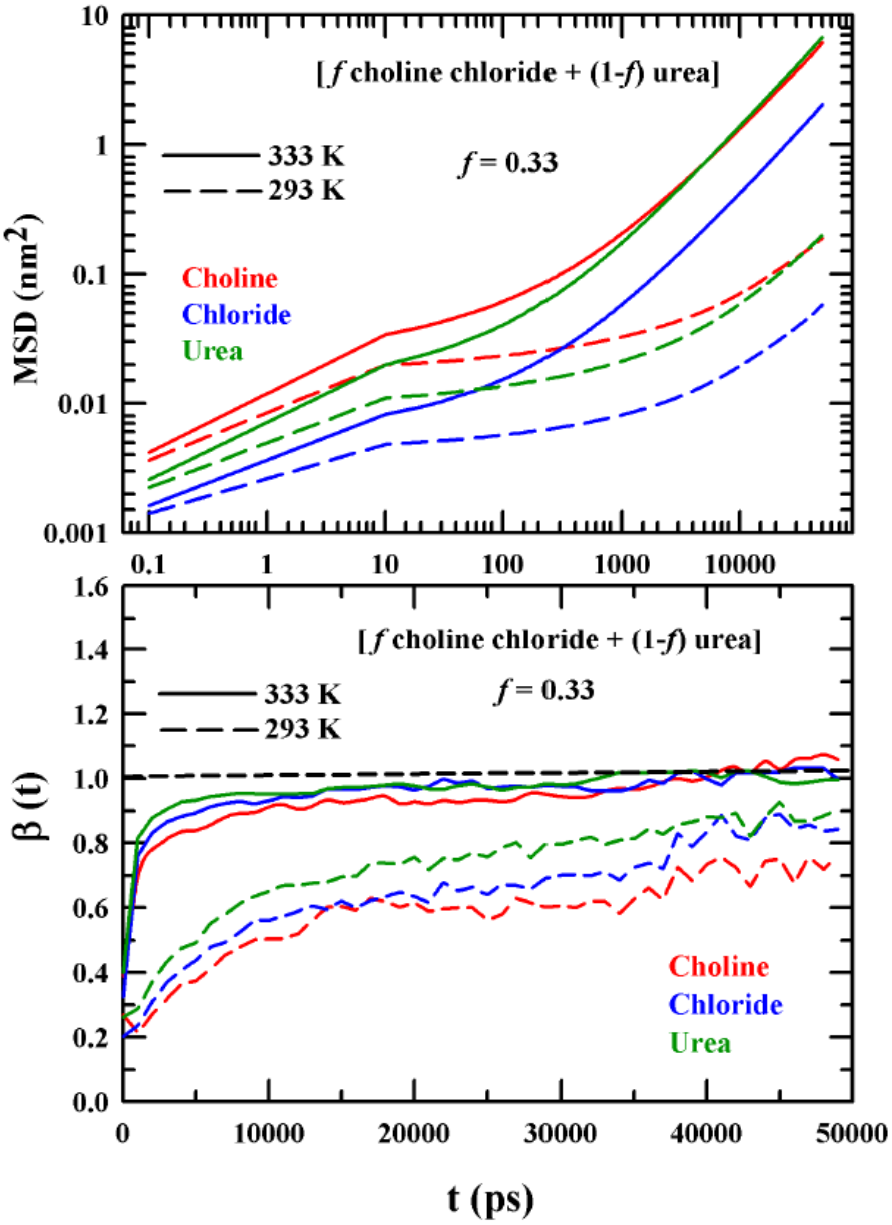

Figure 4.5: Simulated centre-of-mass MSDs, $\langle|\Delta r(t)|^2\rangle$, (upper panel) for of choline, chloride and urea in [*f* choline chloride + (1-*f*) urea] DES for f = 0.33 at temperatures 293 and 333 K. The time dependence of the corresponding $\beta(t)$ in the relation, $\langle|\Delta r(t)|^2\rangle \propto t^{\beta(t)}$, for choline, choline, chloride and urea are shown in the lower panel.

4.5.1.4 Heterogeneity in Translational Dynamics: Reflection Through Non-Gaussian Time Scales

The heterogeneity information contained in the sub-diffusive behaviour of MSDs shown above can be further processed in extracting timescales that are in addition to the collisional and diffusive timescales characterizing dynamically homogeneous systems. As already discussed, we have estimated these timescales via calculating the non-Gaussian and new non-Gaussian parameters, $\alpha_2(t)$ and $\gamma(t)$, respectively. The peak positions on time axis of $\alpha_2(t)$ versus time and $\gamma(t)$ versus time curves provide estimates of those additional timescales in heterogeneous systems - the non-Gaussian (τ_{NG}) and the new non-Gaussian (τ_{NNG}) times. For homogeneous liquids at high temperature where particle motions can be approximated as harmonic vibrations,[105] the peak value of the non-Gaussian parameter, $\alpha_2^{peak}(t) \sim 0.2$ at the sub-diffusive regime (intermediate time) of the relevant MSDs, whereas $\alpha_2(t) = 0$ at both $t \to 0$ and $t \to \infty$. The upper panel of Figure 4.6 represents the simulated $\alpha_2(t)$ for choline ion and urea molecule in these DESs for f = 0.33 at 293 and 333 K. Notice that $\alpha_2^{peak}(t) > 0.2$ for both urea and choline even at 333 K which reinforces the view of the dynamics being significantly heterogeneous in character. The DH timescales, τ_{NG}, are faster at 333 K than at 293 K and appear in the 0.2 – 0.5 ns range, while those at 293 K are much slower and cannot even be identified within the time-window shown here (see Table 4.B.7, Appendix 4.B). The new non-Gaussian timescales (τ_{NNG}) for urea and choline ion have been obtained from the simulated $\gamma(t)$ profiles and are shown the in lower panel of Figure 4.6. The temperature dependence of $\gamma(t)$ is similar to that for $\alpha_2(t)$ but timescales are much longer. For example, τ_{NNG} for these species at these temperatures would be in ≥ 10 ns range (see Table 4.B.7, Appendix 4.B). The large difference between τ_{NG} and τ_{NNG}, particularly at the lower temperature is a reflection of relatively stronger heterogenous character of the relevant particle motions in this DES. Simulations of ionic liquids had shown this feature earlier as well.[101,102] Interestingly, these DH time scales show a correlation with the slow time constants found in the dynamic Stokes shift and fluorescence anisotropy measurements of these DESs using an external solute.[31] Such correlation has also been observed in ionic liquids[124] and in binary mixtures, like cycloether/water,[125] and trehalose/glycerol.[126]

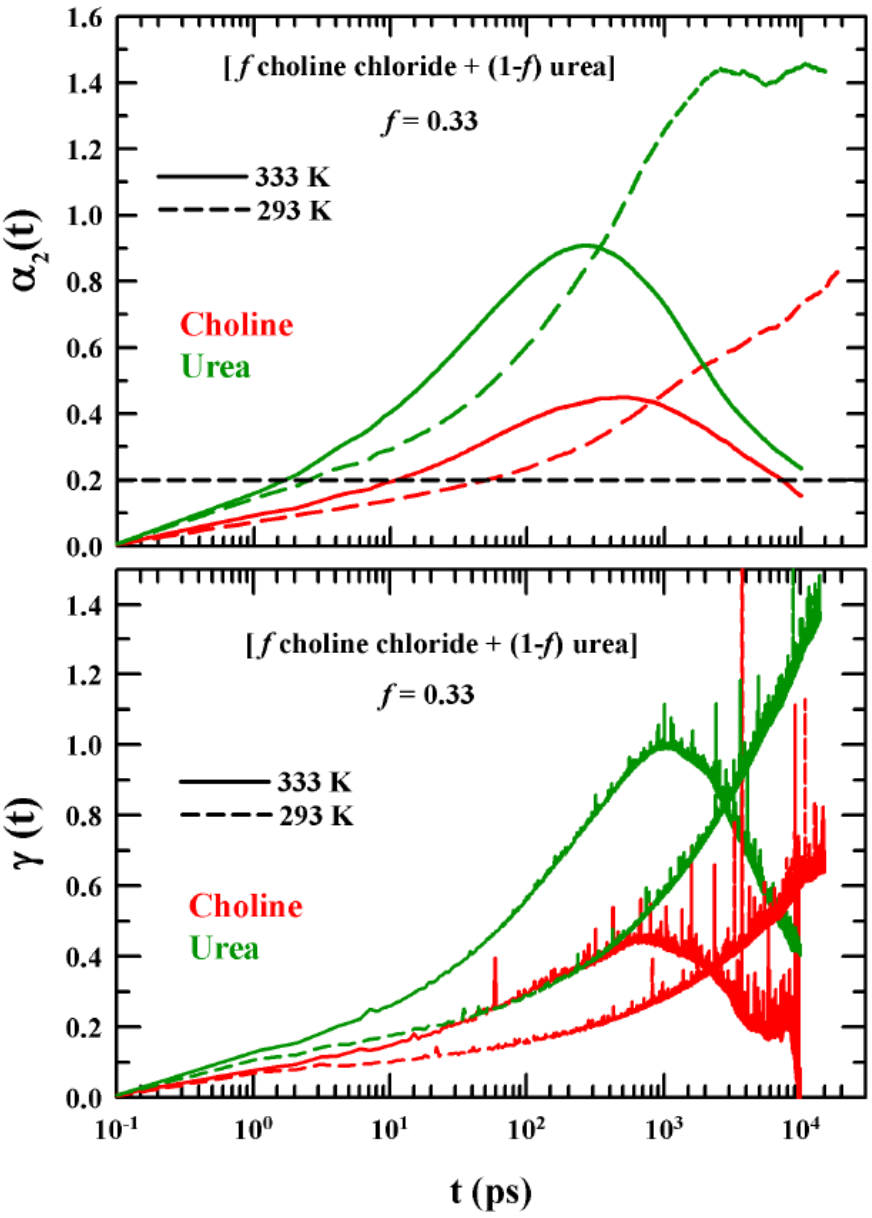

Figure 4.6: Simulated non-Gaussian parameter, $\alpha_2(t)$ (upper panel), and the new non-Gaussian parameter, $\gamma(t)$ (lower panel), for choline and urea in [*f* choline chloride + (1-*f*) urea] for *f* = 0.33 at temperatures 293 and 333 K. Data for choline and urea in both the panels are color-coded.

4.5.1.5 Self-Dynamic Structure Factors and Four-Point Dynamic Susceptibilities: DH Signatures in Multi-point Correlations

The self-dynamic structure factors, $F_s(k,t)$, for choline and urea in the present DES at temperatures 298 and 333 K for f = 0.33 have been calculated in the limit of nearest neighbor wavenumber ($k\sigma \rightarrow 2\pi$, σ being the diameter). The results are presented in Figure 4.7. Note the $F_s(k,t)$ is a two-point correlation functions describing time evolution of density at a given space point, while the dynamic susceptibility connects to four-point correlations as it examines the time evolution of densities simultaneously at two space points. As noticed in the $C_l(t)$ and $C_{HB}(t)$ decays, the complete relaxations of $F_s(k\sigma \rightarrow 2\pi, t)$ can be realized only at higher temperatures. The $1/e$ decay times for these decays are identified as the respective α-relaxation time scales, τ_α, and are indicated by bullet points on the individual decay curves. Note the simulated $F_s(k\sigma \rightarrow 2\pi, t)$ decays for choline are characterized by a strongly stretched exponential long-time kinetics (see Figure 4.A.10, Appendix 4.A), whereas those for urea are multi-exponential in nature**.** The fit data and the corresponding average decay times are summarized in Table 4.B.8 (Appendix 4.B). Note the stretching exponent β ~ 0.2 - 0.4 suggests strongly distributed decay kinetics and pronounced heterogeneity in translational dynamics for choline ions in this DES. Multi-exponential decay kinetics, however, do not exclude the possibility of temporally heterogeneous dynamics because hierarchical relaxations in a supercooled system represent step-wise sequential relaxations possessing widely separated time constants and guided by different correlated length-scales and timescales.

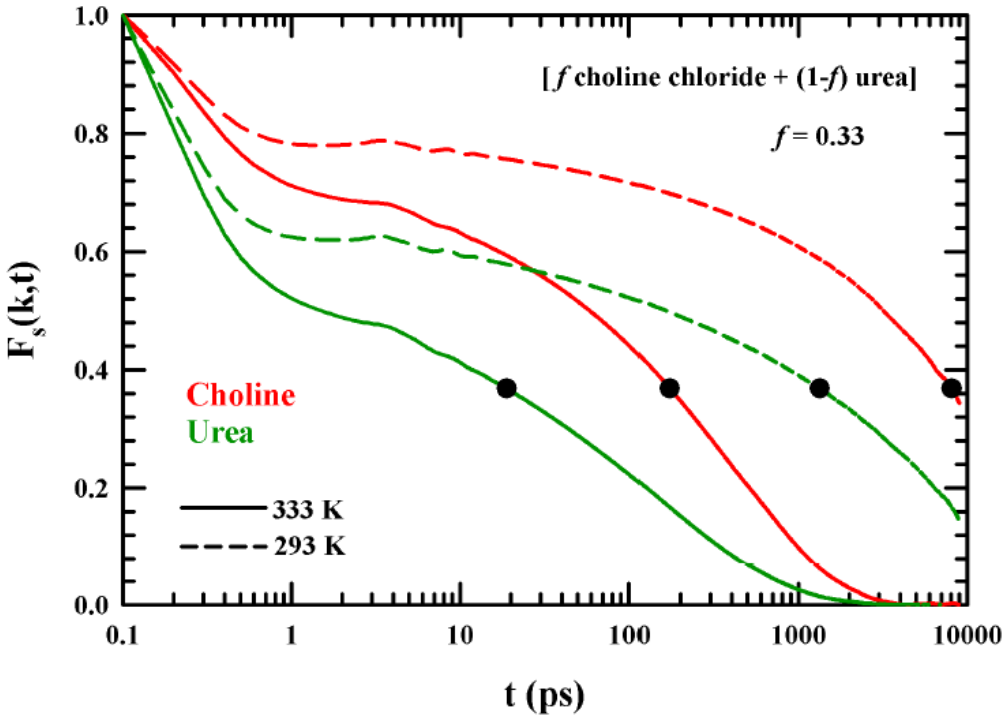

Figure 4.7: Simulated self-dynamic structure factor, $F_s(k,t)$, for choline and urea at the nearest neighbor wavenumber ($k\sigma \rightarrow 2\pi$) in [*f* choline chloride + (1-*f*) urea] DES for *f* = 0.33 at 293 K (dashed line) and 333 K (solid line). 1/e decay times of $F_s(k,t)$ are denoted by the bullet marks.

Next, we calculate the four-point dynamic susceptibility, $\chi_4(k\sigma \rightarrow 2\pi, t)$, by using Eq. 4.16 and the temperature dependent results for urea and choline are shown in Figure 4.8. The maximum time over which the mobility fluctuations at two space points remain correlated is denoted by t_4^{max} and can be obtained from the peak position of the $\chi_4(k\sigma \rightarrow 2\pi, t)$ versus time curves. Results shown in Figure 4.8 suggest that $\chi_4(k\sigma \rightarrow 2\pi, t)$ shifts to longer timescales upon lowering the solution temperature, producing longer t_4^{max}. This means that the temporal correlation increases because of increased heterogeneity upon lowering temperature. A comparison of t_4^{max} with the τ_α in Table 4.5 suggests that density relaxations for choline and urea at 333 K can remain correlated respectively for ~3 and ~10 times longer than their respective cage breaking timescales. As observed for other DH parameters, the peak of $\chi_4(k,t)$

could not be attained at 293 K within this 10 ns time window, suggesting that the cage-breaking timescales could be comparable or even longer than the hydrodynamic diffusive timescales (~20-30 ns) for choline and urea at this temperature. The signature of longer-lived solvent cage has already been reflected in the prolonged sub-diffusive MSDs presented in Figure 4.5.

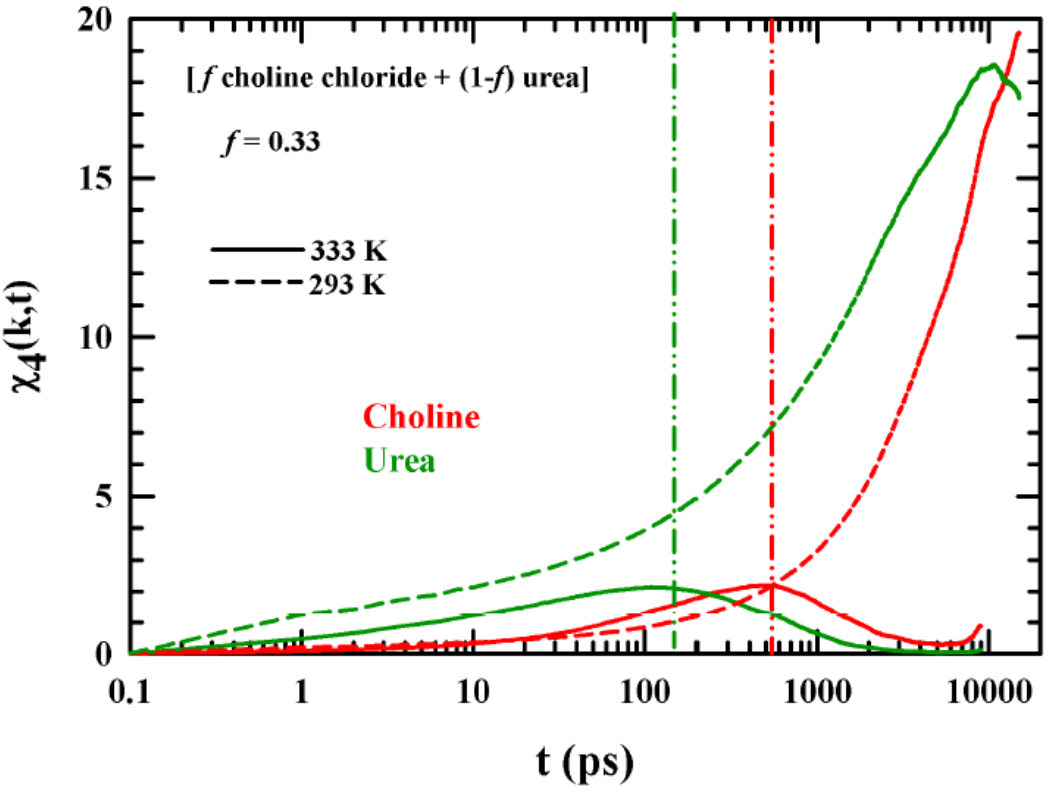

Figure 4.8: Simulated four-point dynamic susceptibilities, $\chi_4(k,t)$, for choline and urea at the nearest neighbor wavenumber ($k\sigma \rightarrow 2\pi$) in [*f* choline chloride + (1-*f*) urea] DES for *f* = 0.33 at 293 (dashed line) and 333 K (solid line).

Table 4.5: Values for τ_α and t_4^{max} obtained from the simulated $F_s(k,t)$ and $\chi_4(k,t)$ respectively for choline and urea in [*f* choline chloride + (1-*f*) urea] DES for *f*= 0.33 at 293 and 333 K.

	T(K)	τ_α (ns)	t_4^{max} (ns)
Choline	293	8.09	>15
	333	0.17	0.54
Urea	293	1.33	>15
	333	0.02	0.15

4.5.2 Temperature Dependent DR Measurements of [*f* choline chloride + (1-*f*) urea] DES: Experimental Supports for Simulated Reorientation Timescales and Heterogeneous Dynamics

4.5.2.1 Experimental DR Spectra of Conducting Solutions: Extraction and Interpretation of Timescales

Figure 4.9 and Figure 4.A.11 (Appendix 4.A) depict the temperature dependent dielectric relaxation spectra of [*f* choline chloride + (1-*f*) urea] DESs for *f* =0.33 and *f* =0.40 respectively. The values of the DR dispersion amplitudes and the associated time constants via 4-Debye fits to these experimental spectra using a sum of HN equations, $\varepsilon^* = \varepsilon_\infty + \sum_j \frac{\Delta\varepsilon_j}{(1+(i\omega\tau_j)^{1-\alpha_j})^{\beta_j}}$), are summarized in Table 4.6. Note that both a characteristic plateau in the limit of zero frequency for the real (ε') and a peak in the imaginary (ε'') components are missing in each of these collected spectra. This is an important issue for analysing DR spectra of conducting solutions and requires careful considerations while accessing and interpreting the timescales. This is because both high solution viscosity and ionic conductivity can individually lead to missing of such characteristic signatures of purely dielectric relaxation. Fit parameters in Table 4.6 suggest that for both the compositions the values of static dielectric constant ($\boldsymbol{\varepsilon_0}$) increase with increasing temperature. In highly viscous conducting solutions where a plateau is missing in $\varepsilon'(\nu)$, the exact estimation of ε_0 is somewhat non-trivial and associates with large uncertainties. This is because of the $1/\nu$ divergence of the conductivity term (in the total DR response) in the limit of $\nu \to 0$. Large solution viscosity alone can also shift both the plateau and the peak outside the lower limit of the measurement frequency window. Interestingly, the estimated ε_0 values summarized in Table 4.6 are in good agreement with those predicted from the steady state fluorescence peak shifts measurements reported earlier.[58] Usually, for common solvents such as water, alcohols, amides and several ionic liquids[127], ε_0 decreases with increase of temperature because of the thermal randomization of the molecular dipoles.[128] However, solvents such as acetic acid and acetic anhydride,[128] ε_0 shows temperature dependent increase. This has been addressed in terms of temperature-induced breakage of molecular associations, enhancing the dipole density.[128]

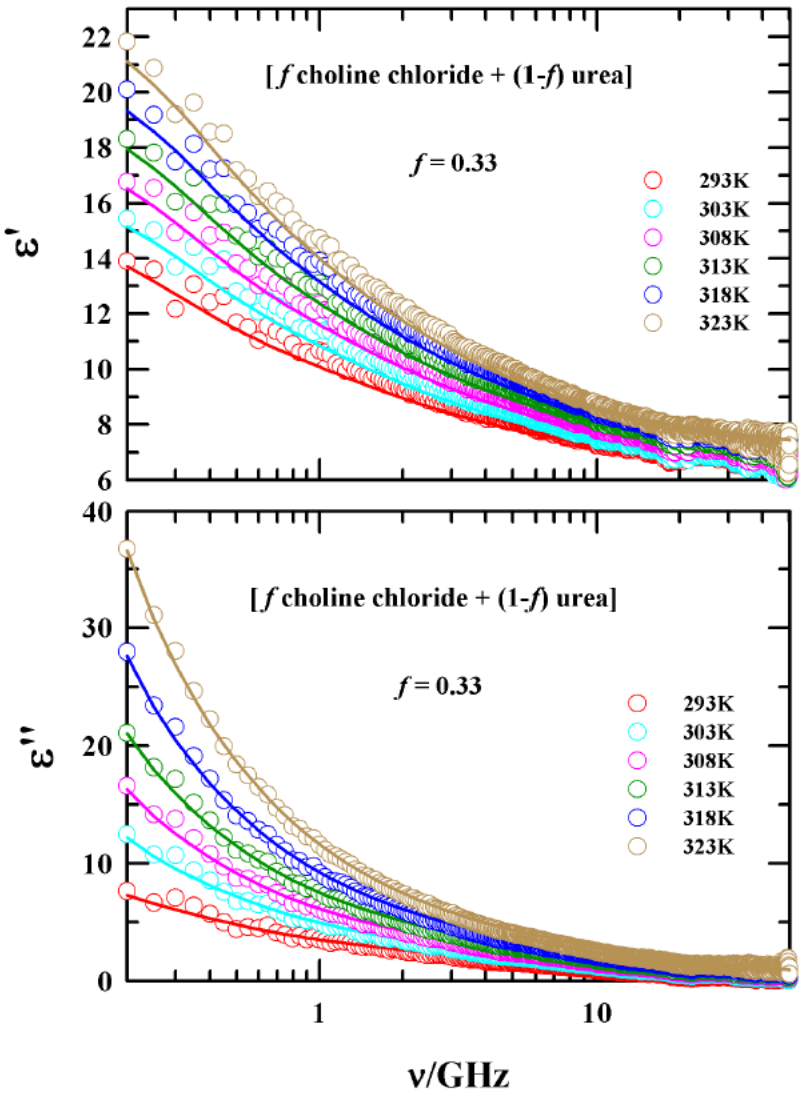

Figure 4.9: Temperature dependent experimental DR spectra of [*f* choline chloride + (1-*f*) urea] DESs for f = 0.33 within the frequency window, $0.2 \leq \nu/GHz \leq 50$. Solid lines passing through the experimental data points denote 4-Debye fits. Representations are color-coded.

Table 4.6*: Parameters obtained from the simultaneous 4-Debye fits to real (ε') and imaginary (ε'') components of the measured DR spectra for [*f* choline chloride + (1-*f*) urea] with *f* = 0.40 and 0.33, DESs at various temperatures.

T(K).	ε_0	$\Delta\varepsilon_1$	τ_1 (ps)	$\Delta\varepsilon_2$	τ_2 (ps)	$\Delta\varepsilon_3$	τ_3 (ps)	$\Delta\varepsilon_4$	τ_4 (ps)	ε_∞	n_D	κ_{fit} (S/m)	χ^2
f = 0.40													
293	13.2[a]	3.2(52%)[b]	553[e]	1.6(26%)	141	1.4	35	0.1	4	7.1	1.439[c]	0.057[d]	0.012
303	14.5	3.6(47%)	503	1.9(25%)	147	1.7	35	0.4	4	6.9	1.436	0.092	0.015
308	16.6	4.8(50%)	482	2.3(24%)	122	1.9	35	0.5	4	7.1	1.434	0.144	0.016
313	18.1	5.3(49%)	463	2.8(26%)	125	2.1	32	0.7	4	7.2	1.433	0.205	0.018
318	19.6	6.2(50%)	444	3.0(24%)	121	2.3	32	0.9	4	7.2	1.432	0.278	0.021
323	20.8	7.0(51%)	428	3.2(24%)	115	2.4	32	1.0	4	7.2	1.430	0.331	0.025
f = 0.33													
293	15.4	5.0(58%)	549	2.1(24%)	110	1.4	30	0.1	5	6.8	1.438	0.052	0.041
303	16.8	5.6(56%)	494	2.6(26%)	109	1.5	30	0.3	5	6.8	1.436	0.103	0.053
308	18.3	6.5(57%)	475	2.8(25%)	102	1.7	29	0.4	5	6.9	1.435	0.145	0.052
313	19.8	7.2(56%)	459	3.1(24%)	104	1.9	29	0.6	5	7.0	1.433	0.194	0.050
318	21.3	7.9(56%)	444	3.5(25%)	104	2.1	29	0.7	5	7.2	1.432	0.263	0.052
323	23.2	9.1(57%)	427	3.8(24%)	103	2.3	29	0.8	5	7.2	1.431	0.359	0.057

[a] ε_0 values have error bar ±2.0 (based on three independent measurements). [b] Numbers within the parenthesis indicates the amplitude of the dispersion step in percentage. [c] Measured refractive index. [d] Extracted dc conductivity value from the fitting of the experimental data points. [e] τ_i (*i*=1-3) are better within ±5% of the enlisted values (based on three independent measurements).

*Dielectric relaxation (DR) measurements have been done by Dr. Kallol Mukherjee at S N Bose National Centre for Basic Sciences, Kolkata, India. This is a part of our submitted paper in J. Rajbangshi, K. Mukherjee, and R. Biswas J. Phys. Chem. B (2021).

In ionic solutions such as these DESs, there exists a possibility of a significant number of dipolar constituents remain irrotationally bound[129–131] to the ionic species at lower temperatures. These irrotationally bound dipoles remain silent to the frequency dependent electric field during DR measurements. Upon increasing solution temperature, these irrotationally bound dipoles may dissociate and start contributing to the relaxation process. We then ask: are these irrotationally bound dipoles configured in an antiparallel orientation of their intrinsic dipoles? Assuming the DESs as an effective one component system, the use of the Onsager-Kirkwood-Frohlich equation,[132]

$$\frac{(\varepsilon_0-\varepsilon_\infty)(2\varepsilon_0+\varepsilon_\infty)}{\varepsilon_0(\varepsilon_\infty+2)^2} = \frac{\rho\mu^2}{9\varepsilon_p k_\beta T} g_k \tag{4.18}$$

where ρ denotes the solvent number density, ε_0 the static dielectric constant, ε_p the vacuum permittivity, μ the dipole moment of the constituent dipoles and g_k the Kirkwood factor. Here, we have assumed $g_k = 1$. We get the effective dipole moment value, μ_{eff} ~ 0.8 D at 293 K by using the relevant fit data for ε_0 and ε_∞ . This value ($\mu_{eff} \sim 0.8$) is smaller by an order of magnitude than the gas phase dipole moment of choline chloride (~8 D)[133] and also substantially smaller than the gas phase dipole moment for urea (~3.83 D).[86] Moreover, if we use the Cavell equation[134] to estimate the dipole moment of the species associated with the slowest relaxation process, it produces a value of ~0.7 D. In a molten mixture where the individual constituents possess high dipole moment values, (μ ~6 D in the molten state[34]), such a low value of μ_{eff} may be a manifestation of molecular association. In associating liquids, the value of g_k is known to deviate from unity. Our attempt for a rough estimate of g_k for urea molecules in this medium leads to $g_k \approx$ 0.2, suggesting a significant association between the dipolar species with antiparallel orientations. Upon increasing temperature (up to 323K), μ_{eff} (via Onsager equation) shows a ~40% increase at 323K over that at 293K. This may be a result of thermal energy induced dissociation and freeing up of individual dipoles. Figure 4.A.12 (Appendix 4.A) depicts the temperature dependence of $\boldsymbol{\varepsilon_0}$ (for both f = 0.33 and 0.40). The temperature coefficient, $-d\varepsilon_0/dt$, has been found to be ~ 0.27±0.01 K^{-1} and independent of 'f'. Similar behavior has also been observed for the temperature coefficients of various ILs.[127]

Fit parameters summarized in Table 4.6 indicate that the fastest time component (τ_4~ 5 ps) in our DR measurements has very small (~ 5%) contribution in the total dielectric response. However, this cannot be neglected because i) The 3D fits to the collected DR spectra produce poorer description compared to 4-D fitting (shown in Figure 4.A.13, Appendix 4.A**)**, ii) such a component has also been observed in molten acetamide, molten urea and their DESs in earlier experimental[34] studies and supported by the simulated reorientational relaxations. Qualitatively similar timescale (~5-15 ps) has also been found here in the $C_2(t)$ relaxation of choline ion (see Table 4.2). Note that a significant amount of dispersion ($[\varepsilon_\infty - {n_D}^2]$ ~30-50%) in the high frequency wing has remained inaccessible in our measurements. This missing dispersion is likely to be shared by the fast rotational relaxations and H-bond fluctuations involving intermolecular vibrations and librations. Their presence is indicated by the significant sub-picosecond relaxation components observed in the simulated $C_l(t)$ and $C_{HB}(t)$ relaxations for this DES. Earlier simulation studies ascribed the fast relaxation components in the neat molten urea and acetamide to the N-H bond vector reorientation coupled to H-bond relaxation.[28] Fast relaxation processes with time constant of ~1-2 was also observed in formamide and N-methyl formamide by DR[135] and OHD-OKE measurements and interpreted in terms fast rotation.[136] All these support the view that the ~5 ps timescale detected in these DR measurements originates from fast dipolar rotations and a part of the missing component arises from the high frequency collective solvent modes involving inter-molecular H-bonds.

Next, we concentrate on τ_3~30-50 ps and τ_2 ~100-150 ps timescales which are contributing ~15-20% and ~20-25% respectively in the DR dynamics detected in the present measurements. The ~30-50 ps timescale is present in both the $C_l(t)$ and $C_{HB}(t)$ relaxations for this DES. This suggests, as before while interpreting the DR dynamics of molten urea,[28] that this timescale is connected to the single particle reorientation dynamics coupled to H-bond relaxations. The DR measurements of neat molten urea and the subsequent simulations of $C_{HB}(t)$ have indicated a presence of relaxation timescales in the ~100-150 ps range. Therefore, the ~100-150 ps DR timescale detected in this DES can be attributed to the collective molecular reorientation dynamics coupled to urea - urea H-bond structural relaxations. Interestingly, dynamic Stokes shift measurements employing a fluorescent neutral dipolar solute in this DES have reported a solvation decay component with time constant of ~100-200 ps,[58] providing a further support to the detected DR timescale in this range.

Next, we explore the origin of the slowest DR timescale detected, τ_1 ~ 400-550 ps. This timescale is ~6 times larger than the slowest DR time of molten urea,[28] and the amplitude associated with it accounts for ~50% of the total DR dynamics detected for these DESs. Earlier measurements and simulations with (acetamide + urea) DESs have revealed that the slowest DR timescale detected in the measurements using the frequency window $0.2 \leq \nu/GHz \leq 50$ is intimately connected to the translational diffusion timescale via the structural H-bond relaxation.[28] The temperature dependent translational diffusion coefficients for choline cation, urea and chloride anion for the present DES are available from the PFGNMR experiments.[66] In addition, simulation results presented in Figure 4.3 have shown that the ratio, $\langle\tau_l\rangle/\tau_{trans}$, correctly reduces to the hydrodynamic predictions (homogeneous limit) at 333 K for both choline cation and urea. Using these informations and the identity, $\tau_{DR} = \langle\tau_l\rangle$ for $l = 1$, we can calculate τ_{DR} at 333 K as follows: $\tau_{DR,cal} = \langle\tau_{l=1}\rangle \approx 0.08 \times \tau_{trans} = 0.08 \times [\sigma^2/D_t]$. Using the diameter for urea as σ = 4.7 Å and D_t= 4.62 × $10^{-11}\, m^2 s^{-1}$, we find $\tau_{DR,cal}$ ~ 380 ps at 333 K. Strikingly, the slowest experimental DR timescale detected for this DES at 333 K (~430 ps) is quite similar to this calculated DR timescale, $\tau_{DR,cal}$, from the measured centre-of-mass diffusion coefficient, establishing the view that this ~400-500 DR timescale detected in the present measurements can indeed originate from the urea-urea structural H-bond relaxations.

4.5.2.2 Comparison of Activation Energies Between Measurements and Simulations: Further Experimental Support to Heterogeneous Dynamics

Figure 4.10 shows a comparison between the activation energies obtained from the temperature dependent experimental average DR times ($\langle\tau_{DR}\rangle$) and the simulated average first rank reorientational correlation times ($\langle\tau_{l=1}\rangle^{*}$) for choline. Note $\langle\tau_{l=1}\rangle^{*}$ do not include the slowest multi-nanosecond time constant found in the respective simulations. It is obvious from this figure that the agreement between experiments and simulations is qualitative in nature where the experimental activation energy is nearly half of that predicted by the simulations. The reason for this is probably lying in the different degrees of viscosity decoupling between the experiments and simulations. For example, our simulated translational diffusion coefficients for urea and choline are ~2-3 times smaller than those found in experiments, suggesting simulations predict more viscosity coupling to translational motion than reflected by the PFGNMR measurements. The present DR measurements also reveal quite a strong viscosity decoupling for $\langle\tau_{DR}\rangle$ as it shows $\langle\tau_{DR}\rangle \propto \eta^{p}$ dependence with $p = 0.1$ (see Figure 4.A.14, Appendix 4.A). This value of the fraction power ($p = 0.1$) is much lower than what was found from temperature dependent viscosity measurements, and dynamic fluorescence Stokes shift and anisotropy experiments.[31] The qualitative nature of the agreement between activation energies from measurements and simulations notwithstanding, we may conclude that the present DR data provide ample evidence in favour of considerable heterogeneous reorientational dynamics in these DESs composed of choline chloride and urea.

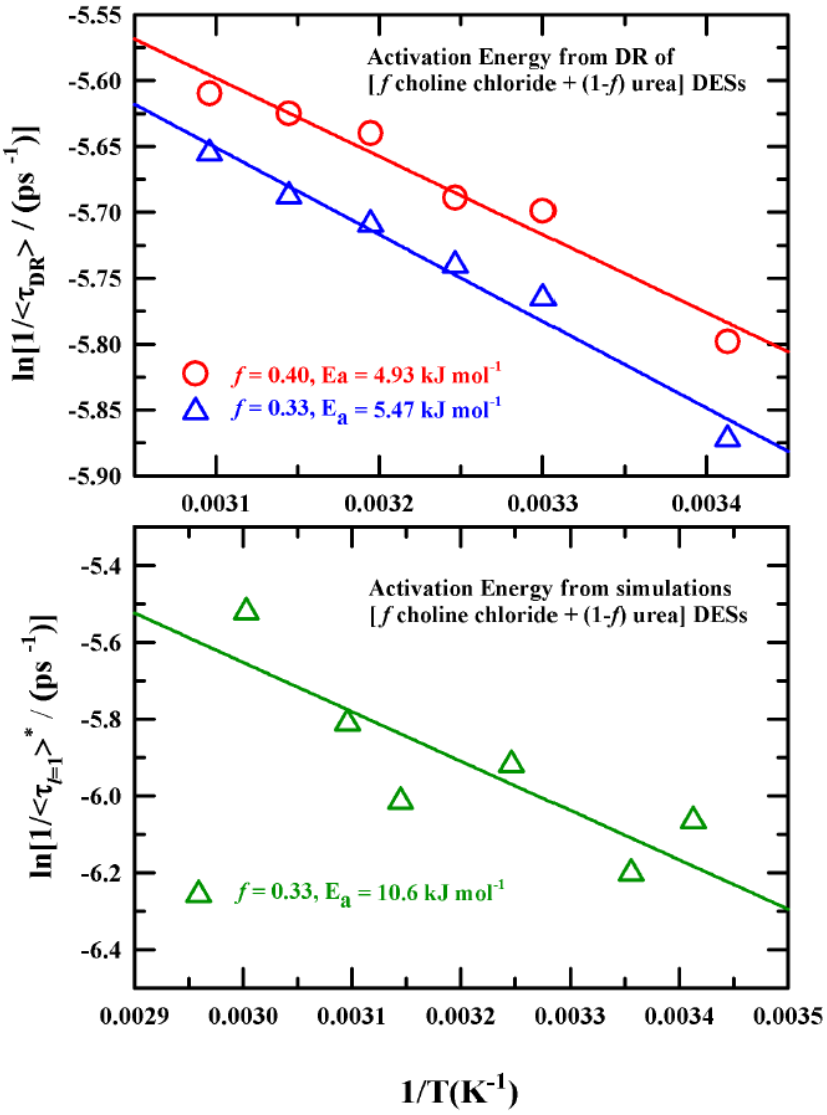

Figure 4.10: Comparison of activation energies (E_a) from DR measurements with that from the simulated first rank reorientational correlation functions, $C_1(t)$, for the [f choline chloride + (1-f) urea] DES under study. Note the average DR times $\left(\langle\tau_{avg}^{DR}\rangle\right)$ have been used for estimating the experimental E_a, while $\langle\tau_{l=1}\rangle^*$ have been used for the simulation counter-part. These average times have been calculated as follows: $\langle\tau_{avg}^{DR}\rangle = \sum_{i=1}^{4} a_i\tau_i / \sum_{i=1}^{4} a_i$, with $\sum_{i=1}^{4} a_i = 1$; $\langle\tau_{l=1}\rangle^* = \sum_{i=1}^{3} a_i\tau_i / \sum_{i=1}^{3} a_i$ with $\sum_{i=1}^{4} a_i = 1$, where the slowest time constant of the simulated first rank reorientational correlation functions has not been included in the averaging. Note the simulated average reorientation times are for choline ion in this DES at f = 0.33.

4.6 Concluding Remarks

To summarize, this combined simulation and experimental study demonstrate unambiguously that the these DESs made of choline chloride and urea are strongly heterogeneous, and the extent of heterogeneity observed through experiments is dependent upon the type of experiments employed. For example, DESs with the general formula, [f choline chloride + (1-f) urea] were studied earlier[31] at f = 0.33 and 0.40 in the temperature range, $293 \leq T/K \leq 333$, via fluorescence-based time-resolved measurements. These measurements indicated a fractional viscosity dependence of the average solute solvation and rotation timescales with fraction power, $0.7 \leq p \leq 0.9$. These values for the fraction power (p) being not too deviated from the unity and p not known for the same fluorescent solute in homogeneous solvent conditions, one cannot confidently comment on how much these DESs are actually temporally heterogeneous. The DR measurements, on the other hand, do not require any external probe, and thus can reflect the heterogeneity inherent to motional features to particles in these DESs. The p value obtained in DR measurements reported here is quite dramatic and places the earlier heterogeneity view from dynamic fluorescence measurements into a strong debate. A strong translation-rotation decoupling found in simulations performed here provides the necessary support to the dynamic heterogeneity view reflected via the DR measurements. Other simulated features, such as, displacement distributions, MSDs and dynamic susceptibilities endorses strong temporal heterogeneity in these DESs. The apparent conflict between the heterogeneity views revealed by DR measurements and time-resolved fluorescence experiments stresses the importance of the lengthscale (solute diameter, for example) in reflecting the inherent heterogeneity of a system via experiments. In other words, the inherent solution heterogeneity can be expressed differently in different measurements because of a competition between the heterogeneity lengthscale (of the system) and the smallest lengthscale that a given experimental technique can probe.[71]

Appendix 4.A

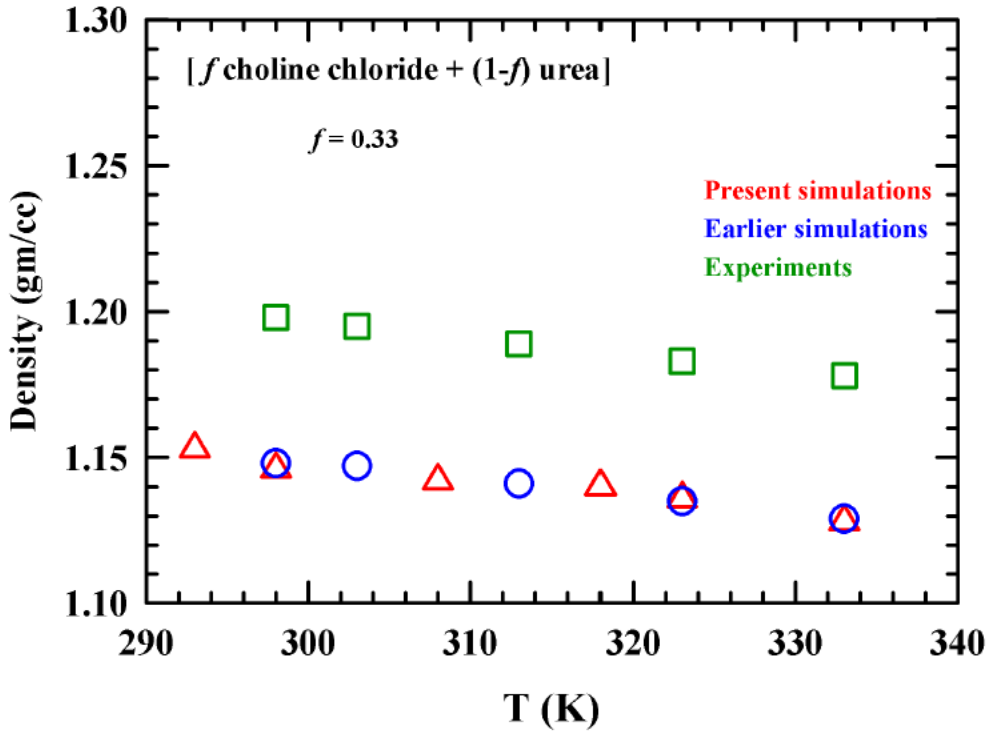

Figure 4.A.1: Comparison of temperature dependent densities of [*f* choline chloride + (1-*f*) urea] DESs for *f* = 0.33 obtained from the present simulations with those from earlier simulation studies and experiments.

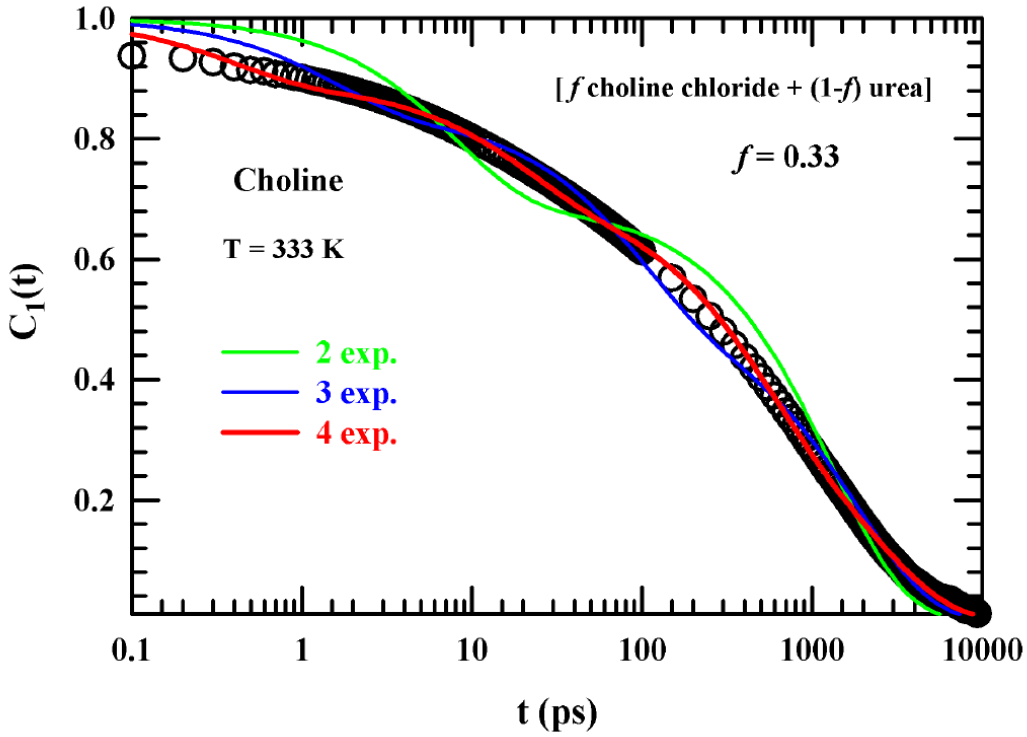

Figure 4.A.2: The figure shows a comparison among various exponential functions (2 exp., 3 exp. and 4 exp.) as fit functions for adequately describing the simulated $C_1(t)$ relaxation for choline ion in [f choline chloride + (1-f) urea] DESs at 333 K. This representative figure suggests that the $C_1(t)$ relaxation requires a four-exponential fit. Similar observation has been made for other temperatures also.

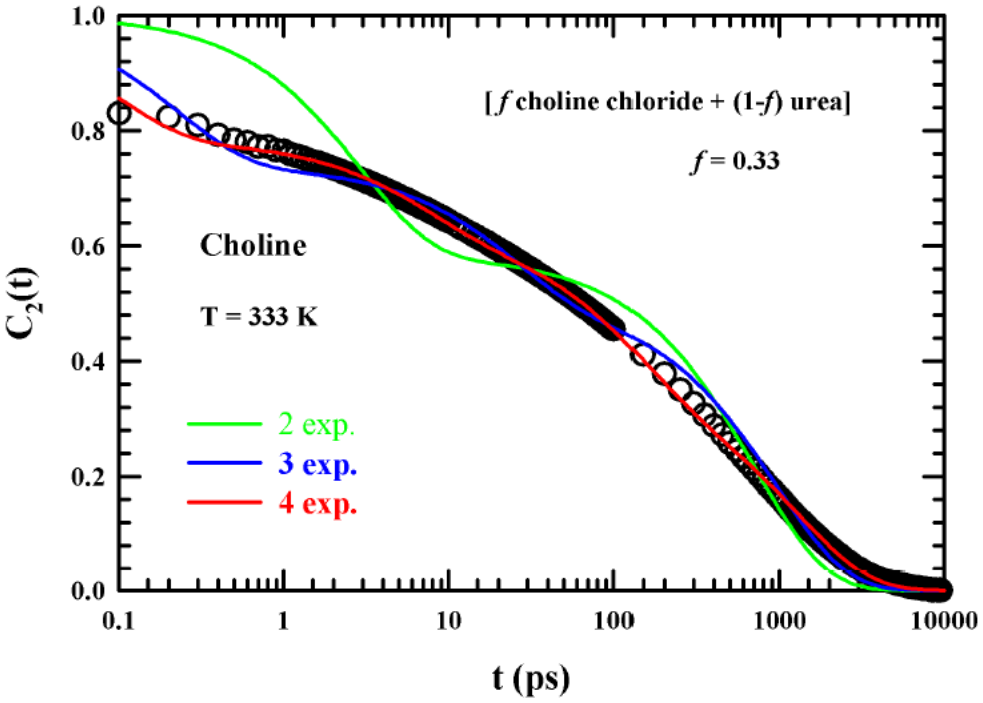

Figure 4.A.3: The figure shows a comparison among various exponential functions (2 exp., 3 exp. and 4 exp.) to fit the simulated $C_2(t)$ relaxation for choline ion in [*f* choline chloride + (1-*f*) urea] DESs at 333 K.

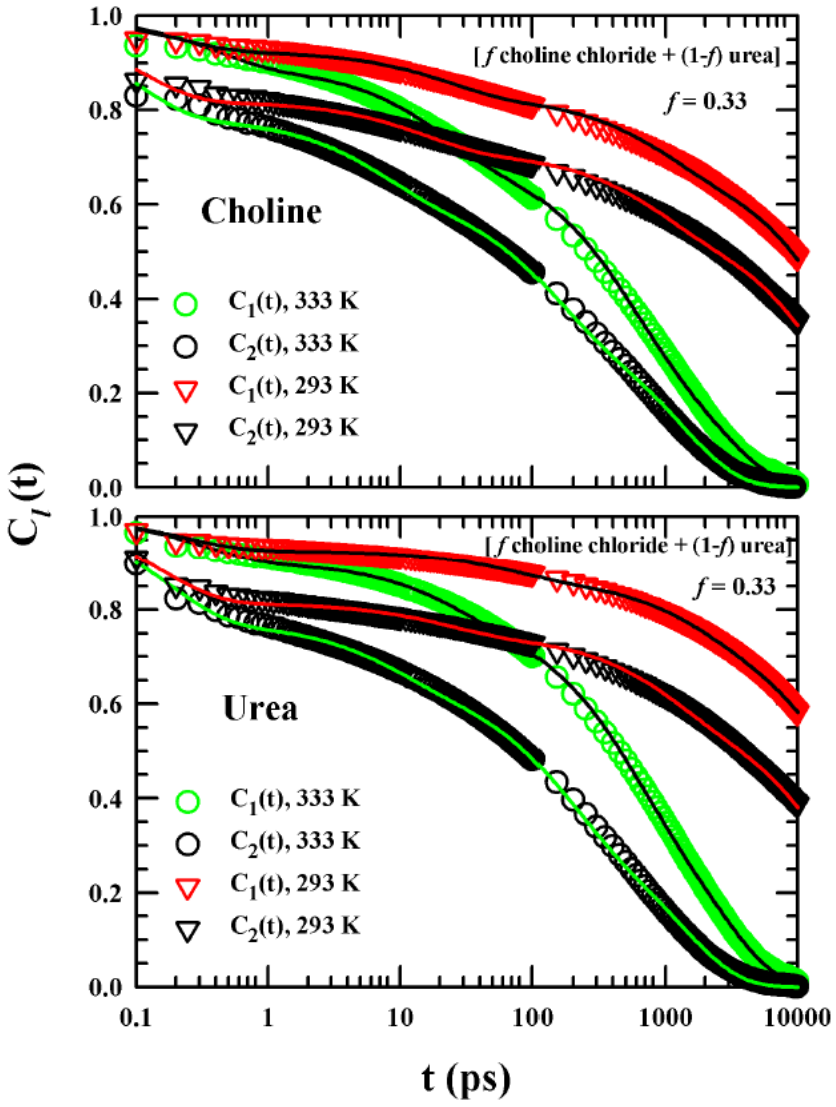

Figure 4.A.4: Simulated rank dependent collective single particle reorientational correlation functions ($C_l(t)$) of rank l =1 and 2 for choline (upper panel) and urea (lower panel) in [f choline chloride + (1-f) urea] DES for f = 0.33 at two representative temperatures, T = 293, 333 K. The lines going through the simulated data are the multi-exponential fits.

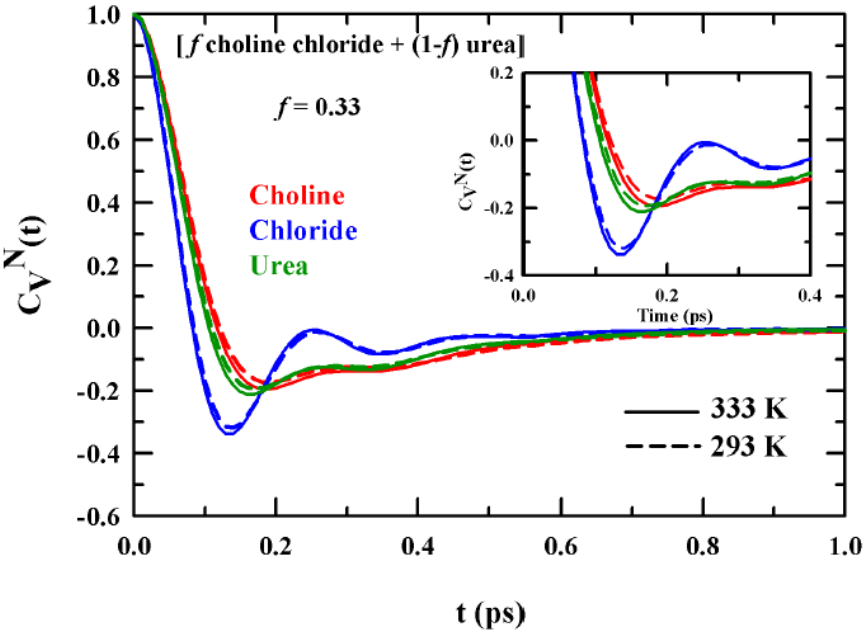

Figure 4.A.5: Normalized velocity autocorrelation functions (VACFs), $C_v^N(t)$, of choline cation, chloride anion and urea in [f choline chloride + (1-f) urea] DES for f = 0.33 at temperatures 293 and 333 K. The inset shows the VACF at short times to highlight the marked cage-rattling of chloride ion in this DES.

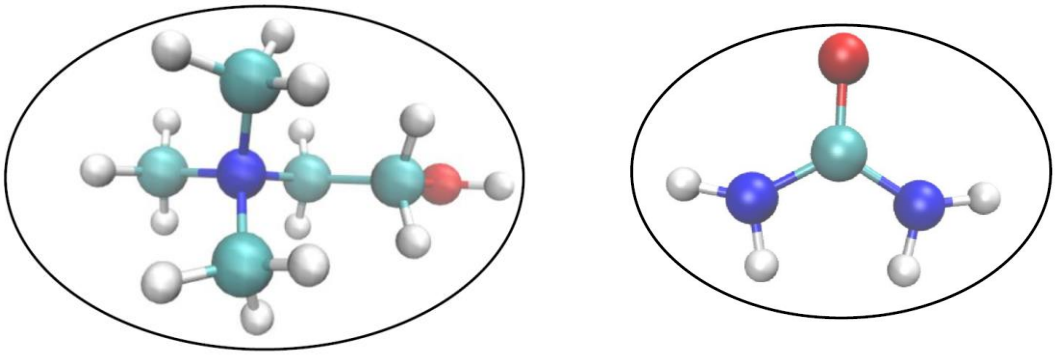

Figure 4.A.6: Shape of choline cation and urea molecule as an approximate oblate spheroid.

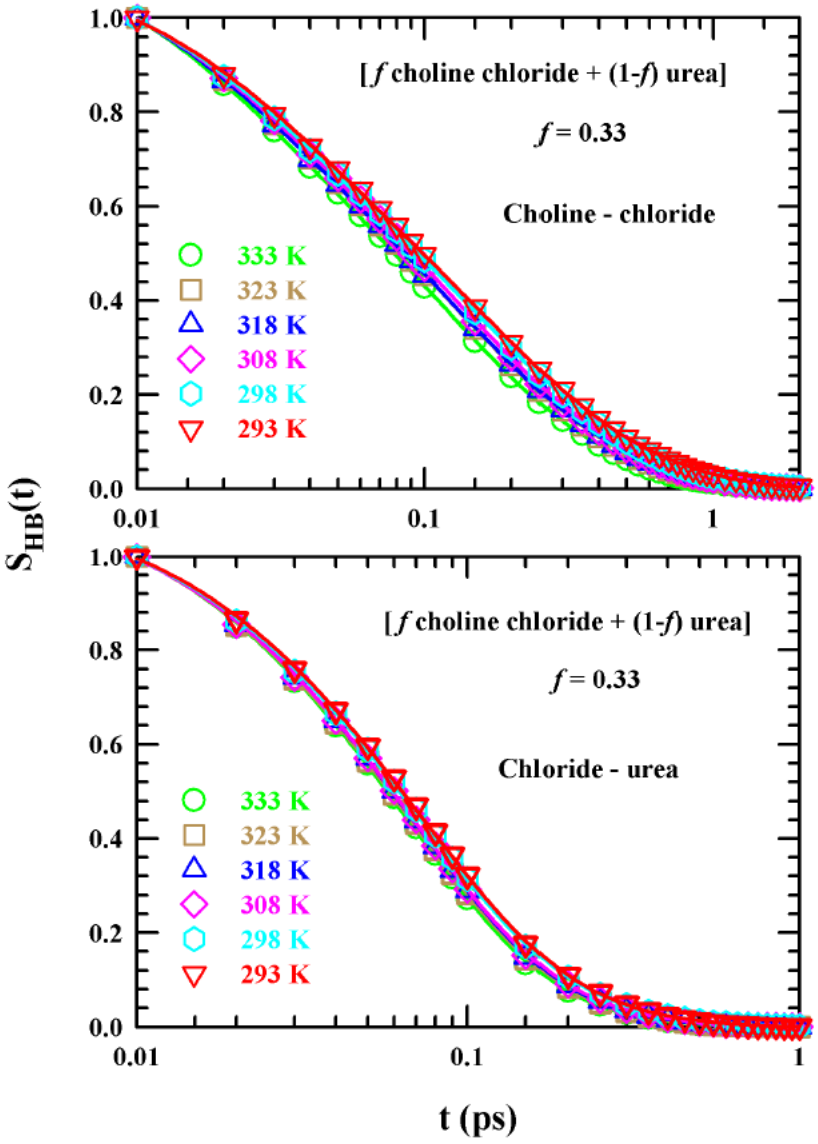

Figure 4.A.7: Temperature dependence of the **s**imulated decays of the continuous H-bond relaxation functions, $S_{HB}(t)$, for choline – chloride (upper panel) and chloride – urea (lower panel) H-bonds in [*f* choline chloride + (1-*f*) urea] DES at *f*=0.33.

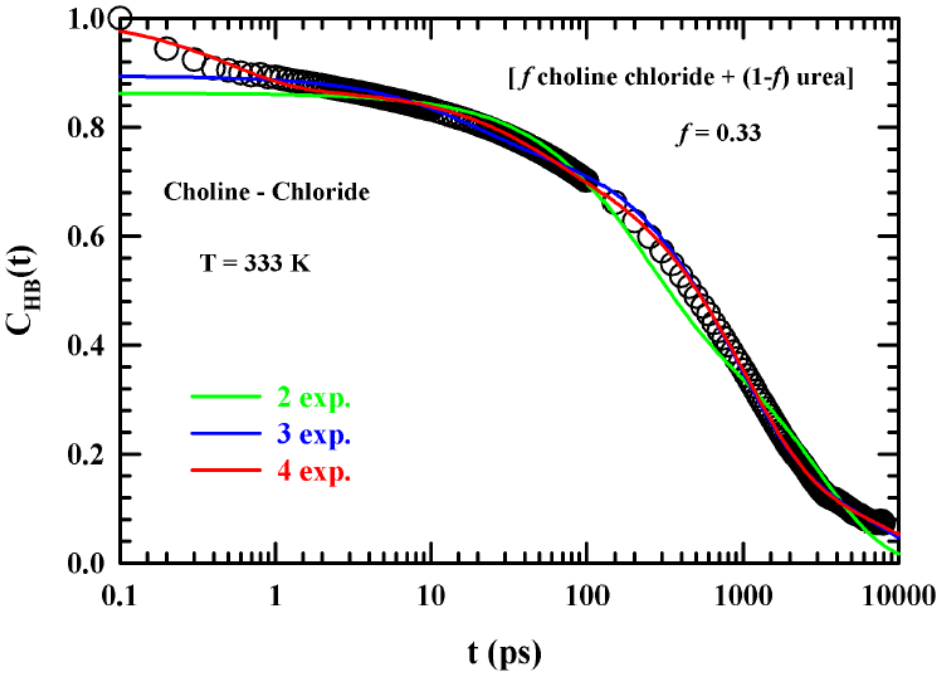

Figure 4.A.8: The figure shows a comparison among various exponential fit functions (2 exp., 3 exp. and 4 exp.) for describing the $C_{HB}(t)$ relaxation for choline – chloride pair in in [f choline chloride + (1-f) urea] DESs at 333 K.

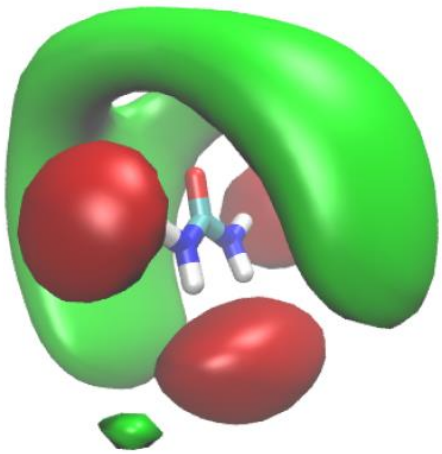

Figure 4.A.9: Spatial distribution functions (SDFs) for choline (green frame) and chloride ion (red frame) around a urea molecule.

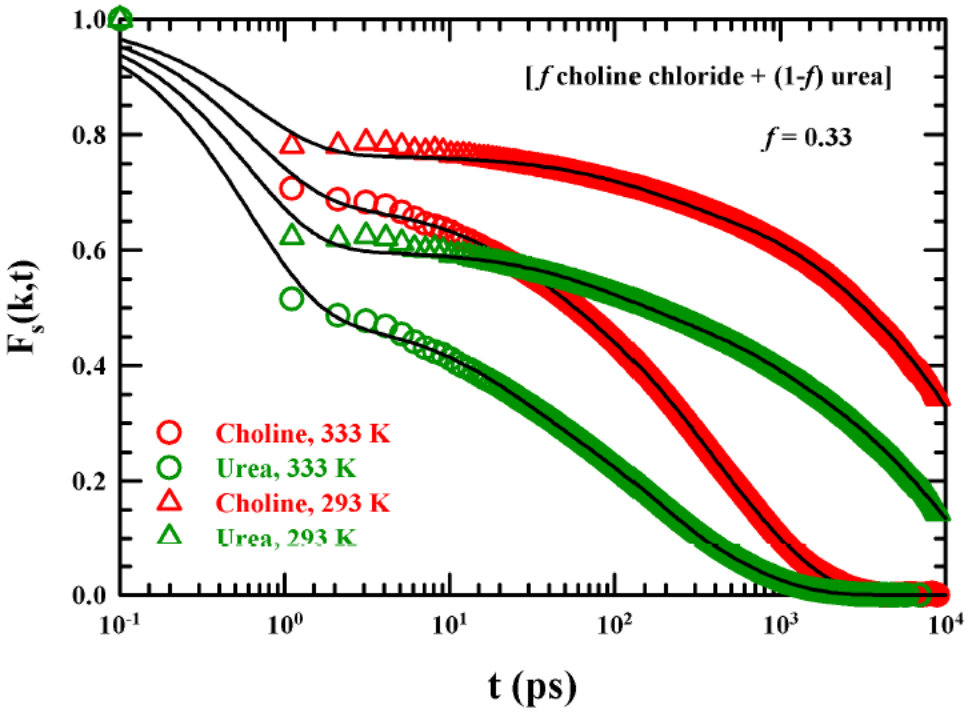

Figure 4.A.10: Simulated self-dynamic structure factor, $F_s(k,t)$ for choline (circle) and urea (triangle) at the nearest neighbor wavenumber ($k\sigma \rightarrow 2\pi$) in [*f* choline chloride + (1-*f*) urea] DES for *f* = 0.33 at temperatures 293 and 333 K. Symbols represent the simulated data and the lines going through the data are the best fits (stretched/multi-exponential).

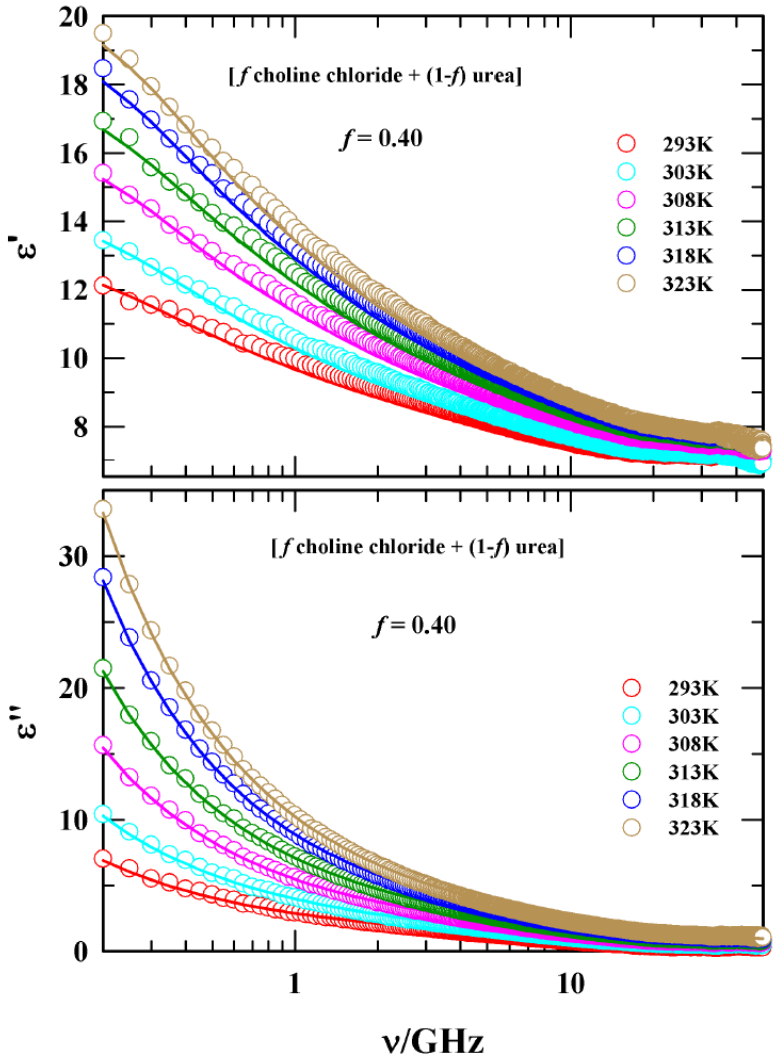

Figure 4.A.11: Temperature dependence of the real (ε') and imaginary (ε'') components of the measured DR spectra for [*f* choline chloride + (1-*f*) urea] DES at *f* = 0.40 within the frequency regime $0.2 \le \nu / \mathrm{GHz} \le 50$. Solid lines through these data represent simultaneous fits using 4-Debye relaxation model. Representations are color-coded.

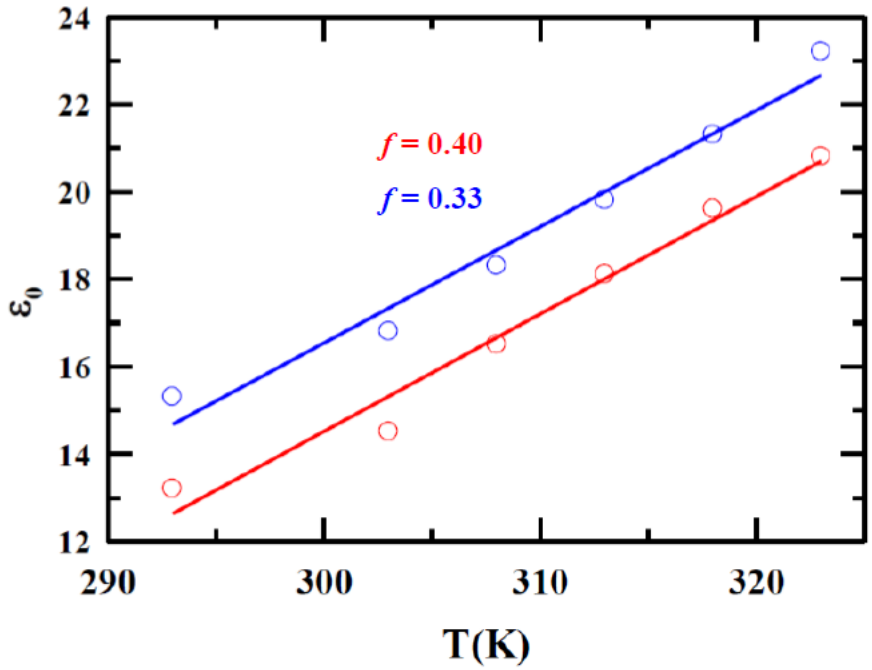

Figure 4.A.12: Temperature dependence of the estimated static dielectric constant (ε_0) for f = 0.40 and f = 0.33. Data for different compositions are color coded.

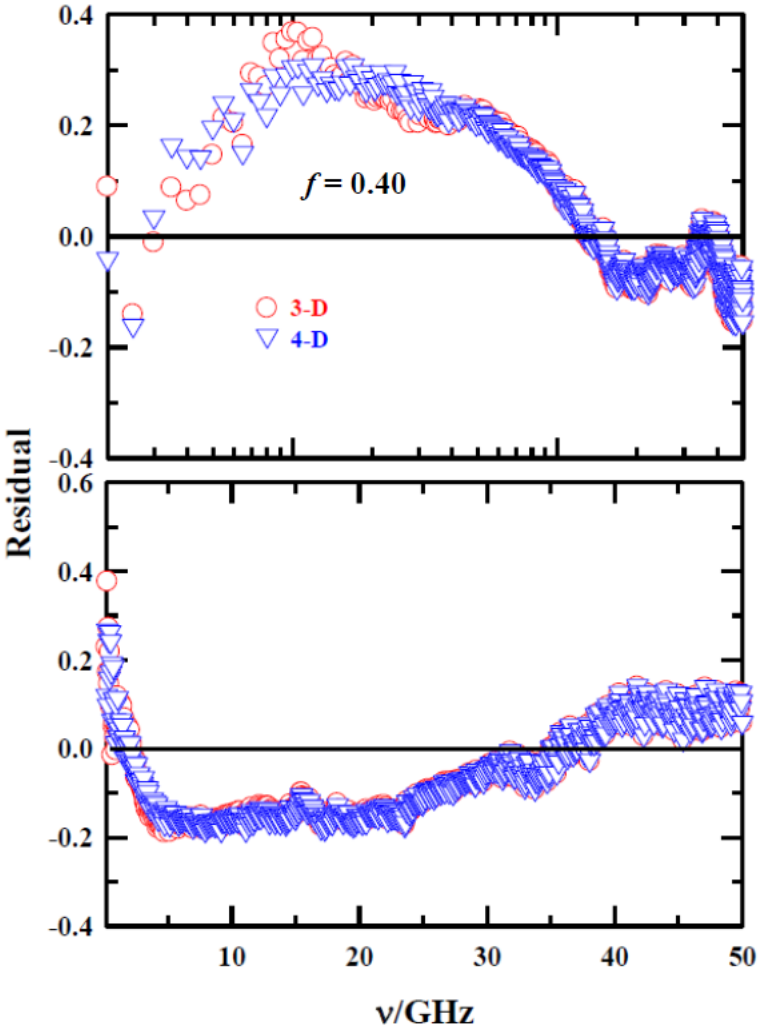

Figure 4.A.13: Comparison between 4-Debye and 3-Debye fits to the ε' (upper panel) and ε'' (lower panel) of the complex DR spectra of [*f* choline chloride + (1-*f*) urea] DES for *f* = 0.40 at 293K.

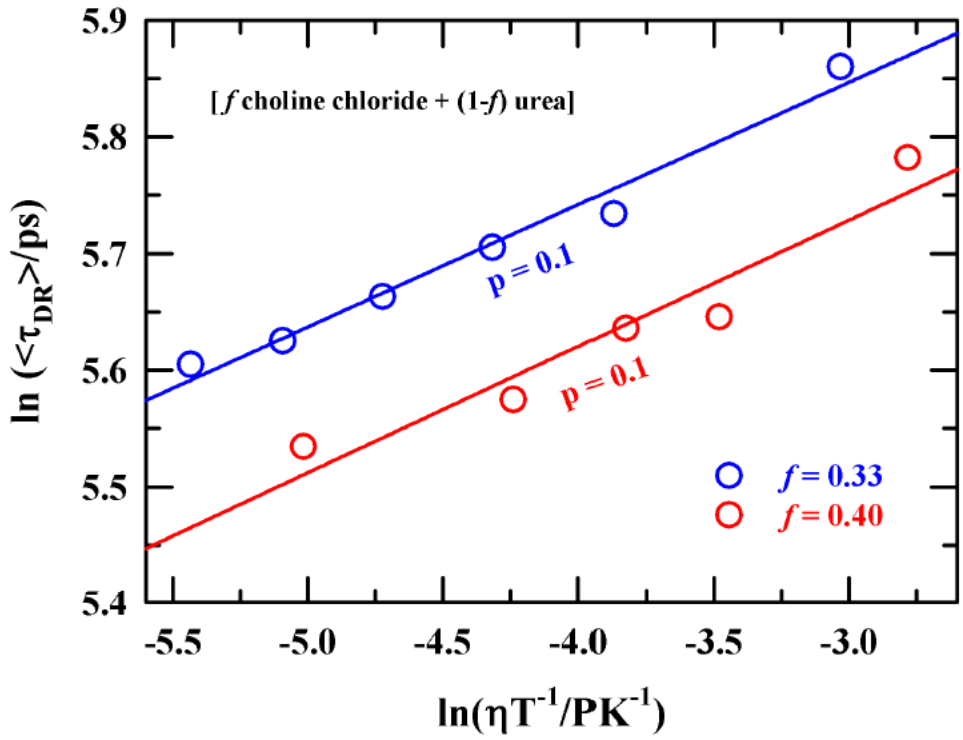

Figure 4.A.14: Viscosity decoupling of average DR times, $\langle \tau_{DR} \rangle$ in [*f* choline chloride + (1-*f*) urea] DES at f = 0.40 (circles) and 0.33 (triangles). Here, the slowest DR times are shown as a function of the temperature-reduced viscosity (η/T). Fits through the data are represented by the solid lines.

Appendix 4.B

Table 4.B.1: Partial charges and Lennard-Jones parameters for choline and chloride ions. Atomic sites of choline ion are denoted as follows:

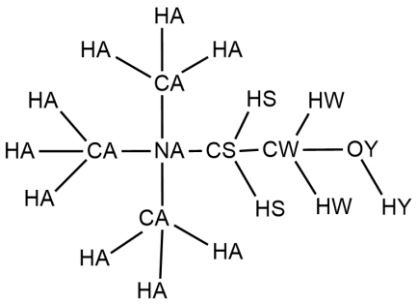

Atoms	Charge (e)	ε (kcal/mol)	σ (Å)
CS	-0.131	0.066	3.50
HS	0.068	0.030	2.60
NA	0.791	0.170	3.25
CA	-0.100	0.066	3.50
CW	0.132	0.066	3.50
OY	-0.468	0.170	3.07
HA	0.033	0.030	2.50
HW	0.034	0.030	2.20
HY	0.275	0.000	0.00
Cl	-0.800	0.148	3.77

Table 4.B.2: Partial charges and Lennard-Jones parameters for urea molecules. Atom sites of urea molecule are denoted as follows:

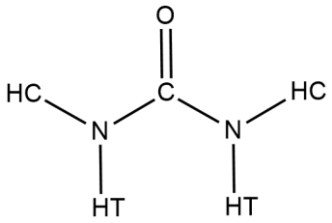

Atoms	Charge (e)	ε (kcal/mol)	σ (Å)
C	0.124	0.1575	3.75
O	-0.322	0.3150	2.96
N	-0.453	0.2550	3.55
HT	0.276	0.0000	0.00
HC	0.276	0.0000	0.00

Table 4.B.3: Temperature dependent experimental viscosity coefficients of [*f* choline chloride + (1-*f*) urea) DES for *f* = 0.33.

T(K)	η (cP)[85]	η (cP)[31]
293	1371.653	1412
298	859.454	1008
303	527.090	631
308	348.248	411
313	237.931	278
318	175.067	195
323	119.721	141
333	-	80

Table 4.B.4: Ratios of average simulated reorientational correlation times obtained from $C_l(t)$ of rank, l = 1 and 2 for choline and urea in [f choline chloride + (1-f) urea] DESs for f = 0.33 at various temperatures.

T(K)	$\langle\tau\rangle_{l=1}$ (ps)	$\langle\tau\rangle_{l=2}$ (ps)	$\frac{\langle\tau\rangle_{l=1}}{\langle\tau\rangle_{l=2}}$
Choline			
293	20038	11754	1.7
298	17971	10364	1.7
308	10405	6223	1.7
318	5090	1963	2.6
323	2513	1772	1.4
333	1057	484	2.2
Urea			
293	29823	14082	2.1
298	25606	11794	2.2
308	13259	6229	2.1
318	5863	2042	2.8
323	2925	1319	2.2
333	1294	489	2.6

Table 4.B.5: Multi-exponential fit parameters for the simulated H-bond relaxations, $S_{HB}(t)$ for choline - chloride and chloride - urea pairs in [*f* choline chloride + (1-*f*) urea] DESs for *f* = 0.33 at various temperatures.

T(K)	a_1	τ_1 (ps)	a_2	τ_2 (ps)	a_3	τ_3 (ps)	$\langle\tau\rangle$ (ps)
Choline - chloride							
293	0.3304	0.0268	0.5313	0.14	0.28	0.45	0.21
298	0.3327	0.0244	0.5264	0.13	0.29	0.40	0.20
308	0.3173	0.0221	0.5277	0.12	0.32	0.35	0.18
318	0.3322	0.0213	0.5333	0.11	0.31	0.34	0.17
323	0.3282	0.0222	0.5432	0.12	0.30	0.34	0.17
333	0.3323	0.0191	0.5429	0.10	0.32	0.29	0.15
Chloride – urea							
293	0.5096	0.0676	0.4616	0.0676	0.1660	0.1947	0.098
298	0.5247	0.0673	0.4751	0.0672	0.1394	0.2118	0.097
308	0.5339	0.0645	0.4870	0.0645	0.1261	0.1927	0.090
318	0.5398	0.0651	0.4957	0.0651	0.1129	0.1876	0.088
323	0.5400	0.0639	0.4968	0.0639	0.1139	0.1799	0.087
333	0.5546	0.0637	0.5123	0.0637	0.0881	0.1851	0.084

Table 4.B.6: Molecular diameter of choline, chloride and urea used in the calculations.

Molecule/ion	Diameter (Å)
Choline	3.29
Chloride	3.62
Urea	4.7

Table 4.B.7: Values for τ_{NG} and τ_{NNG} from simulations of [*f* choline chloride + (1-*f*) urea] DES for *f* = 0.33 at 293 and 333 K.

Molecule/ion	T(K)	τ_{NG} (ns)	τ_{NNG} (ns)
Choline	293	>15	>15
	333	0.52	0.81
Urea	293	2.94	>15
	333	0.28	1.04

Table 4.B.8: Stretched/multi-exponential fit parameters for the simulated self-part of dynamic structure factor, $F_s(k,t)$ for choline ion and urea molecule in [*f* choline chloride + (1-*f*) urea] DESs at 293 and 333 K for *f* = 0.33.

T(K)	Ion and molecule	a_1	τ_1 (ps)	a_2	τ_2 (ps)	a_3	τ_3 (ps)	a_4	τ_4 (ps)	β	$\langle\tau\rangle$ (ps)
333	Choline	0.32	0.6	0.20	184	0.12	27	0.36	279	0.36	142
	Urea	0.52	0.6	0.13	20	0.20	140	0.15	572	1	116
293	Choline	0.24	0.6	0.07	150	0.11	1658	0.58	3129	0.18	2012
	Urea	0.40	0.6	0.09	89	0.40	9170	0.11	778	1	3776

References

[1] H. Zhang, L. Bu, M. Li, K. Hong, A. Visser, R. Rogers, and J. Mays, in (2001), pp. 114–124.

[2] P. Wasserscheid and T. Welton, *Ionic Liquids in Synthesis* (2003).

[3] P.G. Jessop, D.A. Jessop, D. Fu, and L. Phan, Green Chem. **14**, 1245 (2012).

[4] Q. Zhang, K.D.O. Vigier, S. Royer, and F. Jerome, Chem. Soc. Rev. **41**, 7108 (2012).

[5] M. Francisco, A. van den Bruinhorst, and M.C. Kroon, Angew. Chem. Int. Ed. **52**, 3074 (2013).

[6] J.-H. Liao, P.-C. Wu, and Y.-H. Bai, Inorg. Chem. Commun. **8**, 390 (2005).

[7] P. Nockemann, B. Thijs, K. Driesen, C.R. Janssen, K. Van Hecke, L. Van Meervelt, S. Kossmann, B. Kirchner, and K. Binnemans, J. Phys. Chem. B **111**, 5254 (2007).

[8] A.P. Abbott, D. Boothby, G. Capper, D.L. Davies, and R.K. Rasheed, J. Am. Chem. Soc. **126**, 9142 (2004).

[9] A.P. Abbott, G. Capper, D.L. Davies, R.K. Rasheed, and V. Tambyrajah, Chem. Commun. 70 (2003).

[10] D.V. Wagle, H. Zhao, and G.A. Baker, Acc. Chem. Res. **47**, 2299 (2014).

[11] P. Liu, J.-W. Hao, L.-P. Mo, and Z.-H. Zhang, RSC Adv. **5**, 48675 (2015).

[12] D. Carriazo, M.C. Serrano, M.C. Gutiérrez, M.L. Ferrer, and F. del Monte, Chem. Soc. Rev. **41**, 4996 (2012).

[13] C. Gu, X. Xu, and J. Tu, J. Phys. Chem. C **114**, 13614 (2010).

[14] J. Vijayakumar, S. Mohan, S.A. Kumar, S. Suseendiran, and S. Pavithra, Int. J. Hydrog. Energy **38**, 10208 (2013).

[15] A.P. Abbott, G. Capper, D.L. Davies, K.J. McKenzie, and S.U. Obi, J. Chem. Eng. Data **51**, 1280 (2006).

[16] M. Espino, M. de los Ángeles Fernández, F.J. Gomez, and M.F. Silva, TrAC Trends Anal. Chem. **76**, 126 (2016).

[17] I.M. Aroso, R. Craveiro, Â. Rocha, M. Dionísio, S. Barreiros, R.L. Reis, A. Paiva, and A.R.C. Duarte, Int. J. Pharm. **492**, 73 (2015).

[18] B. Guchhait, H. Al Rasid Gazi, H.K. Kashyap, and R. Biswas, J. Phys. Chem. B **114**, 5066 (2010).

[19] B. Guchhait, S. Daschakraborty, and R. Biswas, J. Chem. Phys. **136**, 174503 (2012).

[20] H.A.R. Gazi, B. Guchhait, S. Daschakraborty, and R. Biswas, Chem. Phys. Lett. **501**, 358 (2011).

[21] B. Guchhait, S. Das, S. Daschakraborty, and R. Biswas, J. Chem. Phys. **140**, 104514 (2014).

[22] A. Das, S. Das, and R. Biswas, J. Chem. Phys. **142**, 034505 (2015).

[23] E. Tarif, J. Mondal, and R. Biswas, J. Mol. Liq. **303**, 112451 (2020).

[24] E. Tarif, J. Mondal, and R. Biswas, J. Phys. Chem. B **123**, 9378 (2019).

[25] N. Subba, K. Polok, P. Piatkowski, B. Ratajska-Gadomska, R. Biswas, W. Gadomski, and P. Sen, J. Phys. Chem. B **123**, 9212 (2019).

[26] N. Subba, E. Tarif, P. Sen, and R. Biswas, J. Phys. Chem. B **124**, 1995 (2020).

[27] K. Mukherjee, A. Das, S. Choudhury, A. Barman, and R. Biswas, J. Phys. Chem. B **119**, 8063 (2015).

[28] K. Mukherjee, S. Das, E. Tarif, A. Barman, and R. Biswas, J. Chem. Phys. **149**, 124501 (2018).

[29] K. Mukherjee, E. Tarif, A. Barman, and R. Biswas, Fluid Phase Equilibria. **448**, 22 (2017).

[30] S. Banerjee, P.Kr. Ghorai, S. Das, J. Rajbangshi, and R. Biswas, J. Chem. Phys. **153**, 234502 (2020).

[31] A. Das and R. Biswas, J. Phys. Chem. B **119**, 10102 (2015).

[32] A. Das, S. Das, and R. Biswas, Chem. Phys. Lett. **581**, 47 (2013).

[33] R. Biswas, A. Das, and H. Shirota, J. Chem. Phys. **141**, 134506 (2014).

[34] S.N. Tripathy, Z. Wojnarowska, J. Knapik, H. Shirota, R. Biswas, and M. Paluch, J. Chem. Phys. **142**, 184504 (2015).

[35] T. Pal and R. Biswas, Chem. Phys. Lett. **517**, 180 (2011).

[36] M. Kondo, X. Li, and M. Maroncelli, J. Phys. Chem. B **117**, 12224 (2013).

[37] B.-Y. Zhao, P. Xu, F.-X. Yang, H. Wu, M.-H. Zong, and W.-Y. Lou, ACS Sustain. Chem. Eng. **3**, 2746 (2015).

[38] H. Zhao and G.A. Baker, J. Chem. Technol. Biotechnol. **88**, 3 (2013).

[39] H. Zhao, C. Zhang, and T.D. Crittle, J. Mol. Catal. B Enzym. **85**, 243 (2013).

[40] A. Zhu, T. Jiang, B. Han, J. Zhang, Y. Xie, and X. Ma, Green Chem. **9**, 169 (2007).

[41] Y.A. Sonawane, S.B. Phadtare, B.N. Borse, A.R. Jagtap, and G.S. Shankarling, Org. Lett. **12**, 1456 (2010).

[42] D. Yang, M. Hou, H. Ning, J. Zhang, J. Ma, G. Yang, and B. Han, Green Chem. **15**, 2261 (2013).

[43] A.P. Abbott, G. Capper, D.L. Davies, R.K. Rasheed, and P. Shikotra, Inorg. Chem. **44**, 6497 (2005).

[44] E.L. Smith, A.P. Abbott, and K.S. Ryder, Chem. Rev. **114**, 11060 (2014).

[45] A. Pandey and S. Pandey, J. Phys. Chem. B **118**, 14652 (2014).

[46] M. Pal, R. Rai, A. Yadav, R. Khanna, G.A. Baker, and S. Pandey, Langmuir **30**, 13191 (2014).

[47] A. Yadav and S. Pandey, J. Chem. Eng. Data **59**, 2221 (2014).

[48] A. Kadyan, K. Behera, and S. Pandey, RSC Adv. **6**, 29920 (2016).

[49] D. Dhingra and S. Pandey, J. Chem. Thermodyn. **130**, 166 (2019).

[50] D. Dhingra, Bhawna, A. Pandey, and S. Pandey, J. Phys. Chem. B **123**, 3103 (2019).

[51] S.S. Hossain and A. Samanta, J. Phys. Chem. B **121**, 10556 (2017).

[52] P. Kumari, M. Kumari, and H.K. Kashyap, J. Phys. Chem. B (2020).

[53] P. Kumari, Shobhna, S. Kaur, and H.K. Kashyap, ACS Omega **3**, 15246 (2018).

[54] P. Kumari and H.K. Kashyap, J. Phys. Chem. B **123**, 4550 (2019).

[55] A. Malik, H.S. Dhattarwal, and H.K. Kashyap, J. Chem. Phys. **153**, 164704 (2020).

[56] A. Malik, H.S. Dhattarwal, and H.K. Kashyap, J. Phys. Chem. B (2021).

[57] S. Kaur, S. Sharma, and H.K. Kashyap, J. Chem. Phys. **147**, 194507 (2017).

[58] M.E. Griffin, K.A. Wilson, M.R. White, and P.B. Brown, J. Nutr. **124**, 1685 (1994).

[59] V. Ravindran and R. Blair, Worlds Poult. Sci. J. **49**, 219 (1993).

[60] C.A. Jones, R.T. Koenig, J.W. Ellsworth, B.D. Brown, and G.D. Jackson, Mont. State Univ. Ext. (2007).

[61] C.M. Solomon, J.L. Collier, G.M. Berg, and P.M. Glibert, Aquat. Microb. Ecol. **59**, 67 (2010).

[62] F.S. Mjalli and J. Naser, Asia-Pacific J. Chem. Eng. **10**, 273 (2015).

[63] R.B. Leron and M.-H. Li, Thermochim. Acta **530**, 52 (2012).

[64] S.L. Perkins, P. Painter, and C.M. Colina, J. Phys. Chem. B **117**, 10250 (2013).

[65] B. Doherty and O. Acevedo, J. Phys. Chem. B **122**, 9982 (2018).

[66] C. D'Agostino, R.C. Harris, A.P. Abbott, L.F. Gladden, and M.D. Mantle, Phys. Chem. Chem. Phys. **13**, 21383 (2011).

[67] J. Habasaki and K. Ngai, J. Chem. Phys. **129**, 194501 (2008).

[68] D.A. Turton, J. Hunger, A. Stoppa, G. Hefter, A. Thoman, M. Walther, R. Buchner, and K. Wynne, J. Am. Chem. Soc. **131**, 11140 (2009).

[69] J. Hunger, T. Sonnleitner, L. Liu, R. Buchner, M. Bonn, and H.J. Bakker, J. Phys. Chem. Lett. **3**, 3034 (2012).

[70] A.H. Turner and D. Kim, J. Chem. Phys. **149**, 174503 (2018).

[71] W. Huang and R. Richert, Philos. Mag. **87**, 371 (2007).

[72] Z. Hu and C.J. Margulis, Proc. Natl. Acad. Sci. **103**, 831 (2006).

[73] P.K. Mandal, M. Sarkar, and A. Samanta, J. Phys. Chem. A **108**, 9048 (2004).

[74] U. Kaatze and K. Giese, J. Phys. [E] **13**, 133 (1980).

[75] M.J. Abraham, T. Murtola, R. Schulz, S. Páll, J.C. Smith, B. Hess, and E. Lindahl, SoftwareX **1**, 19 (2015).

[76] S. Páll, M.J. Abraham, C. Kutzner, B. Hess, and E. Lindahl, in (Springer, 2014), pp. 3–27.

[77] H. Bekker, H. Berendsen, E. Dijkstra, S. Achterop, R. Van Drunen, D. Van der Spoel, A. Sijbers, H. Keegstra, B. Reitsma, and M. Renardus, in (World Scientific Singapore, 1993), pp. 252–256.

[78] L. Martínez, R. Andrade, E.G. Birgin, and J.M. Martínez, J. Comput. Chem. **30**, 2157 (2009).

[79] U. Essmann, L. Perera, M.L. Berkowitz, T. Darden, H. Lee, and L.G. Pedersen, J. Chem. Phys. **103**, 8577 (1995).

[80] B. Hess, H. Bekker, H.J. Berendsen, and J.G. Fraaije, J. Comput. Chem. **18**, 1463 (1997).

[81] G. Bussi, D. Donadio, and M. Parrinello, J. Chem. Phys. **126**, 014101 (2007).

[82] H.J. Berendsen, J. van Postma, W.F. van Gunsteren, A. DiNola, and J.R. Haak, J. Chem. Phys. **81**, 3684 (1984).

[83] R.W. Hockney, S. Goel, and J. Eastwood, J. Comput. Phys. **14**, 148 (1974).

[84] W. Humphrey, A. Dalke, and K. Schulten, J. Mol. Graph. **14**, 33 (1996).

[85] H. Shekaari, M.T. Zafarani-Moattar, and B. Mohammadi, J. Mol. Liq. **243**, 451 (2017).

[86] C.J.F. Böttcher and P. Bordewijk, *Theory of Electric Polarization* (Elsevier Science Limited, 1978).

[87] P.R. Bevington and D.K. Robinson, N. Y. **19692**, 235 (1969).

[88] J.-P. Hansen and I.R. McDonald, *Theory of Simple Liquids* (Elsevier, 1990).

[89]J. Soc. Chem. Ind. **48**, 1036 (1929).

[90] K. Seki, B. Bagchi, and M. Tachiya, Phys. Rev. E **77**, 031505 (2008).

[91] D. Laage and J.T. Hynes, Science **311**, 832 (2006).

[92] S. Das, B. Mukherjee, and R. Biswas, J. Chem. Phys. **148**, 193839 (2018).

[93] S. Das, R. Biswas, and B. Mukherjee, J. Phys. Chem. B **119**, 11157 (2015).

[94] S. Das, R. Biswas, and B. Mukherjee, J. Phys. Chem. B **119**, 274 (2015).

[95] A. Luzar and D. Chandler, Phys. Rev. Lett. **76**, 928 (1996).

[96] A. Luzar and D. Chandler, Nature **379**, 55 (1996).

[97] A. Luzar, J. Chem. Phys. **113**, 10663 (2000).

[98] D. Rapaport, Mol. Phys. **50**, 1151 (1983).

[99] S. Indra and R. Biswas, Mol. Simul. **41**, 471 (2015).

[100] A. Chandra, Phys. Rev. Lett. **85**, 768 (2000).

[101] T. Pal and R. Biswas, J. Chem. Phys. **141**, 104501 (2014).

[102] T. Pal and R. Biswas, J. Phys. Chem. B **119**, 15683 (2015).

[103] A. Baksi, P.K. Ghorai, and R. Biswas, J. Phys. Chem. B **124**, 2848 (2020).

[104] T. Pal and R. Biswas, Theor. Chem. Acc. **132**, 1348 (2013).

[105] F. Faupel, W. Frank, M.-P. Macht, H. Mehrer, V. Naundorf, K. Rätzke, H.R. Schober, S.K. Sharma, and H. Teichler, Rev. Mod. Phys. **75**, 237 (2003).

[106] M.S. Shell, P.G. Debenedetti, and F.H. Stillinger, J. Phys. Condens. Matter **17**, S4035 (2005).

[107] K. Kim and S. Saito, J. Chem. Phys. **133**, 044511 (2010).

[108] G. Szamel and E. Flenner, Phys. Rev. E **74**, 021507 (2006).

[109] K. Kim and S. Saito, J. Chem. Phys. **138**, 12A506 (2013).

[110] N. Lačević, F.W. Starr, T. Schrøder, and S. Glotzer, J. Chem. Phys. **119**, 7372 (2003).

[111] S. Franz and G. Parisi, J. Phys. Condens. Matter **12**, 6335 (2000).

[112] C. Donati, S. Franz, S.C. Glotzer, and G. Parisi, J. Non-Cryst. Solids **307**, 215 (2002).

[113] C. Toninelli, M. Wyart, L. Berthier, G. Biroli, and J.-P. Bouchaud, Phys. Rev. E **71**, 041505 (2005).

[114] A.M. Funston, T.A. Fadeeva, J.F. Wishart, and E.W. Castner, J. Phys. Chem. B **111**, 4963 (2007).

[115] B. Bagchi, *Molecular Relaxation in Liquids* (OUP USA, 2012).

[116] B. Bagchi, Annu. Rev. Phys. Chem. **40**, 115 (1989).

[117] T. Hofmann, D. Wallacher, M. Mayorova, R. Zorn, B. Frick, and P. Huber, J. Chem. Phys. **136**, 124505 (2012).

[118] D.W. McCall, D.C. Douglass, and E.W. Anderson, J. Chem. Phys. **31**, 1555 (1959).

[119] G.K. Youngren and A. Acrivos, J. Chem. Phys. **63**, 3846 (1975).

[120] J.T. Edward, J. Chem. Educ. **47**, 261 (1970).

[121] C. Hu and R. Zwanzig, J. Chem. Phys. **60**, 4354 (1974).

[122] S. Das, R. Biswas, and B. Mukherjee, J. Chem. Phys. **145**, 084504 (2016).

[123] J.E. Variyar, D. Kivelson, and R.M. Lynden-Bell, J. Chem. Phys. **97**, 8549 (1992).

[124] T. Pal and R. Biswas, J. Chem. Phys. **141**, 164502 (2014).

[125] S. Indra, B. Guchhait, and R. Biswas, J. Chem. Phys. **144**, 124506 (2016).

[126] S. Indra and R. Biswas, J. Phys. Chem. B **120**, 11214 (2016).

[127] J. Hunger, A. Stoppa, S. Schrödle, G. Hefter, and R. Buchner, ChemPhysChem **10**, 723 (2009).

[128] Y. Marcus, *The Properties of Solvents* (1998).

[129] K. Tielrooij, D. Paparo, L. Piatkowski, H. Bakker, and M. Bonn, Biophys. J. **97**, 2484 (2009).

[130] R. Buchner and G. Hefter, Phys. Chem. Chem. Phys. **11**, 8984 (2009).

[131] R. Buchner, G.T. Hefter, and P.M. May, J. Phys. Chem. A **103**, 1 (1999).

[132] Herbert· Fr 鑌 hlich, *Theory of Dielectrics: Dielectric Constant and Dielectric Loss* (Clarendon Press, 1958).

[133] R. Brown, P. Godfrey, and J. Storey, J. Mol. Spectrosc. **58**, 445 (1975).

[134] E. Cavell, P. Knight, and M. Sheikh, Trans. Faraday Soc. **67**, 2225 (1971).

[135] B. Wurm, C. Baar, R. Buchner, and J. Barthel, J. Mol. Liq. **127**, 14 (2006).

[136] Y.J. Chang and E.W. Castner Jr, J. Chem. Phys. **99**, 113 (1993).

Chapter 5

Dynamic Heterogeneity in a Naturally Abundant Deep Eutectic Solvent [Betaine + Urea + Water]: A Molecular Dynamics Simulation Study

5.1 Introduction

During the past few decades, designing environment-friendly solvents or solvent systems for large scale industrial applications have been an area of intense research. Ionic liquids (ILs)[1] and deep eutectic solvents (DESs)[2–9] are two such liquid systems, which act as alternatives to common organic solvents for many chemical reactions because of their favourable physico-chemical properties such as low vapor pressure, less toxicity etc. DESs are more preferred over ionic liquids because of their low cost, easy synthesis protocol and transportation. [2–9] A combination of biodegradability and reduced toxicity makes several members of this class of solvents as "green solvents". DESs are the mixtures of two or more components at a certain proportion, which has a melting point much lower than the individual melting point of their components [3]. Appropriate selection of the mixture constituents and composition[10–12] helps to achieve the required properties of a targeted DESs. Hence, the choice of constituents for preparation of DESs is critically important. Naturally abundant compounds such as amino acids, urea, sugars etc [2,13–18] as mixture constituents render the eco-sustainability and greenness of the DESs and the resultant DESs are termed as naturally abundant deep eutectic solvents (NADESs) [15,19–25].

An interesting and eco-friendly NADESs have been prepared [26] by using betaine, urea and water at appropriate mole or weight fractions, and the molten phase studied recently by employing time-resolved fluorescence spectroscopy. Betaine is a trimethyl derivative of glycine amino acid and it is present in plants, mammals, invertebrates, bacteria and in various food materials [27,28]. Application of betaine is involved in many biochemical reactions [29], where it is used as a source of methyl group and also in the treatment of many diseases [30–32]. The

second component of the present DES, urea, the most commonly used nitrogenous fertilizers, is known to influence protein stability and functionality [33–35]. As betaine and urea act respectively as osmolyte and protein denaturant, their mutual interactions have an important role in protein stabilization [36,37]. This introduces biological relevance to this NADES [26] and may act as an additional motivation to study this tri-component molten mixture.

There are many studies, where the physical properties of betaine or urea based deep eutectic solvents (DESs) have been investigated [3,38–42] and their applications in the field of biomedical usage [43], protein stabilization[42,44] and extraction of various bioactive compounds [45] have been discussed. The utilisation of any class of solvents can be smarter if the interactions and dynamics are appropriately understood. Attempts to understand them have already been made for several DESs by employing various experimental tools such as dielectric relaxation [12,46,47], pulse field gradient NMR [48,49], time-resolved fluorescence [11,47,50,51], 2D-IR [52] measurements and also through several computer simulation studies [53–57]. However, studies investigating the interaction and dynamics of naturally abundant deep eutectic solvents (NADESs) are still limited. Temperature dependent steady state and time-resolved fluorescence measurements have been performed to explore the interactions and relaxation dynamics in [Bet+Ure+Wat] NADES. This particular system was prepared by mixing betaine, urea and water in (11.7:12:1) weight ratio. Note here that water is present in this DES as an integral yet minor component, and therefore this system is completely different from aqueous solutions of DES. The study reported there has suggested substantial deviation from the hydrodynamic viscosity dependence of solute solvation and rotation times via showing a fractional viscosity dependence with fraction power, $p \approx 0.5 - 0.7$ [26]. This reflects presence of pronounced dynamic heterogeneity in these DESs. Such an experimental observation has motivated us to perform a detailed analysis of structure and dynamics of this DES by employing computer simulations. We have performed molecular dynamics simulations of the experimental [Bet+Ure+Wat] DES at T = 328 K, in order to understand the fractional viscosity dependence of solvation and rotation rates in terms of molecular length-scale structure and microscopic dynamics that are defining this DES.

5.2 Force Field and Simulation Details

The chemical structures of betaine, urea and water of [Bet+Ure+Wat] DES are provided in Figure 5.A.1 (Appendix 5.A). GROMACS 4.5.4[58–60] simulation package was used for simulation purpose. Simulations were done at 328 K. OPLS-AA force field parameters [61–64] were used for representing the urea and betaine, whereas the water molecules were described by the extended single point charge model, SPC/E [63].

The functional forms of urea and betaine FF are given by the following,

$$E_{bonds} = \sum_i k_{b,i}(r_i - r_{0,i})^2 \tag{5.1}$$

$$E_{angles} = \sum_i k_{\theta,i}(\theta_i - \theta_{0,i})^2 \tag{5.2}$$

$$E_{torsion} = \sum_i \left[\frac{1}{2}V_{1,i}(1 + cos\varphi_i) + \frac{1}{2}V_{2,i}(1 - cos2\varphi_i) + \frac{1}{2}V_{3,i}(1 + cos3\varphi_i) + \frac{1}{2}V_{4,i}(1 - cos4\varphi_i)\right] \tag{5.3}$$

$$E_{nonbond} = \sum_i \sum_{j>1} \left\{\frac{q_i q_j e^2}{r_{ij}} + 4\varepsilon_{ij}\left[\left(\frac{\sigma_{ij}}{r_{ij}}\right)^{12} - \left(\frac{\sigma_{ij}}{r_{ij}}\right)^{6}\right]\right\} \tag{5.4}$$

To obtain the experimentally obtained deep eutectic weight ratio (11.7:12:1) of this DES [26], 100 molecules of betaine, 200 molecules of urea and 56 molecules of water were considered. Also, simulation for neat water has been done at 328 K. For every water molecule then there exist approximately five molecules of the other two species together. The initial configurations were built via using the Packmol [65] software and after that those configurations were energy minimized in GROMACS using the steepest descent algorithm. Simulations were carried out in a cubic box employing the periodic boundary conditions. For short ranged interactions, the cut-off was set for 1.2 nm, and the long-ranged coulombic interactions were treated employing the Particle-Mesh Ewald (PME) summation [66] technique. To constrain all the covalent bonds, LINCS algorithm [67] with lincs order 8 was used. The optimized configurations were subjected to a number of equilibration steps using the NPT ensemble. First, the system was equilibrated at 500 K in this ensemble. Then the system was cooled down to 328 K in a stepwise manner with a step size of 50 K and each of these runs were for 500 ps long. Then the system was

equilibrated for 4 ns in the NPT ensemble to obtain the required density of the system, which is further followed by 2 ns run in the NVT ensemble. During the NPT equilibration run, temperature was maintained at 328 K using the v-rescale thermostat [68] with 0.5 ps time constant and pressure at 1 bar using the Berendsen barostat [69] with time constant of 2 ps. The equations of motion were solved by using the leapfrog algorithm with a time step of 2 fs. The production run was for 100ns in the NVT ensemble and the trajectories were saved every after 0.1 ps for data analyses. An additional NVT production run for 10 ns was performed for the H-bond dynamics analyses, where the velocities and trajectories were saved every after 0.01 ps. The simulated density (1.18 g/cm^3) was in well agreement with the available experimental density value (1.20 g/cm^3) [26] with a percentage error. The partial charges and Lennard-Jones parameters for betaine, urea and SPC/E water are described in Table 5.B.1 – 5.B.3 of Appendix 5.B respectively.

5.3 Results and Discussion

5.3.1 Microscopic View of Solution Structure: Radial Distribution Functions (RDFs)

5.3.1.1 Inter-species Radial Distribution Functions (RDFs)

Simulated radial distribution functions (RDFs), g(r) between various species in this [Bet+Ure+Wat] DES provide a microscopic view of the solution structure. The inter-species RDFs between various molecules in this DES are presented in Figure 5.1, where the RDFs are calculated for different atomic pairs.

The upper panel of Figure 5.1 shows the interaction between betaine and water molecules, where the most intense peak (with a peak height of ~ 10) has been obtained for the RDFs between O-atom of water (OW) and O-atom (O06/O07) of carboxylate (-COO$^-$) group of betaine ion, indicating stronger interaction between these two molecules. Therefore, this result suggests that water molecules in the present DES are mostly interacting with the betaine through the carboxylate (-COO$^-$) group.

Again, the interactions between betaine and urea are depicted in the middle panel of Figure 5.1. These RDFs suggest the least interactions between the O-atom of carbonyl group of urea and O-atoms (O06/O07) of carboxylate group of betaine ion. However, stronger interactions between betaine and urea molecules are evident from the higher peak heights (~ 2.5) of RDFs between N-atoms of urea and O-atoms of betaine, suggesting H-bonding interaction between them.

In addition, the RDFs between O-atom (OW) of water and different atoms of urea are presented in the lower panel of Figure 5.1. The following observations can be made from this figure: (i) the first peak for RDFs between OW-atom of water and HT/HC atoms of urea appear at distance ~ 2.3 Å and the peak intensities for OW-HT and OW-HC are ~ 1.3 and ~ 0.8 respectively, (ii) RDF between OW and N-atom of urea occur at ~ 3.3 Å with intensity ~ 1.8 and (iii) interaction between the OW and O-atom of urea is the least, where the peak appears at a larger distance (~ 5.2 Å). The interaction between the hydrogen atom of $-NH_2$ group in the trans orientation to the urea O-atom and the O-atom (OW) of water molecules at shorter distances indicates H-bonding interaction between these two molecules.

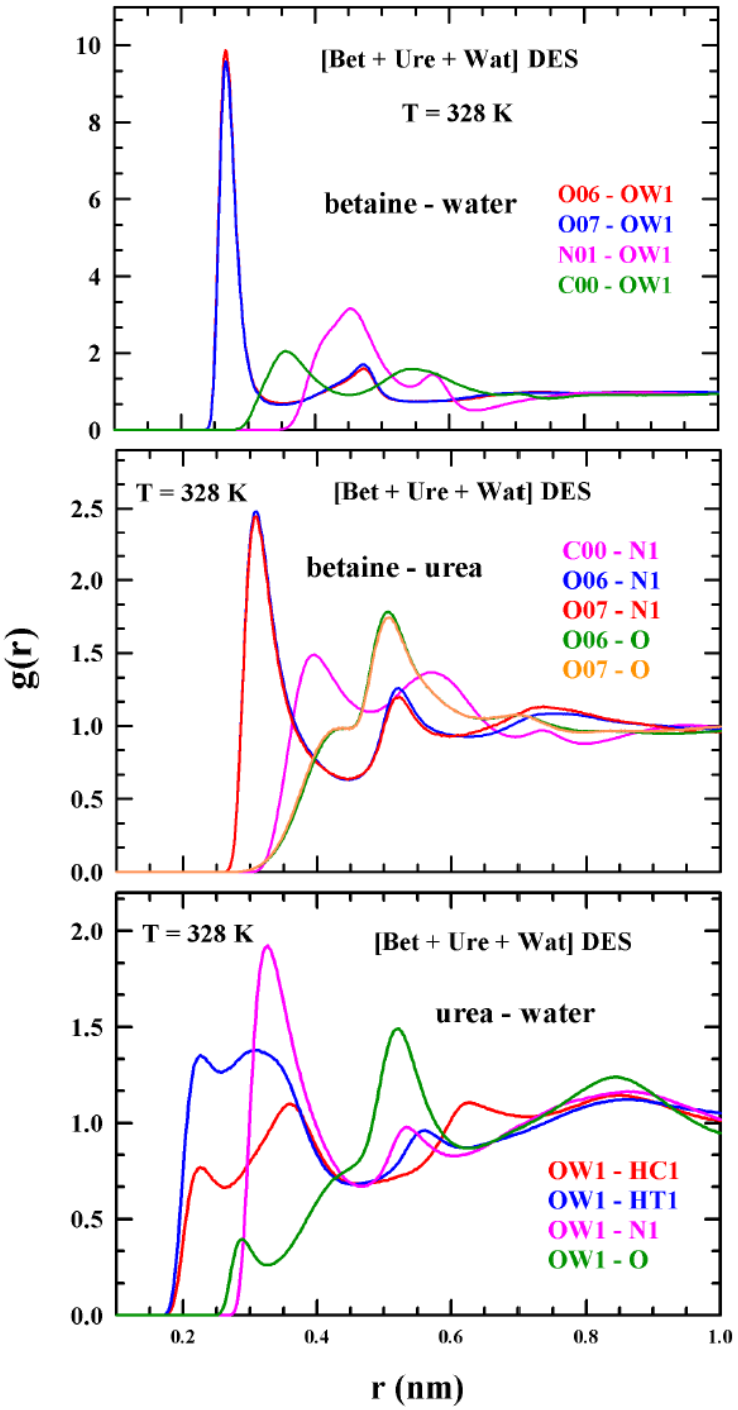

Figure 5.1: Simulated RDFs between betaine – water (upper panel), betaine – urea (middle panel) and urea – water (lower panel) in [Bet+ Ure+Wat] DES at 328 K. Note that these RDFs are calculated between various atomic sites of these pairs.

5.3.1.2 Intra-species Radial Distribution Functions (RDFs)

Figure 5.2 presents the interactions between the different atomic sites of water – water (upper panel), urea – urea (middle panel) and betaine – betaine (lower panel) pairs at 328 K. The upper panel of Figure 5.2 depicts oxygen-oxygen (OW-OW) RDFs between water molecules in DES and that in neat water. It shows a very high and intense first peak ($g(r) \approx 9$) for water molecules in this DES, which is ~ 4 times higher than that in neat water, suggesting the clustering of water molecules in this DES system.

Middle panel of Figure 5.2 shows the interaction between urea molecules via the RDFs between various atomic sites of urea. The first RDF peak for N-atom of one urea molecule and O-atom of another urea molecule appears at a distance of ~ 3.2 Å with peak-height ~ 1.6, suggesting the H-bond interactions between H-atom of -NH_2 group and O -atom of urea molecules.

The RDFs between different atoms of betaine molecules are shown in the lower panel of Figure 5.2, where the RDF peaks for N ($N(CH_3)_3$) and O (COO^-) atoms with peak height of ~1.6 indicates weaker interaction between the betaine molecules. Because of the absence of polar H-atoms, betaine molecules are unable to form H-bonds among themselves.

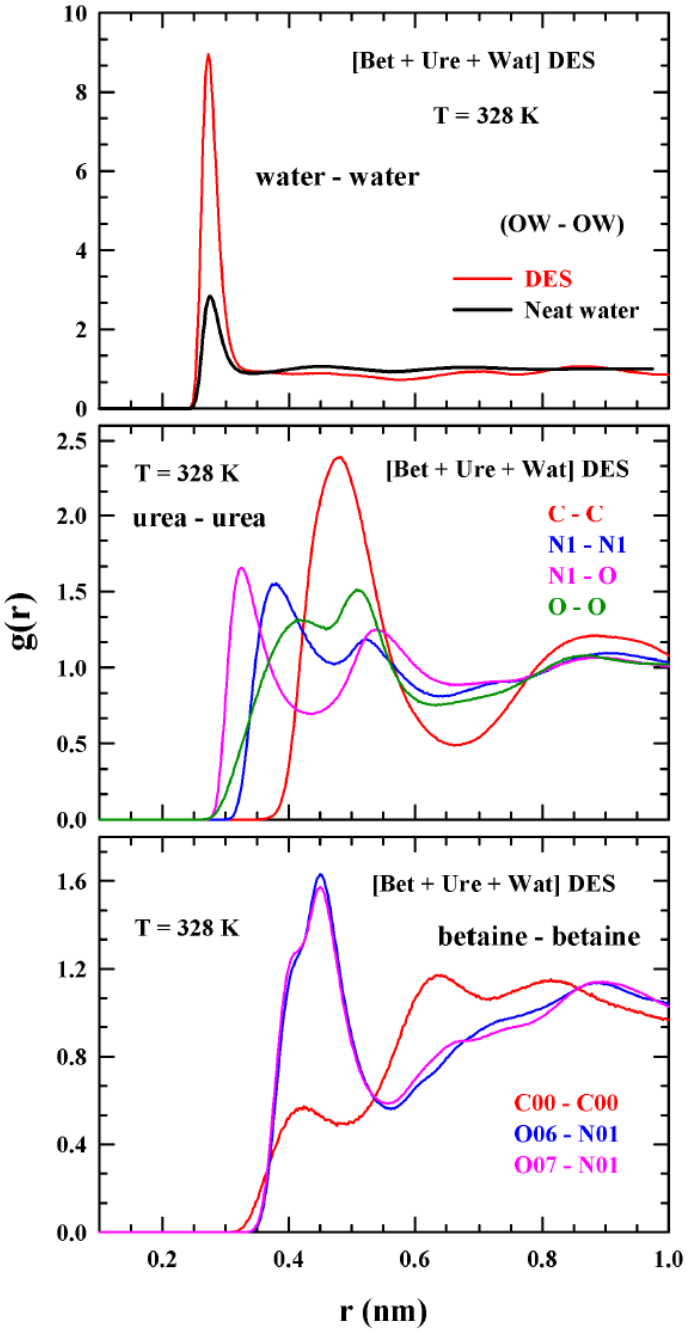

Figure 5.2: Simulated RDFs between water – water (upper panel), urea – urea (middle panel) and betaine – betaine (lower panel) in [Bet+ Ure+Wat] DES at 328 K. Here, the RDFs are calculated between various atomic sites of these pairs. Note the water – water RDFs (black line) in neat water at 328 K is shown in the upper panel for comparison.

5.3.2 Translational Dynamics

5.3.2.1 Mean Square Displacements (MSDs) and Rattling-in-cage Motion

Center-of-mass mean square displacements (MSDs) of betaine, urea and water molecules in [Bet+Ure+Wat] DES at 328 K can be calculated via the following relation[70–72],

$$\langle \delta r^2(t) \rangle = \langle N^{-1} \sum_{i=1}^{N} |\Delta r_i^c(0,t)|^2 \rangle \quad (5.5)$$

Here, r_i^c indicates the center-of-mass of particle i. Simulated MSDs show multiple time dependencies as $MSD \propto t^{\beta}$ and it is associated with three different time regimes - (i) $\beta = 2$ at short times indicating inertial motion, (ii) $\beta < 1$ at intermediate times denoting subdiffusive motion and (iii) $\beta = 1$ long time indicating diffusive dynamics. The simulated MSDs for all the particles in this DES are presented in the upper panel of Figure 5.3, which demonstrates the appearance of sub-diffusive regime at intermediate times. This suggests the rattling-in-cage motion. Note the evidence of such cage-rattling suggests the existence of multiple relaxation time scales in this DES and signals the heterogeneous nature of the system. Earlier experimental observation of fractional viscosity dependence of solute rotation and solvation times [26], $\langle \tau_s/\tau_r \rangle \propto (\eta/T)^p$ with p = 0.5 – 0.7, correlates with this heterogeneous centre-of-mass particle displacements. The simulated dynamical heterogeneity markers explained in next section provide further support to this view.

Next, we calculate the diffusion coefficients for betaine, urea and water in this DES via the Einstein relation [72],

$$D = \lim_{t \to \infty} \frac{\langle \Delta r^2(t) \rangle}{6t} \quad (5.6)$$

The diffusive limit can be determined from the time dependence of the simulated MSDs, $\beta(t)$, which is indicated in the lower panel of Figure 5.3. The time dependence of MSDs can be accessed by,

$$\beta(t) = \frac{d}{d[\ln(t)]} = [ln\langle \Delta r^2(t) \rangle \quad (5.7)$$

The lower panel of Figure 5.3 clearly shows a pronounced sub-diffusive regime for the component particles in this DES, where the diffusive limit (hydrodynamic limit, $\beta = 1$) have been reached at time scales $\sim$10 ns. The calculated diffusion coefficient values for all the particles in the diffusive limit are provided in Table 5.1. Also, the same for neat water at 328 K is given in this table for comparison. This table indicates the strikingly slower diffusion of water in this DES (~ 500 time slower) than that in neat water.

In addition, normalized velocity autocorrelation functions (VACFs) [73,74], $C_v^N(t) = \frac{\langle v(t).v(0)\rangle}{\langle v(0).v(0)\rangle}$ for betaine, urea and water in this DES are presented in Figure 5.4. It shows that the VACF decays enter into the negative region (because of backscattering from the cage), signifying rattling-in-cage motion of the particles. Moreover, the comparison of VACF decay for water in the present DES with that in neat condition suggests that the short-time dynamics of water in DES is drastically different from that in neat water.

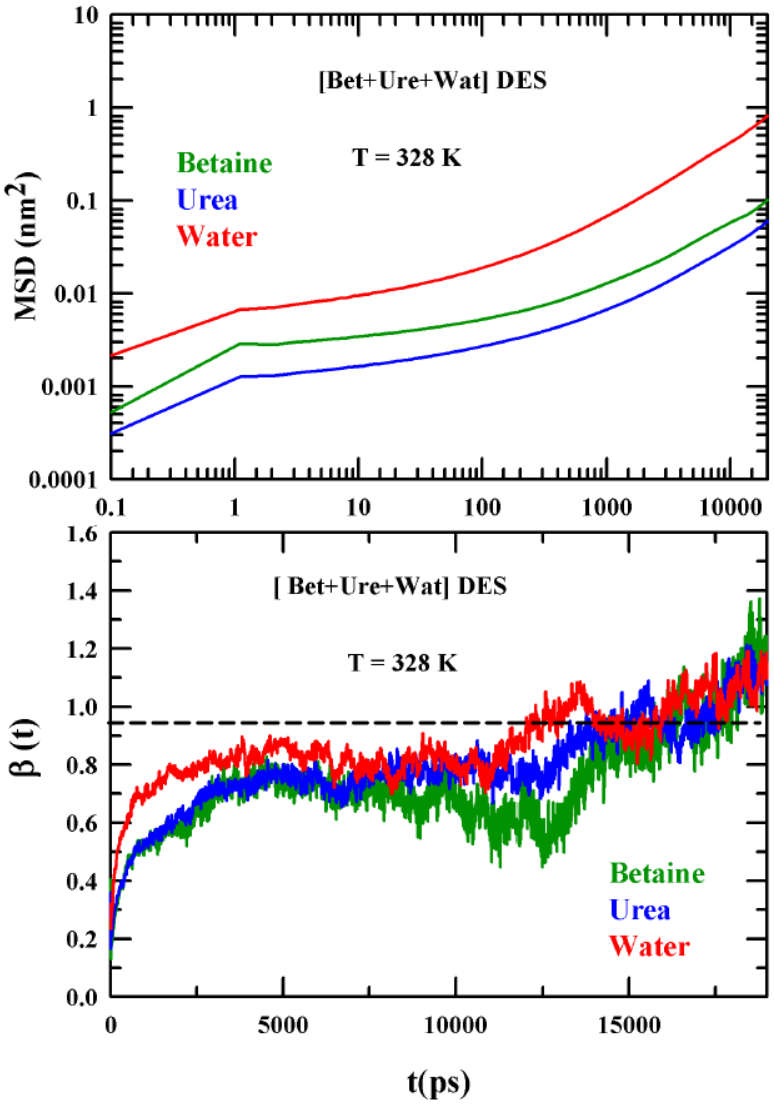

Figure 5.3: The upper panel presents simulated mean square displacements (MSDs) for center-of-mass of betaine, urea and water molecules in [Bet + Ure + Wat] DES at T = 328 K. The lower panel shows the time dependence of the exponent β in this DES, where the black dashed-line indicates the hydrodynamic limit.

Table 5.1: Diffusion coefficient values obtained from linear fitting of the MSDs for betaine, urea and water molecules in [Bet+Ure+Wat] DES at 328 K.

	D_{Bet} $(\times 10^{-12} m^2 sec^{-1})$	D_{Ure} $(\times 10^{-12} m^2 sec^{-1})$	D_{Wat} $(\times 10^{-9} m^2 sec^{-1})$
[Bet+Ure+wat] DES at 328 K	0.764	0.475	0.0067
Water (SPC/E) at 328 K	-	-	3.255

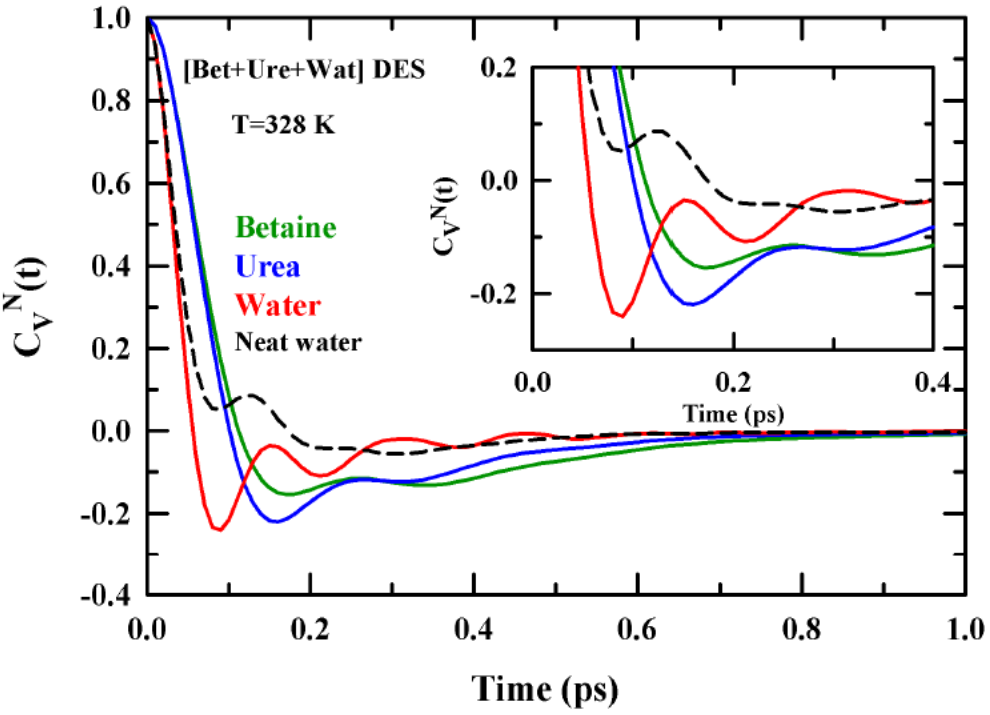

Figure 5.4: Normalized velocity autocorrelation functions (VACFs) for betaine, urea and water in [Bet+Ure+Wat] DES at 328 K. Also, the VACF for neat water is shown by black dashed line for comparison. The inset presents the VACF after zooming on the negative amplitudes to show more clearly the rattling-in-cage motion of particles in this DES.

5.3.2.2 Dynamic Heterogeneity (DH): Emergence of non-Gaussian and new non-Gaussian Features

Heterogeneous dynamics in this DES can be tracked via the calculations of non-Gaussian [75,76], $\alpha_2(t)$ and new non-Gaussian [70,77], $\gamma(t)$ parameters, which can be obtained via the following,

$$\alpha_2(t) = \frac{3\langle \delta r^4(t) \rangle}{5\langle \delta r^2(t) \rangle^2} - 1 \tag{5.8}$$

$$\gamma(t) = \frac{1}{3}\langle \delta r^2(t) \rangle \left\langle \frac{1}{\delta r^2(t)} \right\rangle - 1 \tag{5.9}$$

where $\langle \delta \mathrm{r}^2(\mathrm{t}) \rangle = \langle \mathrm{N}^{-1} \sum_{\mathrm{i}=1}^{\mathrm{N}} |\Delta \mathrm{r}_\mathrm{i}(0,\mathrm{t})^2| \rangle$ and $\langle \delta \mathrm{r}^4(\mathrm{t}) \rangle = \langle \mathrm{N}^{-1} \sum_{\mathrm{i}=1}^{\mathrm{N}} |\Delta \mathrm{r}_\mathrm{i}(0,\mathrm{t})^4| \rangle$.Here, $\Delta \mathrm{r}_\mathrm{i}(0,\mathrm{t}) = \mathrm{r}_\mathrm{i}(\mathrm{t}) - \mathrm{r}_\mathrm{i}(0)$ describes the displacement vector for the i^{th} particle in a system containing N particles and δr is the distance over which a particle moved in time t.

In this type of system, the particles can have different mobilities and their displacements can be larger or smaller than those predicted by the Gaussian distributions for a homogeneous system. The non-Gaussian parameter, $\alpha_2(t)$ is associated with the more mobile particles, and it connects to the faster DH time scales obtained from the peak position of $\alpha_2(t)$. This timescale is known as non-Gaussian time scale (τ_{NG}). There exists another, slower, timescale which is associated with the smaller displacements (relatively less mobile particles). This timescale is denoted as τ_{NNG}, which can be obtained from the peak position of the new non-Gaussian parameter, $\gamma(t)$.

The simulated $\alpha_2(t)$ (upper panel) and $\gamma(t)$ (lower panel) for betaine, urea and water in this DES at 328 K are presented in Figure 5.5 and the same for neat water are also shown for a comparison. The upper panel indicates that the $\alpha_2(t)$ peak heights for all the particles are higher than the peak height predicted for homogeneous liquids (~0.2) [75], reflecting dynamically heterogenous nature of the DES. The values of the non-Gaussian timescale (τ_{NG}) and the new non-Gaussian timescale (τ_{NNG}) are summarized in Table 5.2. Data in this table suggest that τ_{NG} and τ_{NNG} for betaine, urea and water occur in the range 0.3–3 ns and 2–14 ns respectively. Interestingly, such slower time scales can explain the emergence of the nanosecond timescales measured in the dynamic Stokes shift and fluorescence anisotropy measurements [26] of these

systems using a fluorescent solute. Moreover, the upper panel of Figure 5.5 and Table 5.2 clearly demonstrate that τ_{NG} for water in the DES undergo a dramatic increase relative to those in neat water, where the τ_{NG} for water in DES ~ 400 times slower than that in neat water. Again, severe slowing down of new non-Gaussian time scale (τ_{NNG}) for water in DES occurs, which is ~ 1800 times slower than that in neat water (see Table 5.2). The slowing down of DH timescales for water molecules in such a crowded environment suggests that dynamics water in DES is drastically different than in the neat system.

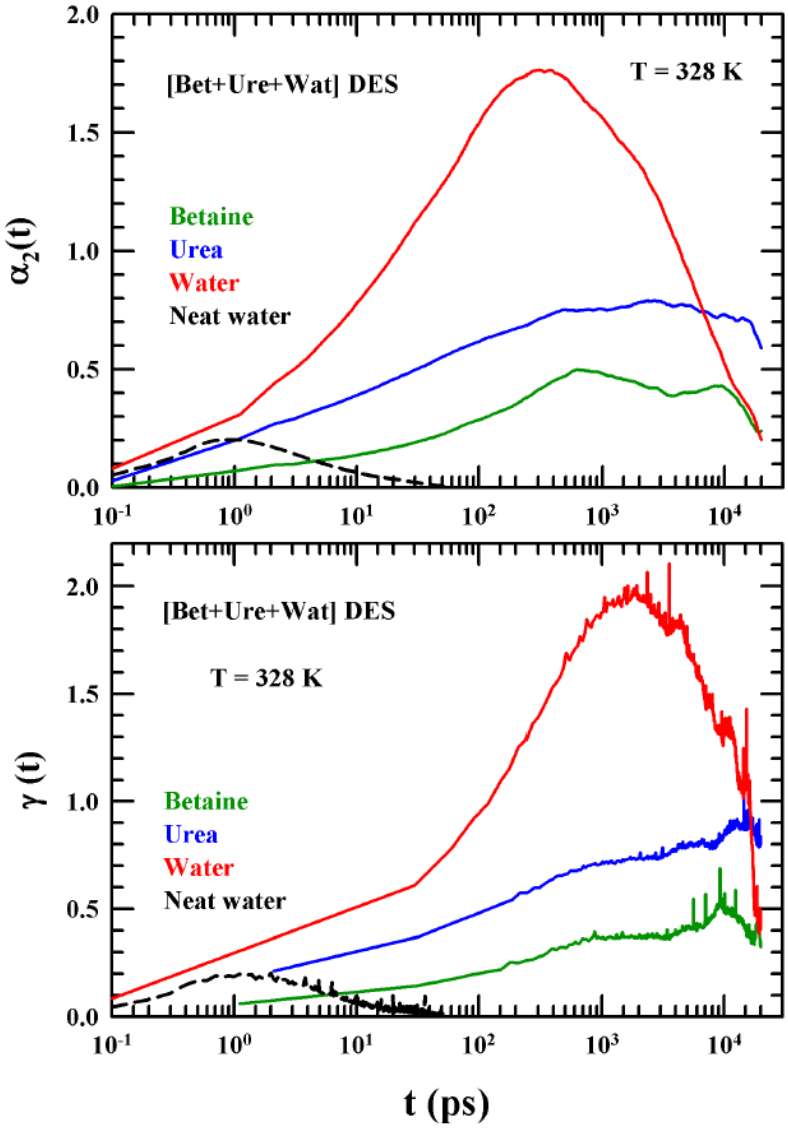

Figure 5.5: Simulated $\alpha_2(t)$ (upper panel) and $\gamma(t)$ (lower panel) for betaine, urea and water in [Bet+Ure+Wat] DES at 328 K. Note $\alpha_2(t)$ and $\gamma(t)$ for neat water are shown in the respective figures.

Table 5.2: Non-Gaussian (τ_{NG}) and new Non-Gaussian timescales (τ_{NNG}) for betaine, urea and water molecules in [Bet+Ure+Wat] DES

	Betaine (ns)	Urea (ns)	Water (ns)	Neat water (ns)
τ_{NG}	0.682	2.82	0.336	~ 0.0008
τ_{NNG}	9.69	14.00	1.89	~ 0.001

5.3.2.3 Self-Intermediate Scattering Function: Inherent Slow Relaxation Time scales

To track the density fluctuation at a given space point, self-intermediate scattering function, $F_s(k,t)$ can be calculated from the real part of the incoherent scattering function[72,77,78] as follows,

$$F_s(k,t) = N^{-1}\sum_i \langle \cos k \times [r_i(t) - r_i(0)] \rangle \quad (5.10)$$

Note $F_s(k,t)$ relaxations are calculated in the limit of the nearest neighbour wavenumber ($k\sigma \rightarrow 2\pi, \sigma$ being the diameter). The e^{-1} decay times of these relaxations provide an estimate of α-relaxation (structural relaxation) time scale, τ_α. The simulated $F_s(k\sigma \rightarrow 2\pi, t)$ profiles for betaine, urea and water molecules in [Bet+Ure+Wat] DES are presented in Figure 5.6, where the corresponding e^{-1} decay time scales are indicated by bullet marks and also these values are summarized in Table 5.3. In Figure 5.6, the $F_s(k\sigma \rightarrow 2\pi, t)$ relaxation for neat water is also shown to realize how the relaxation dynamics of water differs in crowded environment. It is clear from Figure 5.6 and Table 5.3 that there exists much longer α-relaxation time scale (τ_α) for betaine and urea in this DES at 328 K, which lie between ~ 6-17 ns. However, τ_α for water in this DES is approximately 400 times slower than that in neat water.

Next, we compare the diffusion on-set time scales of all the component particles in this DES obtained from simulated MSDs and structural relaxation time scales from $F_s(k\sigma \rightarrow 2\pi, t)$

relaxation in Table 5.3. The approximate diffusion-on-set time scales from MSDs ($\tau_{MSD,\beta}$) are obtained from the time at which $\beta \cong 1$ in the relation, $MSD \propto t^{\beta}$ and as discussed earlier, the structural relaxation time scales (τ_{α}) can be approximated as the e^{-1} decay time of $\mathrm{F_s(k,t)}$ relaxations. For homogeneous liquids, diffusion is expected to occur at timescale similar to this structural relaxation timescale, as after τ_{α}, particle displacements occur only via the diffusive motion. This can be approximated as, $(\mathrm{F_s(k\sigma \rightarrow 2\pi, t) = F_s(k\sigma \rightarrow 2\pi, t = 0)exp\,[-D(k\sigma)^2 t]}$. Deviation from such 1:1 correlation between these two timescales may indicate the heterogeneous relaxation dynamics in a given system. Table 5.3 indicates that these two timescales do not agree, which provides a support to the view of heterogeneous relaxation dynamics in this DES. Also, the relaxation dynamics of water in this DES becomes more heterogeneous than that of neat water, for which the τ_{α} (~ 0.0005 ps) is comparable to the diffusion on-set time scales from MSDs (~ 0.001 ps).

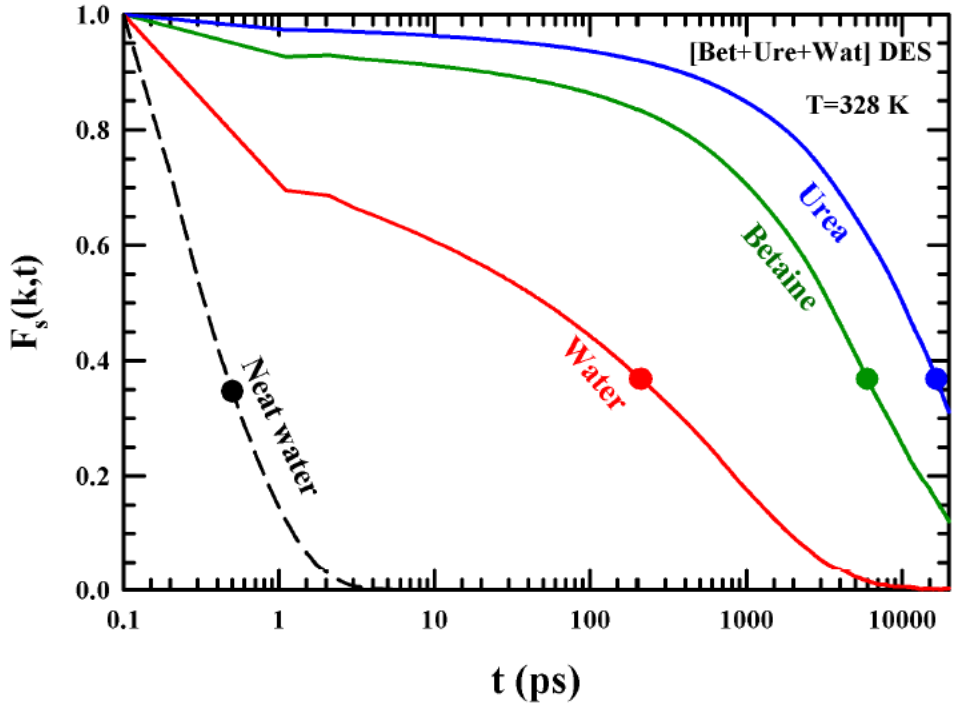

Figure 5.6: Normalized self-part of the intermediate scattering function at the nearest neighbour ($k\sigma \rightarrow 2\pi$), $F_s(k,t)$ for betaine, urea and water in [Bet+Ure+Wat] DES at 328 K. Also, the $F_s(k,t)$ profile for neat water are shown for a comparison. Note the respective e^{-1} decay times are indicated by bullet marks.

Table 5.3: Structural relaxation timescales, τ_α obtained from the simulated $F_s(k\sigma \rightarrow 2\pi, t)$ relaxations and diffusion on-set time scales, $\tau_{MSD,\beta}$ MSDs for all the particles in [Bet+Ure+Wat] DES and for neat water at 328 K.

	Betaine (ns)	Urea (ns)	Water (ns)	Neat water (ns)
τ_α	5.9	16.6	0.21	~ 0.0005
$\tau_{MSD,\beta}$	15.6	13.0	12.0	~ 0.001

5.3.2.4 Four-point Correlations

In slow viscous systems, the particles may have similar mobilities which form cooperative correlated regions. Four-point correlation function, $\chi_4(k, t)$ quantifies the temporal correlations of the local mobilities at two different space points over a certain period of time. Therefore, $\chi_4(k, t)$ can be calculated from the fluctuations of the self-intermediate scattering function, $F_s(k, t)$ [79–82] via the following equation,

$$\chi_4(k, t) = N[\langle F_s(k, t)^2 \rangle - \langle F_s(k, t) \rangle^2] \quad (5.11)$$

The maximum time over which the mobility fluctuations remain correlated is designated as, t_4^{max} and the peak position of $\chi_4(k, t)$ vs time profiles provide these time scales. The $\chi_4(k \rightarrow 2\pi, t)$ for betaine, urea and water in [Bet+Ure+Wat] DES are presented in Figure 5.7. The same for neat water is also shown for a comparison. The corresponding peak times, t_4^{max} , are provided in Table 5.4. Figure 5.7 indicates that the peak of $\chi_4(k \rightarrow 2\pi, t)$ could not be attained within this 20 ns time window employed in our simulations, but it suggests that the time scale may be longer than 20 ns. Interestingly, the correlated timescales for water in the present DES becomes ~ 475 times longer than that in neat water.

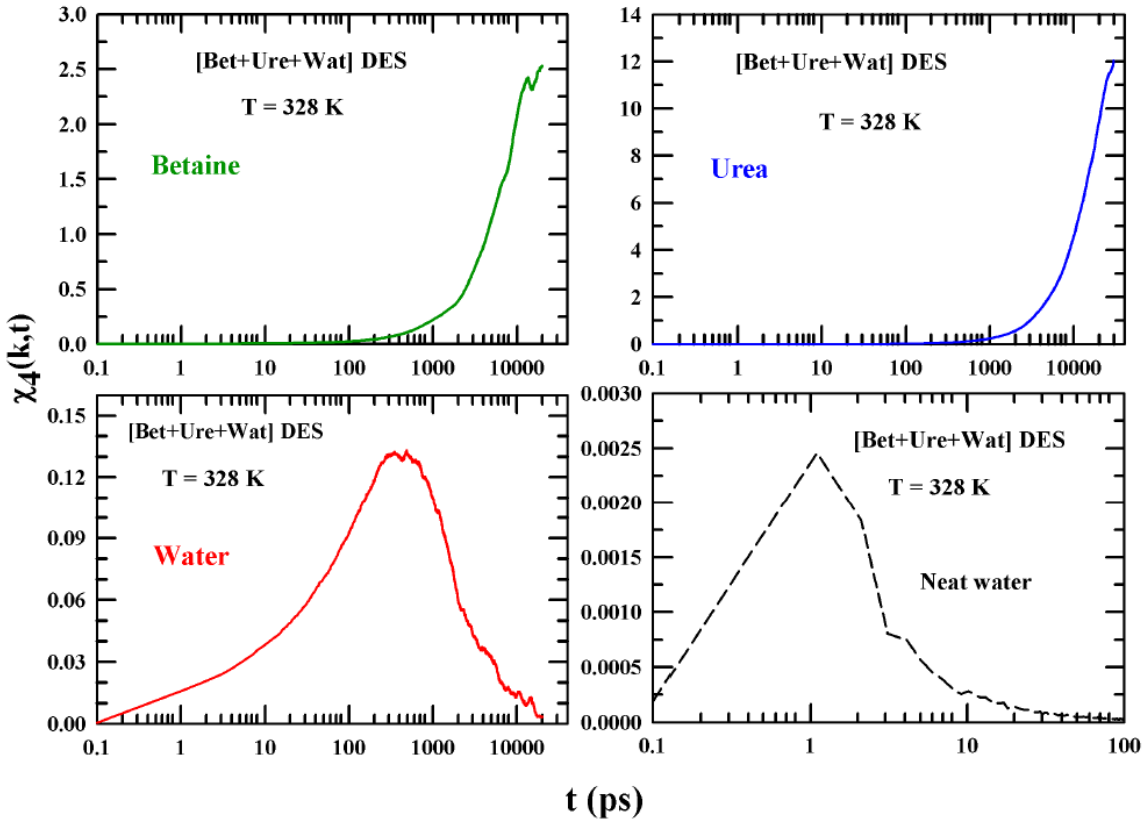

Figure 5.7: Simulated four-point correlation functions, $\chi_4(\mathrm{k},\mathrm{t})$ at nearest neighbour ($k\sigma \rightarrow 2\pi$) for betaine, urea and water in [Bet+Ure+Wat] DES at 328 K. Also, the $\chi_4(\mathrm{k},\mathrm{t})$ profile for neat water are shown for comparison.

Table 5.4: Correlated time scales t_4^{max} obtained from the peak positions of the corresponding $\chi_4(\mathrm{k},\mathrm{t})$ profiles for betaine, urea and water in [Bet+Ure+Wat] DES and that n neat water at 328 K.

Ion/molecule	t_4^{max} (ns)
Betaine	>20 ns
Urea	>20 ns
Water	0.57
Neat water	0.0012

5.3.3 Rotational Dynamics

5.3.3.1 Reorientational Correlation Functions, $C_l(t)$

The normalized reorientational time correlation function, $C_l(t)$ [72] can be calculated via the following relation,

$$C_l(t) = \frac{\langle P_l[\vec{u}_i(t).\vec{u}_i(0)]\rangle}{\langle P_l[\vec{u}_i(0).\vec{u}_i(0)]\rangle} \quad (5.12)$$

Here, P_l corresponds to the Legendre polynomial of rank *l* and $\vec{u}$ is the unit vector. The unit vector for betaine joins the C – O (-COO) atoms, and for urea it connects the two N-atoms of -NH_2 groups. The prediction from Debye's model suggests that for homogenous medium [83,84], the decay of the correlation function is single exponential and the reorientation correlation time can be expressed as,

$$\tau_l = [l(l+1)D_R]^{-1} \quad (5.13)$$

where D_R is the rotational diffusion co-efficient. Hence, for a Debye like rotation, the ratio of average reorientation correlation times of rank, *l* =1 & 2, $\langle\tau_{l=1}\rangle/\langle\tau_{l=2}\rangle = 3$ [83,84] and deviation from this value may suggest the presence of heterogeneous reorientation dynamics, which was previously observed for slow viscous liquid systems [54,85–87].

Figures 5.8 and 5.9 present the simulated reorientation correlation function, $C_1(t)$ and $C_2(t)$ for betaine (upper panel), urea (middle panel) and water (lower panel) in [Bet+Ure+Wat] DES at temperature 328 K. Note the $C_1(t)$ and $C_2(t)$ for neat water are shown in the lower panel of the respective figures. Also, two representative plots showing the comparison between different fit functions to describe the $C_1(t)$ and $C_2(t)$ decays are given in Figures 5.A.2 and 5.A.3 of Appendix 5.A. These plots suggest that the four exponential fit functions are needed to describe these correlation functions. The fitting parameters to these decays are summarized in Table 5.5

and these suggest the timescales in the range of picosecond to nano-seconds. Expectedly, the $C_2(t)$ decays are faster than $C_1(t)$ decays, as $C_1(t)$ is associated with angular displacement of 90° and $C_2(t)$ with ~ 54°. Table 5.5 suggest that the $C_1(t)$ and $C_2(t)$ for betaine, urea and water in the present DES provide timescales in the ranges of ~ 0.1 - 1.5 ps, ~ 10 - 150 ps, ~ 300 - 500 ps and ~ 3 – 5.5 ns. The sub-picosecond time scales are typically observed due to the inertial collective H-bond dynamics at short times [88,89], whereas the sub-nan second and multi-nanosecond timescales may originate from the structural H-bond relaxation dynamics in this DES. This could be the reason because in such extensively H-bonded system where every constituent is capable of forming H-bonds, reorientation of the particles occurs via breaking and reformation of multiple H-bonds. So, detailed analysis of continuous and structural H-bond relaxation dynamics in the present DES is important to understand the complete reorientation dynamics of this system. Also, experimental verification via dielectric relaxation measurements is needed to verify the model potential used in the present simulation.

In addition, the comparison of the simulated reorientational correlation functions, $C_l(t)$, for water in the present DES with that in neat water (see lower panel of Figures 5.8 and 5.9) indicates that average reorientation correlation times obtained from $C_1(t)$ and $C_2(t)$ decays for water in this DES are drastically slower (~ 800 and ~ 200 times respectively) than for neat water.

Next, the ratios of average reorientation correlation times from $C_l(t)$ decays of rank, l =1 and 2, ($\langle\tau_{l=1}\rangle/\langle\tau_{l=2}\rangle$) are provided in Table 5.6, which indicate substantial deviation from Debye's $l(l+1)$ law for stochastic angular displacements for betaine, urea and water in [Bet+Ure+Wat] DES at 328 K. This observation further supports the presence of dynamical heterogeneity in this DES.

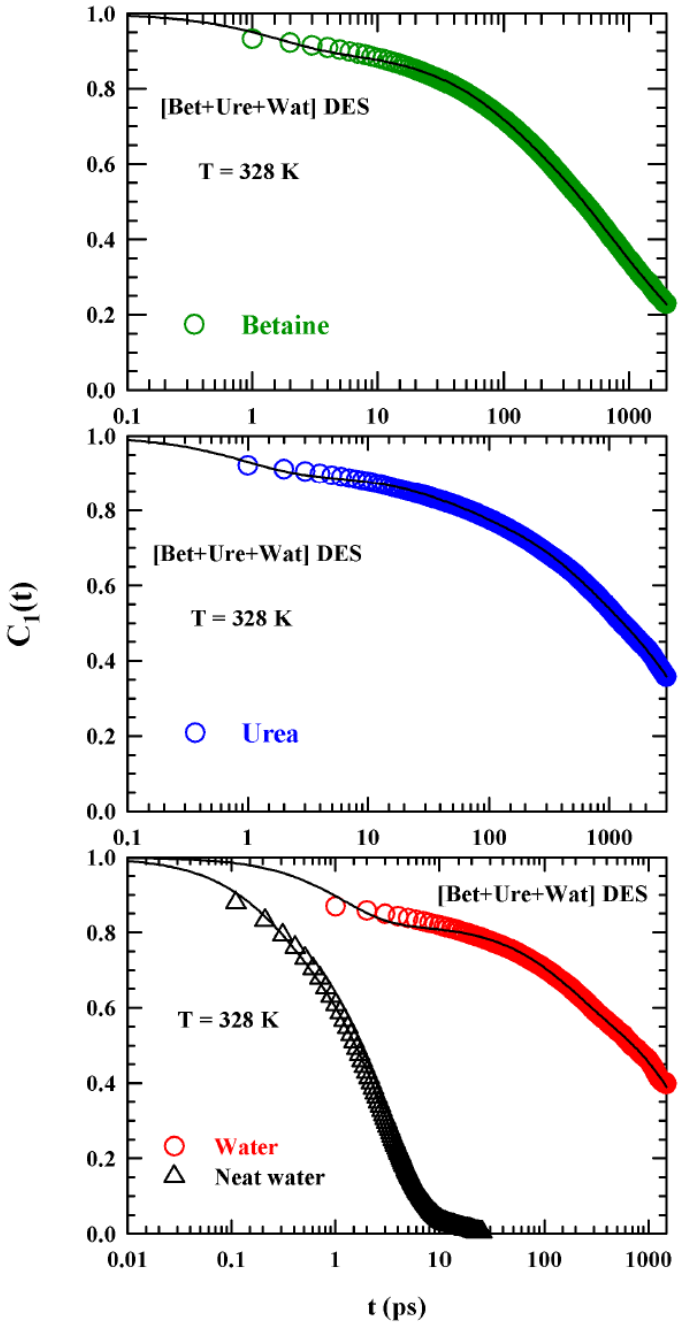

Figure 5.8: Simulated rank dependent reorientation correlation function of rank l = 1, **($C_1(t)$)** betaine (upper panel), urea (middle panel) and water (lower panel) in [Bet+Ure+Wat] DES at 328 K. Lines going through the data represent the fits to these data and the corresponding fit parameters are summarized in Table 5.5. Note the $C_1(t)$ decay for neat water is shown in the lower panel.

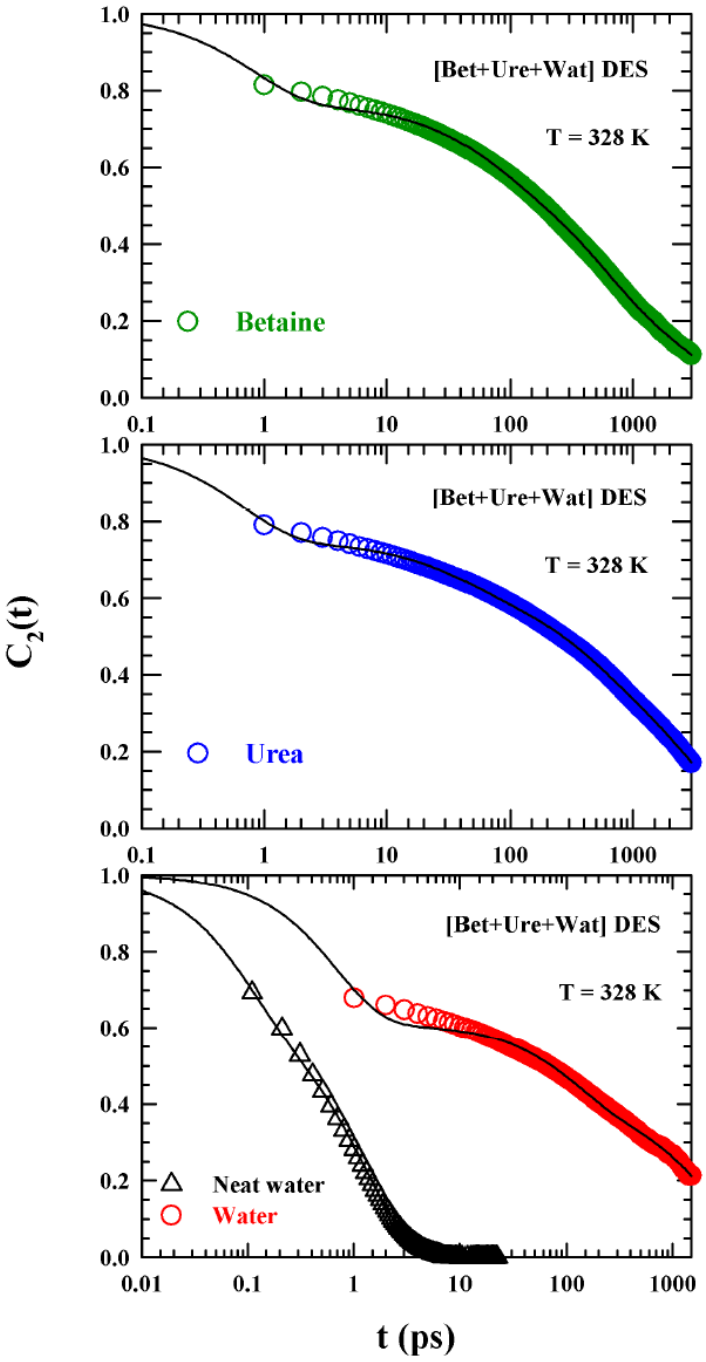

Figure 5.9: Simulated rank dependent reorientation correlation function of rank l = 2, **($C_2(t)$)** betaine (upper panel), urea (middle panel) and water (lower panel) in [Bet+Ure+Wat] DES at 328 K. Lines going through the data represent the fits to these data and the corresponding fit parameters are summarized in Table 5.5. Note the $C_2(t)$ decay for neat water is shown in the lower panel.

Table 5.5: Multi-exponential fit parameters describing the simulated rank (l) dependent reorientation correlation functions of rank l = 1, $C_1(t)$, and =2, $C_2(t)$, for betaine, urea and water in [Bet+Ure+Wat] DES and for neat water at 328 K.

$C_l(t)$	a_1	τ_1 (ps)	a_2	τ_2 (ps)	a_3	τ_3 (ps)	a_4	τ_4 (ps)	$\langle\tau\rangle$ (ps)[a]
$C_1(t)$									
Betaine	0.1	1.5	0.14	76	0.32	446	0.44	2990	1460
Urea	0.1	0.94	0.08	44	0.2	458	0.62	5460	3480
Water	0.2	1.2	0.2	150	0.6	3207	-	-	2028
Neat water	0.2	0.2	0.8	3	-	-	-	-	2.6
$C_2(t)$									
Betaine	0.23	0.8	0.15	62.5	0.33	481	0.29	3170	1070
Urea	0.25	0.7	0.12	39	0.19	380	0.44	3160	1480
Water	0.39	0.7	0.21	115	0.40	2390	-	-	974
Neat water	0.36	0.1	0.64	1.3	-	-	-	-	0.8

[a] Average reorientational correlation time, $\langle\tau\rangle = \sum_i a_i\tau_i$ with $\sum_i a_i = 1$.

Table 5.6: Ratios of the average simulated reorientational correlation times obtained from $C_l(t)$ of rank = 1 and 2 for betaine, urea and water in [Bet+Ure+wat] DES at 328 K.

[Bet+Ure+Wat] DES T=328 K	$\langle\tau_{l=1}\rangle/\langle\tau_{l=2}\rangle$
Betaine	1.36
Urea	2.35
Water	2.08

5.4 Conclusion

To summarize, our simulation study of a recently discovered betaine based naturally abundant deep eutectic solvents (DESs) [{Bet+Ure+Wat} (11.7:12:1)] at 328 K provide results explaining the solution structure and dynamics of these system via calculation of radial distribution functions (RDFs), translational diffusion, various dynamic heterogeneity features and reorientational relaxation. Also, the same for neat water has been simulated to understand, how the structure and dynamics of water molecules differ in this DES, where water molecules are located in a "crowded" environment. Simulated radial distribution functions (RDFs) between betaine and water indicate that the water molecules are strongly interacting with the betaine ion through its carboxylate group. Also, the H-bonding interaction between urea and water is evident from the RDFs between various atomic sites of urea and oxygen atom of water. Moreover, the signature of water clustering in the present DES is reflected from the comparison of water – water RDFs in this DES and that in neat water. Hence, the water structure in such a "crowded" environment will be an interesting feature to explore.

Simulated mean square displacements (MSDs) in this DES provide evidence for rattling-in-cage motion of particles, which indicates the presence of dynamic heterogeneity in the system. Strikingly, the translational diffusion of water in this DES is found to be slowed down by ~ 500 times in comparison to that in neat water. Dynamic heterogeneity (DH) parameters indicate strong microheterogeneity in this DES via providing the DH time scales in the nanosecond range. This result correlates well with the experimental evidence of strong dynamic heterogeneity indicated via a strong departure from the hydrodynamic viscosity dependences of solute rotation and solvation times. Enormous slow relaxation and correlated time scales from self-dynamic structure factor and four-point correlations respectively for water in the present DES in comparison to those in neat water explain the drastically different dynamics of water in this kind of crowded environment. In addition, the ratio of average reorientation correlation times from $C_l(t)$ decays indicate substantial deviation from the Debye's law for stochastic angular displacements, providing further support to the dynamical heterogeneity view of this system. The sub-nanosecond and nanosecond time constants in the $C_l(t)$ relaxation may originate from the structural H-bond relaxation dynamics in this DES. A detailed analysis of H-bond fluctuation dynamics would be needed to fully understand this complex yet exciting solvent system.

Appendix 5.A

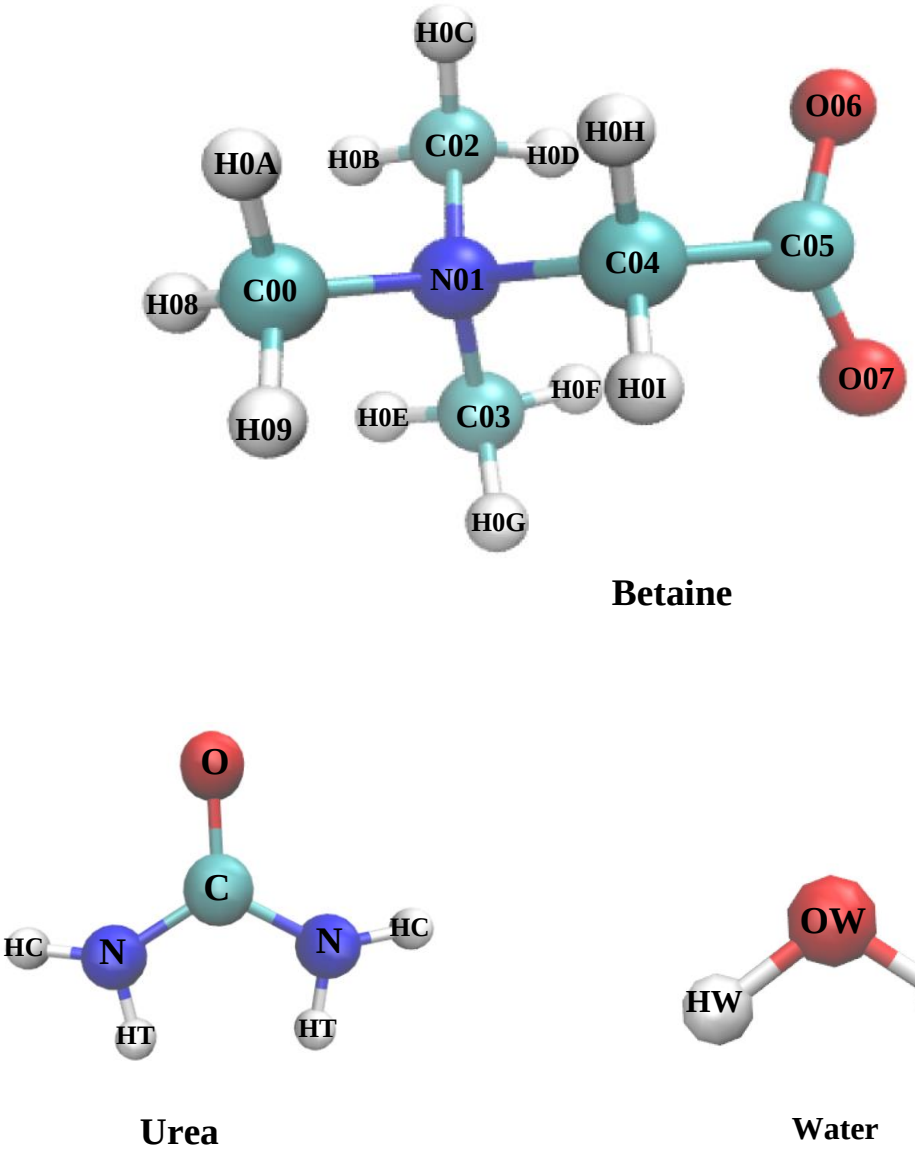

Figure 5.A.1: Chemical structures of betaine, urea and water along with the atomic sites as used in present simulation.

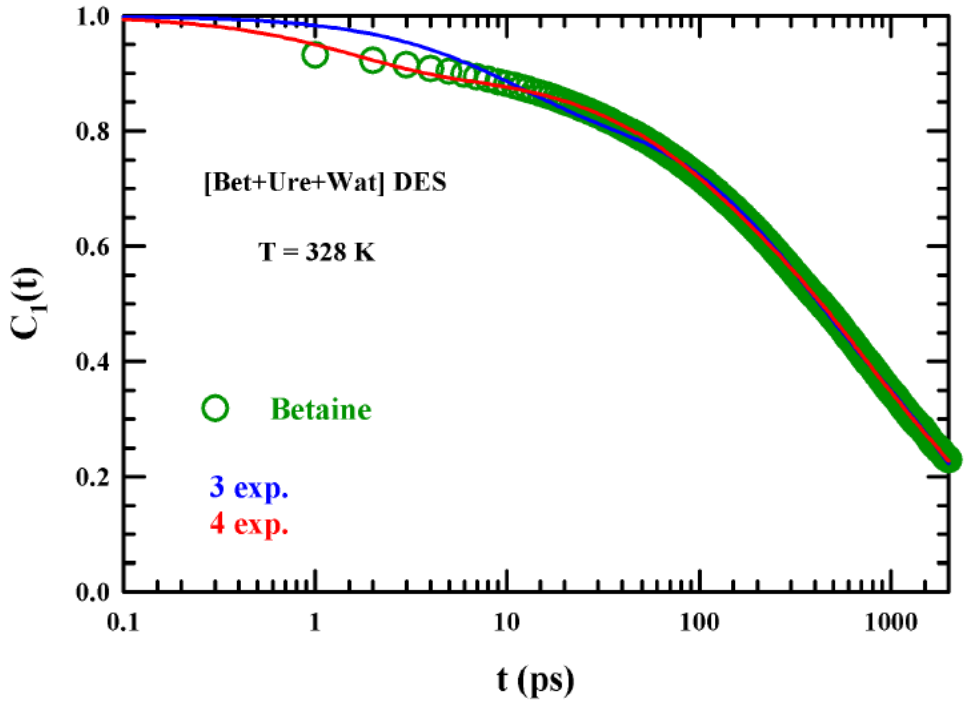

Figure 5.A.2: A representative plot showing a comparison among various exponential functions (3 exp. and 4 exp,) the $C_1(t)$ relaxation for betaine ion in [Bet+Ure+Wat] DES at 328 K. It suggests that four exponential fit function is required to adequately describe the $C_1(t)$ relaxation.

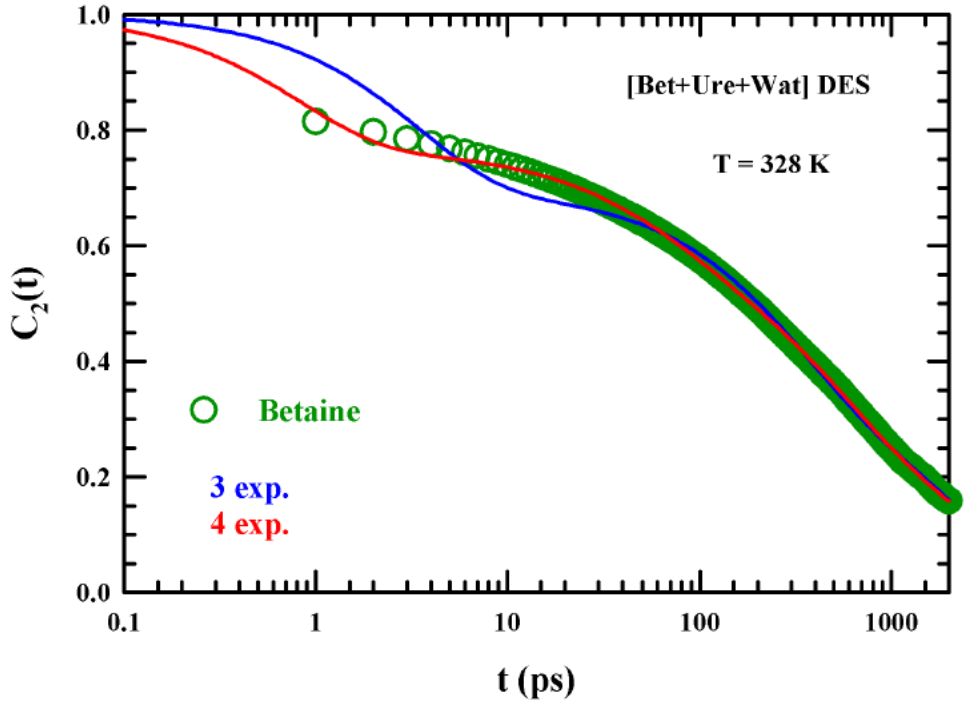

Figure 5.A.3: A representative plot showing the comparison among various fit functions (3 exp. and 4 exp.) to fit the $C_2(t)$ relaxation for betaine ion in [Bet+Ure+Wat] DES at 328 K.

Appendix 5.B

Table 5.B.1: Partial charges and Lennard-Jones parameters for betaine.

Atom types	Charge, e	σ (Å)	ε (kJmol^{-1})
C00	-0.1791	2.96	0.87864
N01	-0.0268	2.50	0.12552
C02	-0.1592	3.55	0.29288
C03	-0.1585	2.50	0.12552
C04	-0.2061	2.50	0.12552
C05	0.4863	3.50	0.27614
O06	-0.6274	2.50	0.12552
O07	-0.6274	2.96	0.87864
H08	0.1335	2.50	0.12552
H09	0.1335	3.50	0.27614
H0A	0.1335	3.50	0.27614
H0B	0.1439	2.50	0.12552
H0C	0.1439	3.25	0.71128
H0D	0.1439	2.50	0.12552
H0E	0.1438	2.50	0.12552
H0F	0.1438	2.50	0.12552
H0G	0.1438	2.50	0.12552
H0H	0.1173	3.50	0.27614
H0I	0.1173	2.50	0.12552

Table 5.B.2: Partial charges and Lennard-Jones parameters for urea.

Atom name	charge	σ (Å)	ε (kJ/mol)
C	0.124	3.75	0.65898
O	-0.322	2.96	1.31796
N	-0.453	3.55	1.06692
HT	0.276	0.00	0.00000
HC	0.276	0.00	0.00000

Table 5.B.3: Partial charges and non-bonded parameters for SPC/E water molecule.

Atom name	charge	σ (Å)	ε (kJ/mol)
OW	-0.8476	3.16	0.65
HW	0.4238	0.00	0.00

References

[1] P. Wasserscheid and T. Welton, Ionic Liquids in Synthesis (2003).

[2] A.P. Abbott, D. Boothby, G. Capper, D.L. Davies, and R.K. Rasheed, J. Am. Chem. Soc. **126**, 9142 (2004).

[3] A.P. Abbott, G. Capper, D.L. Davies, R.K. Rasheed, and V. Tambyrajah, Chem. Commun. 70 (2003).

[4] M. Francisco, A. van den Bruinhorst, and M.C. Kroon, Angew. Chem. Int. Ed. **52**, 3074 (2013).

[5] P.G. Jessop, D.A. Jessop, D. Fu, and L. Phan, Green Chem. **14**, 1245 (2012).

[6] J.-H. Liao, P.-C. Wu, and Y.-H. Bai, Inorg. Chem. Commun. **8**, 390 (2005).

[7] P. Nockemann, B. Thijs, K. Driesen, C.R. Janssen, K. Van Hecke, L. Van Meervelt, S. Kossmann, B. Kirchner, and K. Binnemans, J. Phys. Chem. B **111**, 5254 (2007).

[8] D.V. Wagle, H. Zhao, and G.A. Baker, Acc. Chem. Res. **47**, 2299 (2014).

[9] Q. Zhang, K.D.O. Vigier, S. Royer, and F. Jerome, Chem. Soc. Rev. **41**, 7108 (2012).

[10] B. Guchhait, H. Al Rasid Gazi, H.K. Kashyap, and R. Biswas, J. Phys. Chem. B **114**, 5066 (2010).

[11] B. Guchhait, S. Das, S. Daschakraborty, and R. Biswas, J. Chem. Phys. **140**, 104514 (2014).

[12] K. Mukherjee, A. Das, S. Choudhury, A. Barman, and R. Biswas, J. Phys. Chem. B **119**, 8063 (2015).

[13] M. Espino, M. de los Ángeles Fernández, F.J. Gomez, and M.F. Silva, TrAC Trends Anal. Chem. **76**, 126 (2016).

[14] Y. Dai, E. Rozema, R. Verpoorte, and Y.H. Choi, J. Chromatogr. A **1434**, 50 (2016).

[15] Y. Dai, J. van Spronsen, G.-J. Witkamp, R. Verpoorte, and Y.H. Choi, Anal. Chim. Acta **766**, 61 (2013).

[16] S. Gore, S. Baskaran, and B. Koenig, Green Chem. **13**, 1009 (2011).

[17] W.-C. Huang, D. Zhao, N. Guo, C. Xue, and X. Mao, J. Agric. Food Chem. **66**, 11897 (2018).

[18] Y.H. Choi, J. van Spronsen, Y. Dai, M. Verberne, F. Hollmann, I.W. Arends, G.-J. Witkamp, and R. Verpoorte, Plant Physiol. **156**, 1701 (2011).

[19] A. Paiva, R. Craveiro, I. Aroso, M. Martins, R.L. Reis, and A.R.C. Duarte, ACS Sustain. Chem. Eng. **2**, 1063 (2014).

[20] M. Faggian, S. Sut, B. Perissutti, V. Baldan, I. Grabnar, and S. Dall'Acqua, Molecules **21**, 1531 (2016).

[21] A. Hayyan, M.A. Hashim, M. Hayyan, F.S. Mjalli, and I.M. AlNashef, J. Clean. Prod. **65**, 246 (2014).

[22] M.H. Zainal-Abidin, M. Hayyan, A. Hayyan, and N.S. Jayakumar, Anal. Chim. Acta **979**, 1 (2017).

[23] I.M. Aroso, R. Craveiro, Â. Rocha, M. Dionísio, S. Barreiros, R.L. Reis, A. Paiva, and A.R.C. Duarte, Int. J. Pharm. **492**, 73 (2015).

[24] M.B. Haider, D. Jha, B. Marriyappan Sivagnanam, and R. Kumar, J. Chem. Eng. Data **63**, 2671 (2018).

[25] L. Millia, V. Dall'Asta, C. Ferrara, V. Berbenni, E. Quartarone, F.M. Perna, V. Capriati, and P. Mustarelli, Solid State Ion. **323**, 44 (2018).

[26] E. Tarif, J. Mondal, and R. Biswas, J. Mol. Liq. **303**, 112451 (2020).

[27] W. Xing and C. Rajashekar, Environ. Exp. Bot. **46**, 21 (2001).

[28] S.E.C. Davies, R.A. Chalmers, E.W. Randall, and R.A. Iles, Clin. Chim. Acta **178**, 241 (1988).

[29] L. Hoffmann, G. Brauers, T. Gehrmann, D. Häussinger, E. Mayatepek, F. Schliess, and B.C. Schwahn, Am. J. Physiol.-Gastrointest. Liver Physiol. **304**, G835 (2013).

[30] M. Zhang, X. Wu, F. Lai, X. Zhang, H. Wu, and T. Min, J. Agric. Food Chem. **64**, 4068 (2016).

[31] A. Lawson-Yuen and H.L. Levy, Mol. Genet. Metab. **88**, 201 (2006).

[32] E. Kathirvel, K. Morgan, G. Nandgiri, B.C. Sandoval, M.A. Caudill, T. Bottiglieri, S.W. French, and T.R. Morgan, Am. J. Physiol.-Gastrointest. Liver Physiol. **299**, G1068 (2010).

[33] D. Soletto, L. Binaghi, A. Lodi, J.C.M. Carvalho, and A. Converti, Aquaculture **243**, 217 (2005).

[34] B.J. Bennion and V. Daggett, Proc. Natl. Acad. Sci. **100**, 5142 (2003).

[35] A. Das and C. Mukhopadhyay, J. Phys. Chem. B **113**, 12816 (2009).

[36] P.H. Yancey, J. Exp. Biol. **208**, 2819 (2005).

[37] C.-X. Zeng, S.-J. Qi, R.-P. Xin, B. Yang, and Y.-H. Wang, J. Mol. Liq. **219**, 74 (2016).

[38] E.L. Smith, A.P. Abbott, and K.S. Ryder, Chem. Rev. **114**, 11060 (2014).

[39] A.P. Abbott, G. Capper, D.L. Davies, K.J. McKenzie, and S.U. Obi, J. Chem. Eng. Data **51**, 1280 (2006).

[40] P.B. Sánchez, B. González, J. Salgado, J. José Parajó, and Á. Domínguez, J. Chem. Thermodyn. **131**, 517 (2019).

[41] I.M. Aroso, A. Paiva, R.L. Reis, and A.R.C. Duarte, J. Mol. Liq. **241**, 654 (2017).

[42] S. Khodaverdian, B. Dabirmanesh, A. Heydari, E. Dashtban-moghadam, K. Khajeh, and F. Ghazi, Int. J. Biol. Macromol. **107**, 2574 (2018).

[43] B. Olivares, F. Martínez, L. Rivas, C. Calderón, J. M. Munita, and P. R. Campodonico, Sci. Rep. **8**, 14900 (2018).

[44] N. Li, Y. Wang, K. Xu, Y. Huang, Q. Wen, and X. Ding, Talanta **152**, 23 (2016).

[45] L. Duan, L.-L. Dou, L. Guo, P. Li, and E.-H. Liu, ACS Sustain. Chem. Eng. **4**, 2405 (2016).

[46] K. Mukherjee, S. Das, E. Tarif, A. Barman, and R. Biswas, J. Chem. Phys. **149**, 124501 (2018).

[47] K. Mukherjee, E. Tarif, A. Barman, and R. Biswas, Fluid Phase Equilib. **448**, 22 (2017).

[48] C. D'Agostino, R.C. Harris, A.P. Abbott, L.F. Gladden, and M.D. Mantle, Phys. Chem. Chem. Phys. **13**, 21383 (2011).

[49] C. D'Agostino, L.F. Gladden, M.D. Mantle, A.P. Abbott, E. Ahmed I., A.Y.M. Al-Murshedi, and R.C. Harris, Phys. Chem. Chem. Phys. **17**, 15297 (2015).

[50] A. Das and R. Biswas, J. Phys. Chem. B **119**, 10102 (2015).

[51] A. Das, S. Das, and R. Biswas, Chem. Phys. Lett. **581**, 47 (2013).

[52] Y. Cui and D.G. Kuroda, J. Phys. Chem. A **122**, 1185 (2018).

[53] S. Das, R. Biswas, and B. Mukherjee, J. Chem. Phys. **145**, 084504 (2016).

[54] S. Das, R. Biswas, and B. Mukherjee, J. Phys. Chem. B **119**, 11157 (2015).

[55] S.L. Perkins, P. Painter, and C.M. Colina, J. Chem. Eng. Data **59**, 3652 (2014).

[56] S. Kaur, A. Gupta, and H.K. Kashyap, J. Phys. Chem. B **120**, 6712 (2016).

[57] S. Kaur, A. Malik, and H.K. Kashyap, J. Phys. Chem. B **123**, 8291 (2019).

[58] S. Páll, M.J. Abraham, C. Kutzner, B. Hess, and E. Lindahl, in (Springer, 2014), pp. 3–27.

[59] M.J. Abraham, T. Murtola, R. Schulz, S. Páll, J.C. Smith, B. Hess, and E. Lindahl, SoftwareX **1**, 19 (2015).

[60] H. Bekker, H. Berendsen, E. Dijkstra, S. Achterop, R. Van Drunen, D. Van der Spoel, A. Sijbers, H. Keegstra, B. Reitsma, and M. Renardus, in (World Scientific Singapore, 1993), pp. 252–256.

[61] L.S. Dodda, I. Cabeza de Vaca, J. Tirado-Rives, and W.L. Jorgensen, Nucleic Acids Res. **45**, W331 (2017).

[62] L.S. Dodda, J.Z. Vilseck, J. Tirado-Rives, and W.L. Jorgensen, J. Phys. Chem. B **121**, 3864 (2017).

[63] W.L. Jorgensen and J. Tirado-Rives, Proc. Natl. Acad. Sci. U. S. A. **102**, 6665 (2005).

[64] B. Doherty and O. Acevedo, J. Phys. Chem. B **122**, 9982 (2018).

[65] L. Martínez, R. Andrade, E.G. Birgin, and J.M. Martínez, J. Comput. Chem. **30**, 2157 (2009).

[66] U. Essmann, L. Perera, M.L. Berkowitz, T. Darden, H. Lee, and L.G. Pedersen, J. Chem. Phys. **103**, 8577 (1995).

[67] B. Hess, H. Bekker, H.J. Berendsen, and J.G. Fraaije, J. Comput. Chem. **18**, 1463 (1997).

[68] G. Bussi, D. Donadio, and M. Parrinello, J. Chem. Phys. **126**, 014101 (2007).

[69] H.J. Berendsen, J. van Postma, W.F. van Gunsteren, A. DiNola, and J.R. Haak, J. Chem. Phys. **81**, 3684 (1984).

[70] T. Pal and R. Biswas, J. Chem. Phys. **141**, 104501 (2014).

[71] T. Pal and R. Biswas, J. Phys. Chem. B **119**, 15683 (2015).

[72] J.-P. Hansen and I.R. McDonald, *Theory of Simple Liquids* (Elsevier, 1990).

[73] A. Baksi, P.K. Ghorai, and R. Biswas, J. Phys. Chem. B **124**, 2848 (2020).

[74] T. Pal and R. Biswas, Theor. Chem. Acc. **132**, 1348 (2013).

[75] F. Faupel, W. Frank, M.-P. Macht, H. Mehrer, V. Naundorf, K. Rätzke, H.R. Schober, S.K. Sharma, and H. Teichler, Rev. Mod. Phys. **75**, 237 (2003).

[76] M.S. Shell, P.G. Debenedetti, and F.H. Stillinger, J. Phys. Condens. Matter **17**, S4035 (2005).

[77] K. Kim and S. Saito, J. Chem. Phys. **133**, 044511 (2010).

[78] G. Szamel and E. Flenner, Phys. Rev. E **74**, 021507 (2006).

[79] K. Kim and S. Saito, J. Chem. Phys. **138**, 12A506 (2013).

[80] N. Lačević, F.W. Starr, T. Schrøder, and S. Glotzer, J. Chem. Phys. **119**, 7372 (2003).

[81] C. Donati, S. Franz, S.C. Glotzer, and G. Parisi, J. Non-Cryst. Solids **307**, 215 (2002).

[82] C. Toninelli, M. Wyart, L. Berthier, G. Biroli, and J.-P. Bouchaud, Phys. Rev. E **71**, 041505 (2005).

[83] K. Seki, B. Bagchi, and M. Tachiya, Phys. Rev. E **77**, 031505 (2008).

[84] P. Debye, J. Soc. Chem. Ind. **48**, 1036 (1929).

[85] D. Laage and J.T. Hynes, Science **311**, 832 (2006).

[86] S. Das, B. Mukherjee, and R. Biswas, J. Chem. Phys. **148**, 193839 (2018).

[87] S. Das, R. Biswas, and B. Mukherjee, J. Phys. Chem. B **119**, 274 (2015).

[88] T. Pal and R. Biswas, Chem. Phys. Lett. **517**, 180 (2011).

[89] Z. Hu and C.J. Margulis, Proc. Natl. Acad. Sci. **103**, 831 (2006).

Chapter 6

Structure and Dynamics of Water in a Naturally Abundant Deep Eutectic Solvents (NADES) [Betaine + Urea + Water]: Comparison between Charged and Neutral NADESs

6.1 Introduction

In this chapter, we have investigated how the H-bonded structure and dynamics of water alter in an ionic deep eutectic solvent via all-atom molecular dynamics study at 328 K. We have performed molecular dynamics simulations of an experimentally reported betaine-based ionic naturally abundant deep eutectic solvent (NADES) [1] which is a mixture of betaine, urea and water mixed at 11.7:12:1 weight ratio. Betaine is a trimethyl derivative of glycine (amino acid). It is found in various foods, mammals, bacteria etc [2,3]. Non-toxicity, usage in treatment of several diseases [4–6], and usage as an osmolyte [7] are the main attraction for choosing betaine as a component of a naturally abundant deep eutectic solvent (NADES). Physical properties of betaine or urea based DESs were studied before and used for various purposes. [8–13] Betaine-urea based deep eutectics have been employed for stabilization of proteins [12,14–16], extraction of bioactive compounds [17], on-demand applications to suit biomedical needs [18], etc. For preservation and stabilization of DNA, one needs to understand how DNA molecules interact with these novel solvent systems as DNA-medium interaction play a critical role. [19,20]

Interactions and dynamics of this betaine-based DES have been studied via time-resolved fluorescence measurements earlier[1]. Emergence of decoupling in rotation and solvation dynamics have also been explored[1]. However, a detailed molecular level analysis of this DES is yet to be explored. Water being an integral part of this system plays an interesting and important role in forming this DES. Detailed investigation of water structure and dynamics in the crowded environment of this DES constitutes an interesting aspect of the simulation results presented in this chapter.

Simulations of [Bet/Ure/Wat] DES in the weight ratio (11.7:12:1) have been performed at 328 K. To obtain this weight ratio, 100 betaine, 200 urea and 56 water molecules are considered. This means that approximately 5.4 molecules of betaine and urea together compete for a single water molecule. One, therefore, expects the behaviour of water much deviated from what has been observed for normal neat water. For comparison, neat water has been simulated employing the SPC/E model [21] at the same temperature. As water is a minor yet integral component of this ionic DES, we explore the effects of ionic environment on water structure as well as dynamics via comparing these results with simulation results [22] of another experimentally reported glucose-based neutral DES (Glucose/Urea/Water in 6:4:1 weight ratio) at temperature 328 K. Although for both these NADESs, water structure and dynamics are expected to be drastically deviated from that in neat water because of the crowded environment [23], the impact of ionic nature of the molecular environment on water structure in bulk solutions has not been explored. Effects of ionic environment on water H-bond structure and dynamics have been examined in this chapter via following the tetrahedral order parameter and the H-bond relaxation times of intra-species water molecules.

6.2 Simulation Details

Molecular dynamics simulations of the DES have been performed using the periodic boundary condition at 328 K. 100 molecules of betaine, 200 molecules of urea and 56 water molecules are simulated within a cubic box. Initial configurations are built employing the packmol [24] software. The chemical structures of all constituent particles are provided in Figure 6.A.1 of Appendix 6.A. OPLS-AA force field parameters [21,25–27] were used for the simulations of urea and betaine, whereas the water molecules were described by the extended point charge model, SPC/E [21]. Lennard-Jones parameters and partial charges of betaine, urea and water are summarized in Tables 6.B.1 to 6.B.3 (Appendix 6.B). The short-range interaction cut-off is set to 1.2 nm and long ranged coulombic interactions were treated with Particle-Mesh Ewald (PME) summation [28]. All covalent bonds have been constrained using the LINCS[29] algorithm throughout the simulation run.

The functional forms of urea and betaine force field are given by,

$$E_{bonds} = \sum_i k_{b,i}(r_i - r_{0,i})^2 \quad (6.1)$$

$$E_{angles} = \sum_i k_{\theta,i}(\theta_i - \theta_{0,i})^2 \quad (6.2)$$

$$E_{torsion} = \sum_i \left[\begin{array}{c} \frac{1}{2}V_{1,i}(1 + cos\varphi_i) + \frac{1}{2}V_{2,i}(1 - cos2\varphi_i) + \frac{1}{2}V_{3,i}(1 + cos3\varphi_i) \\ + \frac{1}{2}V_{4,i}(1 - cos4\varphi_i) \end{array} \right] \quad (6.3)$$

$$E_{nonbond} = \sum_i \sum_{j>1} \left\{ \frac{q_i q_j e^2}{r_{ij}} + 4\varepsilon_{ij} \left[\left(\frac{\sigma_{ij}}{r_{ij}}\right)^{12} - \left(\frac{\sigma_{ij}}{r_{ij}}\right)^{6} \right] \right\} \quad (6.4)$$

The energy minimization is performed using steepest descent algorithm. The optimized configuration was subjected to a number of equilibration steps using the NPT ensemble. First, the system was equilibrated at 500 K using this ensemble, then gradually cooled down to 328 K in a stepwise manner with a step size of 50 K and each of these runs were for 500 ps long. Then the system was equilibrated for 4 ns in the NPT ensemble to obtain the required density of the system, which is further followed by 2 ns run in the NVT ensemble. The temperature was maintained at 328 K using v-rescale thermostat [30] with a time-constant of 0.5 ps and the Berendsen barostat [31] with time constant of 2 ps has been employed to maintain the pressure at 1 atm. The equations of motion were solved by using the leapfrog algorithm [32] with a time step of 2 fs. The total production run has been carried out for 100 ns where the trajectories are saved after every 0.1 ps. Another separate production run for analysing H-bond dynamics was carried out for 10 ns using the NVT ensemble, where trajectories are saved after every 0.01 ps. GROMACS 4.5.4[33–35] molecular dynamics simulation package is used for simulating this system. Fidelity check of this force field has been done via the comparison of simulated density (1.18 g/cm^3) with experiments (1.20 g/cm^3).[1]

Note, we denote this [Bet/Ure/Wat] DES as ‘DES1’ from the next section to avoid any possible confusion while comparing our simulation results with those (simulation results) for glucose-based deep eutectic system [Glu/Ure/Wat] DES.

6.3 Results and Discussion

6.3.1 Radial Distribution functions (RDFs)

Interactions between water molecules present in this charged [Bet/Ure/Water] DES1 have been calculated via radial distribution function of oxygen-oxygen atoms of water. These results have been already discussed in details in chapter 5. Here, the water-water interactions are compared with that found in neat water and in neutral [Glu/Ure/Wat] DES in Figure 6.1. Although the interaction between water molecules of this ionic DES1 is somewhat less than that of water molecules in neutral DES [23], a clear signature of a sort of water clustering, similar to neutral DES, is also indicated for DES1. To analyse the qualitative difference between water structure in charged and neutral deep eutectic systems and to measure their departure from that of neat water, we examine the detailed water-water H-bond structure in the next section.

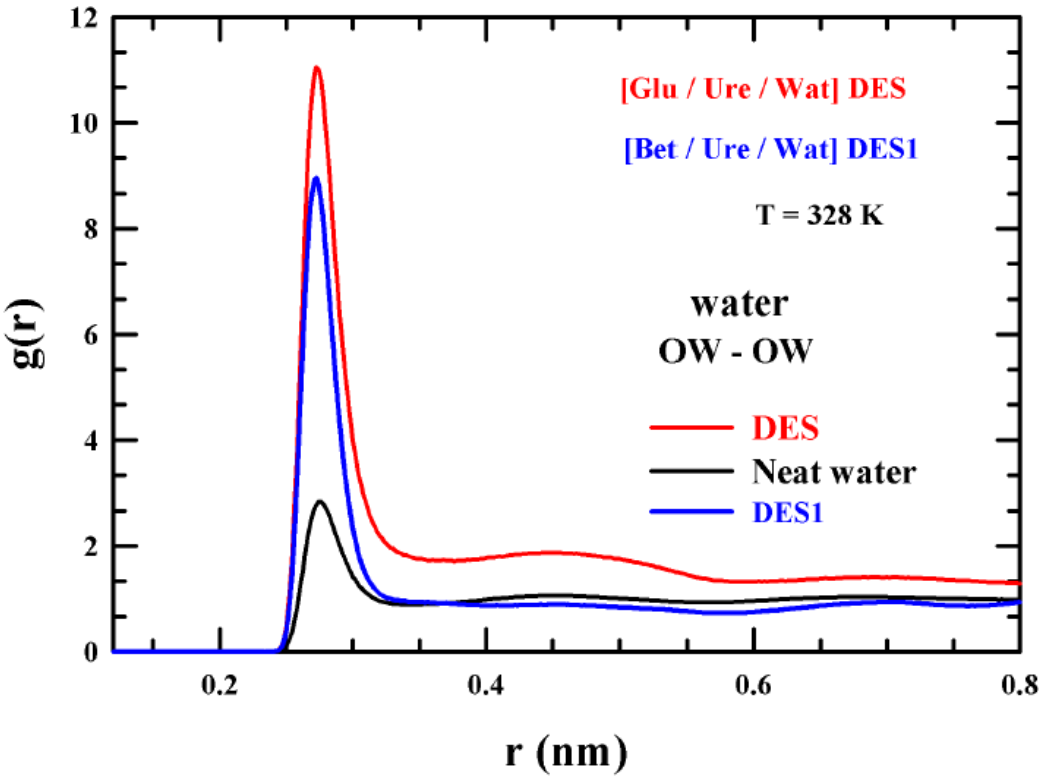

Figure 6.1: Comparison of water – water (OW-OW) RDFs in [Bet/ Ure/ Wat] DES1, [Glu/ Ure/ Wat] DES and in neat water system at 328 K. Various systems are color coded.

6.3.2 Average Number of intra-species H-bonds of Water and Participation Population

We calculate the average number of H-bonds between water molecules of this DES1 and corresponding population participating in water-water H-bonds. These results are compared with glucose-based DES as well as with neat water. The following prescription [36–40] was used for detecting H-bonds between water molecules: a) the distance between the donor oxygen atom and acceptor oxygen atom is less than 0.35 nm, b) the H-O (donor)-O (acceptor) angle is less than 30^{o}, and c) distance between O and H must be less than 0.28 nm.

We find nearly 38% of the total water molecules present in the DES, on average, are H-bonded within themselves with 1.15 average number of H-bonds per water molecule in DES1. This is to be contrasted for the findings in glucose-based DES in which ~78% of them are involved in water-water H-bonding with average number of W-W H-bonds of 1.74 per water molecule.[23] Note that ~100% of them in the neat water participate in W-W H-bonds with average number of H-bonds per water molecule at 328 K is ~3.5. [23] These numbers are schematically shown in Scheme 6.1.

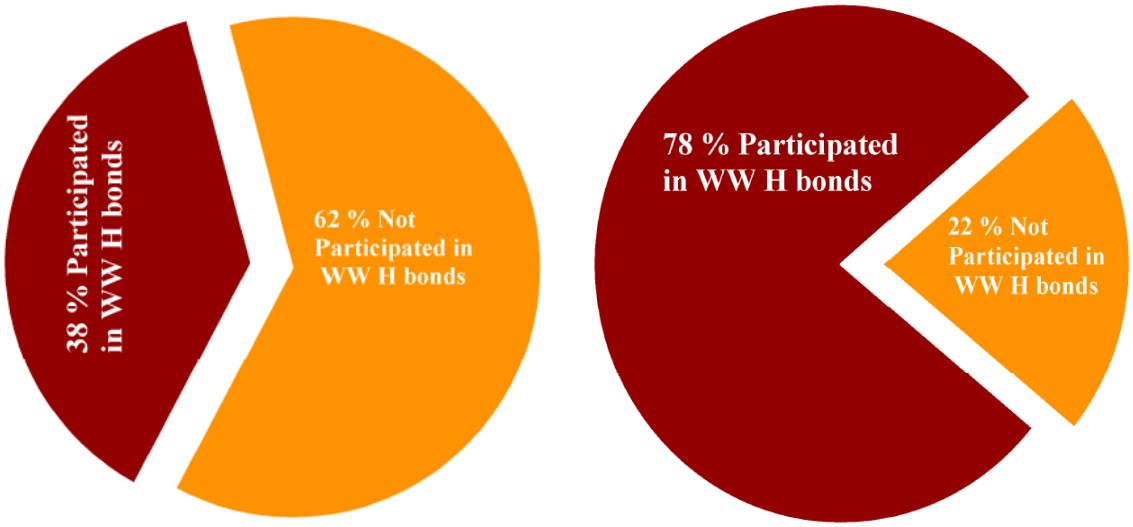

Scheme 6.1: Representation of participant and non-participant water population in the formation of direct water-water H-bonds in [Glu/ Ure/ Wat] DES and [Bet/ Ure/ Wat] DES1 under study.

6.3.3 Number of H-bonds with each water molecule and their distribution

Next, we examine the population $P(N_{HB}/water)$ of water molecules with number of water-water (WW) H-bonds per water molecule $(N_{HB}/water)$. This has been compared with the results for glucose-based DES and neat water in Figure 6.2. In DES1, we find the maximum number of water molecules share one H-bond with other water molecule and there exist much less population of water molecules with two WW H-bonds. Note, neat water system shows maximum probability of water molecules with three and four H-bonds, which reflects the tetrahedral structure of water H-bonds. Comparing this result with glucose-based DES, we find there exist nearly maximum population of water molecules that are connected with one WW H-bonds $(N_{HB}/water = 1)$ in ionic DES1. These results indicate that the water structure is drastically different in the charged betaine-based deep eutectic system (DES1) compared to that in neat water and glucose-based DES. These differences can be attributed to the ionic nature of betaine in DES1.

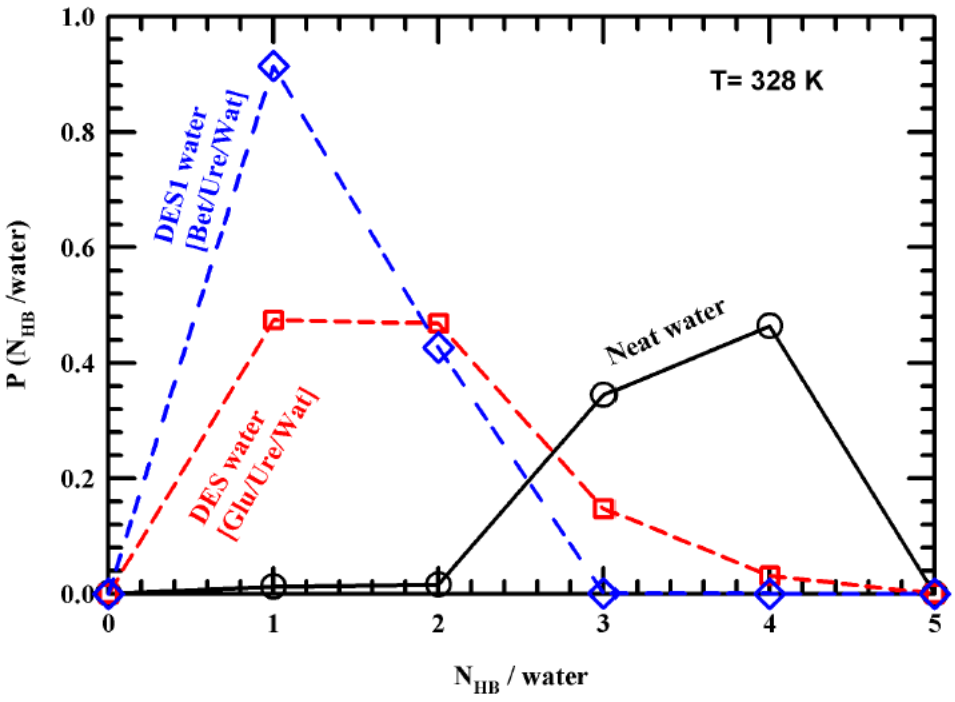

Figure 6.2: Population of water molecules containing a certain number of H-bonds $P(N_{HB}/water)$ as a function of number of H-bonds per water molecule $N_{HB}/water$ in DES and DES1 and they are compared to the corresponding results for the neat water.

6.3.4 Water-Water H-bond length distribution

To examine the qualitative difference of water-water H-bonds, we plot the water-water H-bond length (OW-OW distance of H-bonded water molecules) distribution and compared with those for glucose-based DES and neat water in Figure 6.3. What we find is quite intriguing. While glucose-based DES and neat water show similar H-bond length distributions, water-water H-bonds in DES1 are qualitatively quite different as the population of H-bond lengths around 0.275 nm is significantly higher compared to neat and glucose-based DES system. These results portray the impact of strong electrostatic interaction between betaine and water molecules. Most water molecules are forming water-water H-bond network with a smaller H-bond length.

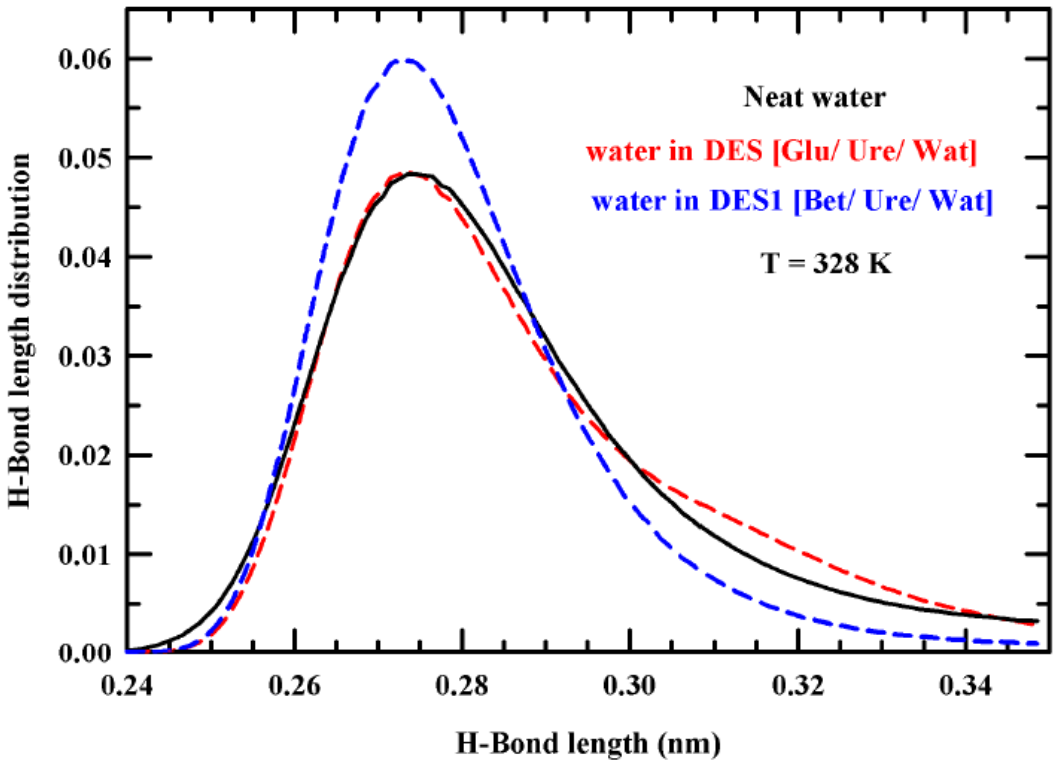

Figure 6.3: Bond-length distribution water-water H-bonds in [Glu/ Ure/ Wat] DES and [Bet/ Ure/ Wat] DES1.

6.3.5 Modification in Tetrahedral Network of Water: Local and Global Orientations

Local orientation of water molecules has been examined via analyzing the probability distribution of water-water-water (j-i-k) angle (θ_{ijk}) $P(\theta)$, where, θ_{ijk}- is the angle subtended by each nearest neighbour pair (designated by *j* and *k*) at central water molecule (designated *i*). This distribution has been compared with neat water and glucose-based DES in Figure 6.4.

Although neat water system shows preference towards $\theta \sim 104^o$ and glucose-based DES towards $\theta \sim 40^o$, interestingly this betaine-based ionic deep eutectic (DES1) shows preferences towards multiple local orientations with $\theta \sim 45^o, 90^o, 140^o$. This is unique as this type of local orientation of water molecules has not been reported earlier. Schematic local orientation of water molecules in neat water, glucose-based Des and in DES1 have been depicted in Scheme 6.2.

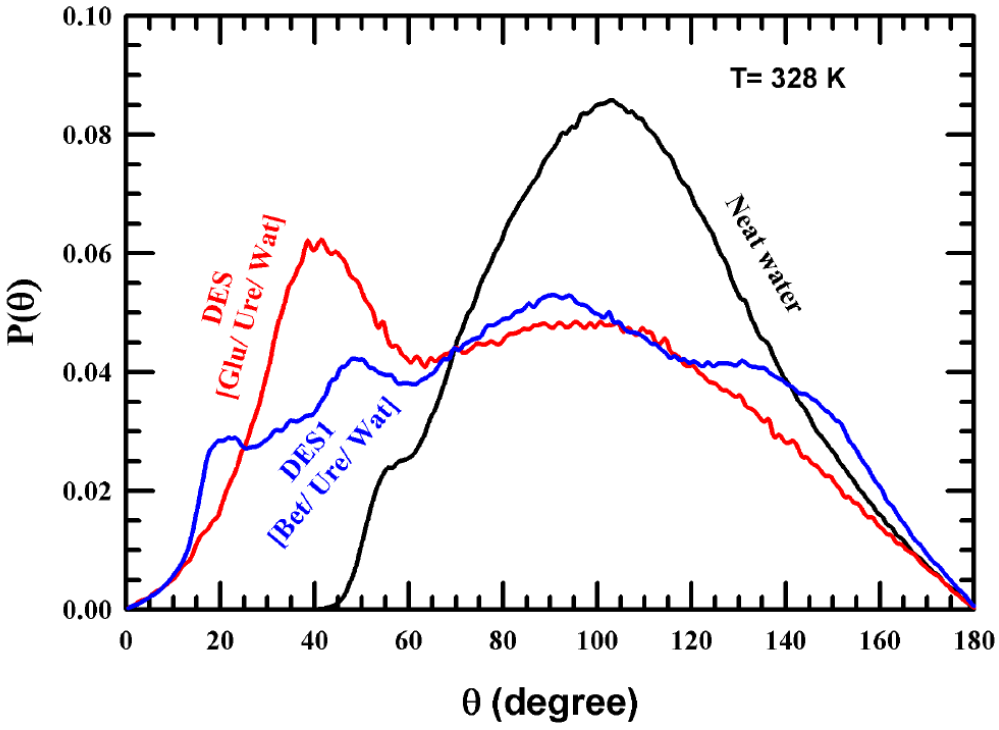

Figure 6.4: Probability distribution of water-water-water angle, $P(\theta)$, of water in neat system, in [Glu/ Ure/ Wat] DES and in [Bet/ Ure/ Wat] DES1.

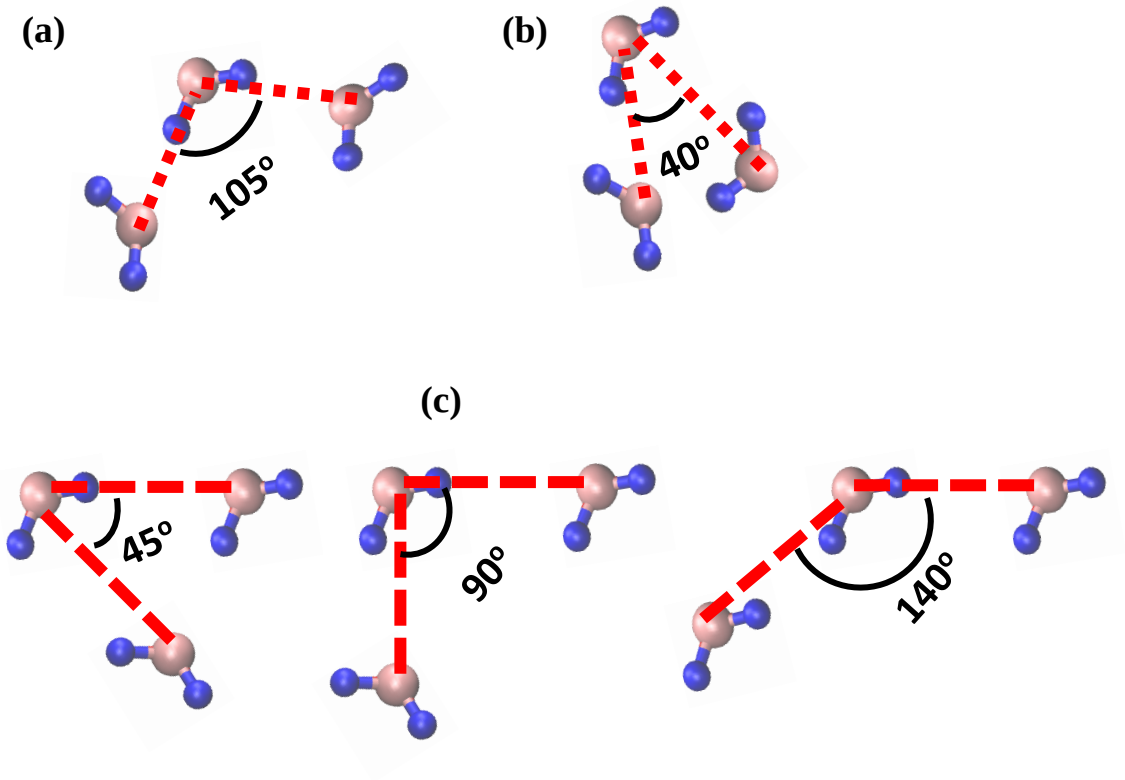

Scheme 6.2: Pictorial representation of the most probable angles subtended by any water molecule with two other nearest water molecules in neat water (a) and in [Glu/ Ure/ Wat] DES (b) and in [Bet/ Ure/ Wat] DES1 (c).

To scrutinize the global orientation of water molecules within the DES1, tetrahedral order parameter Q_i and distribution of Q_i, $P(Q)$, have been computed using the following expression[41],

$$Q_i = 1 - \frac{3}{8}\sum_{j=1}^{3}\sum_{k=j+1}^{4}(cos\theta_{ijk} + {}^{1}/_{3})^2 \text{ and } \langle Q \rangle = \frac{1}{n_{water}}\sum_i Q_i, \quad (6.5)$$

where, Q_i is the tetrahedral order parameter of the i^{th} water, and θ_{ijk} bears the usual meaning mentioned earlier. Ensemble averaged tetrahedral parameter values $< Q >$ for DES1, neat water and glucose-based DES have been schematically shown in Scheme 6.3 for better visualization. While for neat system it has been found that $< Q > \sim 0.6$, for glucose-based DES $< Q > \sim -0.18$, and for this ionic betaine-based deep eutectic system $< Q >$ is found to be nearly -0.04.

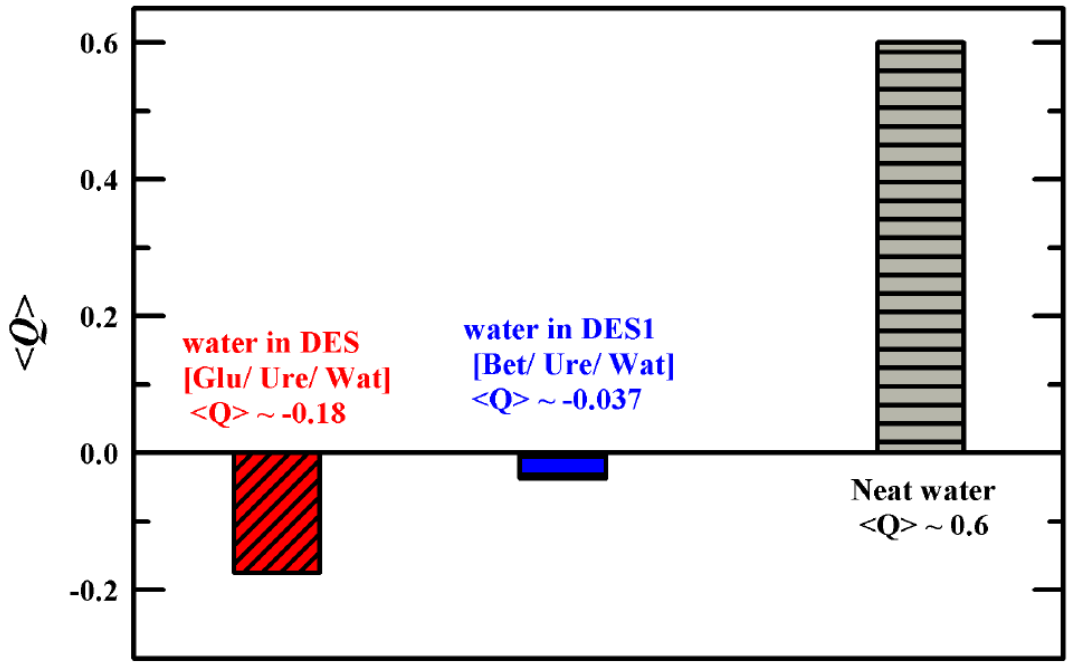

Scheme 6.3: Pictorial representation of overall tetrahedrality of water molecules, $< Q >$, in neat system, in [Glu/ Ure/ Wat] DES and [Bet/ Ure/ Wat] DES1 at 328 K.

This negative $< Q >$ for deep eutectic system does not bear much significance unless we compare the distribution of molecular tetrahedral order parameter, $P(Q)$, with neat water and glucose-based DES. This comparison is depicted in Figure 6.5 where a distinct departure of tetrahedral structure of H-bonded water is found for deep eutectic systems from neat water.

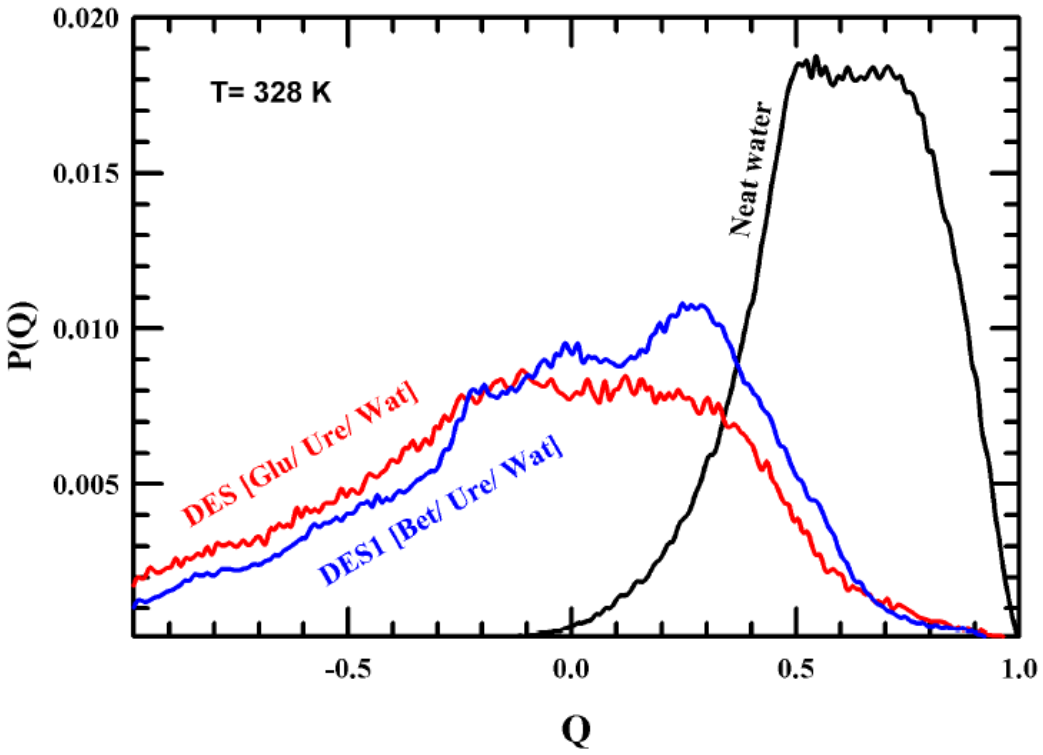

Figure 6.5: Probability distribution of tetrahedral order parameter, $P(Q)$ of water in neat system, in [Glu/ Ure/ Wat] DES and in [Bet/ Ure/ Wat] DES1.

6.3.6 Water Hydrogen bond Dynamics: Continuous and Structural bond Relaxations

The continuous hydrogen bond lifetime is calculated from the time-correlation function, $S_{HB}(t)$, [36,38,39]

$$S_{HB}(t) = \frac{<h(0)H(t)>}{<h>} \quad . \tag{6.6}$$

The structural water-water H-bond relaxation, $C_{HB}(t)$, dynamics has been calculated via the following expression,[36,38,39]

$$C_{HB}(t) = \frac{<h(0)h(t)>}{<h>} \quad . \tag{6.7}$$

Here, *h(t)*, a hydrogen bond population operator, is unity when the particular tagged pair of molecules are hydrogen bonded and zero otherwise. $H(t)$ takes a value 1 if the tagged pair of molecules, for which $h(0)$ is calculated, remains continuously H-bonded for a time t or else $H(t) = 0$. $S_{HB}(t)$ describes the probability that a tagged pair of molecules remain H-bonded for a timespan t and it approaches zero when continuity of the H-bond between them breaks down.

The average continuous H-bond lifetime has been calculated via the time integration of $S_{HB}(t)$, $\langle \tau_S^{HB} \rangle = \int_0^\infty dt\, S_{HB}(t)$. Similarly, average structural H-bond lifetime $\langle \tau_C^{HB} \rangle$ has been calculated using $\langle \tau_C^{HB} \rangle = \int_0^\infty dt\, C_{HB}(t)$.

Figure 6.6 depicts the continuous relaxation (upper panel) and structural relaxation (lower panel) decays of water-water hydrogen bonds in DES1 and they are compared with neat water and glucose-based DES.

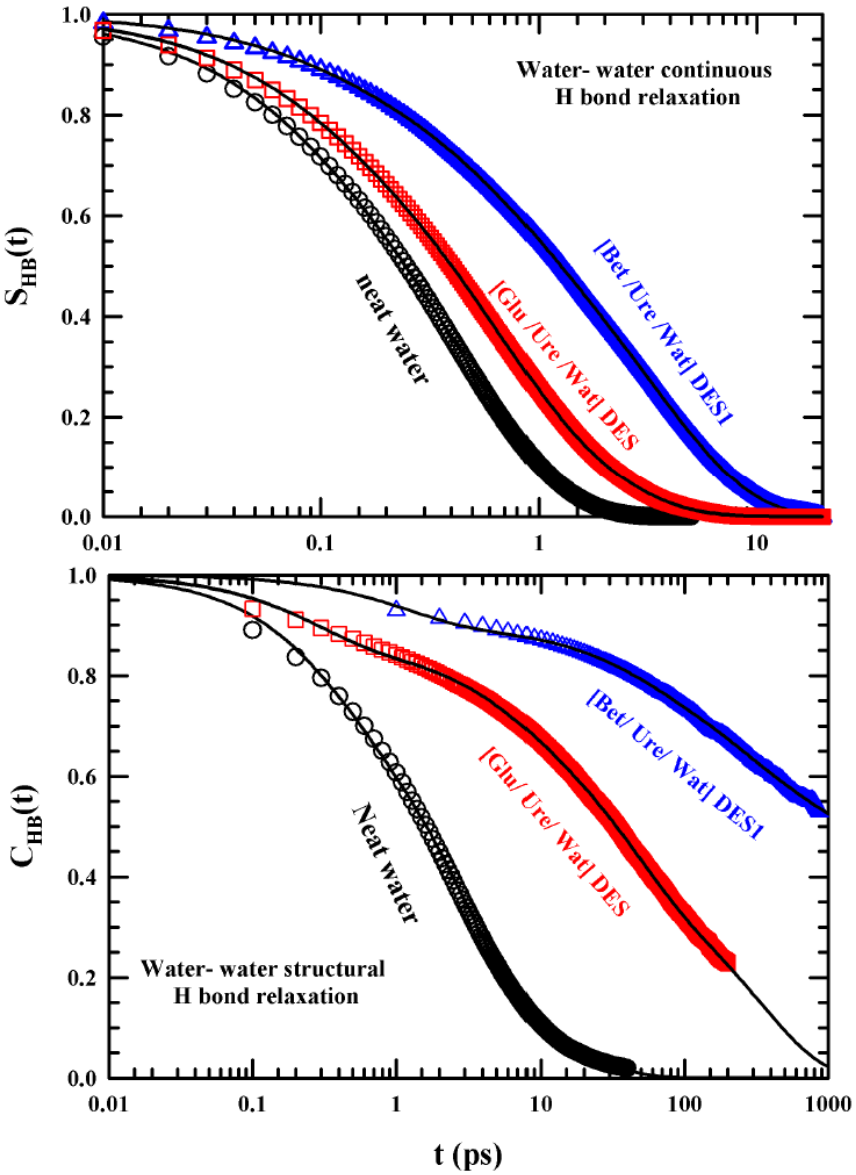

Figure 6.6: Continuous $S_{HB}(t)$ (upper panel) and Structural $C_{HB}(t)$ (lower panel) H-bond relaxation in neat water system, in [Glu/ Ure/ Wat] DES and in [Bet/ Ure/ Wat] DES1 at 328 K.

Table 6.1 and Table 6.2 summarize the multi-exponential decay fit parameters for all these relaxation decays. Both the continuous and structural water-water H-bond relaxations are found to be drastically slowed down in DES1 compared to neat water as well as glucose -based DES. More interestingly, an enormously slowed down nanosecond time component (~8ns with 60% amplitude) in structural water-water H-bond relaxation has been detected in the betaine-based ionic deep eutectic solvent (DES1). Although slowing down of structural as well as continuous water-water hydrogen bond relaxation has been reported [23] in glucose-based DES, no timescale in several nanosecond regime has been found. The slowest time component reported in glucose-based DES is ~350 ps with 40% amplitude. This drastic slow component of water-water structural hydrogen bond may be arising because of the caged motion of water molecules where they are hydrogen bonded with all possible moieties in betaine-based deep eutectic solvent (DES1). Also, this structural H-bond relaxation becomes 10^3 times slower compared to that in neat water system. This correlates well with the sluggish translational motion of water molecules in DES1 (already reported in chapter 5) where diffusion coefficients are found to be nearly 500 times slower than that in neat water system.

Table 6.1: Multi-exponential fit parameters for continuous water-water H-bond relaxations, $S_{HB}(t)$ in DES1, DES and neat water.

$S_{HB}(t)$ WW H-bonds	a_1	τ_1 (ps)	a_2	τ_2 (ps)	a_3	τ_3 (ps)	$\langle\tau\rangle$ (ps)	$\frac{\langle\tau\rangle}{\langle\tau\rangle_{neat}}$
DES1	0.08	0.09	0.25	0.58	0.67	3.57	2.55	6.22
Glucose-based DES	0.15	0.08	0.53	0.53	0.32	1.63	0.82	2
Neat water	0.19	0.08	0.81	0.49	-	-	0.41	1

Table 6.2:Multi-exponential fit parameters for structural water-water H-bond relaxations, $C_{HB}(t)$ in DES1, DES and neat water.

$C_{HB}(t)$ WW H-bonds	a_1	τ_1 (ps)	a_2	τ_2 (ps)	a_3	τ_3 (ps)	a_4	τ_4 (ps)	$\langle\tau\rangle$ (ps)	$\frac{\langle\tau\rangle}{\langle\tau\rangle_{neat}}$
DES1	0.1	1.14	0.09	41.32	0.22	245.1	0.59	7766.9	4664.7	1034.3
Glucose-based DES	0.14	0.26	0.12	5.32	0.35	36.63	0.40	346.60	137.11	34
Neat water	0.22	0.32	0.64	2.98	0.14	17.9	-	-	4.51	1

6.4 Conclusion

We reported in this chapter a thorough molecular dynamic simulation study of a NADES composed of betaine, urea and water. Detailed H-bond structure and dynamics of water molecules have been presented. These results are compared with simulation results of another naturally abundant glucose-based neutral DES ([Glu/Ure/Wat (6:4:1 weight ratio)]) and neat water system at the same temperature. Water molecules, being a minor yet integral part of these DESs, show drastically deviated H-bond structure in these DES compared to neat system. The effects of ionic environment present in this betaine-based DES have been identified. Water hydrogen bond lengths are found to be shorter in this DES compared to glucose-based DES and neat water. The inherent structure of water clustering identified in both these DESs are found to be different. Ionic environment of water molecules in this DES slows down the continuous water-water H-bond relaxation by ~3 to 6 times compared to glucose-based DES and neat system respectively. Structural water-water H-bond relaxations are ~34 times slower and ~10^3 times slower than the glucose-based DES and neat water respectively. These results corroborate well with the sluggish translational mobility of water molecules in this ionic DES reported in chapter 5.

Appendix 6.A

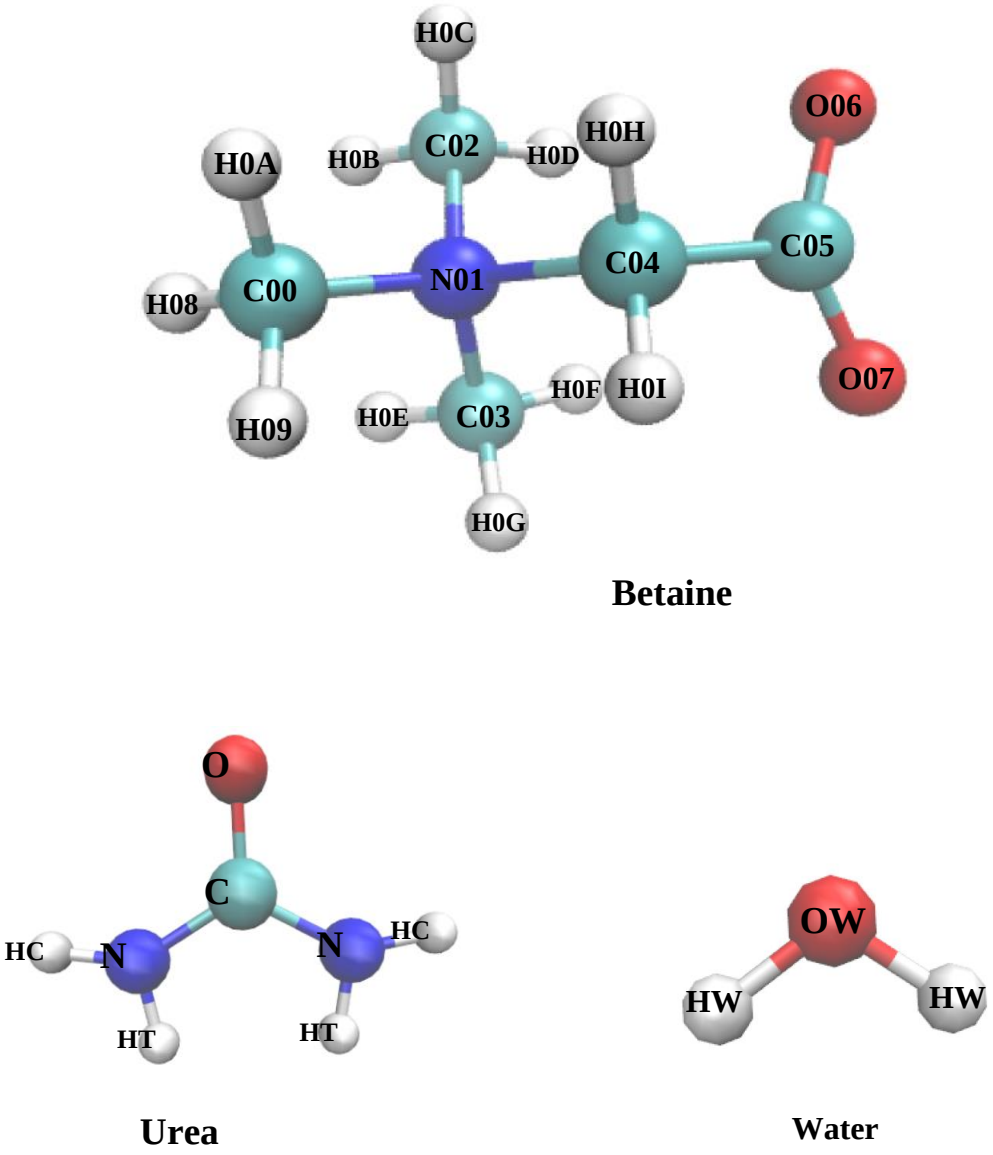

Figure 6.A.1: Chemical structures of betaine, urea and water along with the atomic sites as used in the present simulation.

Appendix 6.B

Table 6.B.1: Partial charges and Lennard-Jones parameters for betaine.

Atom types	Charge, e	σ (Å)	ε (kJ/mol)
C00	-0.1791	2.96	0.87864
N01	-0.0268	2.50	0.12552
C02	-0.1592	3.55	0.29288
C03	-0.1585	2.50	0.12552
C04	-0.2061	2.50	0.12552
C05	0.4863	3.50	0.27614
O06	-0.6274	2.50	0.12552
O07	-0.6274	2.96	0.87864
H08	0.1335	2.50	0.12552
H09	0.1335	3.50	0.27614
H0A	0.1335	3.50	0.27614
H0B	0.1439	2.50	0.12552
H0C	0.1439	3.25	0.71128
H0D	0.1439	2.50	0.12552
H0E	0.1438	2.50	0.12552
H0F	0.1438	2.50	0.12552
H0G	0.1438	2.50	0.12552
H0H	0.1173	3.50	0.27614
H0I	0.1173	2.50	0.12552

Table 6.B.2: Partial charges and Lennard-Jones parameters for urea.

Atom name	charge	σ (Å)	ε (kJ/mol)
C	0.124	3.75	0.65898
O	-0.322	2.96	1.31796
N	-0.453	3.55	1.06692
HT	0.276	0.00	0.00000
HC	0.276	0.00	0.00000

Table 6.B.3: Partial charges and non-bonded parameters for SPC/E water molecule.

Atom name	charge	σ (Å)	ε (kJ/mol)
OW	-0.8476	3.16	0.65
HW	0.4238	0.00	0.00

References

[1] E. Tarif, J. Mondal, and R. Biswas, J. Mol. Liq. **303**, 112451 (2020).

[2] S.E.C. Davies, R.A. Chalmers, E.W. Randall, and R.A. Iles, Clin. Chim. Acta. **178**, 241 (1988).

[3] W. Xing and C. Rajashekar, Environ. Exp. Bot. **46**, 21 (2001).

[4] M. Zhang, X. Wu, F. Lai, X. Zhang, H. Wu, and T. Min, J. Agric. Food Chem. **64**, 4068 (2016).

[5] A. Lawson-Yuen and H.L. Levy, Mol. Genet. Metab. **88**, 201 (2006).

[6] E. Kathirvel, K. Morgan, G. Nandgiri, B.C. Sandoval, M.A. Caudill, T. Bottiglieri, S.W. French, and T.R. Morgan, Am. J. Physiol. Gastrointest. Liver Physiol. **299**, G1068 (2010).

[7] S.A. Kempson, K. Vovor-Dassu, and C. Day, Cell. Physiol. Biochem. **32**, 32 (2013).

[8] A.P. Abbott, G. Capper, D.L. Davies, R.K. Rasheed, and V. Tambyrajah, Chem. Commun. 70 (2003).

[9] A.P. Abbott, G. Capper, D.L. Davies, K.J. McKenzie, and S.U. Obi, J. Chem. Eng. Data **51**, 1280 (2006).

[10] E.L. Smith, A.P. Abbott, and K.S. Ryder, Chem. Rev. **114**, 11060 (2014).

[11] P.B. Sánchez, B. González, J. Salgado, J. José Parajó, and Á. Domínguez, J. Chem. Thermodyn. **131**, 517 (2019).

[12] I.M. Aroso, A. Paiva, R.L. Reis, and A.R.C. Duarte, J. Mol. Liq. **241**, 654 (2017).

[13] S. Khodaverdian, B. Dabirmanesh, A. Heydari, E. Dashtban-moghadam, K. Khajeh, and F. Ghazi, Int. J. Biol. Macromol. **107**, 2574 (2018).

[14] D. Soletto, L. Binaghi, A. Lodi, J.C.M. Carvalho, and A. Converti, Aquaculture **243**, 217 (2005).

[15] A. Das and C. Mukhopadhyay, J. Phys. Chem. B **113**, 12816 (2009).

[16] N. Li, Y. Wang, K. Xu, Y. Huang, Q. Wen, and X. Ding, Talanta **152**, 23 (2016).

[17] L. Duan, L.-L. Dou, L. Guo, P. Li, and E.-H. Liu, ACS Sustain. Chem. Eng. **4**, 2405 (2016).

[18] B. Olivares, F. Martínez, L. Rivas, C. Calderón, J. M. Munita, and P. R. Campodonico, Sci. Rep. **8**, 14900 (2018).

[19] P.H. Yancey, J. Exp. Biol. **208**, 2819 (2005).

[20] C.-X. Zeng, S.-J. Qi, R.-P. Xin, B. Yang, and Y.-H. Wang, J. Mol. Liq. **219**, 74 (2016).

[21] W.L. Jorgensen and J. Tirado-Rives, Proc. Natl. Acad. Sci. U S A **102**, 6665 (2005).

[22] E. Tarif, J. Mondal, and R. Biswas, J. Phys. Chem. B **123**, 9378 (2019).

[23] A. Baksi, J. Rajbangshi, and R. Biswas, Phys. Chem. Chem. Phys. 2021 (submitted).

[24] L. Martínez, R. Andrade, E.G. Birgin, and J.M. Martínez, J. Comp. Chem. **30**, 2157 (2009).

[25] L.S. Dodda, I. Cabeza de Vaca, J. Tirado-Rives, and W.L. Jorgensen, Nucleic Acids Research **45**, W331 (2017).

[26] L.S. Dodda, J.Z. Vilseck, J. Tirado-Rives, and W.L. Jorgensen, J. Phys. Chem. B **121**, 3864 (2017).

[27] B. Doherty and O. Acevedo, J. Phys. Chem. B **122**, 9982 (2018).

[28] U. Essmann, L. Perera, M.L. Berkowitz, T. Darden, H. Lee, and L.G. Pedersen, J. Chem. Phys. **103**, 8577 (1995).

[29] B. Hess, H. Bekker, H.J. Berendsen, and J.G. Fraaije, J. Comp. Chem. **18**, 1463 (1997).

[30] G. Bussi, D. Donadio, and M. Parrinello, J. Chem. Phys. **126**, 014101 (2007).

[31] H.J. Berendsen, J. van Postma, W.F. van Gunsteren, A. DiNola, and J.R. Haak, J. Chem. Phys. **81**, 3684 (1984).

[32] R.W. Hockney, S. Goel, and J. Eastwood, J. Comp. Phys. **14**, 148 (1974).

[33] S. Páll, M.J. Abraham, C. Kutzner, B. Hess, and E. Lindahl, in (Springer, 2014), pp. 3–27.

[34] H. Bekker, H. Berendsen, E. Dijkstra, S. Achterop, R. Van Drunen, D. Van der Spoel, A. Sijbers, H. Keegstra, B. Reitsma, and M. Renardus, in (World Scientific Singapore, 1993), pp. 252–256.

[35] M.J. Abraham, T. Murtola, R. Schulz, S. Páll, J.C. Smith, B. Hess, and E. Lindahl, SoftwareX **1**, 19 (2015).

[36] A. Luzar, Faraday Discus. **103**, 29 (1996).

[37] A. Luzar and D. Chandler, J. Chem. Phys. **98**, 8160 (1993).

[38] S. Balasubramanian, S. Pal, and B. Bagchi, Phys. Rev. Lett. **89**, 115505 (2002).

[39] A. Chandra, Phys. Rev. Lett. **85**, 768 (2000).

[40] T.C. Berkelbach, H.-S. Lee, and M.E. Tuckerman, Phys. Rev. Lett. **103**, 238302 (2009).

[41] J.R. Errington and P.G. Debenedetti, Nature **409**, 318 (2001).

Chapter 7

Concluding Remarks and Future Problems

7.1 Concluding Remarks

The present Thesis reported a detailed investigation on interaction and dynamics of complex liquid systems, via molecular dynamics simulations and compared results with those from experiments wherever possible. These systems are complex because they possess r^{-1} , r^{-2} and r^{-3} interactions (r being the inter-particle distance) in addition to apolar and H-bonding interactions. The molecules are not spherical and the systems are inherently non-homogeneous. Considering these complexities, the simulations presented here have only focused on exploring several relevant phenomena in solution phase and provide qualitative but microscopic understanding of several experimental findings. The systems studied are room temperature ionic liquids, their binary mixtures with common molecular solvents, and deep eutectic solvents (DESs). The DESs considered here are three component molten mixtures with one of the components being water. These solvent systems have already found applications in various chemical industries [1,2], and waiting for further and smarter applications. Addition of small molecular solvents into these ionic liquids can improve upon and add versatility to their role as reaction media. The spatio-temporal heterogeneity of the binary mixtures of ionic liquid and various cosolvents have been explored to understand the structure and dynamics of these systems. The chemical physics view of glassy supercooled systems has been employed to examine various exciting experimental findings for ionic liquids and deep eutectics, and subsequently, attempts have been made to explain them applying the 'glass language'.

Our study on ionic liquid and its binary mixtures with cosolvents have revealed that the structure and dynamics of the ionic liquid in these mixtures respond to both IL concentration and cosolvent polarity. Pronounced aggregation behavior of [BMIM] [PF_6] ionic liquid is obtained at high IL concentrations in non-polar solvent. Signatures for dynamic heterogeneity in IL mixtures have been investigated extensively via non-Gaussian distributions, dynamic structure factor and four-point correlations and the heterogeneity features have been found to soften upon increasing the polarity of the cosolvent. We haven't considered water as a cosolvent as aqueous mixtures of ionic liquids have already been studied via simulations by

several other authors[3,4] in the past. The findings for deep eutectic solvents are also quite exciting as they show strong heterogeneity signatures at temperatures ~50-150K above their respective glass transition temperatures. As these deep eutectics contain water as a minor yet integral component, we used this opportunity to focus entirely on the structure and dynamics of water in such a crowded environment. Both the structure and dynamics of water in these deep eutectics have been found to be dramatically different from those in neat water. We have found reorientation relaxations in these DESs accompany strong translational-rotation decoupling and a considerable deviation from the Debye's law for stochastic angular displacements. This simulation finding has found appropriate support in the dielectric relaxation (DR) measurements of the same system which have revealed a pronounced fractional viscosity dependence of average DR times.

Since conclusions have been provided at the end of each of the chapters in the present Thesis, we refrain from providing an over-all conclusion separately. Instead, we discuss here a few interesting and relevant problems, which can be studied in near future.

7.2 Future Problems

7.2.1 Alkyl chain-length dependence of Spatial and Temporal Heterogeneity in (Ionic Liquid + cosolvent) binary mixtures

Small angle X-ray scattering [5] (SAXS), neutron scattering [6] (SANS), neutron-spin echo [7,8] and molecular dynamics simulations [9,10] of ionic liquids (ILs) have indicated that the aggregation of alkyl groups of IL cation increases with increase in alkyl chain length, inducing spatial heterogeneity in the system. Dependence of spatio-temporal heterogeneity on alkyl chain length has also been observed in fluorescence anisotropy measurements [11] of amide/electrolyte deep eutectic solvents. In our recent simulation study [12], it is revealed that the solution structure and dynamic heterogeneity of the binary mixtures of [BMIM] [PF_6] ionic liquid with three cosolvents of different polarities respond to the mixture compositions and cosolvent polarity. Pronounced aggregation behavior of this ionic liquid is observed in presence of non-polar hexane [12]. The heterogeneity signatures are found to be more pronounced in rich IL solutions and for solutions with less polar cosolvents. So, a comprehensive study on alkyl chain-length dependence of heterogeneity features in binary mixtures of ionic liquids with small molecular cosolvents of different polarities would be exciting not only from the basic science considerations but also would be useful in providing inputs to liquid solvent engineering, focussing on controlling products via tailoring reaction media.

7.2.2 Heterogeneous Orientational Relaxation and Translation-Rotation Decoupling in (Betaine + Urea + Water), a Naturally Abundant Deep Eutectic Solvents: A Combined study of Molecular Dynamics Simulations and Dielectric Relaxation Measurements

Recent temperature dependent dynamic stokes shift and fluorescence anisotropy measurements in (Betaine + Urea + Water) deep eutectic solvents (DESs) revealed the evidences for spatio-temporal heterogeneity in this system[13]. So, for better understanding of the available fluorescence spectroscopic data, a combined study of temperature dependent dielectric relaxation measurements and computer simulations in this DES system is required. Dielectric relaxation measurements can probe the inherent orientational dynamics of the given medium, and provide important information about the coupling between the structural and dynamical properties of polar condensed phases. Simulated reorientational correlations and the H-bond relaxations can explain the microscopic origin of the time scales obtained in DR measurements

in H-bonded systems. Therefore, a combined simulation and experimental study of dielectric relaxation can provide a detailed understanding of the microscopic reorientation dynamics of such DESs.

7.2.3 Effects of Ionic Environment on Heterogeneous Orientation Relaxation and Translation-Rotation Decoupling: Simulation Results of Betaine and Glucose based Naturally Abundant Deep Eutectic Solvents (NADESs)

Presence of heterogeneous dynamics in ionic (Betaine + Urea + Water) [13] and neutral (Glucose + Urea + Water) [14] NADESs have been reflected by the break-down of hydrodynamics via the fractional viscosity dependence of solute rotation and solvation times, obtained from earlier dynamic Stokes shift and fluorescence anisotropy measurements. A comparative study of these two DESs is needed to explore the effects of ionic environment on the orientation relaxation dynamics in these systems. Also, it would be interesting to explore the impact of ionic environment on translation-rotation decoupling in these two systems.

7.2.4 Water Structure and Dynamics in "Crowded" Environments provided by Deep Eutectic Solvents to Room temperature Ionic Liquids: How Different are They?

There exist numerous studies[15–17] exploring extent of perturbation on water hydrogen bonding structure in various binary and ternary mixtures. Most of these studies were aimed to probe the hydrogen bond structure and dynamics where water is a majority in those solutions. Recently, our comparative simulation study of ionic (Betaine + Urea + Water) and neutral (Glucose + Urea + Water) DES, where water is a minor yet integral component, explored the water structure and hydrogen bond dynamics in a crowded bulk environment. This type of study on H-bond structure and dynamics of water is new and novel, and motivates to search for generic features that may exist in multi-component mixtures where water is present at a very low concentration. Molecular dynamics simulations of these DESs, urea-water binary mixtures, water in ionic liquid hosts (for example, [OMIM][BF_4]/[BMIM][BF_4]), aqueous tert-butyl alcohol (TBA) solution at very high TBA concentration etc. can be carried out to uncover commonalities in water structure and dynamics and their differences from the neat water counter-parts. Water, being an inseparable part of life, is still a mystery. The adaptive power of water and its adamant attitude to preserve the tetrahedral H-bond network structure must be

explored in various thermodynamic and chemical conditions for understanding its integral relation to civilisation.

The present Thesis and these future problems are only representative of a vast collection of what could be done to fuel the excitement with these two new classes of solvents which possess the potential to revolutionize the liquid solvent engineering for industrial application, and can address successfully the fundamental relationship between the environment and industry.

References

[1] D. Carriazo, M.C. Serrano, M.C. Gutiérrez, M.L. Ferrer, and F. del Monte, Chemical Society Reviews **41**, 4996 (2012).

[2] P. Liu, J.-W. Hao, L.-P. Mo, and Z.-H. Zhang, RSC Advances **5**, 48675 (2015).

[3] T. Pal and R. Biswas, J. Phys. Chem. B **119**, 15683 (2015).

[4] A. Sharma and P.K. Ghorai, J. Chem. Phys.**144**, 114505 (2016).

[5] A. Triolo, O. Russina, B. Fazio, R. Triolo, and E. Di Cola, Chem. Phys. Lett. **457**, 362 (2008).

[6] C. Hardacre, J.D. Holbrey, C.L. Mullan, T.G. Youngs, and D.T. Bowron, J. Chem. Phys. **133**, 074510 (2010).

[7] O. Yamamuro, T. Yamada, M. Kofu, M. Nakakoshi, and M. Nagao, J. Chem. Phys. **135**, 054508 (2011).

[8] M. Kofu, M. Nagao, T. Ueki, Y. Kitazawa, Y. Nakamura, S. Sawamura, M. Watanabe, and O. Yamamuro, J. Phys. Chem. B **117**, 2773 (2013).

[9] H.V. Annapureddy, H.K. Kashyap, P.M. De Biase, and C.J. Margulis, J. Phys. Chem. B **114**, 16838 (2010).

[10] C.S. Santos, H.V. Annapureddy, N.S. Murthy, H.K. Kashyap, E.W. Castner Jr, and C.J. Margulis, J. Chem. Phys. **134**, 064501 (2011).

[11] B. Guchhait, S. Das, S. Daschakraborty, and R. Biswas, J. Chem. Phys. **140**, 104514 (2014).

[12] J. Rajbangshi, S. Banerjee, P.K. Ghorai, and R. Biswas, J. Mol. Liq. **317**, 113746 (2020).

[13] E. Tarif, J. Mondal, and R. Biswas, J. Mol. Liq. **303**, 112451 (2020).

[14] E. Tarif, J. Mondal, and R. Biswas, J. Phys. Chem. B **123**, 9378 (2019).

[15] A. Baksi and R. Biswas, J. Phys. Chem. B **124**, 11718 (2020).

[16] S. Dixit, J. Crain, W. Poon, J.L. Finney, and A.K. Soper, Nature **416**, 829 (2002).

[17] S. Sarkar, A. Maity, and R. Chakrabarti, Phys. Chem. Chem. Phys. **23**, 3779 (2021).